Morphodynamic evolution of Bogue Inlet, NC, USA: an annual-to decadal-scale geophysical, hydrodynamic, sedimentological, and microfossil analysis

by

Cody David Brown

December 2024

Director of Thesis: David J. Mallinson

Department of Geological Sciences

ABSTRACT

Tidal inlets are the most dynamic and complex sedimentary environments in the coastal zone. The morphologic and hydrodynamic processes acting on the ebb-tidal and flood-tidal deltas aided by the tidal prism allow the transport of sand throughout the complex to drive evolution in correlation with ebb-tidal delta volume. By better understanding these morphodynamic relationships in response to the increase in magnitude and frequency of storms, we can understand the future of coastal siliciclastic systems. This study focused on Bogue Inlet, located on a sediment-starved cuspate embayment, Onslow Bay, on the southeastern coast of North Carolina. The study used a multifaceted approach implementing geospatial, geophysical, sedimentological, micropaleontological, hydrodynamic modeling and a novel stratigraphic model methodology. Geospatial data show that this micro-tidal inlet exhibited migration to the northeast. Furthermore, hydrodynamic and geospatial data suggest the migration pattern is most likely due to the main tidal channel responding to hydraulic changes, forced by back-barrier migration of tidal channels, and the flood tidal delta as the tidal prism changed through time. The hydraulic changes were a function of sediment influx from (natural and unnatural actions),

transported by wave and current interactions from varying atmospheric events, with the most extensive morphologic changes observed in the most highly energetic states, hurricanes, and extratropical-like storms. Specific meteorologic events with varying wind direction and magnitude induced the reversal of tidal and longshore currents, leading to a confluence of currents within the inlet, which supported deposition in specific locations on the flood-tidal delta, middle shoals, and ebb-tidal delta. These meteorologic events led to changes in volumetric discharge through the inlet, causing other erosion areas (inlet thalweg). Sedimentological and foraminiferal data show that important parameters of sediment and foraminiferal transport are storm track, size, and magnitude, which can result in the forcing of heightened sea states, causing onshore transport. The digital stratigraphic model and geophysical data moderately agreed on general locations of relict geomorphic features that suggest similar morphodynamic evolution to what is observed in the geospatial data, corroborated by the hydrodynamic data. However, the novel stratigraphic model and the acoustic sub-bottom data were not expected to agree entirely due to one year, five months, and five days between the data used in creating the stratigraphic model and the data collected with the sub-bottom profiler. The geophysical data and stratigraphic modeling also suggest hydrologic conditions that would transport a specific grain size to the deposition locations, creating the features observed in corresponding locations. The results together help constrain the inlet's evolution through time, varying atmospheric conditions, and human influences.

Morphodynamic evolution of Bogue Inlet, NC, USA: an annual- to decadal-scale geophysical, hydrodynamic, sedimentological, and microfossil analysis

A Thesis

Presented to the Faculty of the Department of Geological Sciences

East Carolina University

In Partial Fulfillment of the Requirements for the Degree

Master of Science in Geology

By

Cody Brown

December 2024

Director of Thesis: Dr. David Mallinson

Co-Director of Thesis: Dr. Stephen Culver

Committee Member: Dr. Hannah Sirianni

Committee Member: Dr. Ryan Mulligan

DEDICATION

I want to dedicate this work to anyone who, in their life, has been put in a situation where conventional wisdom says that one should not overcome the circumstances put in front of them. No matter talent or gifts, dedication, determination, and work ethic will always see one through hard times to the end of the road, reaching goals that seem so untouchable that they are impossible to achieve. One thing is true. Science has taught me that nothing, nothing less than bending the laws of nature, is impossible. No matter the physiological or sociological obstacle, no obstacle is too big to overcome. Precise decision-making and consistency can be the road map for anyone, at least on this rock, to turn their life around and reach for the stars. To be the one they have always wanted to be, the one they have dreamed of. I want to say cheers to anyone on that path; keep looking up, reaching for the next rung, and climb, climb, climb! You will get there in time.

ACKNOWLEDGMENTS

First, I thank family, friends, and loved ones for their support, camaraderie, competitiveness, and inspiration to fight to overcome. Thanks, Mom and Pop. Secondly, I would like to thank the scientific community for creating a space dedicated to truth or the journey to objective truths, not personal or political ones. I would also like to thank my unmatched committee, Dr. David Mallinson, Dr. Stephen J. Culver, Dr. Hannah Sirianni, Dr. Ryan P. Mulligan, and Dr. Stuart Pearson, for their wisdom, guidance, patience, and overall good spirits! Great thanks are given to Geodynamics, LLC, and both Chris Freeman and Rudi Rudolph for the ability to obtain the data that helped drive this study. I thank the department and faculty of Geological Science at ECU for their excellence, friendships, and encouragement on this path and in the future. I thank the National Science Foundation for the NSF grant OCE-1841835, which partially funded this research. I thank everyone, from all the boat captains to the lab mechanics, for aiding in sample collection and helping with any other needs to keep the journey going. I would also like to thank the geography department at ECU, everyone from Dr. Scott Lecce, who encouraged a commitment to ECU, to the chair, Dr. Jeff Popke, and the committee for taking a chance on admitting a student who wanted to pursue a dream to become an active academic scientist. Lastly, I must thank my past mentors, Dr. Patrick Burkhart, Dr. Julie Snow, Dr. Paul Baldauf, Dr. Tamra Schiappa, and Dr. Jack Livingston, for the passion they helped instill for the Earth sciences, the knowledge that was passed down, the opportunities, and unforgettable experiences. I thank every one of you. Cheers!

TABLE OF CONTENTS

LIST OF TABLES

LIST OF FIGURES

LIST OF EQUATIONS

1.0 INTRODUCTION

Morphodynamic processes control the evolution of coastlines and their morphologic features. External and internal feedback factors influence the adjustment in the topography and, therefore, the fluid dynamics in response to sediment transport and deposition, roughly defining morphodynamic processes (Komar, 1998; FitzGerald et al., 2011; Komar, 2018). Physical settings and processes that contribute to coastal evolution include the tectonic setting, whether active or passive, antecedent topography, glacial-isostatic adjustment, climate conditions, sea-level change, sediment flux from various sources (rivers, eroding shorelines, etc.), and atmospheric and ocean dynamics (wind, waves, tides) (Komar, 1998; Riggs et al., 1995; FitzGerald et al., 2011; Mallinson et al., 2018). All factors affect the sediment supply, erosion, transport, and deposition. Those stated dynamics will respond as the earth's climate changes and coastal evolution occurs. Understanding these processes and their geologic record is the basis of this thesis.

The IPCC Assessment Report 6 states, "The extent and magnitude of climate change impacts are larger than estimated in previous assessments (high confidence)" IPCC AR6 (2023). As documented in 2019, atmospheric CO_2 and CH_4 concentrations reached 410 parts per million and 1,866 parts per billion, respectively. Concentrations of CO_2 and CH_4 have increased above pre-industrial concentrations by 47% and 156%, respectively, outpacing the natural multi-millennial changes between glacial and interglacial periods over at least the past 800,000 years IPCC AR6, (2023). Atmospheric CO_2 concentrations are now higher than during the past three million years IPCC AR6 (2023). These greenhouse gas changes directly affect sea-level rise by melting glaciers and ice sheets and the thermal expansion of seawater resulting from increasing global temperatures. Currently, the average global rate of sea-level rise has reached 3.3 mm/yr and continues to accelerate (Figures 1 and 2)

Figure 1. Plot showing sea-level trends versus time (years CE). Data are derived from satellites measuring different components contributing to eustatic sea level rise. The bottom line represents the ARGO satellite and buoy system run by NOAA, which measures the thermal expansion of the oceans. The middle line represents the Grace satellite array and the mass distribution change of our oceans. The top line, reaching back to 1993, represents the mean global sea level measured by altimetry satellites. The last top trend line combines satellite array measurements (ARGO + GRACE/GRACE-FO). Source: IPCC AR6 (2023).

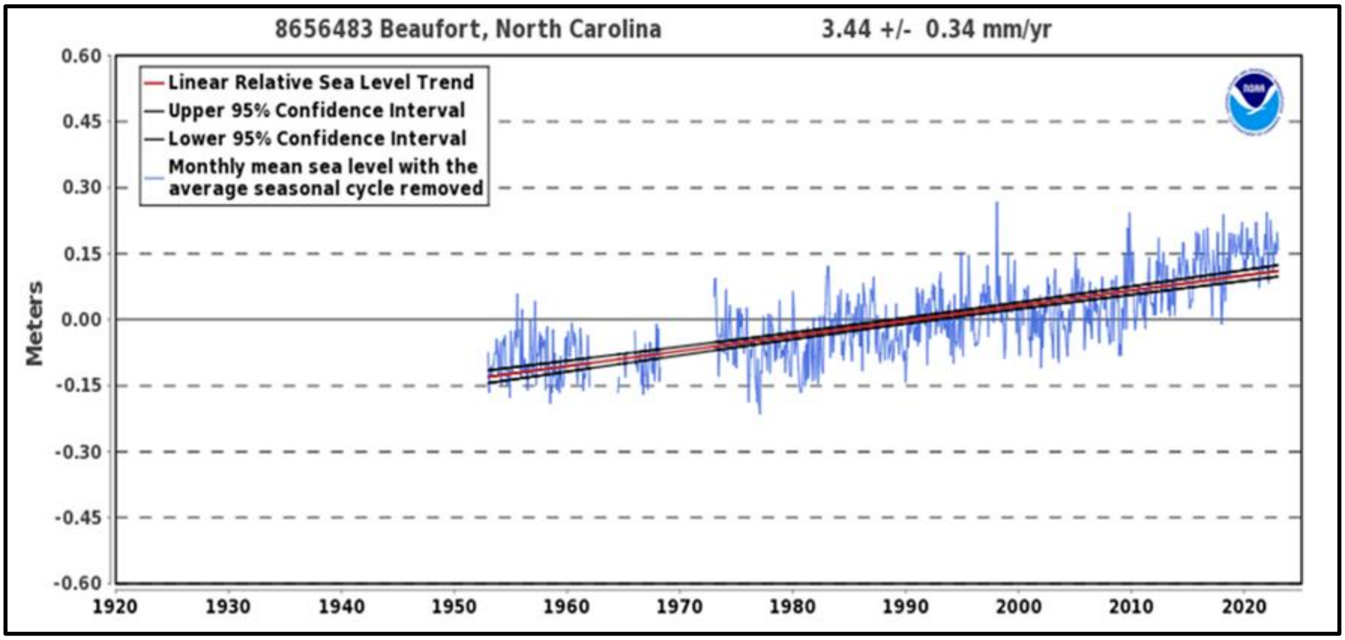

Figure 2. Based on tidal gauge data, the graph shows the relative sea-level trend for Beaufort, North Carolina. The relative sea-level trend is 3.44 millimeters/year with a 95% confidence interval of +/- 0.34 mm/yr. Based on monthly mean sea level data from 1953 to 2023, this is equivalent to a change of 0.5 meters in 100 years. Source: https://tidesandcurrents.noaa.gov/sltrends/sltrends_station.shtml?id=8656483

There is also overwhelming evidence indicating that disruptions in atmospheric patterns are leading to more frequent extreme weather events. The latest IPCC report states that it is likely that the global proportion of major (Category 3–5) tropical cyclone occurrences has increased over the last four decades IPCC AR6 (2023). This observation is echoed by Masters (2022), who showed that in the past 30 years, the Atlantic basin had seen a 14% increase in hurricane activity. All trends indicate a continued acceleration of changes in coastal regions, negatively impacting natural and human habitats. From 2002 to 2022, 46 cyclonic systems were recorded within a 120-mile radius of Bogue Inlet, represented in (Figure 3) with storm numbers, dates, and categories in (Table 1).

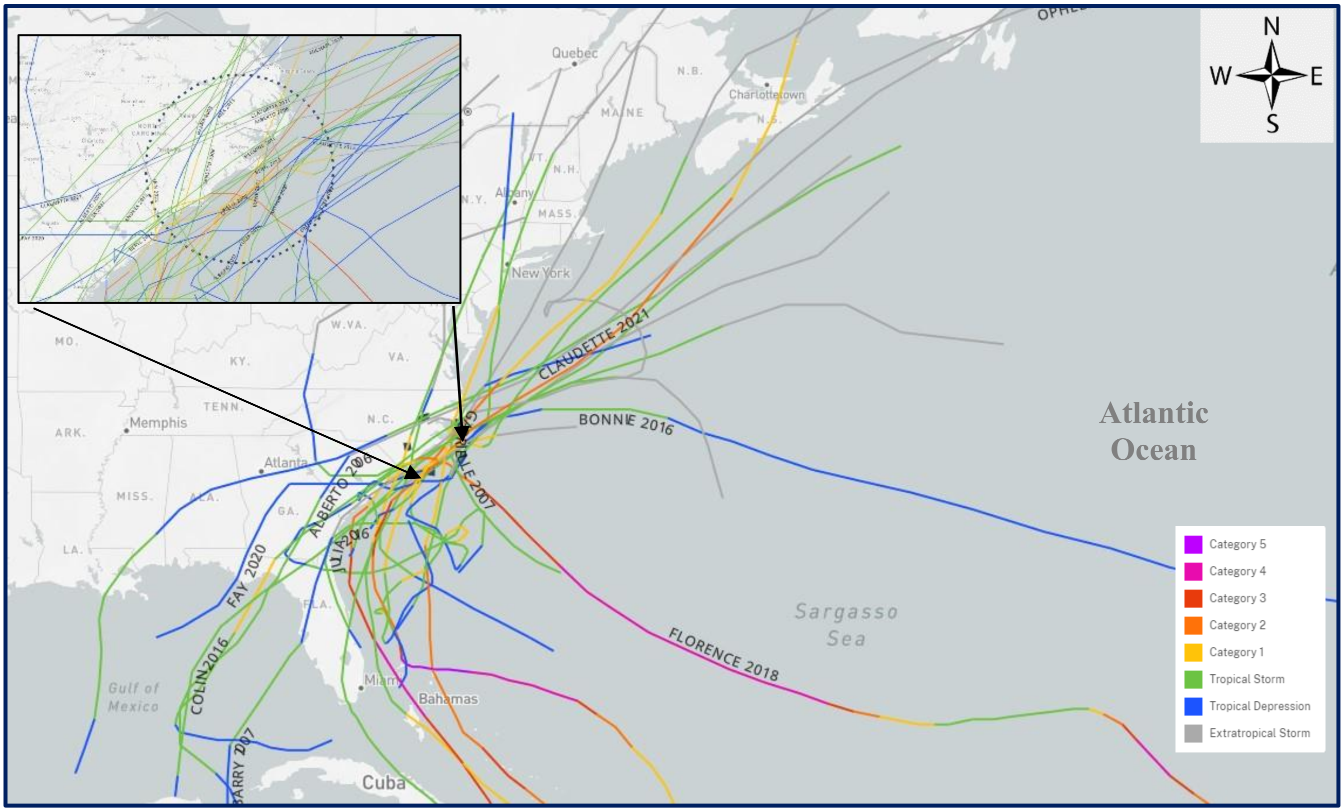

Figure 3. Total of storm tracks in the Atlantic basin. Within 120 nautical miles of Bogue Inlet, from 2002 to 2022, there were 46 tropical cyclones ranging in strength from extratropical storms to Category three hurricanes. Source: https://coast.noaa.gov/hurricane

Table 1. Total of storm tracks in the Atlantic basin. Within 120 nautical miles of Bogue Inlet, from 2002 to 2022, there were 46 tropical cyclones ranging in strength from extratropical storms to Category three hurricanes. Source: https://National Weather Service.gov

Date	# of storms	extra-tropical	TD	TS	Cat 1	Cat 2	Cat 3	Cat 4	Cat 5
2022	2			1	1				
2021	4		2	2					
2020	5	1	2	2	1				
2019	2					1			
2018	2			1		1			
2017	1			1					
2016	6	1	3	1	1				
2015	2		1	1					
2014	1					1			
2013	1			1					
2012	2		1	1					
2011	1				1				
2010	0								
2009	1		1						
2008	2		1	2					
2007	2	1		1					
2006	2	1		1					
2005	1				1				
2004	5	1	2		1	1			
2003	1					1			
2002	3		1	2					
	Total # 46								

A region of significant concern is the low-lying coastal plain along the eastern seaboard of North America. This region is a tectonically passive margin Zhong-Hai and Zhong (2021). It exhibits characteristic features such as a broad coastal plain with a continental shelf that varies in width, extensive barrier island systems and estuaries, and cuspate forelands (cape structure). North Carolina's barrier islands stretch from the northernmost state line with Virginia to the southern state line with South Carolina (Figure 4). Barrier islands are an elongated body of sand or gravel that persists above the mean higher high-water level (Komar, 1998; Burningham and French, 2007) (Figure 5) and are separated from the mainland by a lagoon or estuary and from adjacent islands by tidal inlets. The factors that determine the morphology and evolution of all barrier islands include relative sea-level rise, longshore distribution of sediment and littoral cells, the energy of atmospheric and oceanic factors (waves and tides), and the water exchange through inlet channels (i.e., tidal prism) Komar (1998).

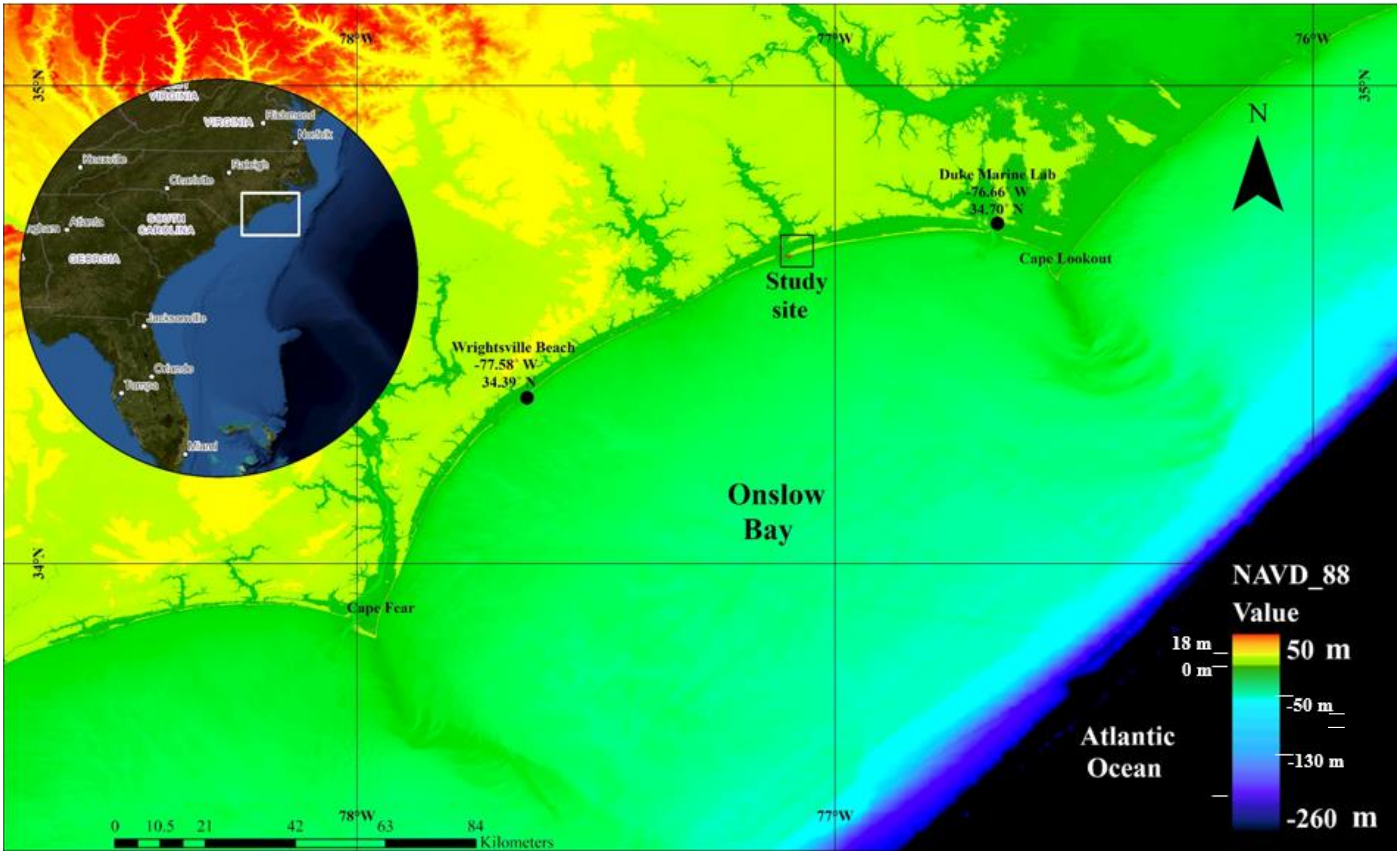

Figure 4. Topographic/bathymetric map of North Carolina, Onslow Bay, and the NC continental shelf. It shows the major subaerial and subaqueous cape structures; the black dots are the observation points used in the hydrodynamic models, and the black square represents the study site location. The datum used in the topo/bathymetric digital elevation data is DWGS 1984, in meters. Data source: https://gis.ngdc.noaa.gov/arcgis/services/DEM_mosaics/DEM_global_mosaic/ImageServer

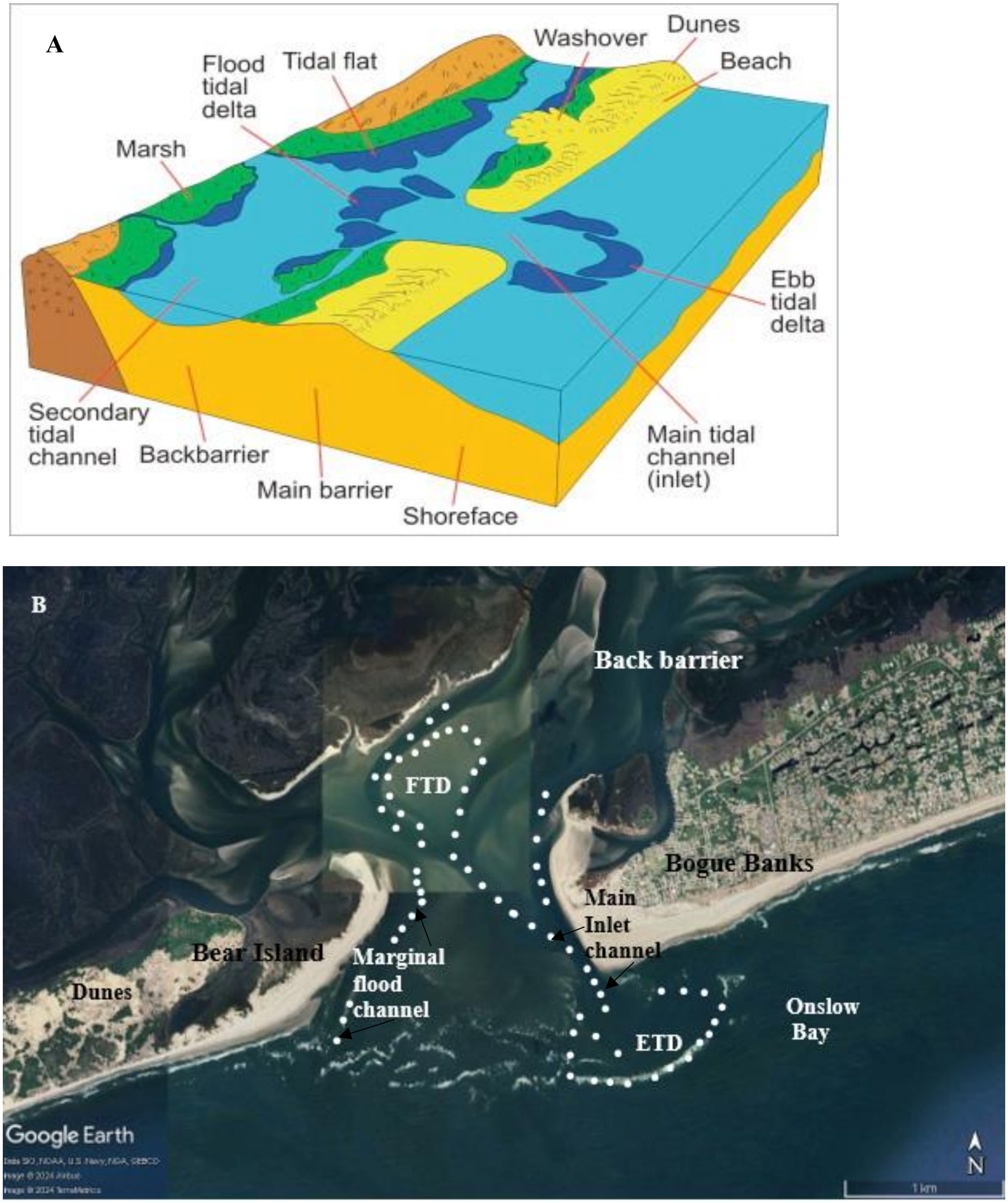

Figure 5. **A)** Diagram depicting a barrier island system's components Slatt (2013). **B)** Aerial image of the study region with morphological features labeled.

Inlets are essential for the health of barrier islands, playing a fundamental role in the transgression of barrier islands due to rising sea levels. They also provide a vital service to the estuarine systems that back them (Riggs et al., 1995; Komar, 1998; FitzGerald et al., 2011; Mallinson et al., 2018; Raff et al., 2018). Fresh water from rivers draining into the estuaries mixes with saline water from the ocean funneled through inlet channels to create the brackish environment vital for shallow water ecosystems Mallinson et al. (2018). Salt marshes and sea grass beds depend on this relationship because they reside in brackish sheltered environments that aid in primary and secondary production Valiela et al. (2002). With adequate protection, the salt marsh vegetation can exhibit a ramped or platform morphology aided by tidal sedimentation, a pivotal factor in barrier island transgression FitzGerald et al. (2008). Furthermore, these estuarine ecosystems greatly benefit society and the biodiversity they harbor, from promoting sustainable fisheries, purifying water, acting as blue carbon sinks, and fighting against ocean acidification, as new studies show Bergstrom (2019). The tidal inlet's morphology, shape, and geometry are all a function of the tidal prism. The tidal prism is the amount of water, in volume, that can travel through the inlet channel in any given half-tidal cycle. Any changes to the morphology of the inlet channel and its morphodynamics will cause the tidal prism to change (Fitzgerald, 1976; FitzGerald et al., 2008; FitzGerald et al., 2011).

Inlet channels and their associated morphology provide for healthy coastal ecosystems, and humans have used them for centuries as navigable conduits between rough open oceans and protected estuarine waters Mallinson et al. (2008). As critical economic assets, inlets nurture trade and commerce in the context of ecotourism and the commercial fishing industries that dot the coasts globally. Inlet morphological features can also be resources for coastal management entities, as their ebb-tidal deltas can also be sediment sinks in the littoral cell and can hold up to

100 million m³ of sand that can be utilized for beach nourishment projects on the adjacent coastlines Cleary (1996). Although inlet systems provide these vital services to society and nature, they are dynamic features. With their shifting sand shoals, the dynamic changes can be dangerous to vessels, causing numerous groundings, especially along the coast of North Carolina. Due to their constant migration through space and time, coastal managers, agencies, and residents must be aware of the workings of inlet systems. Thus, it is crucial to understand inlet morphodynamics and the relationship between the sediment budget, associated barrier island morphology, and how they will react to climate-induced change.

This research aims to study the morphodynamic changes in Bogue Inlet, N.C. (Figures 4 and 5) in response to major storm events and low energy conditions. It also aims to verify observations using a novel computer-generated stratigraphic model Pearson et al. (2022). A better understanding of Bogue Inlet will improve the understanding of coastal evolution and sediment dynamics on the U.S. eastern seaboard and directly benefit the N.C. region where the inlet exists. Due to the acquisition of ten-plus years of bathymetric data, the following hypotheses and objectives can be addressed.

1.1 Hypotheses

Hypothesis 1: The stratigraphic model developed by Pearson et al. (2022) and geophysical CHIRP sub-bottom data will agree on defining units that reflect the inlet's long-term morphologic evolution.

Hypothesis 2: The stratigraphic model indicates the location of units on the seabed that formed at different times and in response to different energies. These units may be distinguished based on sedimentology and microfossil assemblages.

Hypothesis 3: The hydrodynamic modeling will show the mechanisms governing both morphologic and volumetric changes over the temporal period of the surveys analyzed, correlated with times encompassing high storm activity and significant storm events.

1.2 Objectives

To test these hypotheses, this study:

1. Quantifies the volumetric and morphologic change between digital elevation models (DEMs) of Bogue Inlet's ebb-tidal delta to assess the morphodynamic evolution in response to major hurricane events and during low energy conditions.
2. Provides ground truth for the stratigraphic model by collecting and analyzing geophysical CHIRP sub-bottom data.
3. Uses available DEMs to create hydrodynamic models using Delft3D Flexible Mesh modeling. Oceanic and atmospheric conditions define the boundary conditions for the hydrodynamic models to evaluate the potential for morphological changes occurring during storms.
4. Analyzes sediment samples acquired from modeled and seismically imaged units for sedimentological and microfossil characteristics to inform on sediment transport.

2.0 BACKGROUND

2.1 Physical settings

Bogue Inlet is located between two barrier islands, Bear Island to the southwest and Bogue Banks to the northeast (Figures 4 and 5). The inlet is located in the northwest of Onslow Bay, a broad embayment just south of Raleigh Bay, making up the top portion of the South Atlantic Bight. The bay is positioned between two cuspate forelands. It is bounded by Cape Lookout to the north and Cape Fear to the south. Cape Fear and Cape Lookout interact with wave energy from the Atlantic and influence the evolution of Bogue Inlet and other inlets in Onslow Bay (Riggs et al., 1995; Park & Wells, 2005). The region is microtidal, 1.0 m to 1.7 m, with significant wave heights of 1.2 m (Sea level trends - NOAA tides & currents, 2023). This wave-dominated region harbors ten inlets in Onslow Bay. Due to the low tidal range, constituting micro-tidal and predominant wave energy, the barriers in Onslow Bay exhibit long and narrow morphologies. Sitting along the mid-latitudes at 34.49˚ N and 76.54˚ W, Bogue Inlet is in the path of tropical and extratropical cyclones (Figure 3). Upper-level atmospheric steering patterns like the Bermuda High steer hurricanes into the bay, and nor-easters (intense extratropical cyclones) commonly form off Cape Hatteras to the northeast Robert (1993). Not every cyclonic system has to make landfall with a region of the coast to cause adverse effects. From the center of circulation, Hurricane-force winds, 119 kph and up, can reach 75 nm to the right of the depression and 50 nm to the left, depending on the depression size (Figure 6). This geographical location coincides with high amounts of wave energy produced by these events.

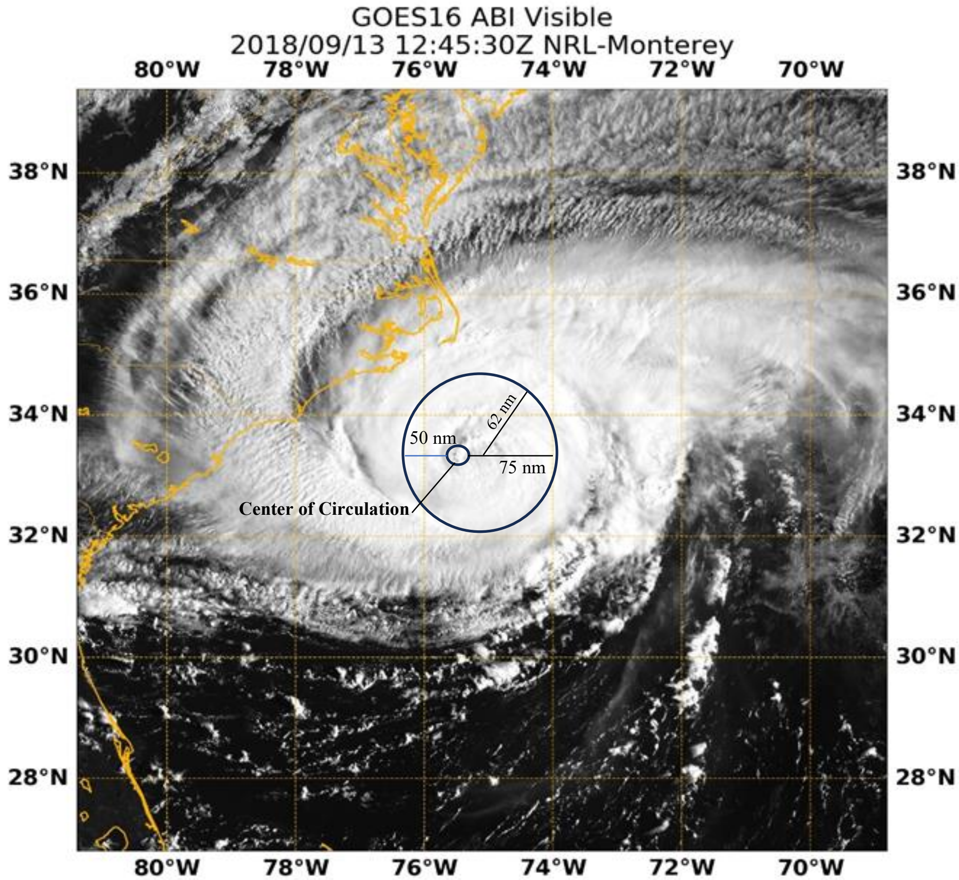

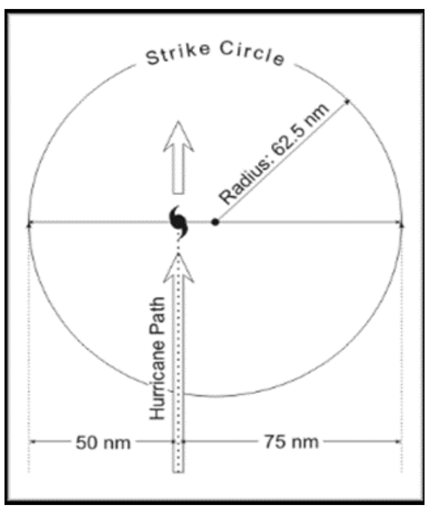

Figure 6. Top and bottom "strike circle": For any location, a hurricane strike occurs if that location passes within the hurricane's strike circle, a circle of 125 nm diameter, centered 12.5 nm to the right of the hurricane center (looking in the direction of motion). This circle is meant to depict the typical extent of hurricane-force winds, approximately 75 nm to the right of the center of circulation and 50 nm to the left—source: reworked from the National Weather Service "tropical landfall and impact statistics" (https://www.weather.gov/mhx/TropicalImpacts). The above is a visible satellite image of Hurricane Florence. Source; (https://www.weather.gov)

Along with these tropical and extra-tropical events, passing frontal boundaries and even high-pressure systems cause elevated sea states that can cause a morphodynamic reaction (Wright et al., 1993; Marshall, 2004). The longshore current directions along the coast of Onslow Bay differ seasonally as prevailing wind directions change due to changing atmospheric conditions. Although the longshore current is primarily due to wave height, breaking angle, and beach slope, at lower shoreface and inner shelf depths, 14 m to 30 m, respectively, wind-driven, subtidal currents mirror local wind forcing guiding currents in the same direction (Wright, 1995; Thieler, 1996; Xu and Wright, 1998; Marshall, 2004; Wren and Leonard, 2005). Along with these sub-tidal wind-driven currents, the breaking of gravity waves is the primary driver of nearshore currents, sediment transport, and morphological changes. Tidal currents, composed of semi-diurnal, diurnal, and longer period constituents, along with wave orbital velocity, all contribute to sediment transport in the along-shore and across-shore direction in Onslow Bay (Wright et al., 1991; Wright et al., 1993; Marshall, 2004). Due to the geometry of the bay and where Bogue Inlet is located, wave energy from the SW, S, and SE (typical summer mode) is the most dominant annually and interacts with the coastline obliquely. The direction of wave energy is a function of Cape Lookout and the structure's roughly 25 km long shoals at a water depth of 10 m or less McNinch and Wells (1998) that dissipates energy coming from the north to northeasterly directions shown from previous hindcast data (Jarrett, 1977; Van Gaalen, 2016). The dominant wave direction would help to drive current reversals in the nearshore depending on how the wave energy interacted first with the inner-shelf morphology (Langfelder, 1968; Riggs et al., 1996; Marshall, 2004; Wren and Leonard, 2005; Bodge et al., 2006; Van Gaalen, 2016). The current direction reverses when the prevailing winds shift, coming from the north (primarily during the winter), creating a southwest longshore current; however, extratropical cyclones, which may cross the region once a week (or even more frequently) during the winter, can cause current reversals on short-time scales as well (Wright et al., 1993; Marshall, 2004). The long-period waves and higher than mean significant wave heights of these events are most important for across-shore transport, in the offshore and onshore direction. The transport is due to the increased velocity of near-bottom layer boundary currents from increasing wave orbital velocities, which then, in turn, raises bed shear stress, entraining the sediment, which is then transported with the help of tidal currents and wind-driven currents (Thieler, 1996; Marshall, 2004; Wren and Leonard, 2005).

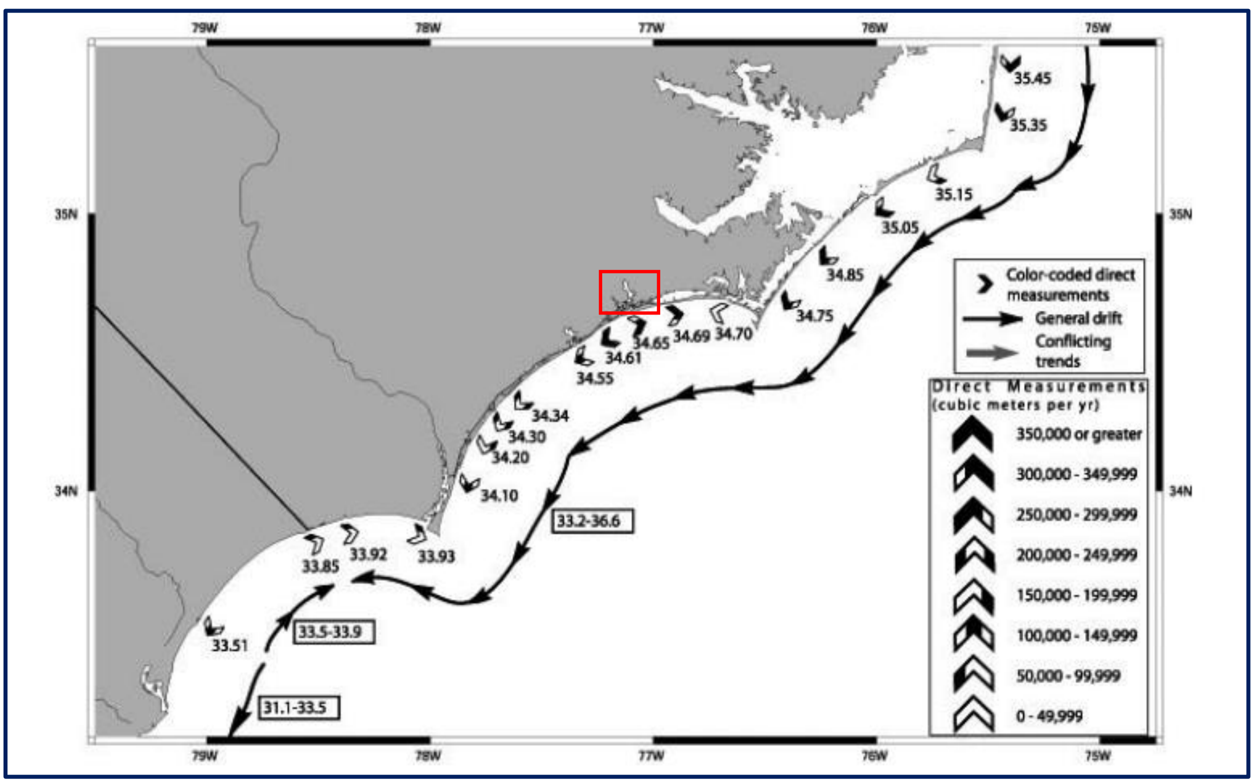

Figure 7. The figure shows the general longshore drift direction off the North Carolina coast. The conflicting trends are the color-coded measurements from Van Gaalen et al. (2016). The red square is the study location, which coincides with the estimated longshore drift.

Furthermore, it may be the case that the action of wave orbital currents is the most contributing factor to sediment transport along the shoreface and nearshore. However, according to modeled simulations, it is not the only factor pertaining to the changing morphology of ebb-tidal deltas and shoreface sub-environments; tidal currents and back-barrier hydraulic changes also play a significant role (Nienhuis and Ashton, 2016; Seminack and McBride, 2017; Lenstra et al., 2019). However, the hydrodynamic responses of near-bottom currents to the highly irregular morphology of a sediment-starved shallow embayment with rocky outcrops cannot be understated Riggs et al. (1996).

Passive margin coastlines with limited sand supplies, such as the U.S. east coast, commonly have barrier islands perched upon pre-modern stratigraphic units that occur beneath and seaward of the shoreface. The stratigraphic units dictate shoreface morphology and influence beach dynamics, sediment composition, and fluxes (Pearson, 1979; Riggs, 1979; Crowson, 1980; Riggs et al., 1996). Depending upon the composition and geometry, this underlying platform will act as a submarine headland, influencing the shoreface dynamics and resulting profiles. For example, if these submarine headlands are composed of compact muds, limestones, or sandstones, there will be a more significant effect upon both the planform of barriers and morphology of the shoreface and inner shelf than shorefaces composed of unconsolidated sands and soft muds. Second, along many parts of the coastal system, bathymetric shoal features occur on the inner shelf. These features will modify incoming waves and current energy, affecting the patterns of sediment erosion, transport, and deposition on the adjacent beaches Szczyrba et al. (2023).

The coastal zone south of Cape Lookout is dominated by features that crop out across the continental shelf consisting of Tertiary and Cretaceous units, with thin veneers of Quaternary units preserved in specific locations along the inner to middle shelf. Ancient drainage systems (fluvial valleys) flank these outcrops and are filled with younger coastal sediments split by topographic highs (interfluves) of older stratigraphic units Riggs et al. (1996). Onslow Bay exhibits this antecedent framework, where the middle portion is dominated by the Onslow submarine headland, and the northern region of the bay comprises the paleo White Oak/New River valley fill. The paleo White Oak River valley fill portion resides under the western portion of Bogue Banks. An interfluve separates it from the eastern portion of the island, where the Paleo New River valley fill stretches from the eastern portion of Bogue Banks to Cape Lookout, where this antecedent geologic framework plays a role in shoreface and inlet morphology Riggs et al. (1996). The Geology of Onslow Bay is composed of an irregular hard-bottom morphology consisting of ledges and scarps that can be ten meters in elevation (Riggs et al., 1996, 1998). Hardbottoms, which is a generic term used to describe the make-up of the seafloor with a semi-hardened to hardened surface, are critical benthic habitats on high-energy, sediment-starved, passive continental margins like the shallow sediment-starved shelf that make up the majority of Onslow Bay (Riggs et al., 1986; Riggs et al., 1996; Wilson and Palmer 1992; Riggs et al., 1998). In Onslow Bay, the hardbottoms have widely variable compositions, which range from mudstone, dolostone, and sandstone to fossiliferous limestone, with different morphologies, different compositions, and noticeably different benthic communities (Riggs et al., 1986; Riggs et al., 1996; Renaud et al., 1996a; Renaud et al., 1996b; Riggs et al.,1998). Miocene and Oligocene strata occur offshore of the study area and underly a thin layer of Quaternary deposits (Waters and Snyder, 1986; Riggs et al., 1998; Culver et al., in review) (Figure 8). The Miocene strata belong to the Pungo River Formation, characterized by sedimentary phosphorites that intersect the coastline along Bogue Banks and provide a source of phosphatized fossil foraminifera to the sediments of Bogue Banks (Shmorhun et al., 2022; Culver et al., in review). The Pungo River Formation unconformably overlies the light green, calcareous quartz sand of the late Oligocene to early Miocene Silverdale Formation (Waters and Snyder, 1986; Culver et al., in review), which provides non-phosphatized fossil foraminifera to the shoreface sediments.

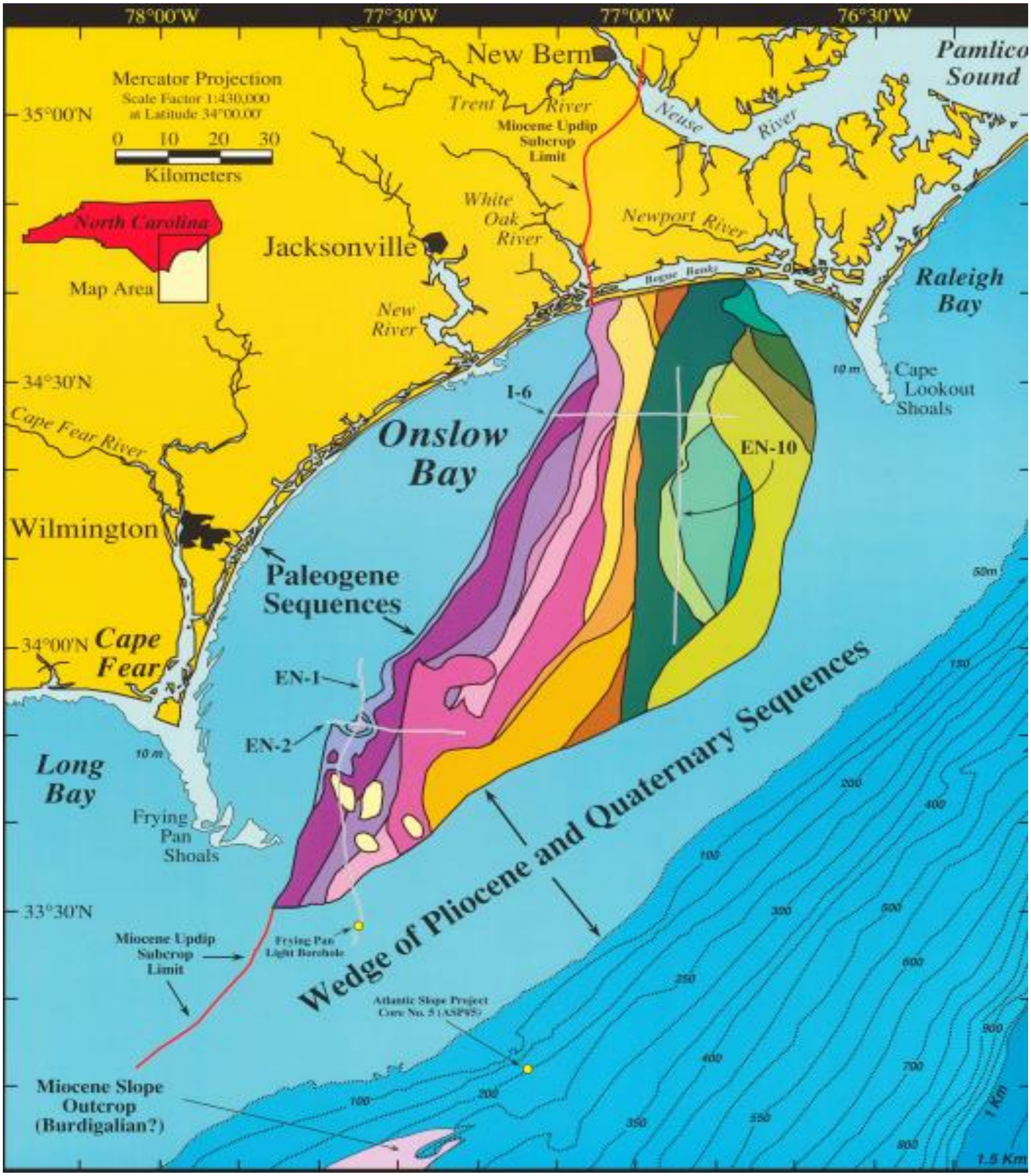

Figure 8. Geologic map of Onslow Bay and the locations of Paleogene, Miocene, Pliocene, and Quaternary stratigraphic sequences. Note that the Miocene sequences (colored sequences) stretch from the west portion of Bogue Banks to the east, ending before reaching Beaufort Inlet. Source: https://www.deq.nc.gov/energy-mineral-and-land-resources/geological-survey/assorted-maps/miocene-geology-continental-shelf-onslow-bay-north-carolina/open.

2.2 Novel stratigraphic model

Pearson et al. (2022) created a computer program written in MATLAB to model geomorphic change and predict the possible stratigraphy of the Ameland ebb-tidal delta in the Netherlands as a case study. The program utilizes a graphic user interface for the user to construct a transect anywhere within the model's extent. The model constructs an inferred stratigraphic sequence using bathymetry coded into the model. This means the bathymetric surveys are laid on top of each other over the time periods of the surveys to output the stratigraphic interpretation. The authors proposed that the stratigraphy would showcase the delta's depositional behavior through space and time and provide a modern analog for the evolution of the ebb-tidal delta.

This study used DEMs constructed from bathymetric surveys collected between 2005 and 2022 from Bogue Inlet, NC, and analyzed it using Pearson's model. The purpose of using this program is to compare it to sub-bottom geophysical seismic data, a widely used methodology for observing stratigraphy in many geologic settings. This is the first time the novel stratigraphic model has been compared to other geophysical data based on the physical properties of the stratigraphy. The model is compared to sub-bottom data collected in Bogue Inlet to analyze the shortfalls and strengths of the model's stratigraphic output.

2.3 Hurricane Matthew

On the 28th of September 2016, about 27 km west-northwest of Barbados, tropical storm Matthew formed in the Atlantic basin. As an atmospheric layer ridge to the storm's north directed it westward, it moved across the Windward Islands in the Caribbean. The tropical cyclone gradually strengthened and reached hurricane status by the 29th of September, 265 km northeast of Curaçao Stewart (2017). Matthew underwent rapid intensification between September 30th and October 1st. The storm reached an estimated peak intensity of 267 kph Category 5 on October 1st. An eastward-moving mid-latitude trough over the central United States directed the major hurricane toward the north-northwest on October 7th. Matthew then weakened to a Category 3 hurricane on October 7th and continued to weaken to a Category 2 hurricane by October 8th. Hurricane-force wind gusts made landfall around October 8th just north of Charleston, South Carolina Stewart (2017). The hurricane moved back offshore and remained off the coast of North Carolina through October 9th.

Figure 9. Map showing Hurricane Matthew's track and intensity. Refer to the legend at the bottom right, which shows the color that represents the category of the storm through its evolution.

The northwestern edge of Matthew's large eyewall extended well inland and brought hurricane-force wind gusts and heavy rains to coastal regions of the Carolinas Stewart (2017). As Matthew moved east-northeastward, south of eastern North Carolina (Figure 9), the storm encountered an extratropical transition and an increasing pressure gradient from an approaching cold front, causing sustained hurricane-force winds over the Outer Banks and creating a storm surge. Matthew maintained its east-northeastward trajectory and lost its tropical storm status by 9 October (Figure 9). The extratropical low merged with a frontal system on October 10, east of Cape Hatteras, North Carolina, and moved north Stewart (2017).

2.4 Hurricane Florence

Hurricane Florence became a hurricane on September 4, 2018, 1,931 km east-northeast of the Lesser Antilles. After undergoing rapid intensification over the next 30 hours, it became a 212 kph Category 4 hurricane on September 5^{th}. After briefly weakening, the storm intensified and peaked at 255 kph, a strong Category 4 on September 11^{th}, 1,342 km east-southeast of Cape Fear, North Carolina Stewart et al. (2019) (Figure 10). The Bermuda-Azores high-pressure ridge kept the storm on its west-northwestward motion. Florence began weakening, likely because of cold upwelling and the onset of an eyewall replacement cycle Stewart et al. (2019). As steering currents collapsed, the result was a slow westward motion of around nine kph, and the hurricane made landfall as a 148 kph hurricane (Category 1) near Wrightsville Beach, North Carolina, around 11:15 pm on September 14^{th} (Figure 10). The estimated barometric pressure at landfall was 956 mbar based on combined pressure and wind data from a National Ocean Service (NOS) observing site located on Wrightsville Beach, North Carolina (JMPN7) and reconnaissance dropsondes, one hour prior to landfall. The highest land-based sustained wind measured in Florence was an average velocity of 133 kph recorded around 2:00 am September 14^{th} at Cape Lookout, North Carolina (CLKN7). This wind was measured north and well outside of Florence's eyewall. On the coastline of NC, the maximum storm surge reached an estimated 1.5 m-2.4 m above Mean Sea level in Onslow Bay Stewart et al. (2019). A USGS storm tide pressure sensor at Wrightsville Beach measured a wave-filtered water level of 2.73 m NAVD88, which converts to about 2.19 m MHHW. On Emerald Isle, a USGS sensor on the back side of the barrier in a wave-protected area measured a peak water level of 2.36 m NAVD88, about 2.13 m MHHW Stewart et al. (2019).

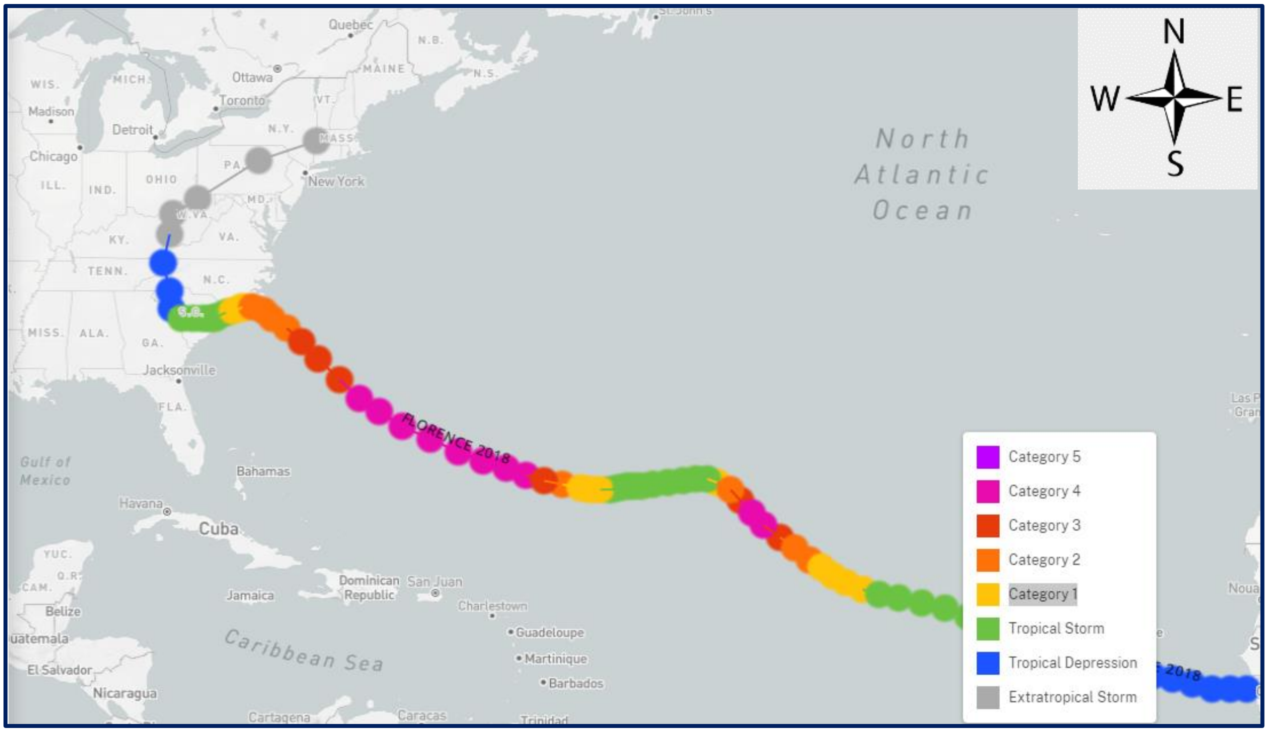

Figure 10. Map showing Hurricane Florence's track and intensity. Refer to the legend at the bottom right, which shows the color that represents the category of the storm through its evolution.

2.5 Hurricane Dorian

The fourth named storm and the first major hurricane of the 2019 hurricane season was Dorian. The storm formed on August 24th from a tropical wave in the central Atlantic basin and strengthened as it traveled towards the Lesser Antilles. From August 28th, rapid intensification occurred, and the storm became a Category 4 hurricane on August 31st. Dorian reached Category 5 on September 1st with maximum sustained winds of 297.7 kph and a barometric pressure of 910 mbar as it made landfall in Elbow Cay, Bahamas (Figure 11). This storm was the second strongest in recorded history in the Atlantic basin. As the storm progressed, the system underwent an eyewall replacement cycle and cold-water upwelling, drastically weakening the hurricane to a Category 2. Dorian slowly began to move north-northwest on September 3rd. On September 6th, the hurricane weekend to a Category 1 as it gained forward momentum and turned to the northeast. Through this time, Dorian tracked northeast along the North Carolina coast, south of Bogue Banks (Figure 11). The storm clipped Cape Lookout before making landfall at Cape Hatteras on September 6th. While the storm tracked just south of the Bogue Banks, peak wind gusts were recorded at 131 kph at Cape Lookout, respectively. Storm surge flooding occurred up and down the southeastern United States, from Florida to Virginia. The most significant surge occurred on portions of the North Carolina Outer Banks 1.69 m Avila et al. (2020), a NOAA National Ocean Service gauge at the U.S. Coast Guard Station Hatteras on the Pamlico Sound side of the Outer Banks. The combined effect of the storm surge and high tides produced 1.52 to 2.1 m levels above sea level on parts of Hatteras Island. A United States Geological Survey (USGS) storm tide pressure sensor recorded a peak wave-filtered water level of 2.10 m above the North American Vertical Datum of 1988 (NAVD88), 2.04 m MHHW Avila et al. (2020). USGS pressure sensors on the northern portions of the Outer Banks measured peak water levels of 1.58 m MHHW. Elsewhere along the North Carolina coast, inundation levels were generally 0.9 m or less from Cape Lookout southwestward to the South Carolina border, and only a few isolated USGS sensors measured water levels of 0.9-1.2 m MHHW Avila et al. (2020).

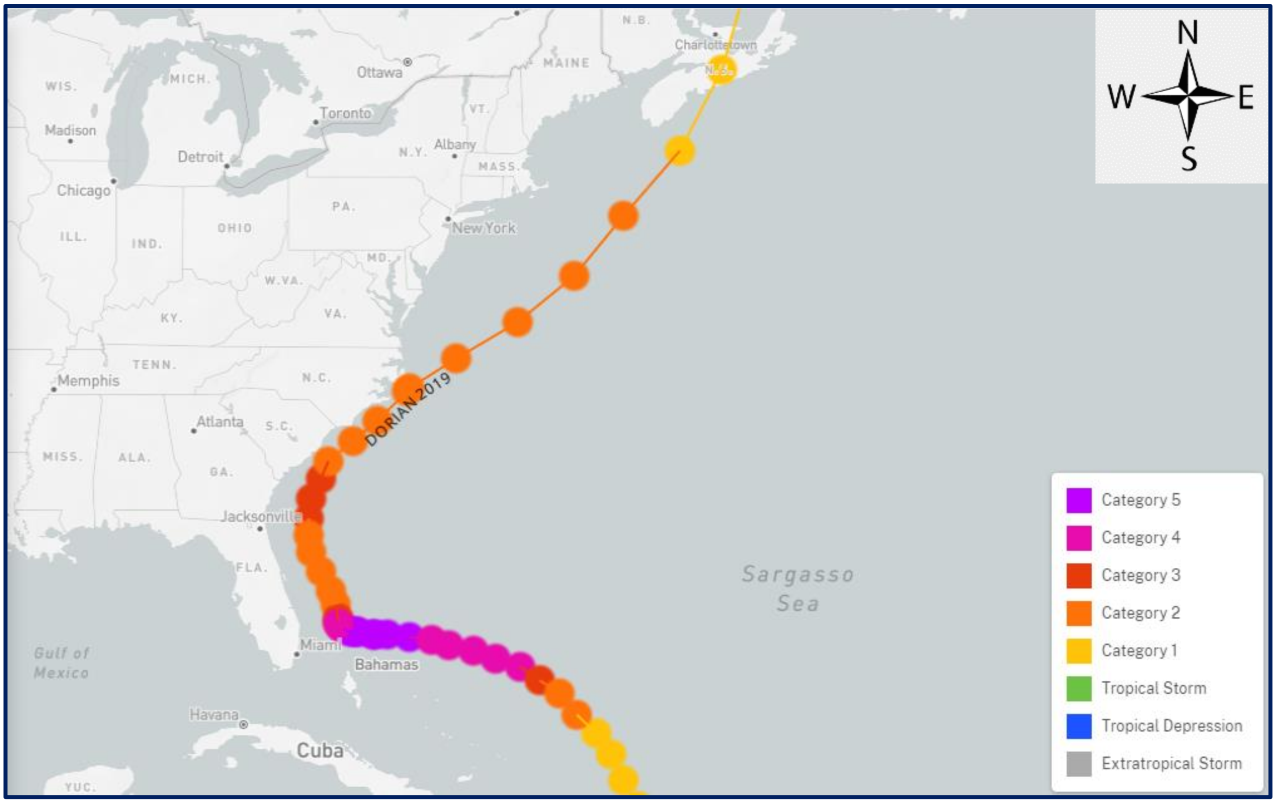

Figure 11. Map showing Hurricane Dorian's track and intensity. Refer to the legend at the bottom right, which shows the color that represents the category of the storm through its evolution.

2.6 Foraminifera species distribution

Foraminifera distributions have been widely documented worldwide since the late 19th century. Many factors contribute to the distribution of both benthic and planktonic species. At first, the distribution of foraminifera was thought to be controlled primarily by abiotic factors, such as temperature and salinity (Culver, 1993; Buzas, 2002; Culver, 2023). More recently, the distributional patterns of foraminifera have been explained by both biotic and abiotic factors (Buzas et al., 1977; Buzas, 2002). Distributions are considered at many scales, from square centimeters to global ocean basins. These interrelated factors that control distribution are salinity, temperature, calcium carbonate in solution, pH, dissolved oxygen, turbidity, illumination, substrate hydrostatic pressure, currents, tides, food availability, predation, and competition (Buzas et al., 1977; Culver, 1993; Buzas, 2002; Culver, 2023).

Cape Hatteras is a major geographic boundary of foraminifera on the eastern margin of the United States (Buzas and Culver, 1980; Culver and Buzas, 1981). North of this geographic boundary, shelf species associated with the colder waters of the Labrador Current reside (Buzas and Culver, 1980; Culver and Buzas, 1981). South of the boundary, the shelf is characterized by warmer water species (Buzas and Culver, 1980; Culver and Buzas, 1981). Due to foraminifera comprising a significant portion of the benthic biomass in shallow to deep marine ecosystems, they are utilized in paleoenvironmental, paleoclimatic, and paleoceanographic reconstructions (Miller et al., 2005; Rasmussen et al., 2016; Kemp, 2017). Isotopic analysis conducted on foraminiferal tests can be used to estimate paleotemperatures; paleodepths, the movement of water masses, and tectonic plate motion can be recognized using foraminiferal data like the composition of foraminiferal assemblages and distributional studies Culver (1993). Their unsurpassed value for solving geologic problems drives motivation for future foraminiferal research Culver (1993).

In this study, the distribution of modern and fossil benthic species transported from Onslow Bay, originating from the Pungo River Formation, will be utilized to infer sediment provenance. It is also feasible that outer shelf species like *Epondies repandus,* sampled at around 95 m Schnitker (1971), could be transported onto the inner shelf through oceanographic processes like deep water meanders (filaments) from the Gulfstream into Onslow Bay (Webster, 1961; Atkinson et al., 1980) or the wave base of a major hurricane, where wave base can reach up to 100 m for some higher end category storms Peters and Loss (2012). The Quaternary specimens could then be reworked by weaker tropical or extratropical storms that pass through the embayment and near the study site of Bogue Inlet and deposited in the nearshore and foreshore sub-environments. Distribution analysis, along with sedimentological data, has been used with relative success in the literature to be an indication of the onshore transport of sediment from the shelf by tropical cyclones, extra-tropical depressions, and tsunamis (Horton et al. 2011; Hawkes and Horton 2012; Hippensteel et al. 2013; Hippensteel and Garcia, 2014)

2.7 Bogue Inlet

Bogue Inlet is a wide and relatively deep (5-9 m) inlet compared to others along the North Carolina coast Cleary and Marden (2004). The inlet is classified as a transitional inlet, being wave-influenced compared to the wave-dominated to the north. Unlike the inlets in the northern Outer Banks, Bogue has a well-developed ebb-tidal delta Cleary and Marden (2004) with an estimated volume of 10 million cubic meters. Bogue also exhibits characteristics of migrating inlets, migrating over a hundred meters. However, based on its geometry and Bogue Inlet’s ebb-tidal delta size, the inlet is intermediate between a wave-dominated or tidally dominated category.

The inlet's width has varied over the past 84 years, ranging from 400 m to 1.9 km. The zone in which the inlet has migrated (from west to east) is 2.5 km wide and has stayed in this region for the past 200 years Cleary (2008). Most likely, the restricted lateral migration is due to the inlet residing in the paleo river valley of the White Oak River (Hine and Snyder, 1985; Riggs et al.,1996; Cleary, 2008). Also, the configuration and orientation of the inlet have changed significantly since the 1930s. In contrast to today, during the late 1930s, the main ebb channel had a southwest orientation with a large spit protruding off Bogue Banks, and the flood tidal delta had larger lobes that extended to the east (Figure 12). Oertel (1975, 1988) observed that channel rotation along tide-dominated tidal inlets is dependent on tides and net longshore sediment transport direction. Inlet-channel rotation in wave-dominated to wave-influenced tidal inlets is controlled by estuarine accommodation space (space available for sediment deposition) and flood-tidal delta deposits Seminack and McBride (2018).

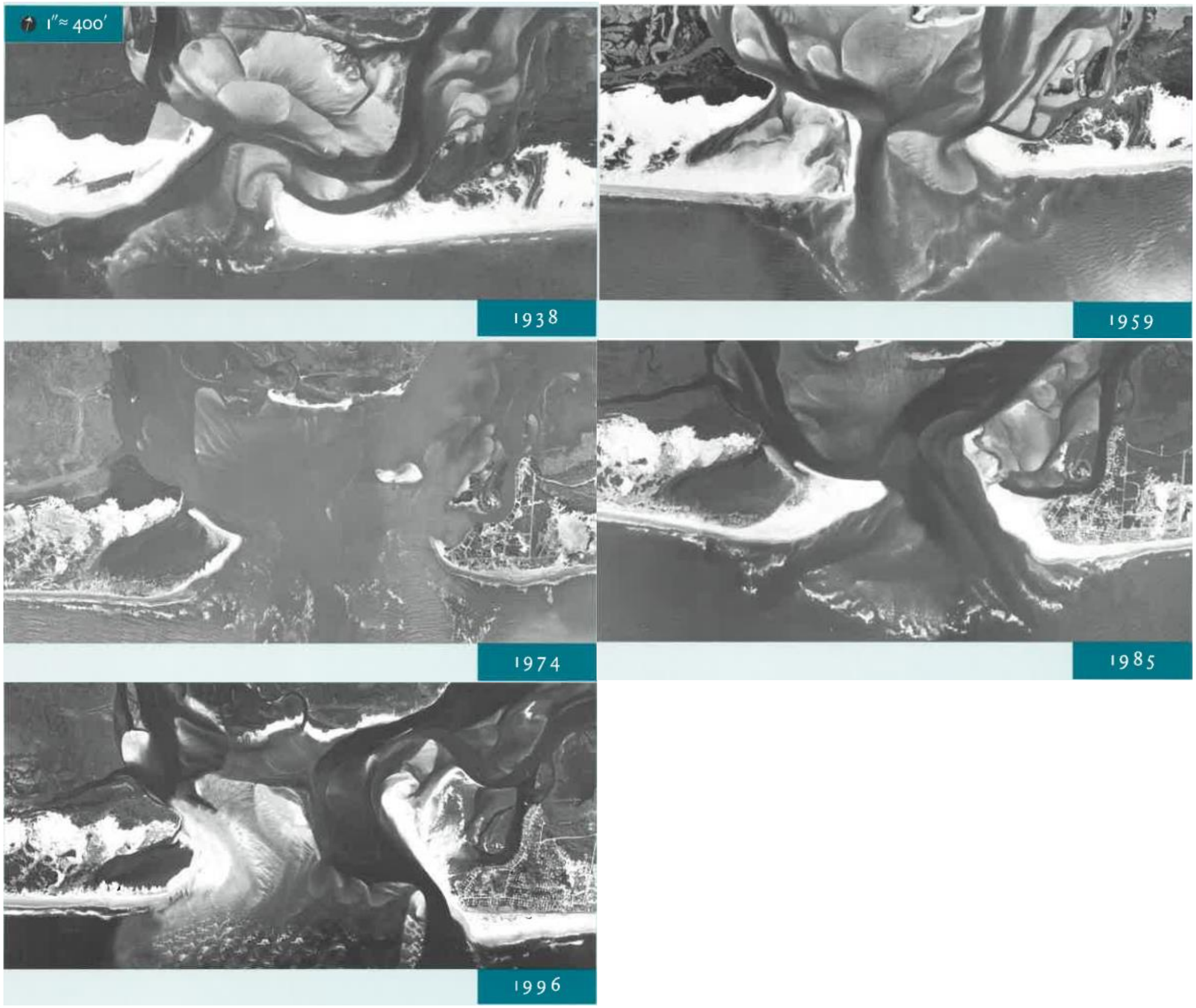

Figure 12. Aerial photographs of Bogue Inlet from 1938-1996. Reworked from Cleary and Marden (2004)

As the FTD deposits accumulate and regions become subaerial, the flood tidal channels must migrate to find more space to allow for the tidal prism and influx of sediment to be transported into the estuary; if not, the tidal inlet will shoal and fill Seminack and McBride (2018). The rotation is a function of the inlet system trying to maintain hydraulic efficiency (Hudson and Kesel, 2000; Seminack and McBride, 2018). Channel rotation is a natural process; however, it will react to human-induced changes like dredging and sediment influxes from beach nourishment actions.

2.8 Anthropogenic factors

(Figure 13) shows the historical quantities of beach nourishment since the 1980s, amounting to hundreds of millions of dollars and tens of millions of cubic yards of sand. The total economic cost and material used in beach nourishment are depicted in (Figure 14), reported from data stretching back to 2002.

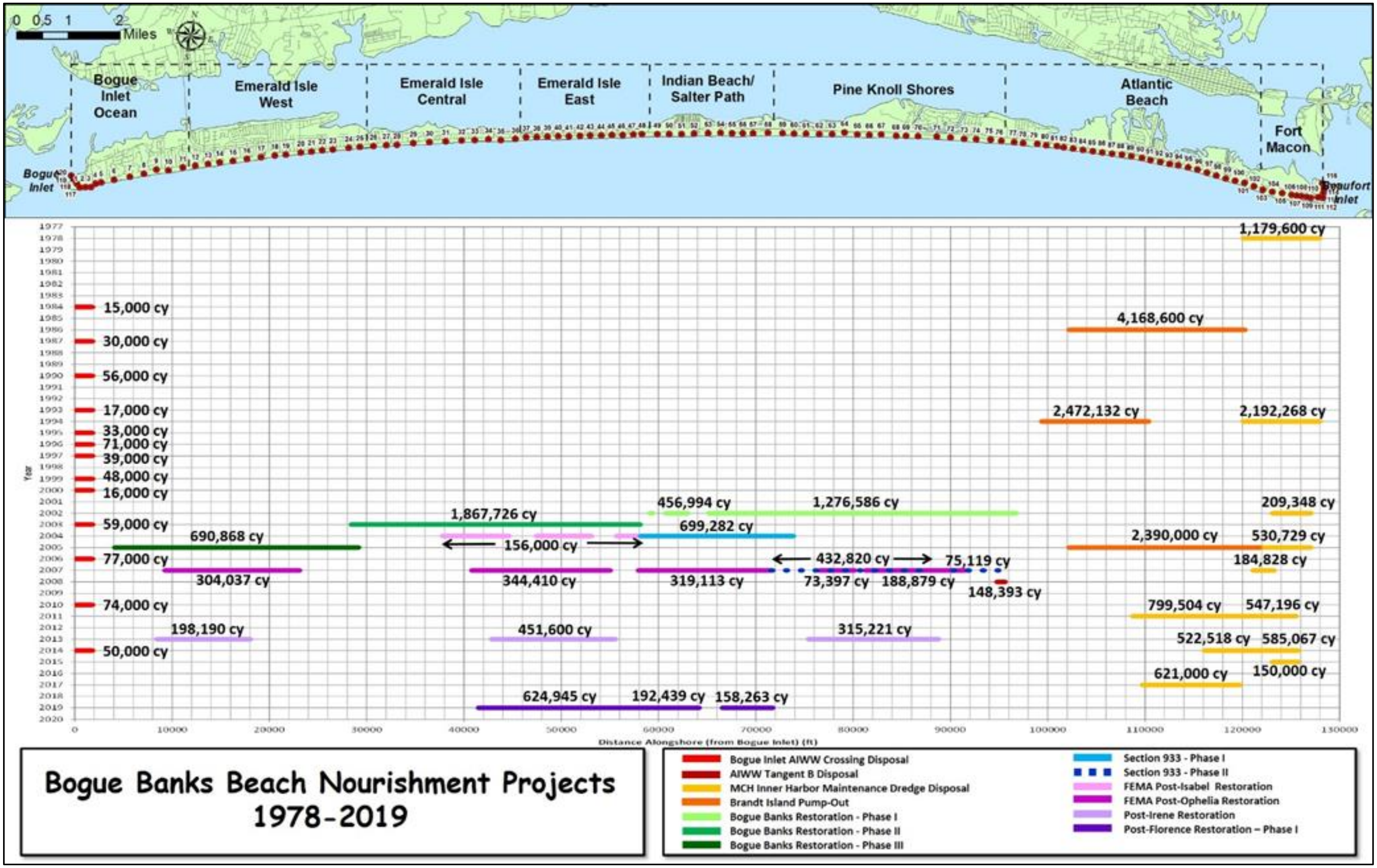

Figure 13. Historical quantities of beach nourishment projects across Bogue Banks from 1977 to 2020. Colors represent a specific project and location on the barrier island—source: (Beach Preservation Plan, gov/www.carteretcountync.gov).

Cumulative Costs and Volume

Project	County ($)	Pine Knoll Shores	Indian Beach	Emerald Isle	State ($)	Federal ($)	Total ($)	cubic yards
Phase I ('01-'02)	$0	$8,307,000	$3,393,000	$0	$900,000	$0	$12,600,000	1,733,580
Phase II ('03)	$0	$0	$0	$11,800,000	$0	$0	$11,800,000	1,867,726
Phase III ('05)	$0	$0	$0	$7,100,000	$3,800,000	$0	$10,900,000	690,868
933 Phase I ('04)	$0	$66,542	$333,458	$0	$1,200,000	$3,800,000	$5,400,000	699,282
Pump-Out ('04-'05)	$0	$0	$0	$0	$1,000,000	$9,600,000	$10,600,000	2,920,729
933 Phase II ('07)	$0	$678,000	$0	$0	$2,000,000	$7,600,000	$10,278,000	507,939
Harbor ('10-'11)	$0	$0	$0	$0	$0	$12,762,429	$12,762,429	1,346,700
Harbor ('14)	$0	$0	$0	$0	$0	$9,415,774	$9,415,774	1,107,585
Isabel ('04)	$0	$0	$0	$0	$0	$1,956,175	$1,956,175	156,000
Ophelia ('07)	$0	$0	$0	$0	$0	$13,773,768	$13,773,768	1,229,836
Irene ('13)	$5,920,405	$511,798	$0	$1,443,607	$0	$7,076,155	$14,951,965	965,011
TOTALS	**$5,920,405**	**$9,563,340**	**$3,726,458**	**$20,343,607**	**$8,900,000**	**$65,984,301**	**$114,438,111**	**13,225,256**
%	**5%**	**8%**	**3%**	**18%**	**8%**	**58%**	**100%**	

Figure 14. The total economic cost and material used in beach nourishment projects are reported from 2002 to 2013—source: (Beach Preservation Plan, gov/www.carteretcountync.gov).

The western portion of Bogue Banks has been one of the most consistently nourished beaches since the 1980s (Beach Preservation Plan, gov/www.carteretcountync.gov). Although since the 1960s, the USACE has maintained a 5 km long 2 m deep channel to the Atlantic Intracoastal Waterway from Bogue Inlet, and that dredged material has been deposited on the oceanfront adjacent to the inlet and the inlet's eastern margin throughout the inlet's maintenance (Figure 16 A, B, C) (www.carteretcountync.gov/655/Bogue-Inlet-AIWW-Crossing). Historical dredged volumes are totaled and presented in (Figure 15) (www.carteretcountync.gov/655/Bogue-Inlet-AIWW-Crossing).

Table 1

Summary of AIWW Dredge Disposal to Western Emerald Isle

Fiscal Year	Fill in cubic yards
1984	15,000
1987	30,000
1990	56,000
1993	17,000
1995	33,000
1996	71,000
1997	39,000
1999	48,000
2000	16,000
2003	59,000
2006	77,000
2010	74,000
2014	50,000
Total	585,000
Avg. per event	45,000

Figure 15. History of AIWW dredge disposals to western Emerald Isle from 1984 to 2014. (www.carteretcountync.gov/655/Bogue-Inlet-AIWW-Crossing).

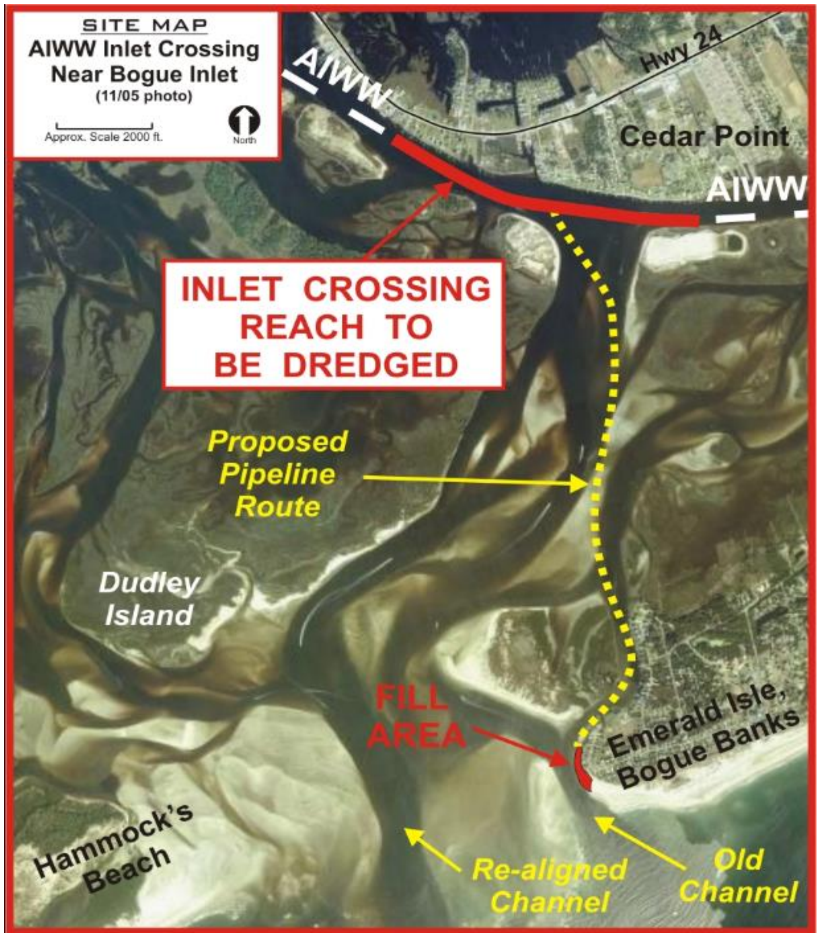
SITE MAP
AIWW Inlet Crossing
Near Bogue Inlet
(11/05 photo)
Approx. Scale 2000 ft.
North
AIWW
Hwy 24
Cedar Point
AIWW
INLET CROSSING REACH TO BE DREDGED
Proposed Pipeline Route
Dudley Island
FILL AREA
Emerald Isle, Bogue Banks
Hammock's Beach
Re-aligned Channel
Old Channel

A


BOGUE INLET
AIWW CROSSING
(Site Map 2014)
aerial image = 12/31/11
North
2,000 ft.
AIWW
Cedar Point
AIWW
DREDGING
AIWW Crossing
Generalized Pipeline Route
Dudley Island
Hammock's Beach
Emerald Isle, Bogue Banks
FILL AREA
Increase elevation ~ 1 - 2 feet

B

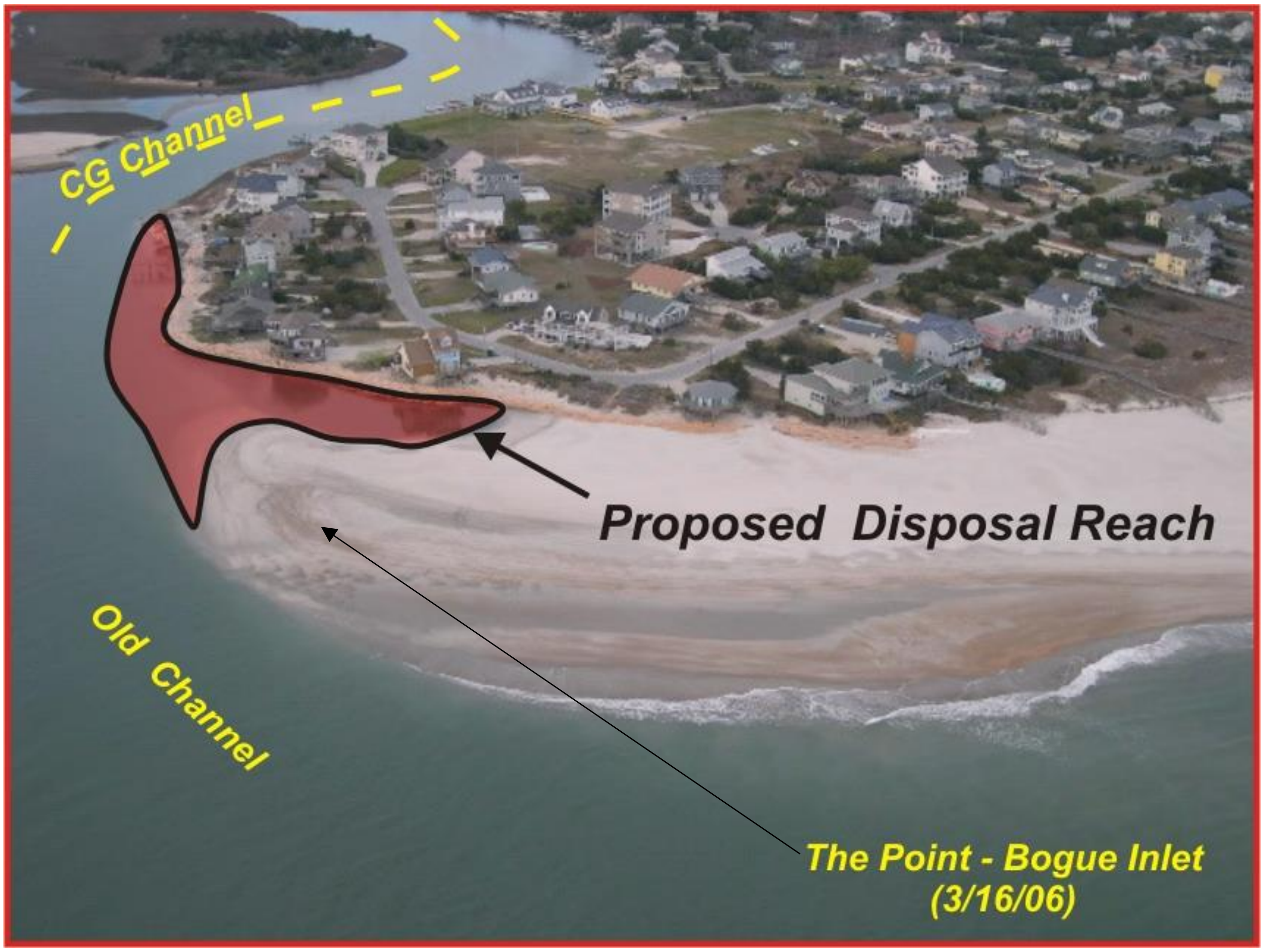

C

Figure 16. A) The fill location from the dredging of the AIWW, 2009; **B)** the fill area and elevation of disposed dredged material in 2014; **C)** the proposed disposal reach from dredging in 2006**.** (www.carteretcountync.gov/655/Bogue-Inlet-AIWW-Crossing).

There have also been other associated disposal/nourishment projects not mentioned in the above figures that have been deposited within the littoral system that could directly affect the morphodynamics of Bogue Inlet. These nourishment projects usually happen after intense periods of high wave energy as major tropical systems travel through Onslow Bay. Hurricane Ophelia was estimated to have eroded 841,010 m^3 from Bogue Banks in total, and it cost 13.8 million in total for renourishment (Beach Preservation Plan, www.carteretcountync.gov/313/Preservation-Plan). In 2007, 200,374 m^3 of sand was deposited within the MHW contour on the western portion of Bogue Banks, and on August 27th, 2011, after Hurricane Irene, 153,898 m^3 of nourishment sand was deposited. In 2019, phase one of the post-Hurricane Florence project did not renourish Bogue Banks close enough for the longshore current to transport large amounts of sediment into the vicinity where it would have substantial morphologic effects, but in phase two of the project, 271,673 m^3 was deposited 1,066.8 m from the point at Bogue Inlet (Beach Preservation Plan, www.carteretcountync.gov/313/Preservation-Plan). Lastly, in phase three of the project, 130,124 m^3 was deposited directly on the point at Bogue Inlet, and 573,328 m^3 was deposited roughly 3.2 km to the east of the inlet (Beach Preservation Plan, www.carteretcountync.gov/313/Preservation-Plan).

The reported anthropogenic actions mentioned above directly affect the morphology and, therefore, the hydrodynamics of the inlet. It should be noted that these historical data should be considered when comprising any future sedimentologic, morphological, and foraminiferal studies of the region. If the historical data are not reflected, grain size statistics, foraminiferal assemblages, and morphological volume changes could be altered after disposal, along with source interpretations of these data, which could be misinterpreted when attempting to understand such complex and dynamic environments.

In 2005, with funding from the N. C. Division of Coastal Management, Carteret County, and the Carteret County Shore Protection office along with the USACE, the county undertook the Bogue Inlet Realignment Project to relocate the main inlet channel to the west by dredging a new inlet channel Rich (2017) (Figure 17).

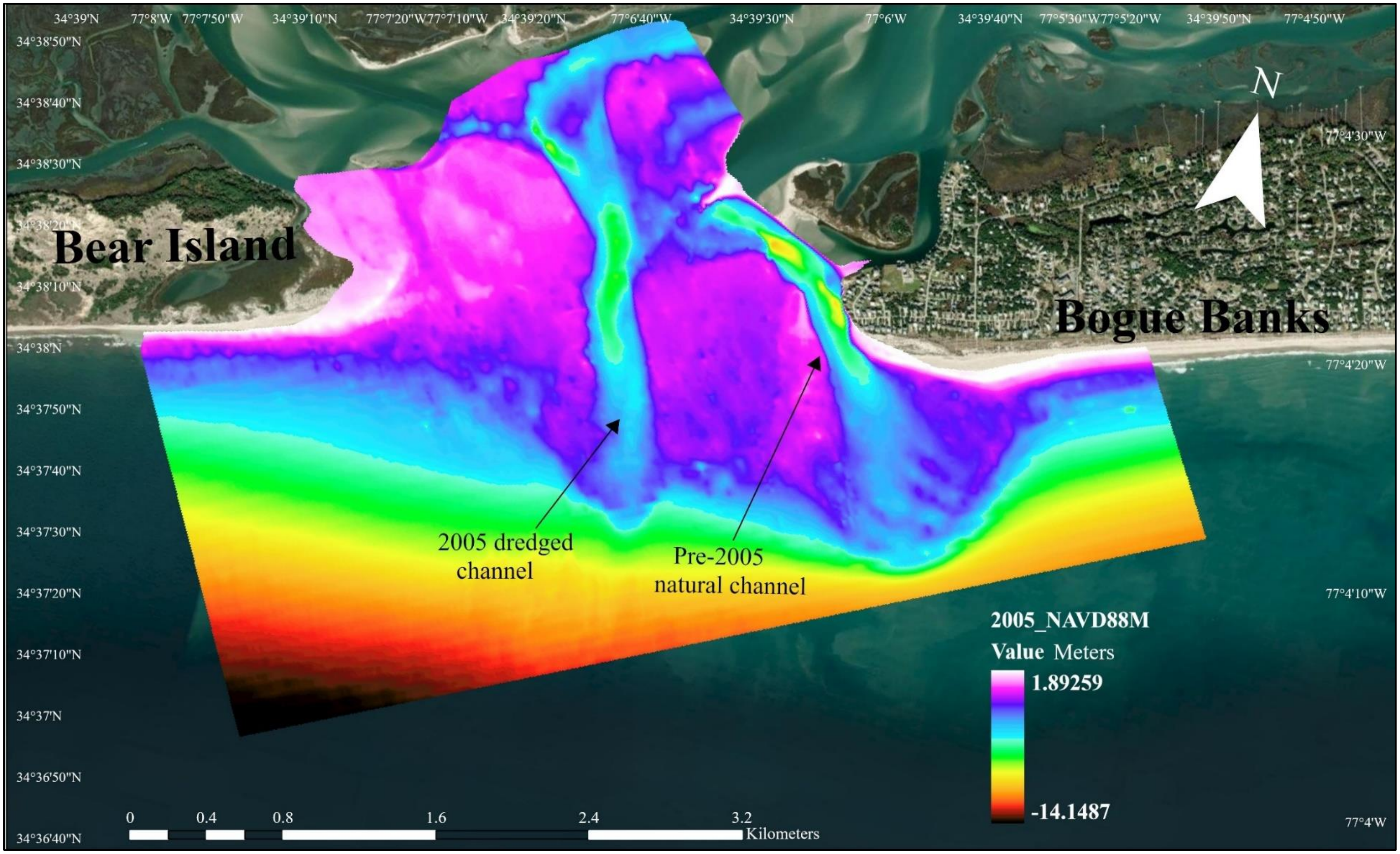

Figure 17. Map showing the location of the newly dredged channel in Bogue Inlet. This channel was dredged in 2005 to capture the tidal prism and help natural processes fill the old channel to prevent erosion of the downdrift flank of Bogue Inlet. Datum (NAVD88).

This was done because of the eastward migration of the inlet channel, which threatened coastal structures (private dwellings) on the western end of Bogue Banks (the town of Emerald Isle). The Bogue Inlet Channel Realignment Project consisted of a few major objectives. The first objective was to realign the main inlet throat channel to a centrally located position within the Bogue Inlet floodway that separates Bogue Banks from Bear Island. The second objective was constructing a sand dike that closed the old main inlet channel throat as the realignment was completed. The installation of the dike was proposed to enhance the shoaling effect to infill the northernmost end of the main inlet channel, thereby promoting the new inlet to capture the majority of the tidal prism and become the major tidal corridor. The final objective was to nourish the beach along 7.2 km of the western Emerald Isle shoreline. The sand utilized for this objective was dredged shoal material encountered during the realignment of the inlet. This material allowed for the appropriate grain size to be used for the energy within the littoral system. Five hundred and forty-two thousand eight hundred and thirty-three cubic meters of sand were used for the beach fill, with the balance utilized for dike construction (up to 226,308 m^3) (Beach Preservation Plan, www.carteretcountync.gov/313/Preservation-Plan).

Since the 2005 realignment, no additional dredging has occurred, and the main inlet channel has migrated to the east once again. Thus, the data used in this investigation are the product of the inlet's readjustment over the last two decades. This proposed investigation of the inlet will advance the understanding of the processes influencing this important inlet and coastal science in general.

3.0 METHODOLOGY

3.1 Geospatial Information Science analysis

3.1.1 Bathymetric and topographic surveys

Geodynamics LLC collected single-beam echosounder data to construct Digital Elevation Models (DEMs) from the eastern side of Bogue Inlet (Figure 18), which included the main inlet channel and eastern portions of the ebb-tidal delta and flood-tidal delta.

Bathymetric Surveys conducted by Geodynamics started in 2005 and were conducted in 2007, 2008, and 2009 but have only been conducted twice yearly, in the summer and fall, every year from 2012 to 2022. These were the survey data years provided to this study from Geodynamics. Surveys from 2005 to 2012 were only included in the cross-sectional profile analyses, and the bathymetric surveys presented in Appendix A, B, and C to help show the morphologic change over the study's temporal period.

The accuracy and quality of the final product were based on the survey design. The survey design was structured to follow the contours of the inlet and foreshore instead of the perpendicular grid pattern conducted in the past; this was done to improve the resolution of the morphologic features and post-processing when combined with the topographic data. Geodynamics did not report the assessed accuracy of the topo-bathy data (vertical RMSE). The single beam data were collected with an Odom CV100 digital echosounder and a POS MV Wave Master inertial motion unit (IMU) for accurate positioning and motion-compensated real-time tidally corrected elevations. The Odom CV100 digital echosounder has a resolution of 0.01m. Surveys utilized the system's operating frequency in the 200 kHz band. The AML Oceanographic Minos X SV&P sound velocimeter was used to obtain accurate sound velocity profiles throughout the survey area. The system contains a sound velocity probe attached to the data collector, which helps the survey technician log the sound velocity profile data as the probe is deployed (Moffat & Nichol; Geodynamics, 2022).

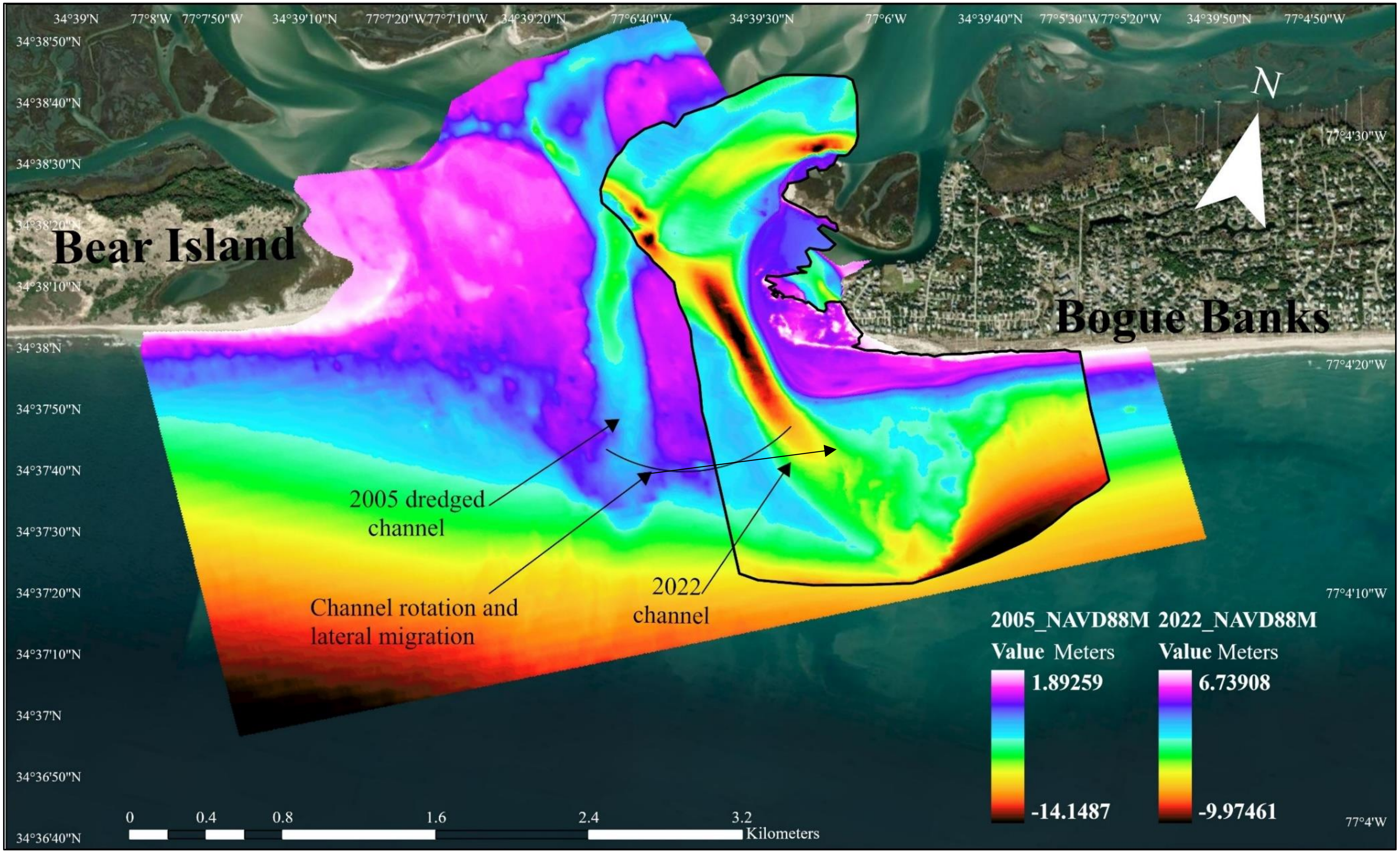

Figure 18. Composite bathymetric map of Bogue Inlet derived from surveys 2005 and 2022. There is a 17-year gap between the surveys, and a clear direction of migration can be observed. Datum (NAVD88).

Topographic data were collected using a RIEGL VZ-400i mobile laser scanner system and a Trimble R10 RTK-GNSS rover backpack system. After adding the bathymetric data, the X, Y, and Z plane datasets were reconfigured into the 6 m x 6 m final grid. The Emerald Isle, Point Monitoring Project, and topo-bathy surveys were conducted twice a year in the summer and fall only from 2012-2022, not 2005, 2007, 2008, and 2009. The topographic and bathymetric data were overlayed, processed, analyzed, and archived in a database provided in NAD83 NCSPF (horizontal), with additional elevations in NAVD88 (vertical). The vertical datum for the final survey data is the North American Vertical Datum of 1988 (NAVD88). The DEMs' pixel resolution is 6 x 6 m. The surveys were acquired semi-annually from 2012 to 2022, with a year gap between 2013 and 2014 (Appendix B) (Moffat & Nichol; Geodynamics, 2022). The data aided in observing morphologic change between the two consecutive surveys when hurricanes or extratropical cyclones occurred. They were used to construct the stratigraphic model Pearson et al. (2022) and create the hydrodynamic models.

3.1.2 Ebb-tidal delta volumetric analysis

Esri's geospatial platform, ArcGIS Pro version 3.0, was used to observe and quantitatively measure the morphodynamic change over time. Changing the bathymetric color ramp and converting the data to a 3D scene allowed for more precise morphological identification. The following geospatial workflow was used to perform the volumetric measurements. The surface volume geoprocessing tool was first used. This tool was utilized to calculate the sediment volume change between surveys within a polygon encompassing the ebb-tidal-delta. The difference in the sediment volume between surveys is a direct function of the sediment entering versus leaving (i.e., flux in versus flux out) the polygon. The ebb-tidal delta was chosen because volumetric extents of ebb-tidal deltas are reported in the literature and are shown to vary in morphology as a function of wave and tidal energies Fitzgerald et al. (2011). The largest extent of the delta lobe was delineated using a polygon. After digitization, the clip-to-raster function was utilized to clip the polygon, meaning data were clipped from each year of the bathymetric surveys so that the dimensions were the same to conduct the measurements. This action was taken so that no extra data were incorporated when the measurements were made (Figure 19). The specific clipped raster was chosen and set to be the reference surface from which the tool would read elevation data. The reference plane was set at MSL. The geoprocessing tool calculated the volume underneath the reference plane, from MSL down to the seafloor (i.e., the water column volume or the storage volume). The sediment volume change was calculated by subtracting the storage volume of a later survey (Survey 2) from the volume of the earlier survey (Survey 1) (Equation 1). A negative volumetric difference means a net loss of material out of the polygon, and a positive value indicates a net gain of material into the digitized polygon. The data were then plotted on time series graphs.

Eqn. 1.

$$\text{Volume Survey 2} - \text{Volume Survey1} = \Delta\text{Sed Vol}/\Delta\text{Time} \quad (1)$$

A positive value represents a net gain in sediment, and a negative value represents a net loss.

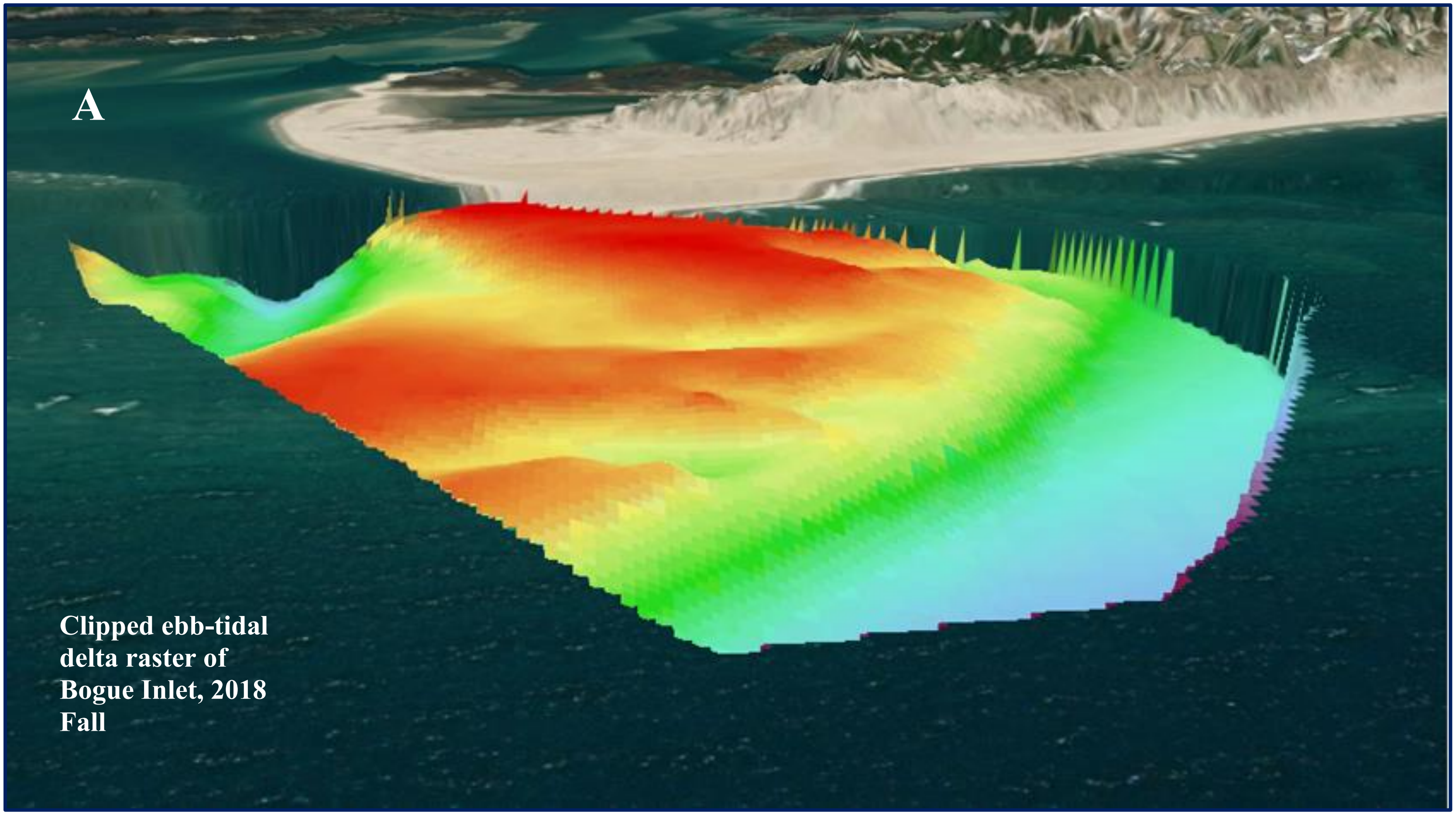

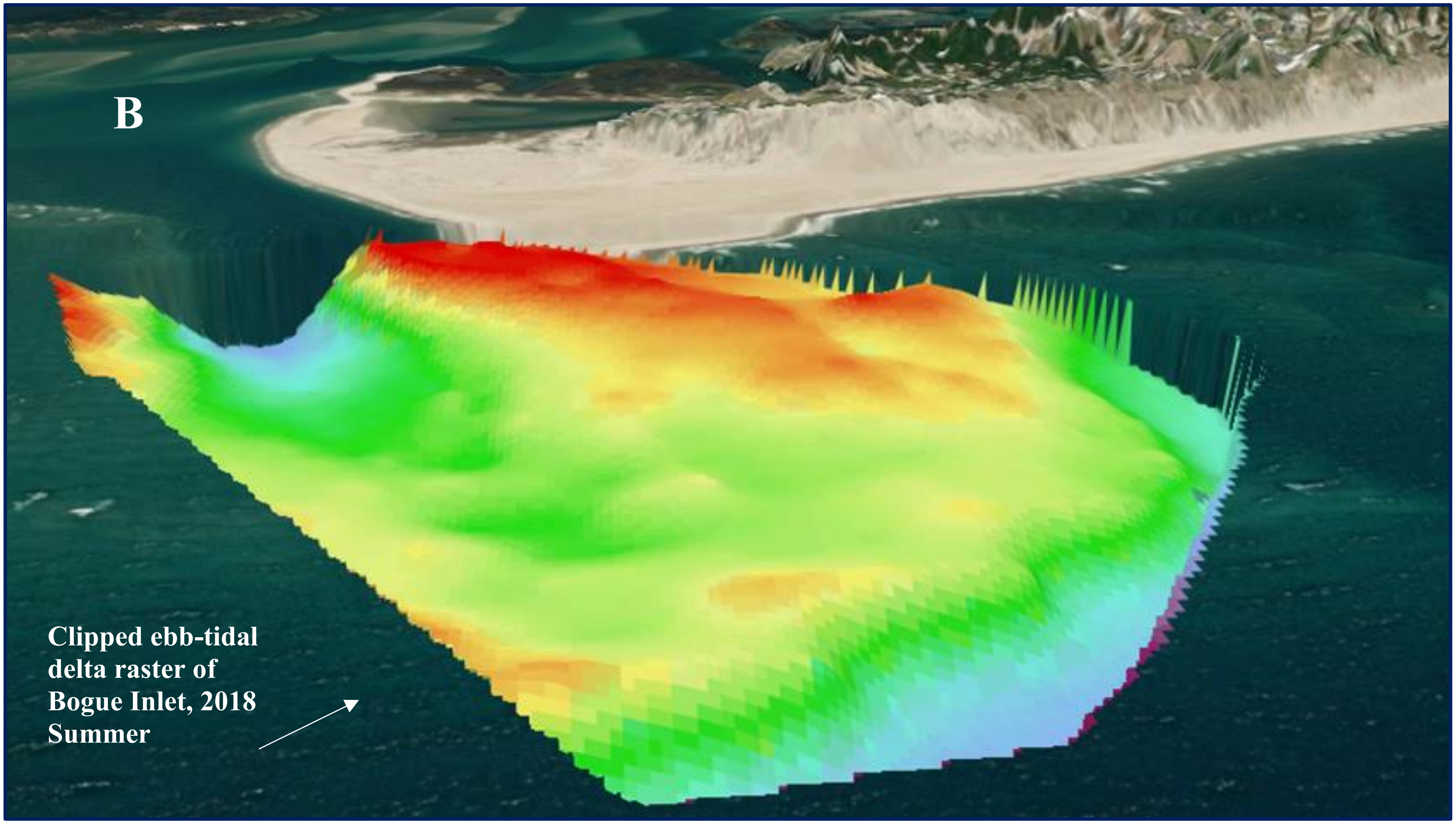

Figure 19. **A)** 2018 Fall and **B)** 2018 Summer are the digital elevation data clipped to ensure no other elevation data is considered in the volumetric calculations when running the Surface Volume geoprocessing tool. After the tool has been run to calculate the volume from MSL, reference plane, to the sea floor, those two values are subtracted from one another to find the amount of material or the difference in volume that has moved either in or out of the clipped extent. Datum (NAVD88).

3.1.3 DEM of volumetric change

The DEM of difference method was performed using the raster calculator geoprocessing tool to create a new raster map showing the elevation change of the difference between selected bathymetric surveys. This methodology is commonly used in morphologic studies to constrain fluvial bed morphology change and in aeolian settings (Lane et al., 1994; James et al., 2012; James et al., 2017; Kaliraj et al., 2017; Sirianni et al., 2020). Sirianni et al. (2020) used this method to estimate the volumetric change of Sugarloaf Island along the North Carolina coast from 2014-2020, a time that encompassed hurricanes and winter storm events. The process compared two rasters through time to identify pixels that have changed due to long-term or immediate differences in elevation and spatial extent, allowing a full, small-scale spatial distribution of volumetric changes in the chosen surveys. In the raster calculator geoprocessing tool, the selected rasters were the surveys that came after a chosen time and were subtracted from those that predated the chosen temporal period. This tool uses an algorithm that calculates spatial changes from pixel to pixel in the X, Y, and Z planes. Therefore, the seafloor's horizontal and vertical distribution can be observed as a raster dataset. After running the tool, the data output was a new raster dataset. The pixel dimensions, 6 x 6 m, were multiplied by the pixel count to determine the average volume change within an elevation range. The DEMs were referenced to the vertical coordinated system of NAVD88, MSL, processed by Geodynamics. The vertical accuracy was not reported by the provider if accuracy was performed. The elevation change was divided into seven classes so that the values of no change would fall around 0 m plus or minus 0.1 m. The classes were averaged and then multiplied by the perimeter of the number of pixels, giving the average volumetric change.

3.1.4 Shoreline change/beach and inlet channel cross-sectional profiles

Historic shoreline positions were collected using the USGS's Coastal Change Hazards Portal from 1830 until 2017. Near the study site, historical shoreline positions only go back to 1933. From 2018 until 2022, the Geodynamic elevation models were used to digitize shoreline positions for the remaining time, which the USGS's data do not cover. The elevation models were reclassified to have all pixels from 0.03 m to the greatest extent represent a specified numerical value of 2. All pixels from -0.03 m to the lowest extent are set to a value of 1. Using this geoprocessing method, the rasters were split where the elevation changed from positive to negative. This allowed for an accurate digitization of the position of the shoreline. The shoreline was digitized from 2018-2022 based on (NAVD88) and compared to the past historical data to infer how the system changed over time. The USGS data complemented the shoreline data obtained by Geodynamics from 2018 to 2022.

Cross-sectional inlet channel and beach profiles were constructed to show a 2D representation of the nearshore environment, beach face, and across the ebb-tidal delta. A 3D scene was created in ArcGIS Pro, and then the 3D exploratory analysis tool was used to digitize these sub-environments within the extent of each survey (Appendix A and B). This technique captured the migration of the ebb-tidal delta and inlet channel along with semi-annual morphological changes.

3.2 Geophysical data collection

An EdgeTech 216SB (2 to 16 kHz) CHIRP sub-bottom profiler was utilized with a 3100-P acquisition system to acquire the geophysical data. The profiler was towed alongside the R/V

Tomcat approximately 1 m below the sea surface at 3-4 knots. Surveys were designed to image the subsurface primarily within the dimensions of the bathymetric DEMs, which formed the basis for the digitality-derived stratigraphic model Pearson et al. (2022). Data were collected using a Garmin WAAS-enabled GPS and were processed and analyzed using Chesapeake Technology, Inc. SonarWiz (v.7.1) software. Processing included bottom tracking, application of a swell filter, and adjusting automatic gain control (AGC) settings. Acoustic reflections were then digitized to provide the seismic stratigraphic framework.

3.3 Delft3D hydrodynamic modeling

The Delft3D Flexible Mesh software was implemented to model the hydrodynamics of the continental shelf into the nearshore and the inlet/inlet sub-environments. The modeling helped improve the understanding of the natural flow dynamics of the nearshore environment, ebb-tidal delta, and inlet channel during time intervals associated with high-energy events (i.e., hurricanes or nor'easters) as well as time intervals with no high-energy events. The Delft3D model uses a flexible mesh grid setup and solves shallow water fluid momentum equations on these computational grids. The discretization of these equations through time conserves mass and momentum (Rodi, 1984; Delft Hydraulics, 2021). The model equations and numerical implementation are explained in detail in Lesser et al. (2004), and a relevant application of the Flexible Mesh grid was completed by Manchia et al. (2023), who simulated the waves and storm surge generated by Hurricane Florence. The current study analyzed only water level, current vectors, and current velocity excluding wave action due to the FM-flow model not being coupled with a wave model. Not coupling a wave model to the FM-flow model does not give a total representation of how wave action superimposed on water level (storm surge) could affect morphologic change.

First, a curvilinear grid was set up in the Delft3D graphic user interface with grid cell sizes ranging from 80 m in the NE-SW direction to 150 m in the NW-SE direction within the inlet area (Figure 20). Offshore of the inlet, on the continental shelf, the grid cell sizes ranged from 420 m in the NW-SE direction to 2,140 m in the NE-SW direction (Figure 21). Topo/bathymetry DEM data obtained directly from Geodynamics LLC and bathymetric data acquired through the Delft dashboard software were interpolated to the grid from two sources: 1) the course database supplied with Delft3D (in the Delft dashboard) with 91 m resolution, and 2) the high-resolution bathymetry provided by Geodynamics at 6 m resolution. The model simulates the 2-dimensional (depth-averaged) hydrodynamic response to several major storm events. The major input parameters consisted of seawater density at 1025 (kg/m^3), air density at 1.205 (kg/m^3), gravity at 9.813 (m/s^2), uniform friction coefficient (bottom friction) of 0.023 (s/m(1/3), with the uniform friction type set at (manning), and horizontal eddy viscosity of 0.1 (m^2/s). These parameters are default parameters set in Delft's graphic user interface. The model user time step consisted of 1 hour, with the initial and initial max time steps at 1 second and 30 seconds.

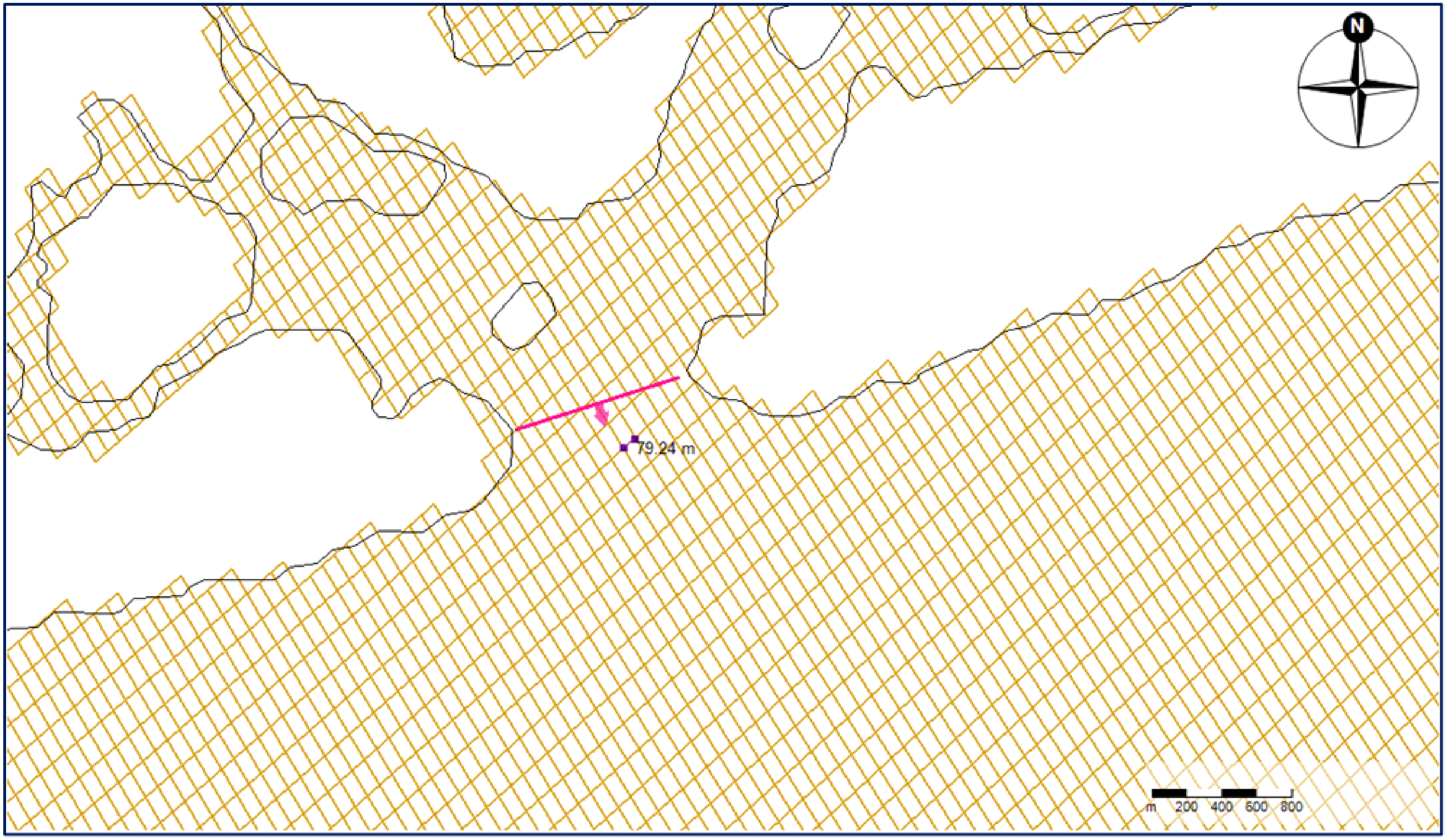

Figure 20. The dimensions of the Delft3D computational grid on the NE-SW axis, located within Bogue Inlet. The extent is ca. 80 m x 150 m.

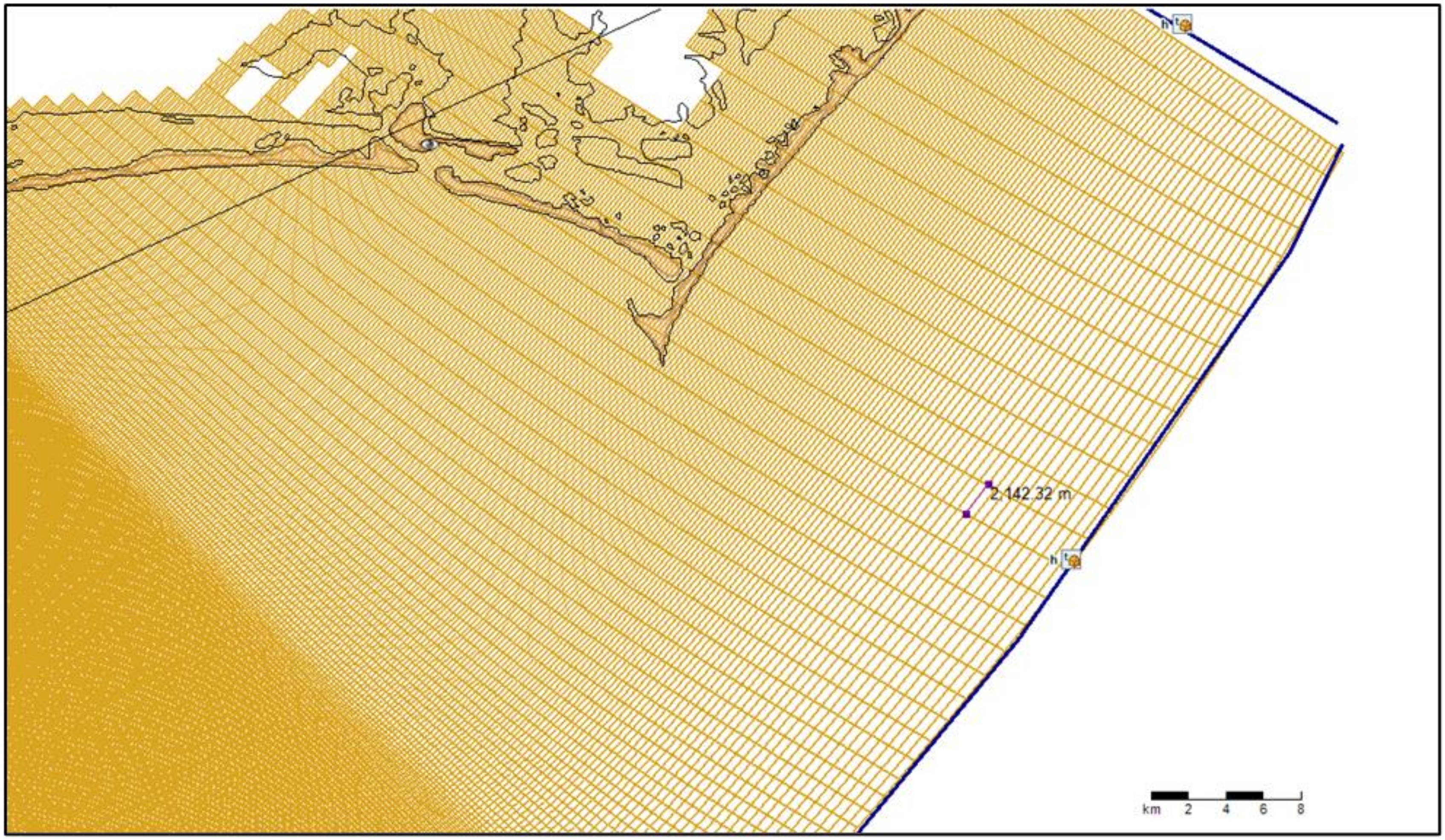

Figure 21. The dimensions of the Delft3D computational grid on the NE-SW axis are located near the margin of the grid extent. The cell dimension is ca. 420 m x 2,140 m.

The model was forced by water levels applied at the boundaries and spatially varying wind and pressure fields applied over the grid. Boundary conditions and physical parameters, such as astronomical tidal constants (water levels) and metrological data, were forced into the model. Water levels are the overall vertical position of the water surface, including the effects of tides, currents, and storm surges, despite wave activity. Astronomical constants were collected from NOAA's tides and currents database (https://tidesandcurrents.noaa.gov) along with wind speed, direction, and barometric pressure. These data locations at Duke Marine Lab and the Wrightsville Beach buoy were used as inputs and observation points to compare modeled outputs (Figure 22). The specific Hurricane events were collected through the Delft dashboard with spatially varying wind and pressure fields plotted on a spiderweb grid. The spiderweb grid is a spherical grid that best represents the spatially varying wind and atmospheric pressure values of the eye of a cyclone as it moves through time, unlike a uniform pressure and wind field that can be used to force atmospheric boundary conditions in an FM-flow model.

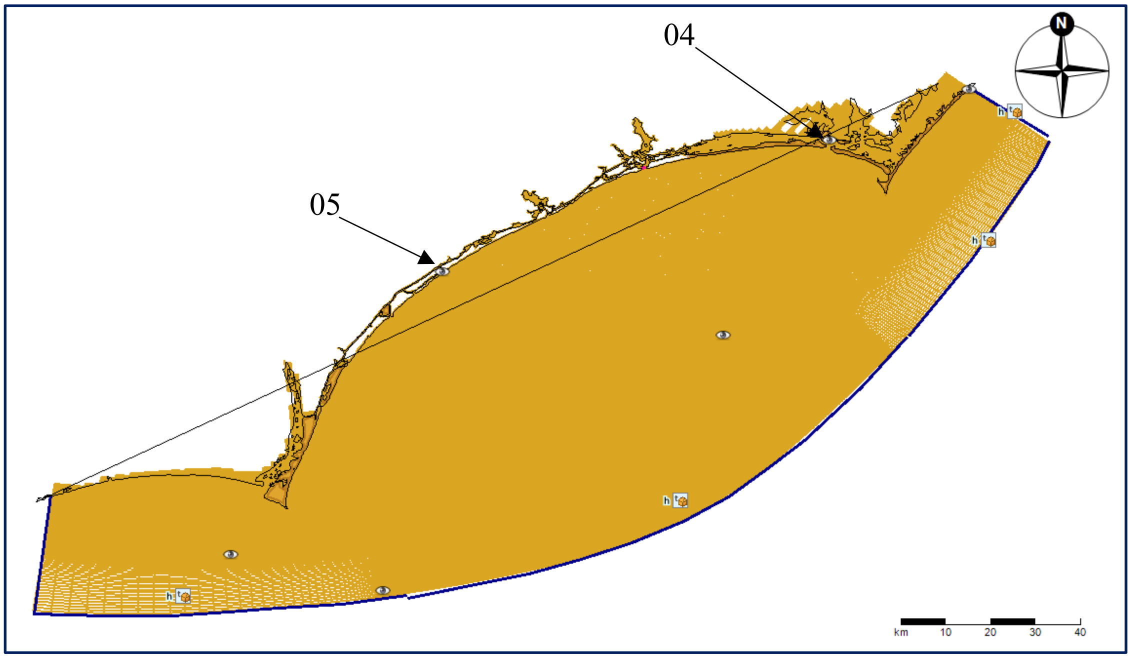

Figure 22. The Delft3D computational grid, with input data and observation point locations, 04 and 05. Locations are numbered; refer to the input data, observation point name, and Lat; Long in Table 2.

Table 2: The locations of input data and observation points.

Lat; Long	Observation site name	Observation site model#
34.70˚ N -76.66˚ W	**Duke Marine Lab, NC (Water levels)**	**# 04**
34.39˚ N -77.58˚ W	**Wrightsville Beach, NC (Water levels)**	**# 05**

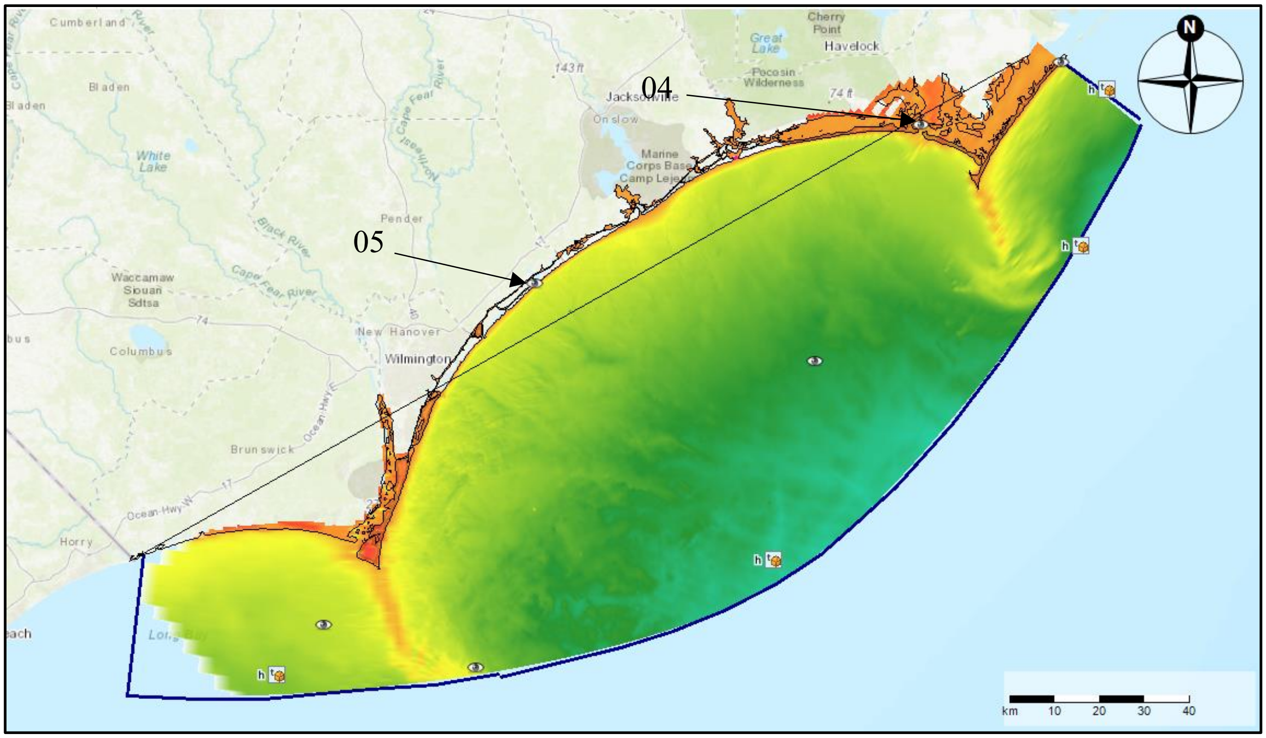

Figure 23. The Delft3D computational grid is shown, with the interpolated bathymetry, input data, and observation points recorded in Table 2. The locations are numbered; refer to the input data and observation points' names and locations in Table 2.

By forcing the models with data from Duke Marine Lab and the Wrightsville Beach buoy, realistic conditions at the model's boundaries would produce simulations that agree with observed phenomena, such as storm surge (water level), current velocity, and direction. With these parameters in place, the models have a 24-hour spin-up time and were run for two to three weeks, with the storms residing approximately in the middle of the simulated periods. RMSE values were calculated with input data from Duke Marine lab and Wrightsville Beach compared to the output data from these locations. Data were also compared to the observations from the corresponding GIS, geophysical, sedimentology, and microfossil data to advance the understanding of the morphodynamics of Bogue Inlet.

3.4 Sedimentology

Fifteen sediment samples from the seabed were collected using Ponar and Shipek grab samplers. The sediment samples were washed with DI water, weighed, and then placed in an oven and dried at 95°C for 24 hrs. When the samples were dry, they were weighed again and then split using a sediment splitter to a 40–50-gram mass. Samples were then sieved at 0.5 phi intervals from 4 phi to -2 phi for 15 minutes using a Ro-tap machine. Grain-size statistics were calculated using the GRADISTAT-2008 worksheet and the Folk and Ward (phi) method (Folk, 1974; Blott and Pye, 2001).

3.5 Micropaleontology

Sixty grams of sediment from the grab samples were collected and wet-sieved over 710- and 63-micron screens. The samples were taken from the top 1 cm of the sediment when collected from the Shipek grab sampler. However, most of the material was used to meet the necessary mass requirements for analysis due to problems faced when sampling in the field with the Ponar grab sampler. The foraminifera within the 63-to-710-micron fraction were then concentrated using the sodium polytungstate floating method (Munsterman & Kerstholt, 1996; Skipp and Brownfield, 1993). This technique allows the foraminifera tests to float in the dense liquid and the siliciclastic grains to sink to the bottom due to the difference in the density of the material and air trapped in the pores of the foraminifera tests. The float material was washed with DI water to remove excess heavy liquid and then placed in weigh boats to dry overnight in an oven at 40° C. After the samples were dried, the float material was weighed. A random numbers table was used to select the squares on the picking tray to be picked. Approximately 100 specimens per sample were picked and transferred to microfossil slides prepared with dilute gum tragacanth to facilitate sorting. The fraction of the float material picked was recorded. After identifying the benthic specimens to the species level using published literature (Schnitker, 1971; Waters and Snyder, 1986; Ruth and Low, 1981), the number of modern specimens and fossil specimens in 50 g of sediment was calculated. The number of specimens and relative abundance (percents) for modern and fossil specimens were recorded. Further, fossil specimens were separated into those with a) phosphatic or b) sugary (calcite overgrowths) and orange/yellow stained categories, and count and relative percents were recorded. The number and relative percentage of planktonic foraminifera were also recorded.

4.0 RESULTS

4.1 Geospatial analysis

4.1.1 Ebb tidal-delta volumetric change

The bathymetric DEMs are shown in (Appendix C). Based on the GIS analysis, bathymetric data show that the main inlet channel of Bogue Inlet and the associated features (i.e., ebb-tidal delta, marginal flood channels, etc.) have migrated in a northeasterly direction since the relocation project in 2005 (Figure 24). As the migration occurred, the channel mouth rotated towards Bogue Banks (Figure 24).

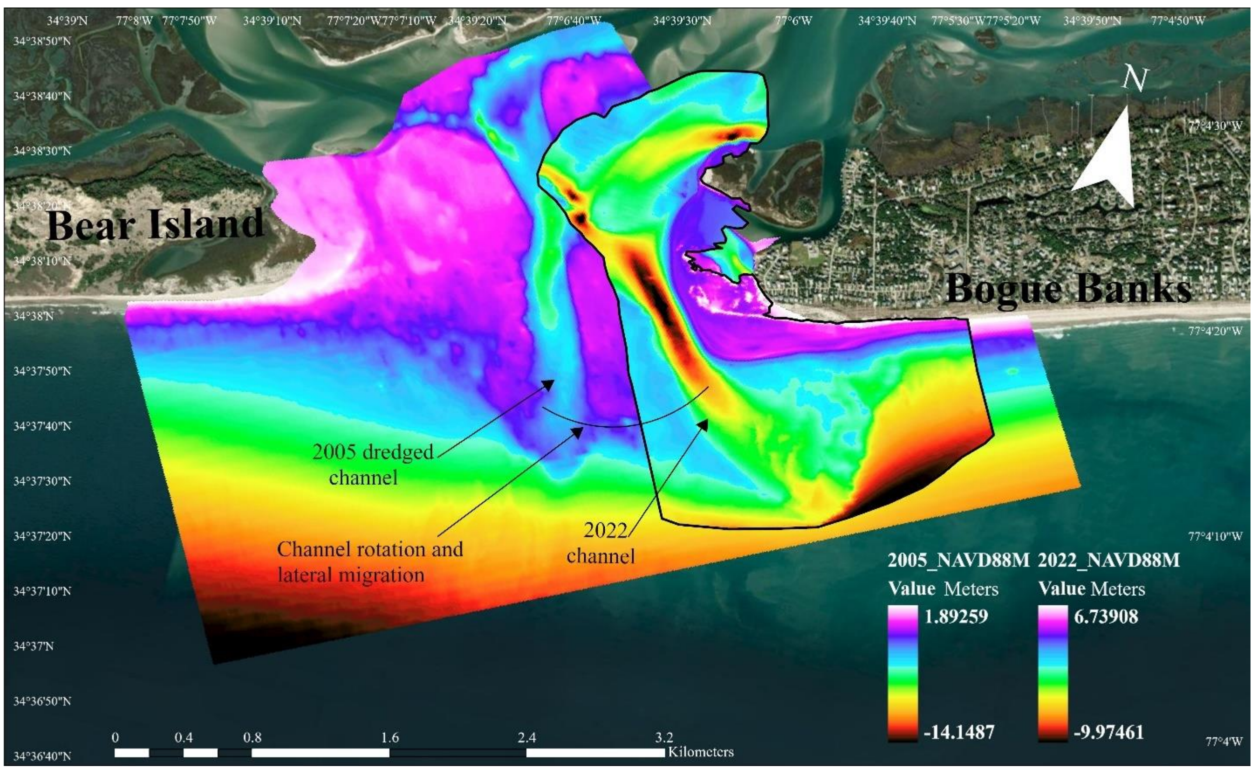

Figure 24. Aerial image and DEMs showing the location of the newly dredged channel in 2005 and the direction of the inlet throat's migration and channel mouth rotation ending in 2022. The survey's extent for 2022 is outlined with a black line. Note the almost linear connection to the back barrier tidal creek in 2022, but in 2005, there is a slight meander around the subaerial spit off Bear Island.

Volumetric measurements in the bar graphs (Figure 25 A) show the storage volume decreasing over time, which equates to the ebb-tidal delta sediment volume, within the measured extent, increasing over time. The time series data also show the period of the most extensive volumetric changes and the quickest rate of change, 2016-2019 (Figure 25 A red box), which coincides with the most documented storm tracks within 120 miles of Bogue Inlet and the most intense landfalling hurricanes between 2016 and 2019 (Figure 3 and Table 1). However, this could be a function of the dredged material disposal at Bogue Point and Bogue Banks.

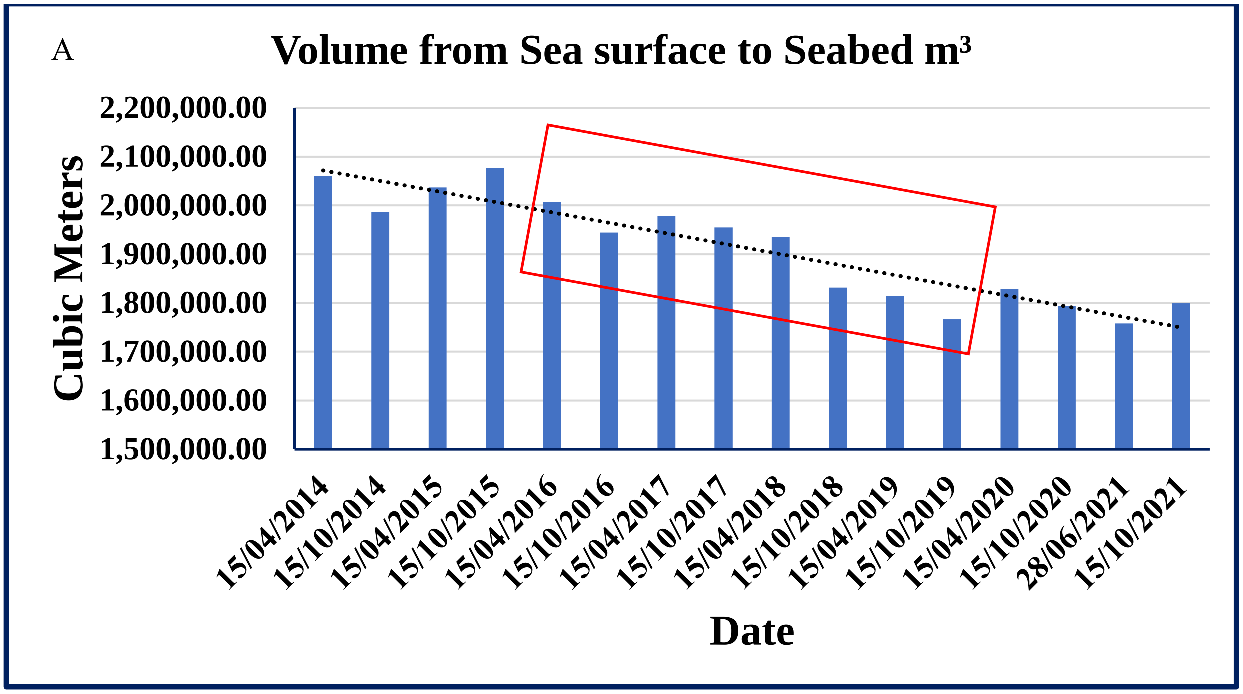

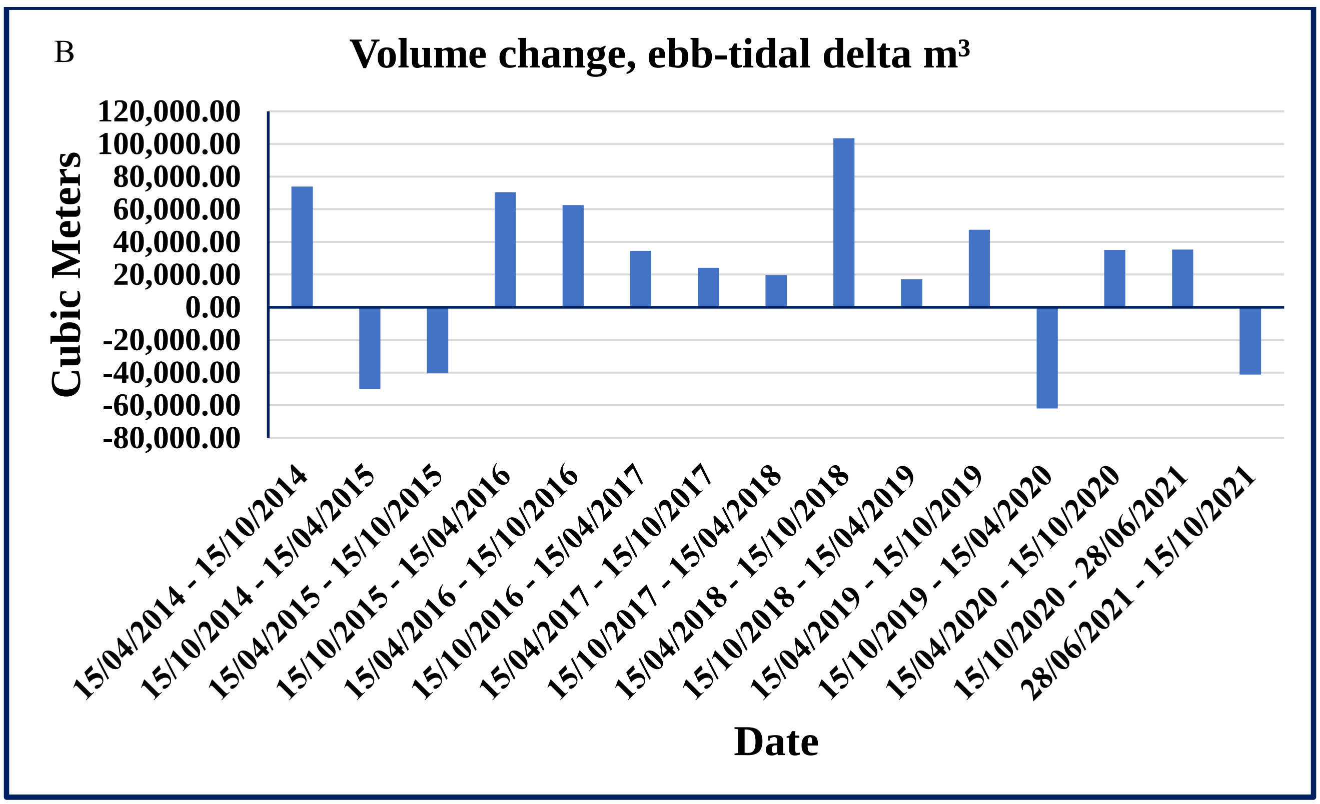

Figure 25. A) Represents the data collected when calculating the storage volume (i.e., water column) over the ebb-tidal delta. Refer to (Figure 18) for the methodology for calculating water column volume using the surface volume geoprocessing tool. **B)** is the difference of the volumetric values calculated in **A)**, that is, the true function of material being deposited or eroded from the ebb-tidal delta. Refer to (Figure 18) for methodology. The red box in **A)**

shows the fastest rate of volumetric change from 2016 to 2019, with the most storms possibly transporting sediment from the shelf and beach nourishment projects to the measured extent.

In Figure 25 B, data represents the difference between the volume calculations of the polygon extent from the previous survey minus the next impending survey.

4.1.2 DEM of difference, volumetric change

The raster data sets were created using the digital elevation model of difference method to show the spatial variability within the survey, including the extent of erosion, deposition, or no elevation change (Figures 26 A and 27A). Figure 26 represents the time between the surveys of 2017 F and 2018 S. Figure 26 shows the largest difference between net loss and net gain, skewed positive at + 730,921 cubic meters. Figure 27 shows the largest difference between net loss and net gain, skewed negative at -600,000 cubic meters. These two figures do not depict the largest calculated values of net loss or net gain; refer to (Table 3) for the true values. Figure 28 only represents the differences between net gain and net loss. The statistics used to calculate the true values are presented with histograms (Figures 26 B and 27 B), breaking down the number of pixels that fell within a range of elevation change. By knowing the perimeter of each pixel (6 m x 6 m) and the number of each of those pixels that came within a range of elevation change, volumetric estimates could be calculated. DEM of volumetric change estimates was also conducted for periods encompassing the storms, which are presented in the discussion section of this study.

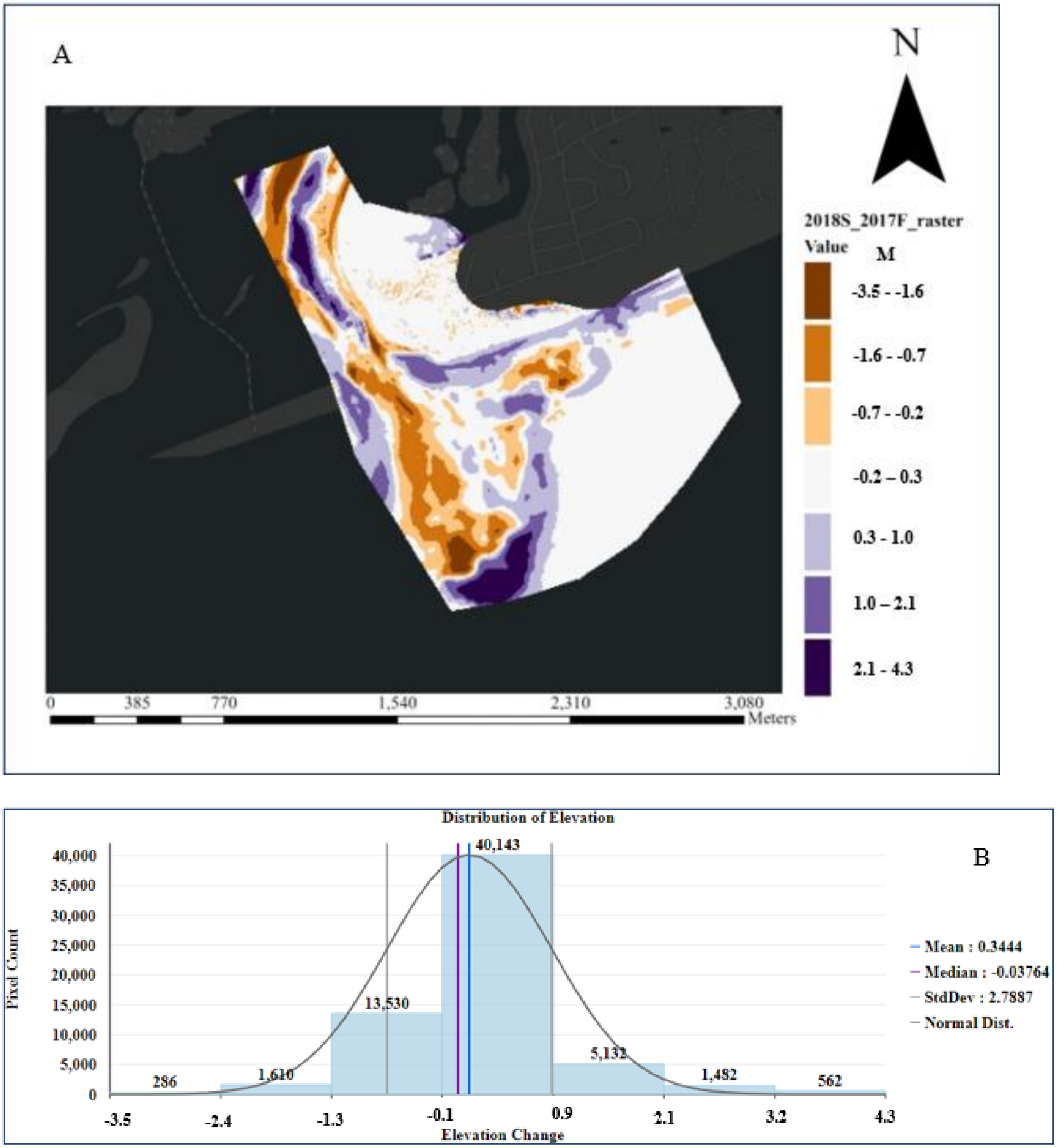

Figure 26. **A)** Shows the raster output of the DEM of difference method used in ArcGIS Pro Version 3.0. The raster represents elevation change in differing shades of purple and brown. The purple shades show deposition, and shades of brown show erosion. 2017 F to 2018 S was when the most significant positive volumetric difference (net sediment gain) occurred. **B)** shows the histogram used to calculate the estimated volumetric values of erosion and deposition by averaging the range of elevation change on the x-axis multiplied by the number of pixels that fell within that range on the y-axis. The y-axis is the number of pixels (6 m x 6 m per pixel) that fall within a range of elevation change. The x-axis represents the range of elevation change measured in meters. The range of elevation change is averaged. Then, the perimeter of a pixel is calculated (6 m x 6 m) and multiplied by the number of pixels in the specific range of elevation change to find the total perimeter of those pixels. Lastly, the range of elevation

change is multiplied by the total perimeter of the pixels that fell within the averaged elevation change, giving an estimate of the volume of the specific perimeter of the pixels in that range.

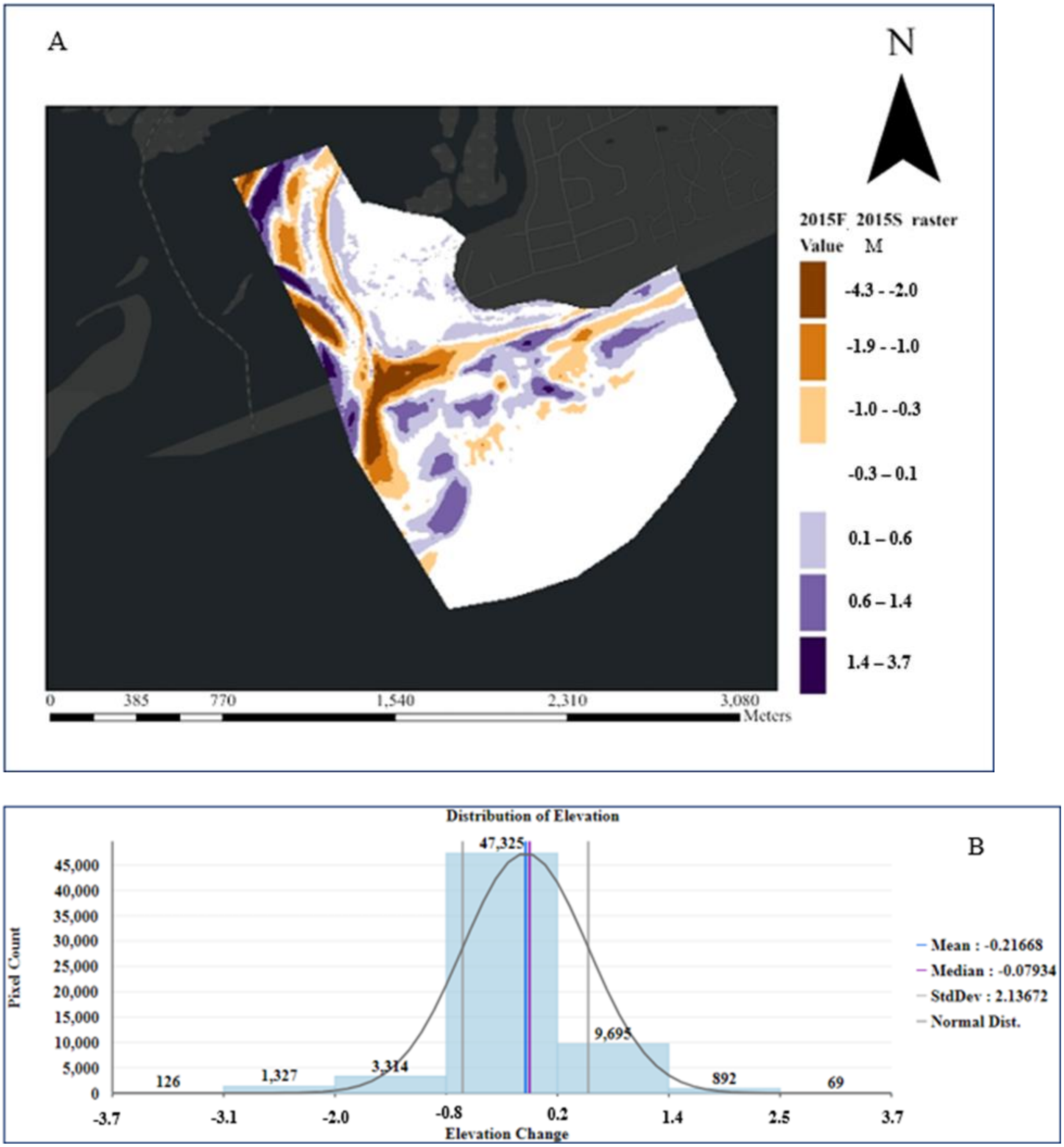

Figure 27. A) Shows the raster output of the DEM of difference method used in ArcGIS Pro Version 3.0. The raster represents elevation change in differing shades of purple and brown. The purple shades show deposition, and shades of brown show erosion. 2015 S to 2015 F was when the most significant negative volumetric difference (erosion) occurred. **B)** shows the histogram used to calculate the estimated volumetric values of erosion and deposition by averaging the range of elevation change on the x-axis multiplied by the number of pixels that fell within that range on the y-axis. The y-axis is the number of pixels (6 m x 6 m per pixel) that fall within a range of elevation change. The x-axis represents the range of elevation change measured in meters. The range of elevation

change is averaged. Then, the perimeter of a pixel is calculated (6 m x 6 m) and multiplied by the number of pixels in the specific range of elevation change to find the total perimeter of those pixels. Lastly, the range of elevation change is multiplied by the total perimeter of the pixels that fell within the averaged elevation change, giving an estimate of the volume of the specific perimeter of the pixels in that range.

Surveys from 2005, 2007, 2008, and 2009 were excluded because their boundary extents were either twice as large or a third of the size of the surveys from 2012-2022 and had a longer temporal span between surveys.

From 2012 to 2022, data indicate that significant volumetric changes occurred over the temporal spans encompassing tropical cyclone seasons and months that fell within the times from fall to summer, where years would change from past to present. Furthermore, from the fall of 2016 to the spring of 2017, the survey extent was almost in equilibrium at only a net gain of 19,818 m^3 (Table 3).

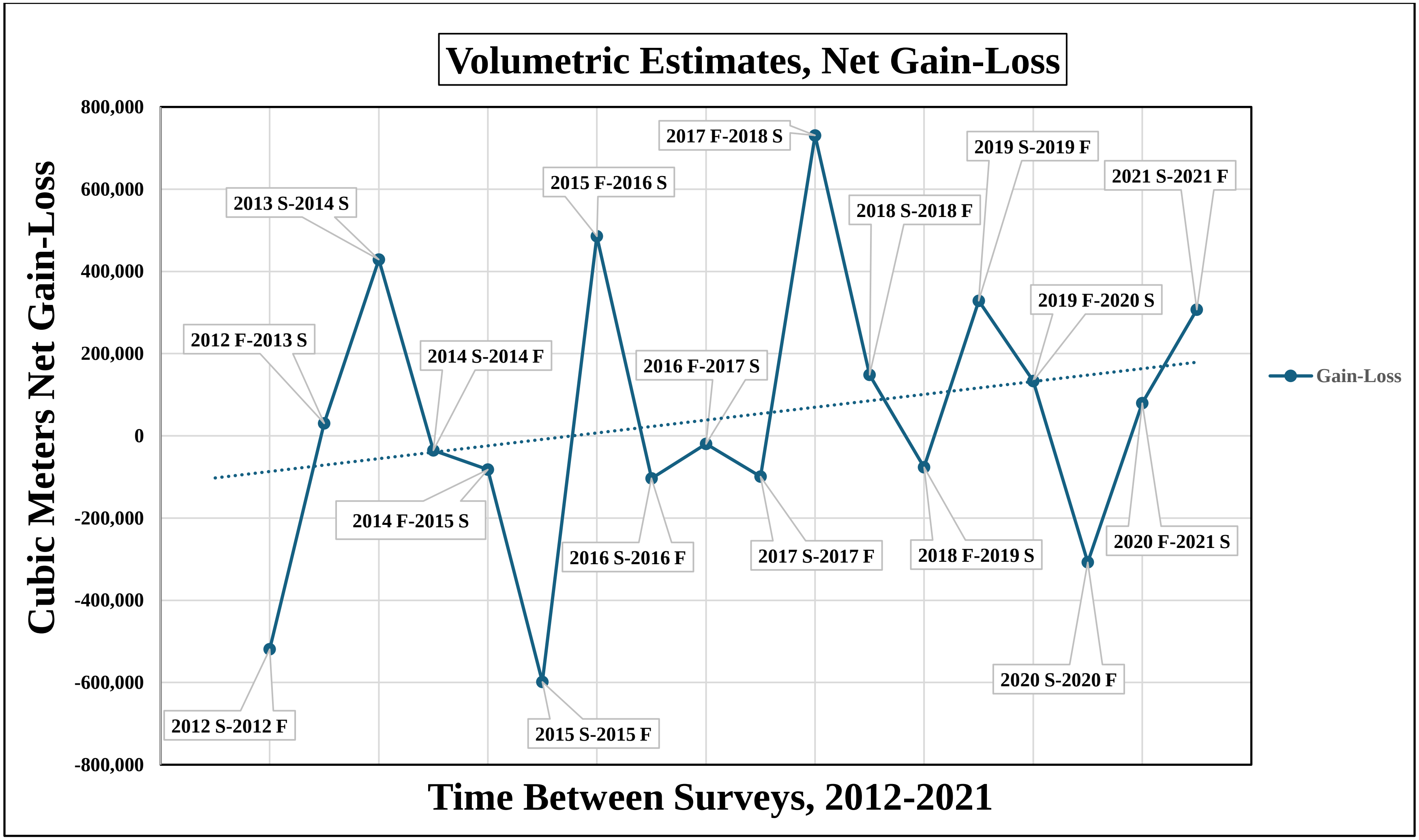

Figure 28. The time series graph shows the difference between the net gain and net loss estimated volume calculations presented in Table 3. The difference in the calculations is presented in cubic meters, positive or negative on the y-axis and time on the x-axis. The graph shows a positive trend line as the full survey extent is gaining material over the time.

Table 3. The table records the estimated net gain and net loss, total deposition, and erosion of each raster output using the DEM of difference technique. The table also shows whether the survey extent represents a net gain/ loss or is in equilibrium. The time that the DEMs bookend is recorded as summer (summer to fall) or winter months (from fall to the new year). S = summer when the first digital elevation was taken, and F = fall when the second DEM was taken from Geodynamics LLC.

DOD date to date	Net loss of material cm^3	Net gain of material cm^3	Equilibrium	Season
2012 S – 2013 F	673,112	703,500	✓	Winter
2013 F – 2014 S	561,076	989,916	x	Winter
2014 S – 2014 F	1,194,053	1,158,627	✓	Summer
2014 F - 2015 S	776,510	694,423	x	Winter
2015 S – 2015 F	1,129,547	531,028	x	Summer
2015 F -2016 S	723,274	1,208,596	x	Winter
2016 S -2016 F	693,882	590,677	x	Summer
2016 F – 2017 S	730,485	710,667	✓	Winter
2017 S – 2017 F	865,440	766,338	x	Summer
2017 F – 2018 S	578,090	1,309,011	x	Winter
2018 S – 2018 F	746,837	895,301	x	Summer
2018 F – 2019 S	669,725	593,148	✓	Winter
2019 S – 2019 F	764,554	1,093,122	x	Summer
2019 F – 2020 S	1,042,979	1,176,349	x	Winter
2020 S – 2020 F	1,308,905	1,001,205	x	Summer
2020 F – 2021 S	704,262	783,718	✓	Winter
2021 S – 2021 F	583,812	890,895	x	Summer
2021 F - 2022 S	1,376,489	1,449,805	✓	Winter

4.1.3 Beach and inlet channel cross-sectional profiles

Elevation profiles were created across the inlet, beach, and ebb-tidal deltas based on survey data (Appendices A and B). The beach and ETD profile line extends south-southeast over the dune crest to the beach, onto the shoreface, and extends to the furthest extent of the bathymetric surveys to depict morphological change (Appendix A). The full extent of the surveys along this transect was used from 2005 until 2022 because this transect location is present in every survey. Data show that in the inlet cross-sectional profiles, the main inlet channel migrated to the east by 152.4 m from 2013 to 2022. Also, the dimensions of the main inlet channel expanded from its narrowest extent of roughly 175 m in the summer of 2013 to 250 m in the summer of 2021. The Beach profiles recorded longshore bars' onshore and offshore migration, accretion to the beach face, and the migration of the ebb-tidal delta.

4.1.4 Shoreline analysis

The largest lateral migration, 1,591 m from west to east, occurred from 1933 until 1997 (Figure 29). Within this temporal span, there were intervals of westward migration. From 1997 until the present, the shoreline on the westernmost extent of Bogue Banks started to migrate westward and prograde seaward. The most significant north-south movement of the westernmost margin of the island occurred from 1973 until 2022 (Table 4).

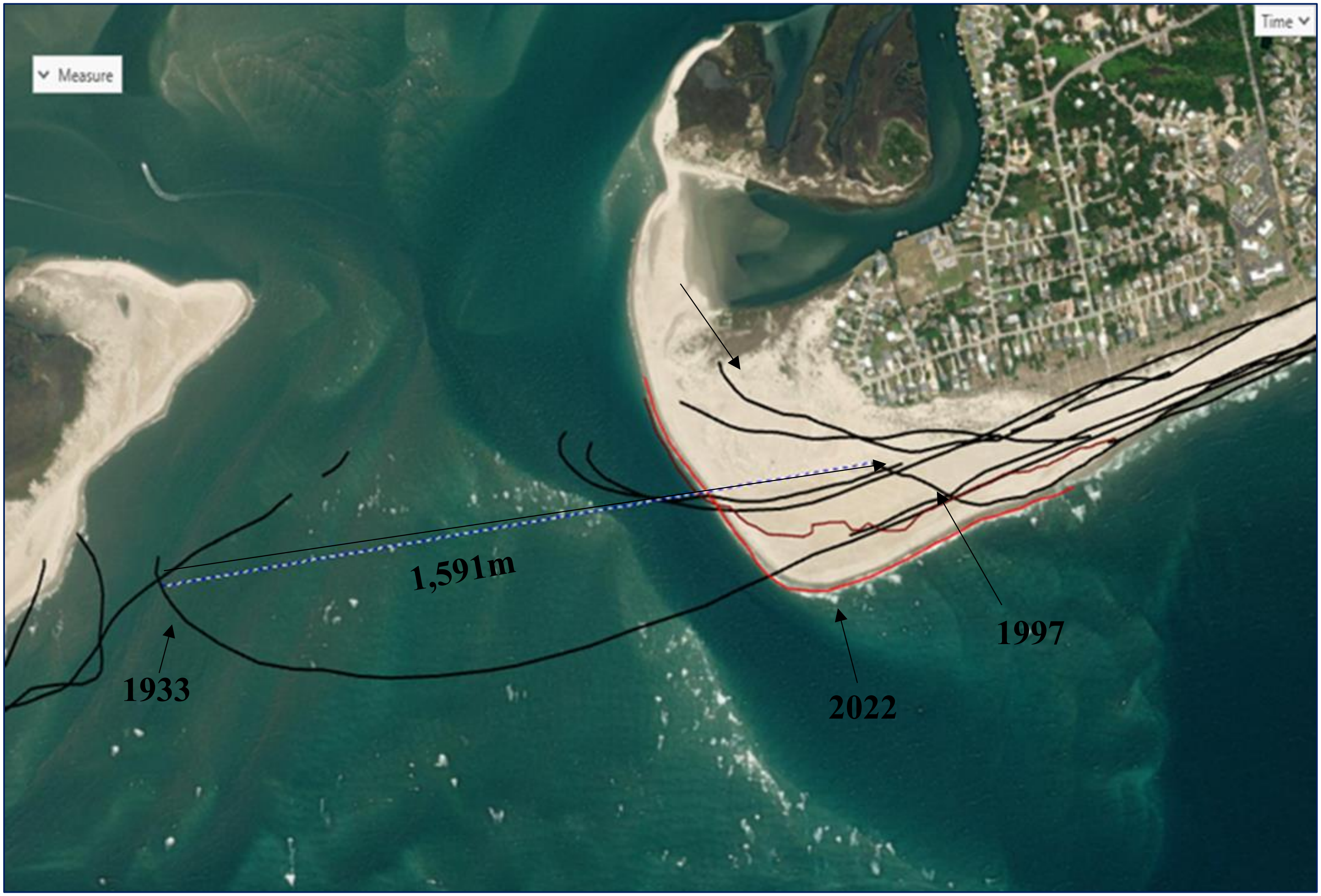

Figure 29. Aerial photograph showing the largest migration on Bogue Banks's western shoreline, measured at 1,591 m. The measurements and shoreline digitization were conducted in ESRI's ArcGIS Pro version 3.0.

Table 4. Shoreline analysis data: This table summarizes the measurements made and directions of change. Data from the USGS Coastal Hazards Portal and Geodynamics bathymetric surveys were digitized to measure position changes. Source https:// USGS Coastal Hazards Portal.gov

Largest Shoreline Migration and Direction

Shoreline date to date	Migration in m	Change of direction	Accretion vs Erosion
1933-1997	1,591	E-W	Erosion laterally
1973-2022S	457.9	N-S	Accretion seaward
2019S-2022S	165.59	NW-SE	Accretion seaward
2018F-2022S	156.69	NNW-SSE	Accretion seaward
2018F-2021F	148.41	NNW-SSE	Accretion seaward
2020S-2020F	100.14	N-S	Accretion seaward
2019F-2020S	96.83	NW-SE	Accretion seaward
2019F-2020S	91.72	NNW-SSE	Accretion seaward
2019S-2019F	80.92	N-S	Accretion seaward
2019F-2020F	71.37	NW-SE	Accretion seaward
2021S-2021F	23.49	NW-SE	Accretion seaward

The shoreline accreted 457.8 m seaward (Figure 29) from 1973 to 2022. As observed in the lateral movement of the shoreline through time, there is also variability in the north-south direction. Although morphology change is spatially variable, a trend is seen in the surveys acquired twice a year, in the summer and the fall. The summer shoreline is typically farther landward than the shoreline positions digitized in the fall (Figure 30).

Figure 30. The base aerial image is from 07/2023 and sourced from Google Earth. Maps of shorelines digitized in ArcGIS Pro version 3.0 using Geodynamics' topo/bathymetric data. The three maps show the spatially varying shoreline movement from Summer to Fall 2019, 2020, and 2021.

4.2 Geophysical data

Three of the sub-bottom survey lines lie within the extent of the digital stratigraphic model created by Pearson et al. (2022): transects D-D', E'-E, and the majority of A-A' (Figure 31). Transects D-D' and E'-E were chosen for interpretation because they have the best acoustic data (Figures 34 and 35).

Transect D-D' tracks over a portion of the western ebb-tidal delta swash platform across the broadest region of the distal main inlet channel and ebb-tidal delta shoals (Figure 33).

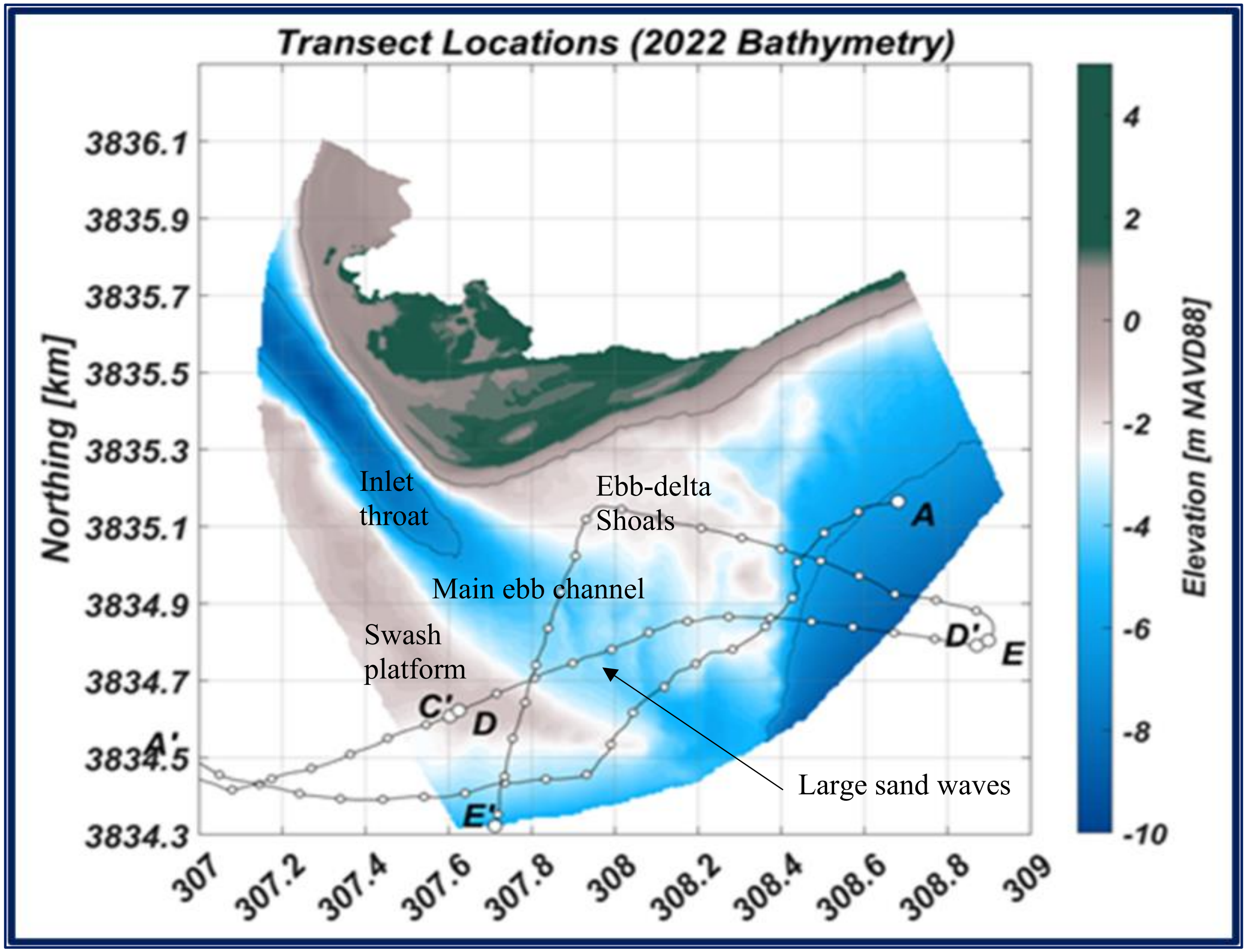

Figure 31. Map produced using the graphical user interface (GUI) from Pearson et al. (2022). The GUI allows the user to draw a transect line and then have the scripted program run to create the digitally derived stratigraphic model. In the GUI above, the GPS-recorded transect lines of the geophysical sub-bottom data were coded into the interface so that the stratigraphic model outputs would match the waypoints of the transect lines. Model outputs are presented in (Fig. 32 and 33). Each transect line was labeled as such to be compared to the raw geophysical acoustic data and the interpretations. Each dot represents 100 m. The bathymetric data used to create the outputs are one year, five months, and five days older than the acoustic data.

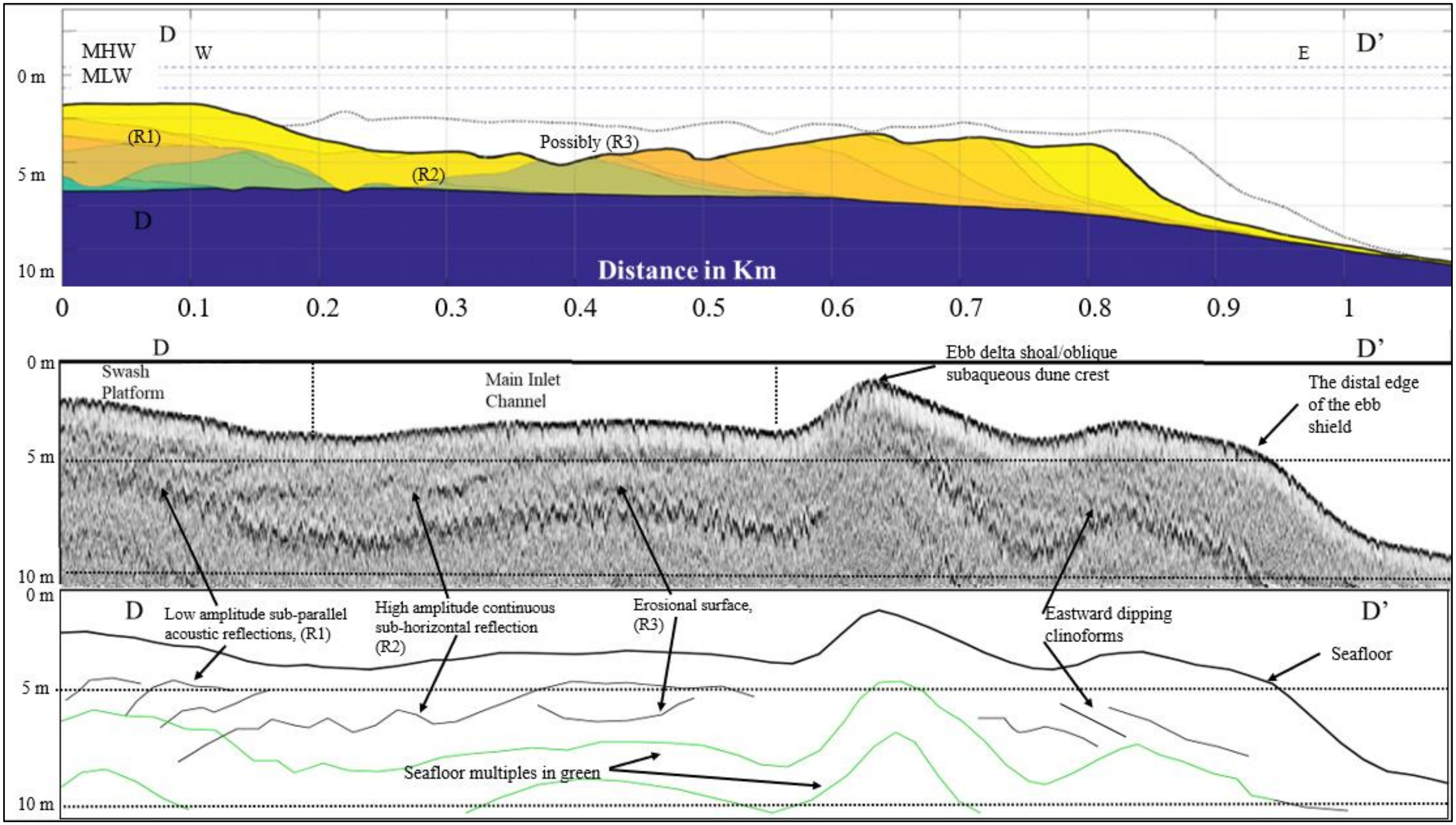

Figure 32. Figure of the stratigraphic model along transect D-D' produced using the Graphical User Interface (top) with the corresponding CHIRP data (middle) and CHIRP data interpretation (bottom) The arrows point to locations of agreement between all sections. The green line in the interpretation is the seafloor multiples, and the bathymetric data used to create the outputs are 1 year, 5 months, and 5 days older than the acoustic data in the middle.

The survey line then crosses the distal edge of the ebb-tidal delta to the east (Figure 31). Low amplitude sub-parallel acoustic reflections, gently dipping to the east, are visible in the sub-bottom data near the western end of the survey, Reflection surface one (R1). The acoustic reflections terminate as they reach the seafloor, pointing in the NE direction towards the middle of the channel (Figure 32). At roughly 100 m to 150 m from the start of the transect, refection surface two (R2), a high-amplitude continuous sub-horizontal reflection runs to roughly 500 m from the start of the survey line before terminating at the 500 m mark. Directly underneath the high amplitude reflection (R2), reflection (R3), from 325 m to 475 m, is a low amplitude parabolic reflection captured in the portion of the data that crosses over the middle of the channel (Figure 32). As the transect travels over a shore oblique subaqueous dune and off the distal ebb-tidal delta lobe from 750 m to 850 m, gently dipping sub-parallel acoustic reflections (clinoforms) are observable dipping basinward to the east (Figure 32).

The survey E-E' (west to east) tracks in the NNE direction starting on the southwestern edge of the ebb-tidal delta's distal lobe, crossing over a narrow margin of the swash platform before crossing the main ebb channel towards the shoreface (Figure 31). As the survey line crosses over the main ebb channel and onto the adjacent northeastern portion of the swash platform, the transect turns approximately 90 degrees and heads east-southeast, back off the swash platform, and over the distal edge of the delta. At the beginning of the transect, reflection surface one (R1), which starts approximately 180 m from the start of the survey line, is a low amplitude sub-parallel, discontinuous reflection that dips roughly 45 degrees down toward the NNE. The discontinuous reflection fades out around 420 m. Starting at 350 m, underneath the end of (R1) is reflection surface two (R2). R2 is a sub-horizontal, medium amplitude acoustic reflection that stretches from 350 m to 780 m before terminating at the directional change on the northeastern shoal complex, close to the western margin of Bogue Banks (Figure 35). At roughly 700 m, refection surface three (R3) can be observed as a very low amplitude sub-horizontal reflection dipping to the east at approximately 15 degrees. The reflection surface extends to 900 m before fading out (Figure 33). At the end of the survey line, medium amplitude acoustic reflections dipping gently to the east are observed. The set of clinoforms starts at 950 m and runs to 1.3 km before traveling over a large oblique bar (Figure 33).

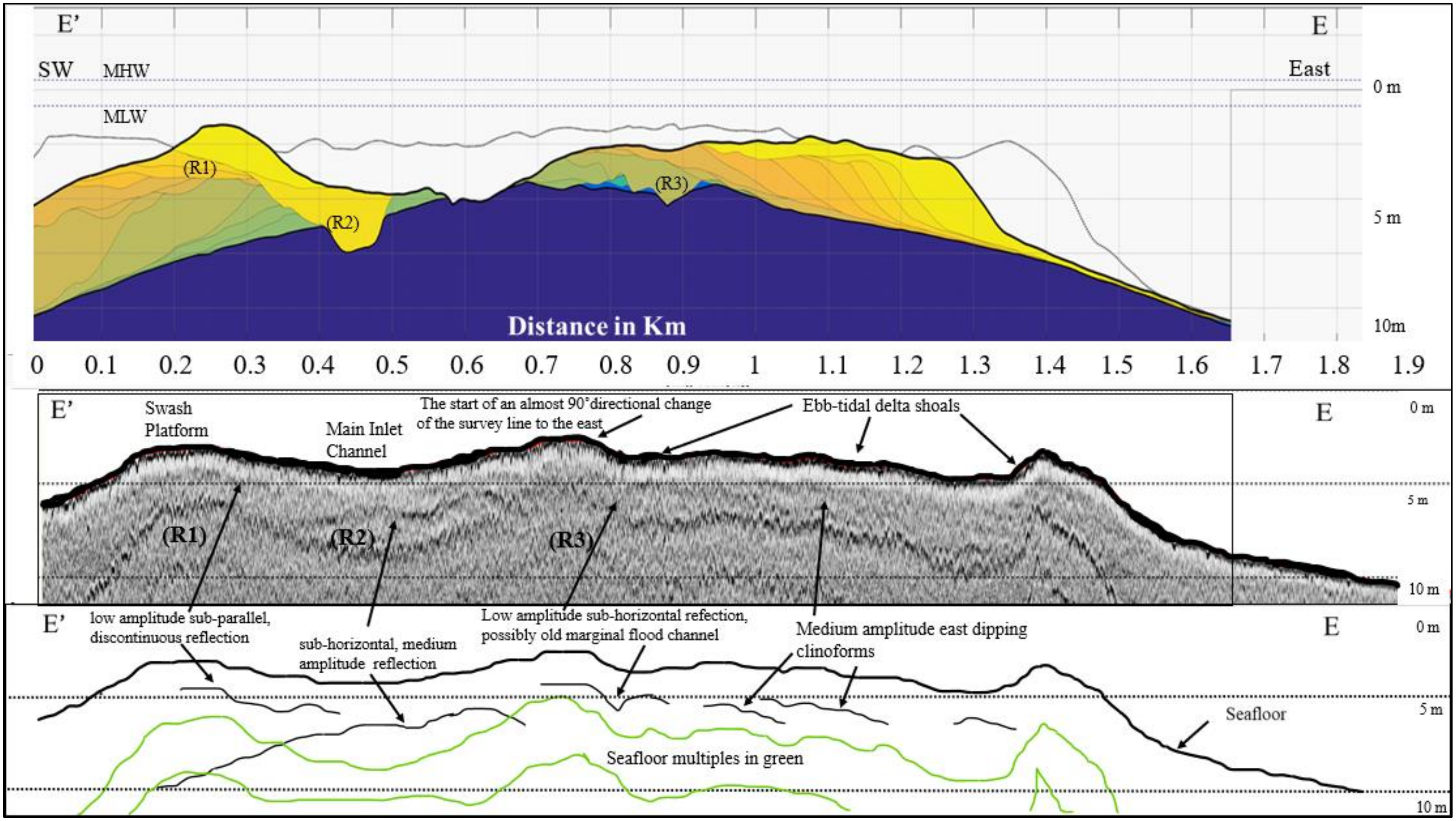

Figure 33. Figure of the stratigraphic model along transect D-D' produced using the Graphical User Interface (top) with the corresponding CHIRP data (middle) and CHIRP data interpretation (bottom). The arrows point to locations of agreement between all sections, and the green lines in the interpretation are the acoustic multiple reflections of the sea floor that is not a natural boundary surface that reflects energy to the receiver due to any physical or chemical difference in structure.

4.3 Hydrodynamics

Three hurricanes were chosen to create model simulations in this study due to the proximity of their tracks to the study location and the point of landfall on the North Carolina coast. The Storms were Hurricane Matthew (2016), Florence (2018), and Dorian (2019). Also, January 2018 was chosen to simulate a temporal span with no recorded tropical storms.

Observation and input data points at Duke Marine Lab and Wrightsville Beach were chosen to force water levels into the models and calculate RMSE values to compare to the model outputs. The RMSE of the modeled water levels for individual storms ranges from 0.47 m to 0.13 m and are based on N=373 to N=710 number of observation data points, showing good agreement with the observed water levels at the chosen observation sites (Table 5).

Table 5: (RMSE) of Model Outputs Delft3D
The statistical calculations of the (RMSE) of water levels from the model outputs compared to the observations from the input data/observation sites. The input data/observation site name, latitude, longitude, and number are also presented.

Observation sites and RMSE model outputs

Lat; Long	Observation site name	Observation site model#	RMSE in m
34.70˚ N -76.66˚ W	Duke Marine Lab, NC (Water levels)	# 04	0.27 m Dorian 0.31 m Florence 0.24 m Matthew 0.41 m Winter model
34.39˚ N -77.58˚ W	Wrightsville Beach, NC (Water Levels)	# 05	0.47 m Dorian 0.28 m Florence 0.24 m Matthew 0.13 m Winter model

The values vary by model simulation and spatially from site to site. The observation site with the closest value to zero was recorded at Wrightsville Beach, with an (RMSE) of 0.13 m from observed values during the simulation of (January 2018) (Table 5). A value closest to zero shows the best agreement with observed phenomena, showing high confidence in the model outputs for the simulation modeling in January 2018 in that geographic region. The (RMSE) greatest value was 0.47 m, recorded at Wrightsville Beach during the model simulation of Hurricane Dorian (Table 5). For the model simulation of Hurricane Dorian, RMSE values were (0.27 m at Duke Marine Lab and 0.47 m at Wrightsville Beach) (Table 5). These error values show good agreement with the observed water levels compared to other simulated tropical cyclones in the literature (Manchia and Mulligan, 2022; Manchia et al., 2023). The simulated hurricane with the best RMSE values was Hurricane Matthew. The RMSE values are 0.24 m at Duke Marine Lab and 0.24 m at Wrightsville Beach. Hurricane Florence's RMSE values were calculated at 0.31 m at Duke Marine Lab and 0.28 m at Wrightsville Beach (Table 5). Lastly, the model simulation of January 2018 RMSE produced values of 0.41 m at Duke Marine Lab and 0.13 m at Wrightsville Beach (Table 5). All the modeled outputs show a range of agreements from medium to high confidence.

4.4 Grain size data

The sediment samples collected show a grain-size distribution from very coarse sand to fine sand throughout the sample locations (Table 6, Figure 34). The gravelly composition comprises coarse angular shell clasts and well-rounded siliciclastic grains (Table 6).

Table 6: Grain size characteristics of Bogue Inlet

SAMPLE #		BI-23-01	BI-23-02	BI-23-03	BI-23-04	BI-23-05	BI-23-06	BI-23-07
	SIEVING ERROR:	0	0	0	0	0	2.10%	0
	SAMPLE TYPE:	Unimodal, Poorly Sorted	Unimodal, Moderately Sorted	Unimodal, Very Well Sorted	Unimodal, Moderately Well Sorted	Unimodal, Moderately Well Sorted	Unimodal, Moderately Sorted	Unimodal, Moderately Sorted
	TEXTURAL GROUP:	Gravelly Sand	Slightly Gravelly Sand	Slightly Gravelly Sand	Slightly Gravelly Sand	Slightly Gravelly Sand	Gravelly Sand	Gravelly Sand
	SEDIMENT NAME:	Very Fine Gravelly Coarse Sand	Slightly Fine Gravelly Medium Sand	Slightly Fine Gravelly Fine Sand	Slightly Very Fine Gravelly Coarse Sand	Slightly Very Fine Gravelly Medium Sand	Very Fine Gravelly Coarse Sand	Fine Gravelly Medium Sand
FOLK AND	MEAN	0.41457411	1.321260129	2.02730046	0.729178973	1.654208093	0.639654146	0.769085183
WARD METHOD	SORTING	1.094173798	0.782687059	0.324455122	0.678816879	0.598009892	0.908659435	0.970886222
(f)	SKEWNESS	-0.27767482	-0.24599246	-0.176652162	-0.058892365	-0.168118077	-0.165021537	-0.310074673
	KURTOSIS	1.38734159	1.601349994	0.760987144	1.387235665	0.87690004	1.356532643	1.425031907
FOLK AND	MEAN:	Coarse Sand	Medium Sand	Fine Sand	Coarse Sand	Medium Sand	Coarse Sand	Coarse Sand
WARD METHOD	SORTING:	Poorly Sorted	Moderately Sorted	Very Well Sorted	Moderately Well Sorted	Moderately Well Sorted	Moderately Sorted	Moderately Sorted
(Description)	SKEWNESS:	Coarse Skewed	Coarse Skewed	Coarse Skewed	Symmetrical	Coarse Skewed	Coarse Skewed	Very Coarse Skewed
	KURTOSIS:	Leptokurtic	Very Leptokurtic	Platykurtic	Leptokurtic	Platykurtic	Leptokurtic	Leptokurtic
SAMPLE #		BI-02-ATS	BI-03-ATS	BI-04-ATS	Shipek-104	Shipek-105	Shipek-106	
	SIEVING ERROR:	0	0	0	0	0	0	
	SAMPLE TYPE:	Bimodal, Moderately Sorted	Unimodal, Very Well Sorted	Unimodal, Moderately Well Sorted	Unimodal, Well Sorted	Polymodal, Poorly Sorted	Bimodal, Poorly Sorted	
	TEXTURAL GROUP:	Slightly Gravelly Sand	Slightly Gravelly Sand	Slightly Gravelly Sand	Sand	Gravelly Sand	Gravelly Sand	
	SEDIMENT NAME:	Slightly Fine Gravelly Medium Sand	Slightly Very Fine Gravelly Fine Sand	Slightly Very Fine Gravelly Coarse Sand	Well Sorted Medium Sand	Fine Gravelly Medium Sand	Very Fine Gravelly Coarse Sand	
FOLK AND	MEAN	1.397088315	2.064381127	0.716312031	1.874697748	-0.021250205	-0.42535507	
WARD METHOD	SORTING	0.863113057	0.313647163	0.610103268	0.388590944	1.534134723	1.209140636	
(f)	SKEWNESS	-0.169526631	-0.286086716	-0.121122157	-0.013032588	-0.268782665	-0.317351524	
	KURTOSIS	1.290180296	0.866378821	1.108497185	0.971299837	0.87227512	0.940052491	
FOLK AND	MEAN:	Medium Sand	Fine Sand	Coarse Sand	Medium Sand	Very Coarse Sand	Very Coarse Sand	

WARD METHOD	SORTING:	Moderately Sorted	Very Well Sorted	Moderately Well Sorted	Well Sorted	Poorly Sorted	Poorly Sorted	
(Description)	SKEWNESS:	Coarse Skewed	Coarse Skewed	Coarse Skewed	Symmetrical	Coarse Skewed	Very Coarse Skewed	
	KURTOSIS:	Leptokurtic	Platykurtic	Mesokurtic	Mesokurtic	Platykurtic	Mesokurtic	

Figure 34. Aerial photograph from Google Earth, 09/2024, showing the grain size sample locations from both surface sampling methods, the Ponar and the Shipek grab sampler. Samples labeled BI-23 were collected on 07/13/23, red boxes; samples labeled BI-ATS were collected on 09/25/23, green triangles; and samples labeled Shipek were collected on 11/06/23, white stars.

Across the inlet from sample BI-23-01, located on the western margin of the inlet, to sample BI-23-07, located on the eastern margin of Bogue Inlet, mean grain sizes show a range from 0.415 phi (coarse sand) to 2.027 phi (fine sand) (Figure 34, 35, and Table 6)

The average mean grain size of all the samples collected within the inlet throughout multiple sub-environments, ebb-tidal delta swash platform, main inlet channel, marginal flood channels, flood tidal delta ramp, channel margin linear bar was 1.01 phi (coarse-medium sand).

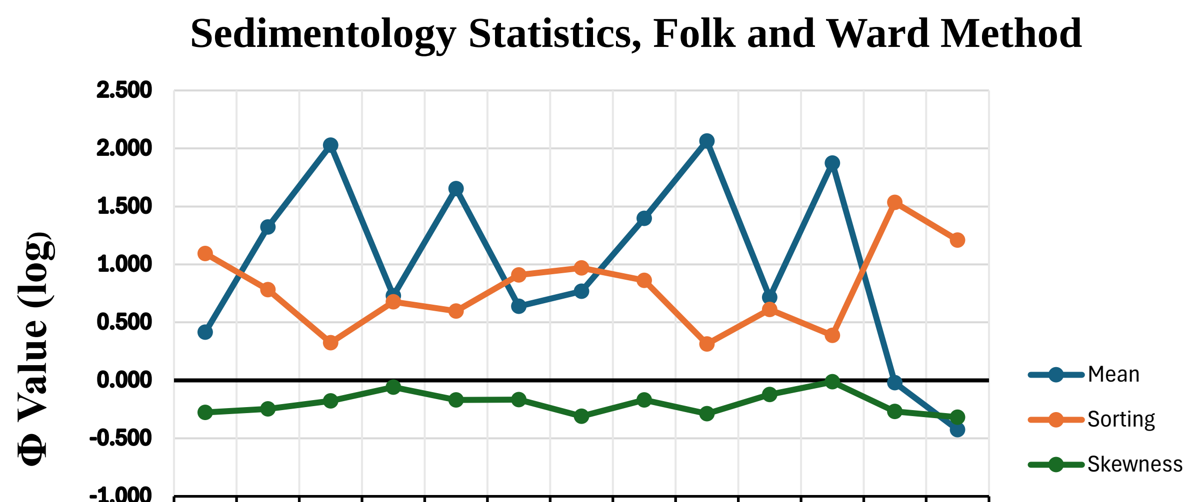

	BI-23-01	BI-23-02	BI-23-03	BI-23-04	BI-23-05	BI-23-06	BI-23-07	BI-02-ATS	BI-03-ATS	BI-04-ATS	Shipek-104	Shipek-105	Shipek-106
Mean	0.415	1.321	2.027	0.729	1.654	0.640	0.769	1.397	2.064	0.716	1.875	-0.02	-0.42
Sorting	1.094	0.783	0.324	0.679	0.598	0.909	0.971	0.863	0.314	0.610	0.389	1.534	1.209
Skewness	-0.27	-0.24	-0.17	-0.05	-0.16	-0.16	-0.31	-0.17	-0.28	-0.12	-0.01	-0.26	-0.31

Figure 35. Sedimentology statistics of surface samples collected in Bogue Inlet are plotted in graphical form, mean, sorting, and skewness using the Folk and Ward method.

The samples were mostly coarse and skewed to symmetrical. Two samples were very coarsely skewed, BI-23-07 and Shipek-106 (Table 7). From the middle of the inlet channel

Shipek-106, moving seaward towards Shipek-104, the grain size characteristic trended from coarse sand to medium sand (Figure 34, Tables 6 and 7).

Samples across the inlet ranged from poorly sorted to very well sorted (Figure 34, Table 6). Poorly sorted samples resided on the western margin of the inlet, in the marginal flood channel (BI-23-01), and nearly in the center of the main channel (Shipek-104 and Shipek-105). Moderately sorted samples (BI-23-02, BI-23-06, BI-ATS-02, and BI-23-07) are located near the channel margin linear bars on both the western and eastern sides of the main channel (Figure 34, Tables 6 and 7).

Table 7. The location of sediment and foraminifera samples, geomorphic sub-environment descriptions, latitude and longitude of sample locations, methods of collection, and depth of collection.

Sediment and Foraminifera sample location and geomorphic sub-environment

Sample number	Geomorphic Sub-environment	Latitude	Longitude	Sample acquisition	Depth collected
BI-23-01	Swash zone, off Bear Island spit	34°38'43.34"N	77° 6'49.40"W	Ponar sampler	-1.8 m
BI-23-02	Western flood channel	34°38'45.86"N	77° 6'43.90"W	Ponar sampler	-0.9 m
BI-23-03	Flood ramp of flood tidal delta	34°38'44.91"N	77° 6'29.21"W	Ponar sampler	-2.7 m
BI-23-04	North end of main inlet channel	34°38'44.05"N	77° 6'26.45"W	Ponar sampler	-4.2 m
BI-23-05	Eastern margin of main inlet channel	34°38' 45.95"N	77° 6'21.36"W	Ponar sampler	-2.7 m
BI-23-06	Eastern margin channel bar	34°38' 45.00"N	77° 6'16.82"W	Ponar sample	-1.5 m

BI-23-07	Foreshore/swash zone off the western margin of Emerald Isle, in Bogue Inlet	34°38' 45.31"N	77° 6'13.14"W	Ponar sampler	-2.1 m
BI-02-ATS/ Waypoint 73	Easternmost marginal flood channel/western margin of Emerald Isle, in Bogue Inlet	34°38′ 43.29″ N	77°6′ 11.70″W	Ponar sampler	-5.7 m
BI-03-ATS/ Waypoint 75	The western slope of the main channel	34°38′39.94″ N	77° 6′28.59 ″	Ponar sampler	-3 m
BI-04-ATS/ Waypoint 76	Flood tidal delta ramp	34°38′55.33″ N	77°6′28.23 ″	Ponar sampler	-3.9 m
BI-05-ATS/ Waypoint 77	Eastern channel margin linear bar complex	34°38′54.18 N	77°6′15.38	Ponar sampler	-2.1 m
Shipek-104	Ebb tidal delta swash platform	34°38'23.61"N	77° 6'17.52"W	Shipek sample	-3.6 m
Shipek-105	Western marginal channel bar of the main inlet channel	34°38'32.07"N	77° 6'20.18"W	Shipek sample	-3.9 m
Shipek-106	Western margin of inlet channel	34°38'38.11"N	77° 6'24.22"W	Shipek sample	-3 m
Total:	**14 samples**				

The moderately well-sorted samples (BI-23-04, BI-23-05, and BI-ATS-04) are all located near the proximal FTD flood tidal delta ramp (Figure 34). Very well-sorted samples, BI-23-03 and BI-ATS-03, are very close to one another and located either on a portion of the swash platform or swash bars further in the middle of the inlet. Lastly, the well-sorted sample, Shipek-104, is located on the distal portion of the swash platform, the furthest sample seaward (Figure 34).

4.5 Foraminifera data analysis

Twenty modern benthic species were identified in the 12 samples collected throughout Bogue Inlet. These specimens represented 86.5% of all specimens picked. The most dominant species, in order of decreasing relative abundance, are *Elphidium excavatum* (47.7%), *Quinqueloculina seminula* (10.3%), *Quinqueloculina lamarckiana* (9.3%), *Ammonia parkinsoniana* (6.2%), and *Eponides repandus* (5.5%) (Appendix F). Seven modern planktonic specimens were recorded, representing 0.53 % of the total modern specimens picked. Planktonics live in Gulf Stream water that flows over the continental slope of North Carolina (Figure 38). Fossil specimens, both phosphatic and sugary, had a combined relative abundance of 13.5 % of the total specimens picked (Figure 37); the vast majority were phosphatic (Figure 37).

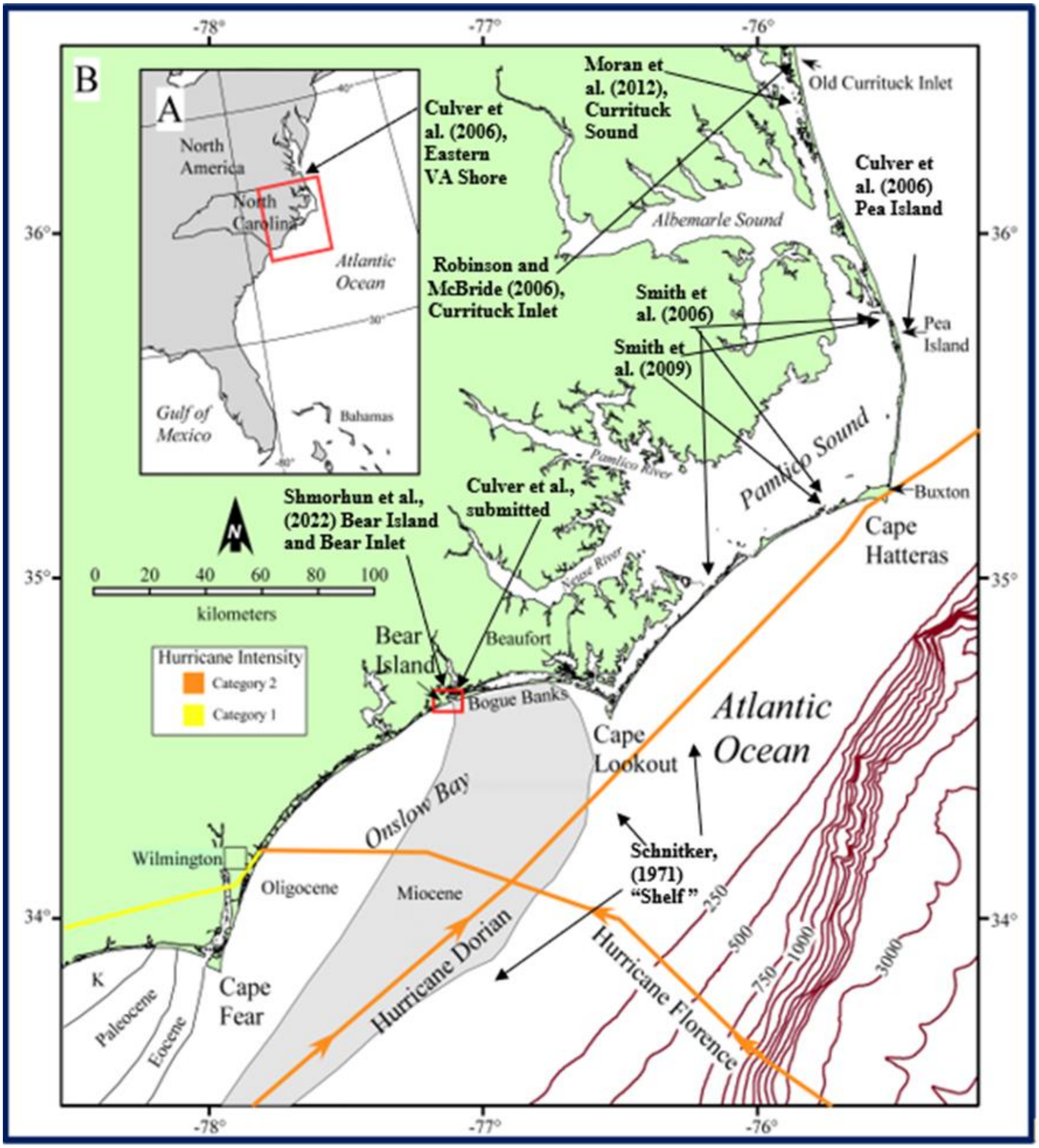

Figure 36. Maps showing **A)** the eastern seaboard of the United States and **B)** the North Carolina Coast. The map also shows the study site in red and the tracks of hurricanes Florence and Dorian. The map has the labeled locations of some of the foraminiferal literature along the coast of NC. Lastly, the figure shows the location of the Miocene Pungo River formation in Onslow Bay, which represents the likely source of the (sugary) and (phosphatic) fossil foraminifera. The figure was reworked, source; Culver et al. (in review).

Elphidium excavatum represents 34-55 % of the modern specimens in all samples. *Quinqueloculina seminula* has its highest relative abundance (18-28%) closest to Bear Island near the westernmost marginal flood channel and on adjacent bar complexes (in 0.9 to 1.8 m water depth) (Appendix F). The lowest relative abundance for *Q. seminula* occurs in the middle of the main inlet channel. *Ammonia parkinsoniana* occurs, in decreasing order, with relative abundances of (13.2%), flood-tidal delta ramp (10.6%), eastern marginal linear bar complex (10.1%), swash zone off Bear Island's spit, and on the western bank of the eastern marginal flood channel (Appendix F). These samples, in order, are BI-23-03, ATS-05, BI-23-01, and BI-23-06. *Eponides repandus* is located in the western marginal flood channel (9.3%), eastern marginal flood channel (8.3%), the ebb-tidal swash platform (8.4%), and on the eastern bank of the main ebb channel at (6.4%). The highest percentage per sample (10.2%) was on the distal portion of the ebb-tidal delta. *Quinqueloculina lamarckiana* occurred on the flood tidal delta ramp (19.3%), eastern ebb-tidal delta swash platform (18.6%), and on the distal ebb-tidal delta swash platform (10.9%). The two distribution patterns of fossil specimens are evident, with the highest relative percentages occurring on the eastern marginal linear bar complex (23%) and the eastern marginal flood channel (22.7%). The majority were phosphatic *Elphidium excavatum* in the eastern marginal flood channel and the eastern marginal linear bar complex.

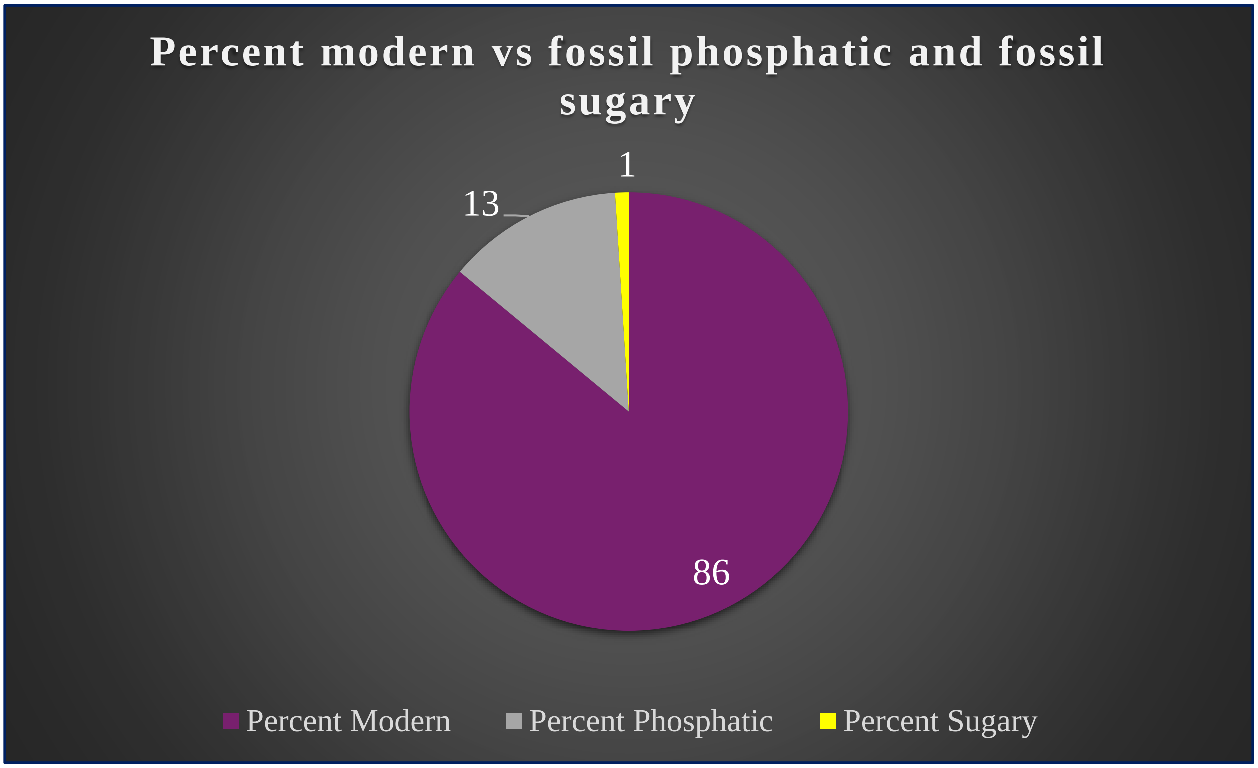

Figure 37. The pie graph shows the breakdown of fossil foraminifera (sugary) and (phosphatic) vs. modern.

5.0 DISCUSSION

5.1 Morphologic changes and hydrodynamic models

5.1.1 Morphologic changes

From 2005 until fall 2012, the cross-sectional profiles, bathymetric surveys, and volumetric calculations recorded substantial morphologic change (Appendix A, B, and C). In April 2005, a second primary channel was dredged in Bogue Inlet, and a dike was built across the proximal portion of the old ebb channel landward to block the hydrodynamic flow and aid in the capture of much of the tidal prism by the newly dredged channel from the pre-2005 ebb channel (Appendix C).

From 2005 to 2012, two large beach nourishment projects were finished on April 4, 2005, with 528,206 cm^3, and on February 2, 2007, with 200,374 cm^3 deposited within the littoral cell (Moffatt & Nichole; Geodynamics, 2020). Also, in 2006 and 2010, there were two separate dredge disposals of unconsolidated material at the point of Bogue Inlet (the western end of Bogue Banks) (Figure 16) at a combined total of 115,447 cm^3 (Moffatt & Nichole; Geodynamics, 2020), creating an ample sediment supply to be worked on by hydrodynamic processes. The sand dredged for the beach nourishments was from the inner shelf, with a mean grain size of 0.2 mm to 0.4 mm Beach Preservation Plan (2020). In addition to human impacts (e.g., dredging and beach nourishment), the region encountered 12 tropical systems from 2005 to 2012, two of which were Category 1 hurricanes (Table 1). Hurricane Ophelia occurred in mid-September 2005, and Hurricane Irene occurred in late August 2011.

From 2005 to 2007, the distal portion of the old ebb channel, furthest seaward, filled from a depth of -6 m to -3.7 m, and the old ebb shoal started to dissipate (Appendix A and B). The inlet profile captures channel infilling (Appendix B). Appendix B shows the region where the old inlet channel was in 2005, as the channel encroached on Bogue Banks's western margin and the closing of that channel evident in the profile of 2012, where there were roughly 9 meters of fill that closed the old pre-2005 channel (Appendix B).

The observed morphodynamic change from 2005 to 2007 is a combination of wave-current interactions within the inlet, shoreface, and nearshore morphology, aided by a human-influenced sediment flux (the two beach nourishment projects in 2005 and 2007 and the dredged disposal in 2006). Intermediate to strong wave energy would have created heightened wave orbital velocities during the passage of Hurricane Ophelia through Onslow Bay. Hurricane Ophelia exceeded current velocity and bed shear stress at 13 cm per second, enough to suspend fine to medium-grained sediment as the wave orbital energy interacted with the old ebb-delta shoal. After suspension, subtidal mean currents, semidiurnal tidal currents, and wave action would keep sediment in suspension and transport both bedload and suspended load to the point of deposition. The influx of sediment deposited along Bogue Point in 2005 and the nourishment updrift before Ophelia could have been entrained by wave orbital energy at higher than mean wave heights during the storm event and transported by subtidal and tidal currents to regions of the ebb platform, adding in the infilling of the old inlet channel as the constructed dike near the FTD ramp would have decreased fluid velocities causing deposition. Even though Ophelia was a Category 1 storm, the track and presumed mean wave direction (from the south and southeast) would be most conducive to oblique wave crest interaction with the old ebb shoal, creating the alongshore and cross-shore current velocities to induce morphologic change; as Castelle and Masselink (2022) stated, depth-induced gravity wave breaking is the main mechanism of nearshore currents, sediment transport, and morphological changes in the nearshore region. Although Ophelia passed through the bay in 2005, it was one of five low-pressure systems that would have created the parameters for morphologic change. As presented in Marshall (2004), even a strong high-pressure system, i.e., anticyclone, classified as fair-weather conditions with sustained winds from the southeast at approximately 20 knots for around 36 hours, can create a heightened sea state to entrain at the very least, fine-grained sand and mobilize it as bedload. The fair-weather event Marshall (2004) reported also netted an onshore across-shore sediment transport direction and a longshore current to the northeast. The action from the fair-weather event indicates atmospheric parameters like this would contribute to the net gain of sediment in the current study area, as observed in (Figures 19 and 25).

CSE (2005) measured fluid velocities at different depths of the newly dredged inlet channel in a complete tidal cycle on a fair-weather day. The semi-diurnal currents had high enough velocities to create enough bed shear stress to transport fine-grained sediment other than at slack water. CSE (2005) also estimated the cross-sectional area of the old and new inlet channels in 2005. The new channel dredged in 2005 had an estimated cross-sectional area of ~ 929 m^2, roughly 27 % larger than the old pre-2005 channel at ~ 678 m^2 encroaching on Bogue Banks infrastructure. However, water propagating over the shoals adjacent to the new and old channels was not accounted for. Furthermore, CSE (2005) recorded that Bogue inlet is ebb tidally dominated.

Data from the summer of 2007 to the fall of 2012 (Appendix C) record shoreline accretion, the appearance of a longshore bar, and an overall beach state that resembles an intermediate-stage longshore bar and trough profile (Wright and Short 1984; Castelle and Masselink 2022). A portion of the shoreline accretion could be a function of the added sediment supply from the large-scale oceanfront nourishment project in February 2007 and the Bogue Inlet point disposals in 2006 and 2010. Ample time would have passed by 2012 for both energetic and relatively calm sea states to create the morphological profile observed in the spring of 2012. Multiple nearshore parallel bars point to the influx of sediment as a substantial factor in the evolution of this system. Olsen Associates (2006) indicates that along the whole of Bogue Banks, the barrier experiences a nearly equal, large volume of sand moving east and west along the shoreline annually due to reversing longshore currents. Gross sediment transport potential increases westward when measured near Bogue Inlet based on hindcast wave data presented by USACE (2001) and Olsen Associates (2006). Olsen Associates (2006) also suggests that along western Emerald Isle, within about 6.1 km of Bogue Inlet, the net westerly transport potential accelerates significantly toward the inlet. Any unconsolidated material used for beach nourishment updrift of the inlet from roughly 3.2 to 4.8 km has the potential to be transported in the direction of the inlet by the mean currents. The only other sediment input to this region's sediment-stricken system would be the process of shoreface bypassing (Swift 1976; Riggs et al. 1996). This process would likely happen more often on the western portion of Bogue Banks due to the island's western section sitting atop the paleo-White Oak River valley fill. Sand within this fluvial fill may be exposed and eroded in high energy conditions, and transported shoreward from the inner shelf, e.g., during a long-duration nor-easter or a hurricane with the right track and intensity Riggs et al. (1996).

Although numerical modeling was not conducted from 2005 through 2012, the atmospheric forced bottom boundary currents from the two hurricanes working with the tidal currents would aid in entraining bedload transport and migrating subaqueous dunes that contributed to the infilling of the old channel and changes to the shoreface and beach Castelle and Masselink (2022). Net sediment transport is a function of the unevenness between the onshore-directed sediment transport and offshore-directed sediment transport, driven by near-bottom wave orbital velocities and the action of the undertow, along with infragravity waves ejecting suspended sand either onshore or offshore (Ruessink et al. 1998; Smith and Mocke, 2002; Castelle and Masselink 2022).

In the summer and fall of 2012, the main inlet channel dimensions showed a narrow, deep profile (Appendix B). The cross-sectional area calculated in the summer of 2012 was roughly 854 m^2, measured at the -1.5 m contour, which excludes the volume of water that passes over the relatively shallow shoals. Even though this method leaves out a portion of the volume of water moving through the inlet, it suggests that the cross-sectional area of the ebb channel decreased relative to the cross-sectional area in 2005 at 929 m^2, making the channel less hydraulically efficient and unstable Seminack and McBride (2018). Furthermore, from the fall of 2012 to the summer of 2013, the primary inlet ebb channel orientation slightly straightened. The cross-sectional area grew as the channel attempted to reach a hydraulic equilibrium Hughes (2002). From the summer of 2013 to the summer of 2014, the ebb channel shifted back to the west.

As evident in the bathymetric surveys in 2012 through 2016, the inlet shows a small radius (i.e., an acute bend around the protruding spit built off Bear Island) (Appendix C). The geometry of the inlet represents the inlet channel being inefficient Seminack and McBride (2018). The radius of curvature is directly related to the hydraulic efficiency of a fluvial channel Hudson and Kesel (2000). A large radius of curvature is more hydraulically efficient (shorter distance from the oceanfront to the back-barrier) than an inlet channel exhibiting a small radius of curvature (longer distance from the oceanfront to the back-barrier region). When a channel is shorter (exhibiting a more gradual bend and having a larger radius), the energy produced from the difference in the hydraulic head from the back-barrier to the oceanfront, or visa-versa, would not have to be as high to propel the tidal jet through the flood or ebb flow (Hudson and Kesel 2000; Seminack and McBride 2018). Furthermore, less energy would be lost from the fluid medium interacting with the friction of an obtuse channel meander; therefore, less energy would be needed to move the tidal prism through a channel with this geometry. Another way to describe a fluvial channel's hydraulic efficiency would be the ability of the system to conduct water with minimum energy loss.

From the fall of 2012 to the summer of 2015, the channel thalweg scoured to a depth of -8 m. The channel orientation stayed steady from the summer of 2014 to the summer of 2016, exhibiting an acute meander around the protruding spit built off of Bear Island (Appendix C), as the thalweg continued to deepen to -8.5 m between the fall of 2015 and the summer of 2016. Channel scouring suggests that multiple events created a large enough volumetric discharge through the channel that exceeded the maximum cross-sectional area that could have withstood the amount of water flowing through the channel, leading to a change in channel morphology from 2012 to 2015 Hughes (2002). If the discharge of the inlet increases and the channel width cannot keep up, the channel should deepen by scouring Hughes (2002), as evident when the cross-sectional profile width decreased from 2005 to 2012, and scouring occurred from 2012 to 2016 as the channel width slowly grew (Appendix B).

As mentioned, many atmospheric events can force wave action superimposed on the semidiurnal tidal currents that transport sediment onshore and into the inlet. From the straight channel orientation in 2005, the channel’s tidal prism was captured by the deepest back barrier tidal channel located on the western portion of the flood tidal delta lobe (Figure 24). As the tidal prism was mainly captured by the most westward tidal channel that wraps around the flood tidal delta, flood tidal delta deposits continued to fill the limited estuarine accommodation space directly behind the inlet in front of Dudley Island (Figure 38). In front of the subaerial island, covered with tidal marshes, sediment deposited on the western flood tidal delta lobe continued to build to the west. From 2010 to 2016, the flood-tidal delta forced the most hydraulically dominant tidal creek channel to shift laterally as the meander's cut bank migrated to the west. The westward lateral migration is recorded in (Figure 38) where from 2010 to 2021, the tidal creek channel and flood tidal delta lobe migrated 224 meters in total. The migration was due to high wave energy from approximately 29 named and no-name low-pressure systems that created heightened wave orbitals interacting with flood currents to transport entrained sediment and any excess sediment added to the littoral system to the back-barrier environment. Furthermore, Dudley Island is bisected by many small tidal creeks, implying that the island is most likely a relic of the inlet's flood tidal delta that has been exposed enough where permanent salt marsh has taken over, pointing to a decrease in estuarine accommodation space directly behind the inlet.

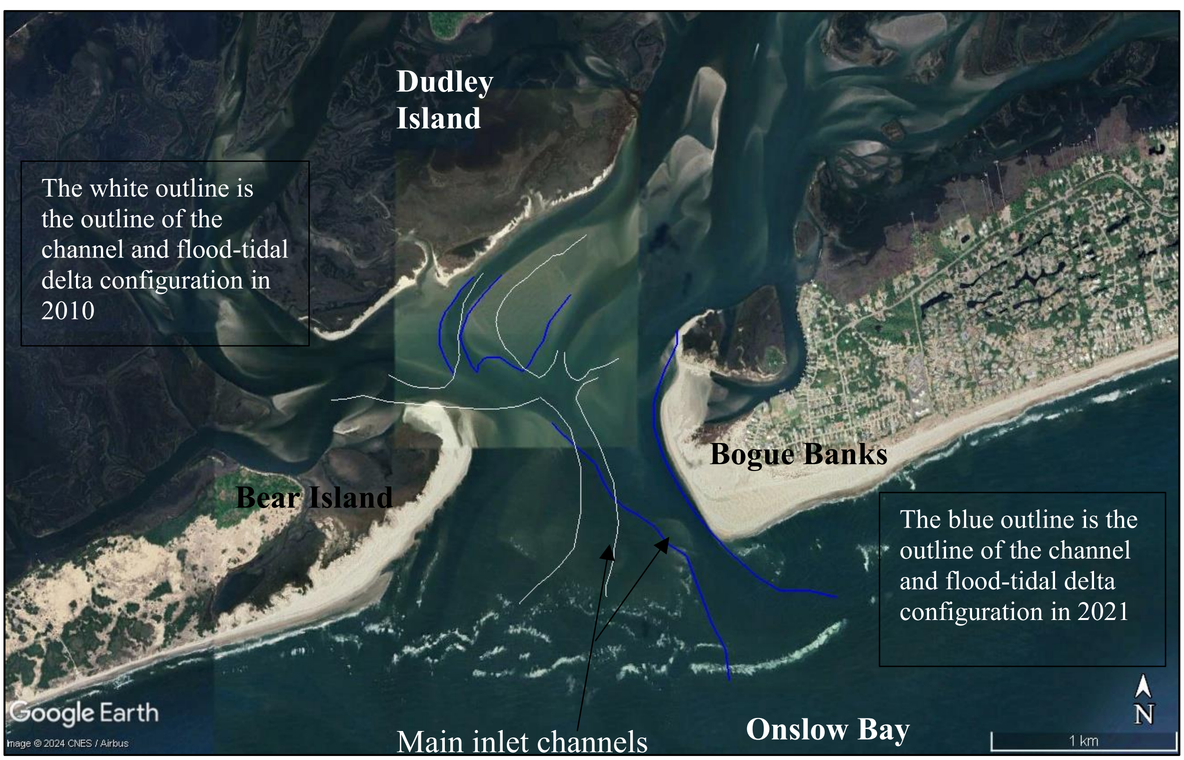

Figure 38. The base image of Bogue Inlet was captured on 09/24 and obtained from Google Earth. The white outline of the channel and flood-tidal delta lobes is traced from an aerial image from 05/2010. The blue outline of

the channel and flood-tidal delta lobes is traced from an aerial image from 07/2021. The outlines represent the migration of the flood-tidal delta; starting in 2010, the flood-tidal delta migrated to the west 224 meters.

The navigable channel, which is the most hydraulically dominant, is dredged every two to three years, connecting the inlet's ebb channel to the AIWW (Figure 16, A, B, and C) (Bogue Inlet AIWW Crossing, 2024). The ebb channel became less efficient as sedimentation occurred on the FTD. The cross-sectional area of the inlet channel narrowed from 2005 to 2012 and slowly grew from 2012 to 2016 as the tidal prism fluctuated, causing the main inlet channel to migrate to the east while the back-barrier portion migrated westward. A wave-dominated inlet channel's natural processes will cause the channel to migrate laterally, rotate, and eventually infill, resulting in excess sediment deposition within the flood-tidal delta, as observed at Bogue Inlet. During the rotation process, the inlet channel lengthens while experiencing a decrease in the radius of curvature, hydraulic efficiency, and tidal prism Seminack and McBride (2018). However, it is unlikely that Bogue will ever completely infill due to dredging and being a mixed energy inlet system where tidal currents flush the main channel of most sediment deposited.

There were three more significant hurricanes, from the summer of 2006 to 2016, Irene 2011, Arthur 2013, and Hermine 2016, that would have created high enough wave orbital energy along with enhancing the tidal currents, as to be presented with the numerically modeled hurricanes of this study, to have deposited enough sediment on the flood-tidal delta to cause its westward migration, therefore, producing an eastward migration of the main ebb channel. Also mentioned again, there was an influx of sediment into the littoral system from the beach nourishment projects further east on Bogue Banks and at the point of Bogue Inlet, allowing the hydrodynamics of the inlet and the shoreface to produce the observed morphologic change.

The cross-sectional area of the main inlet channel was calculated again for the summer of 2016. The cross-section of the main ebb channel was approximately 1,364 m^2 measured from the -1.5 m contour. The cross-sectional growth from 2012 to 2016 is roughly a 50% increase. The growth implies that the channel has evolved to a more efficient state, as the tidal prism would have grown with the cross-section (FitzGerald, 1996; Hughes, 2002). As the channel widened, the thalweg stopped scouring vertically in the summer of 2016. Eastward scouring was observed from the summer of 2016 to the fall of 2016, causing the channel to migrate roughly 20 m as the channel thalweg elevation increased from -8.5 m to -7.8 m, suggesting deposition as this period encompasses Hurricane Matthew's passing (Appendix B). Numerical modeling of Hurricane Matthew points to the storm's atmospheric parameters, aiding in inlet channel deposition, specific locations of erosion, and further eastward migration. As Matthew's track paralleled the coast, the large wind field of onshore winds forced a significant storm surge obliquely into the coast and Bogue Inlet (Figure 9 and Appendix D).

Matthew produced a cross-sectional growth of water in the inlet (storm surge) of 2,450 m^2 over roughly 1,700 m^2 (Figure 42) at the peak of the inlet's semi-diurnal flood tide inflow.

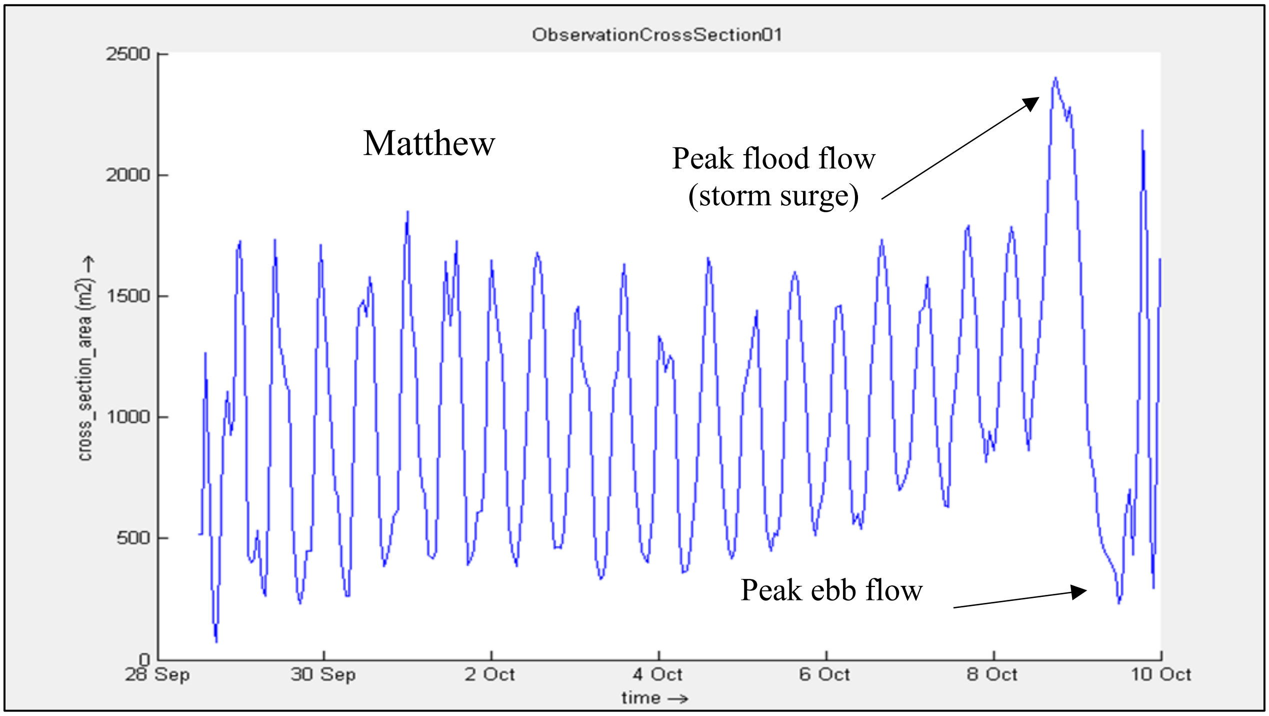

Figure 39. Data was produced from the model simulation of Hurricane Matthew in Delft3D. The cross-sectional area growth of the water in Bogue Inlet while Hurricane Matthew passed through Onslow Bay.

The storm's parameters, track, wind field size, and intensity lead to volumetric discharge values of 790 m^3 per second for the inflow and 1100 m^3 per second for the outflow (Figure 40). Data corroborates the findings of CSE (2005), showing that Bogue Inlet is ebb tidally dominated due to the asymmetry in the tidal wave propagation through the tidal marsh channels and inlet, even in highly energetic events. Ebb-tidal dominance would suggest that most of the sediment deposited in the main inlet channel could be flushed out from the ebb flow to be deposited on the ebb-tidal delta, pointing to the ebb-tidal delta's growth through time (Figure 25). However, the inlet cross-section recorded approximately 0.7 m of deposition (Appendix B).

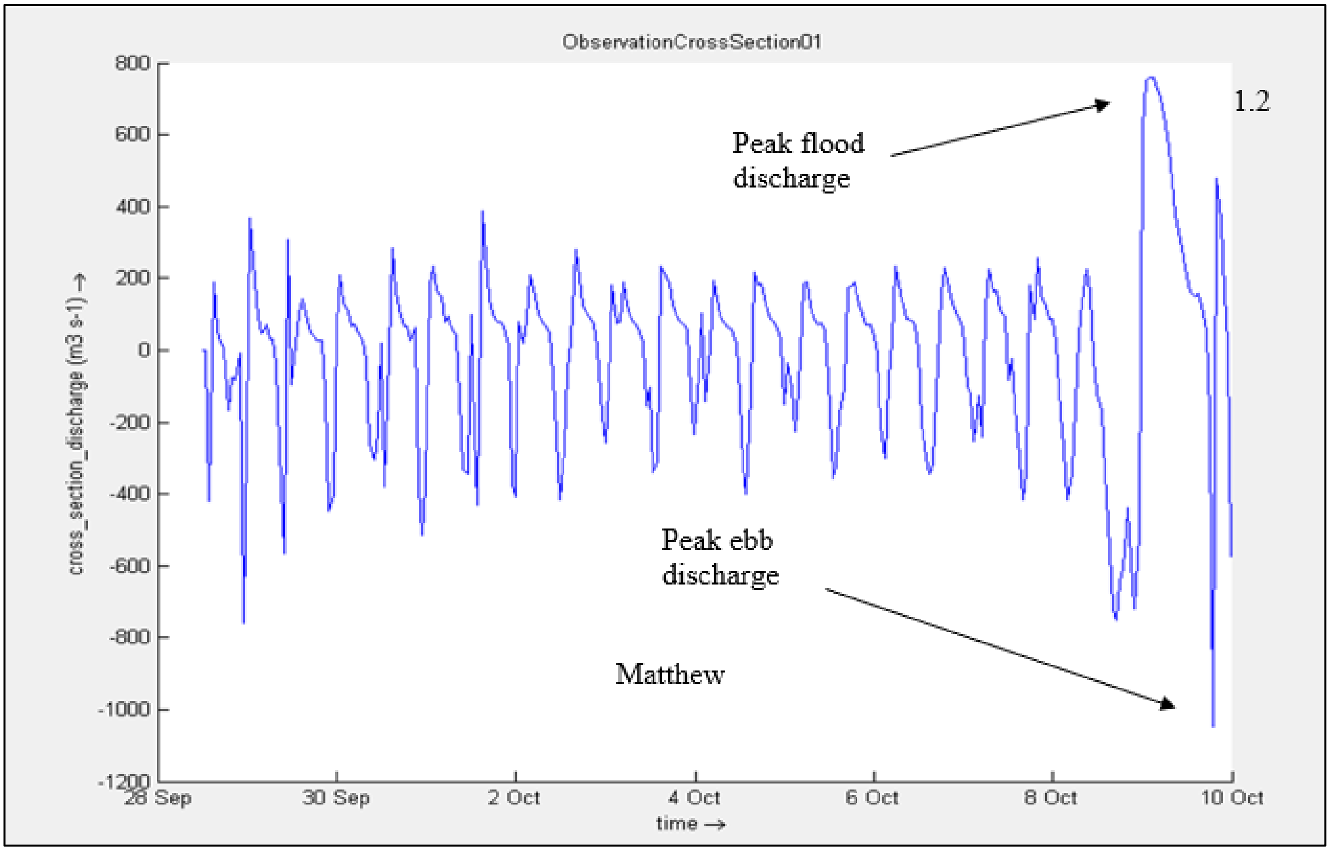

Figure 40. Data was produced from the model simulation of Hurricane Matthew in Delft3D. The cross-sectional discharge of Bogue Inlet was recorded in cubic meters per second during Hurricane Matthew.

From Oct 08, 22:00 GMT, to Oct 09, 01:00 GMT, the onshore winds were recorded at 26 to over 30.42 meters per second (Appendix D). This is roughly 4 hours of non-fetch limited winds directed at Bogue Inlet. The wind forcing produced peak fluid velocities ranging from 1.6 to 1.87 meters per second. However, the peak fluid velocity data was recorded on Oct 09, 04:00 GMT, on the ebb flow as Hurricane Matthew departed Onslow Bay. During the storm, the winds started from the SE and shifted from E to NE as the storm passed, forcing water back through the inlet at the estimated velocities (Figure 41 and Appendix D). Throughout the storm's passing, the along-shore current direction was forced to the southwest (Figure 41). Furthermore, two localities of converging currents (confluence-flow interaction) were captured in the hydrodynamic data along the eastern margin of the main ebb channel. The fluid interaction could have created vertical eddies similar to the action in a cut bank when moving through the tidal cycle, where there would have been localized erosion and scouring into the eastern ebb channel's bank (Hughes, 2002; Randle 2006; Shaheed et al., 2021). The centrifugal force created by the curvature of the meander would have created helical flow (Sylvester et al., 2019; Shaheed et al., 2021). Helical flow can be considered as a vertical circulating eddy that would increase bed shear stress on the eastern portion of the meanders bank, causing the eastward scour as Hurricane Matthew forced significantly larger discharges through the inlet channel (Hughes 2002; Sylvester et al., 2019; Zulkifli et al., 2024).

In the passing of the storm, both the maximum inflow and outflow discharges exceeded the maximum discharge per unit width through the inlet. In other words, the increase in discharge caused additional scour due to the exceeded maximum cross-sectional area for that flow condition, as evident in (Appendix B). The scouring can also have been due to the confluent flow interaction in combination with the increase in discharge values. The confluence is only captured at certain times in the semidiurnal tidal cycle. The confluence of flow was observed in the data at low tide in the ebb tidal flow and as the winds were blowing offshore when Matthew was departing the embayment, forcing water back through the inlet as the predicted semidiurnal tidal change was supposed to be transitioning to high tide through the flood flow (Figure 41). The confluence of flow could be a function of a phase lag between low and high tide and at the time of slack water, as reported by CSE (2005).

Phase lags are typical in single inlet systems because of the inertial effects of flows through the channels Nummedal and Humphries (1978). Phase lags also increase with attenuation of the tidal wave into marsh lagoons. For example, the measured tide range in the mouth of the old channel was ~1.2 m on the day CSE made flow measurements. Predicted tide ranges in the White Oak River were of the order of 0.6 m CSE (2005). This difference, combined with the propagation of the tide wave, changes the high and low tide times throughout the estuary. The result is varying heads of water produced by height and time differences that continue to drive currents while low or high tide occurs at a particular point CSE (2005).

FitzGerald and Nummedal (1983) showed that the hypsometry of a back-barrier marsh and tidal creek system led to higher inlet efficiency at low than high tide. Therefore, the bay-tide phase lag is more significant at high than low water, resulting in a more prolonged flood than ebb duration. A shorter ebb duration produces a strong ebb-tidal dominance of the main inlet channel, which would lead to a potential net ebb transport of sand if there was a low occurrence of storms that transport sediment into the back-barrier region during storm surges as observed in Bogue Inlet CSE (2005). The complex nature of the back-barrier regions of the barrier islands (extensive marshes and tidal flats cut by numerous tidal channels), as exists behind Bogue Inlet, would create a more extended flood portion of the tidal cycle to fill the back-barrier region than it takes that region to empty when the tide falls. This means that the flood phase would be longer than the ebb phase, which results in the ebb currents being stronger than the flood currents.

These strong ebb currents sweep sand brought into the inlet by the wave-generated and flood-tidal currents out of the inlet and deposit it on the ebb-tidal delta. However, depending on the track, duration, and intensity of a low-pressure system, significant quantities of sediment can be transported to the flood-tidal delta and the back-barrier region, as occurred from 2010 to 2016, as this sedimentation caused the inlet to become less hydraulically efficient and unstable. An increase in sediment volume serves as a destabilizing factor Seminack and McBride (2018).

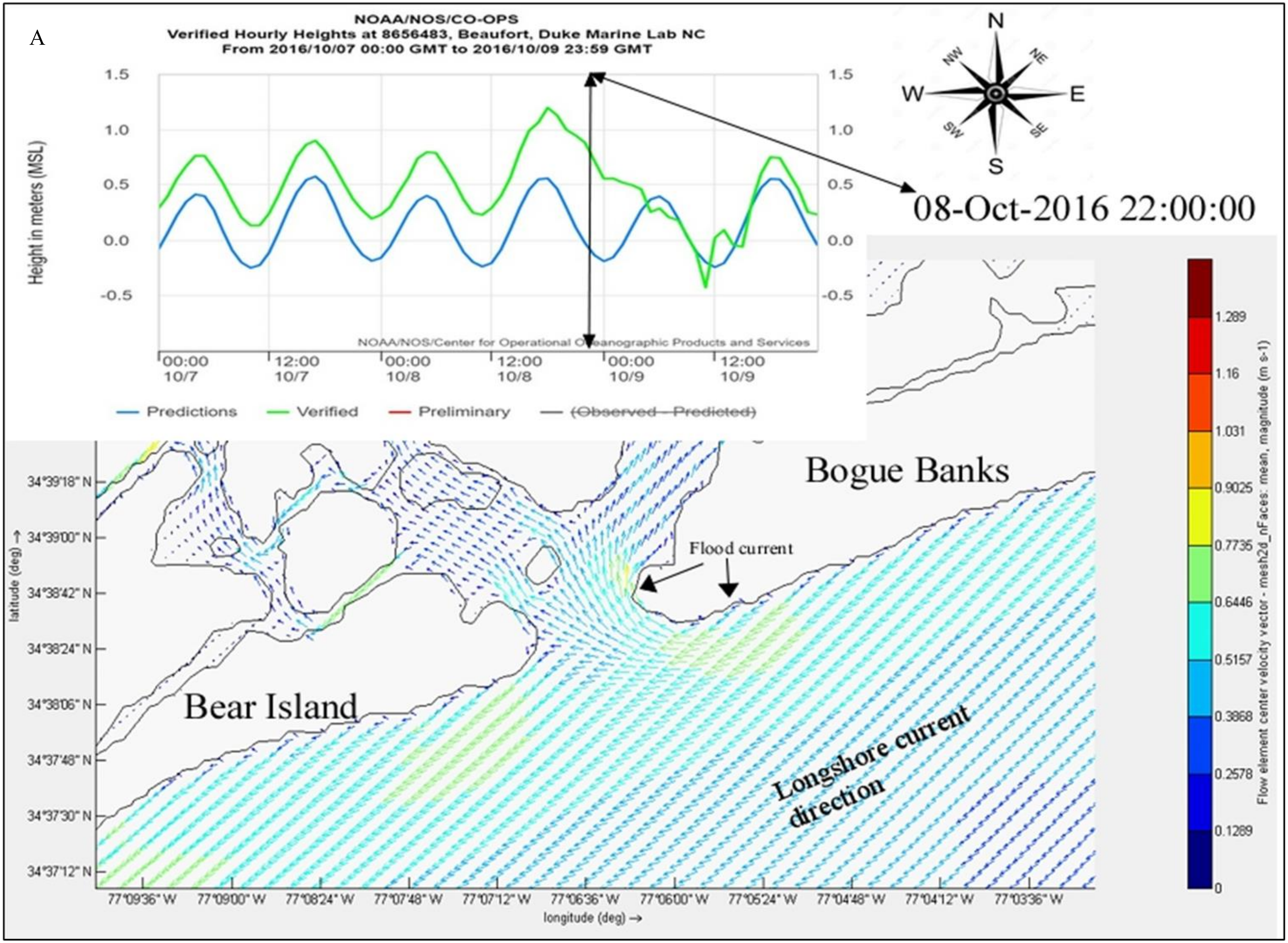

A
NOAA/NOS/CO-OPS
Verified Hourly Heights at 8656483, Beaufort, Duke Marine Lab NC
From 2016/10/07 00:00 GMT to 2016/10/09 23:59 GMT
Height in meters (MSL)
NOAA/NOS/Center for Operational Oceanographic Products and Services
Predictions
Verified
Preliminary
(Observed - Predicted)
N
E
S
W
08-Oct-2016 22:00:00
Bogue Banks
Flood current
Bear Island
Longshore current direction
latitude (deg)
longitude (deg)
Flow element center velocity vector - mesh2d_nFaces: mean, magnitude (m s-1)

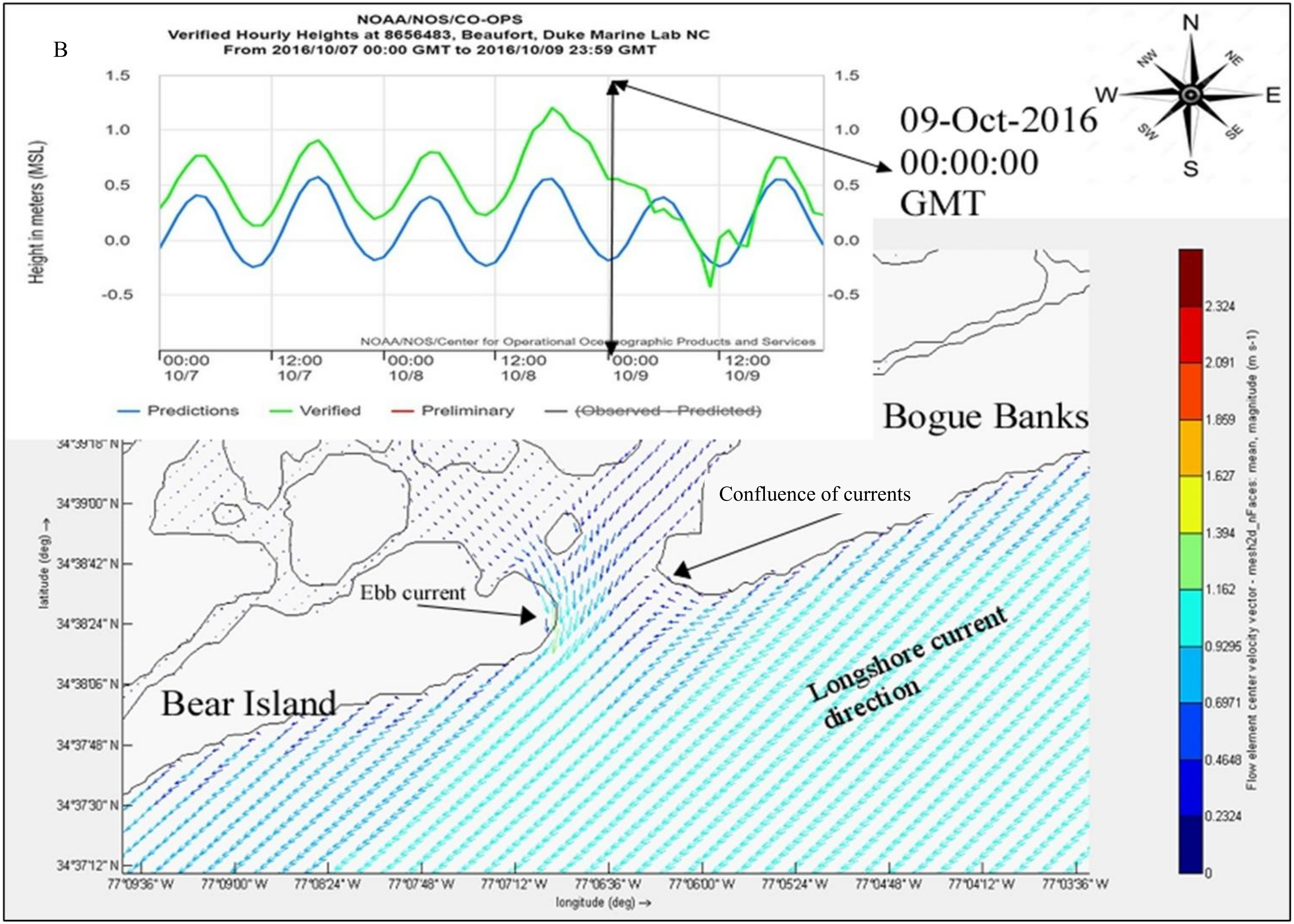

B
NOAA/NOS/CO-OPS
Verified Hourly Heights at 8656483, Beaufort, Duke Marine Lab NC
From 2016/10/07 00:00 GMT to 2016/10/09 23:59 GMT
Height in meters (MSL)
NOAA/NOS/Center for Operational Oceanographic Products and Services
Predictions
Verified
Preliminary
(Observed - Predicted)
09-Oct-2016
00:00:00
GMT
Bogue Banks
Confluence of currents
Ebb current
Bear Island
Longshore current direction
latitude (deg)
longitude (deg)
Flow element center velocity vector - mesh2d_nFaces: mean, magnitude (m s-1)

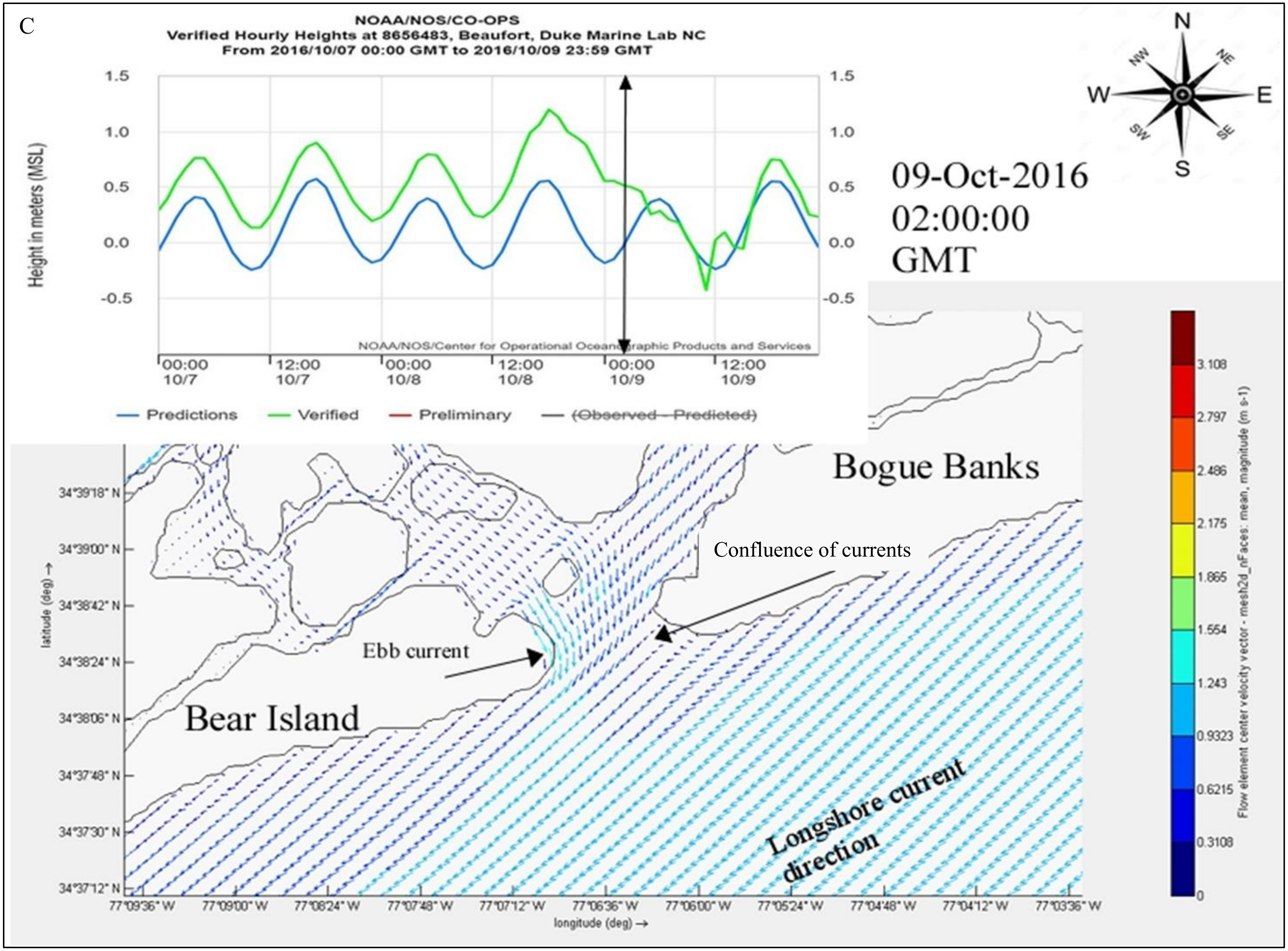
C
NOAA/NOS/CO-OPS
Verified Hourly Heights at 8656483, Beaufort, Duke Marine Lab NC
From 2016/10/07 00:00 GMT to 2016/10/09 23:59 GMT
Height in meters (MSL)
NOAA/NOS/Center for Operational Oceanographic Products and Services
Predictions
Verified
Preliminary
(Observed - Predicted)
09-Oct-2016
02:00:00
GMT
N
S
E
W
Bogue Banks
Confluence of currents
Ebb current
Bear Island
Longshore current direction
latitude (deg)
longitude (deg)
Flow element center velocity vector - mesh2d_nFaces: mean, magnitude (m s-1)

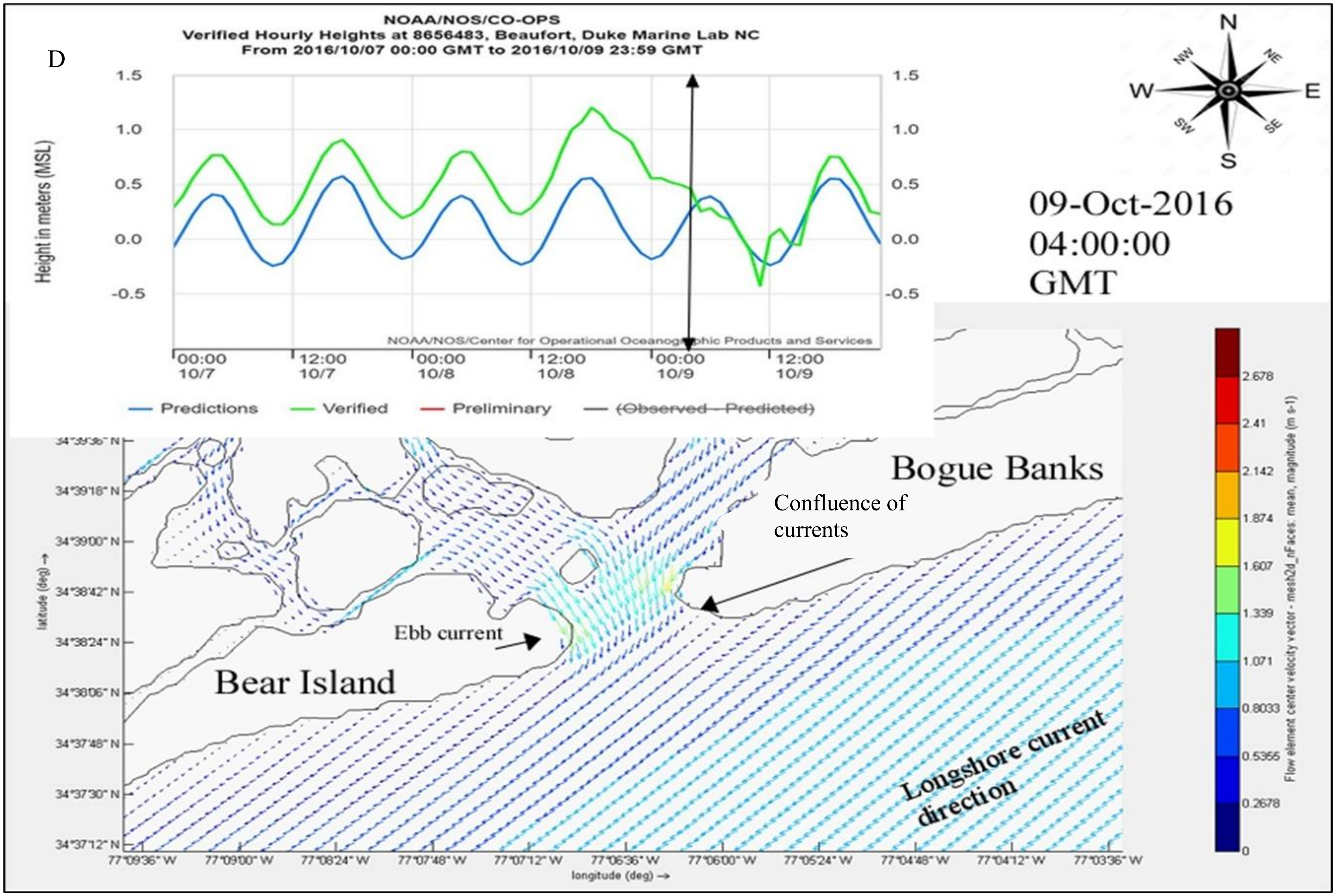

Figure 41. Hurricane Matthew's varying current vectors and magnitudes within Bogue Inlet and the foreshore of Bogue Banks and Bear Island. Time steps from October 8th, 2016, at 22:00 GMT to October 9th, 2016, 04:00 GMT, recorded at two-hour intervals. The x-axis represents latitude, and the y-axis represents

longitude: the color bar to the figure's right is presented in meters per second. The additional water levels, blue and green lines in the central portion of the figure, are data taken from Duke Marine Lab to show the specific time within the tidal cycle when the varying current vectors and magnitudes occur. The x-axis represents the water levels in meters above and below mean sea level, and the y-axis is time. Time steps are labeled (A-D), source; https://tidesandcurrents.noaa.gov/.

Along with scouring into the western margin of Bogue Banks, deposition is observed on the westernmost margin of the inlet channel in the 2016 S-2016 F raster (Figure 42). The brown shades along the eastern portion of the channel in the raster represent scouring/erosion, and the purple shades to the west represent deposition. The elevation raster (Figure 42) used to calculate volumetric changes throughout the survey supports the proposed explanation of the helical flow caused by the increase in discharge from Hurricane Matthew and the geometry of the channel. Like a meander in a fluvial system, the material on the outside of the channel meander (the eastern portion of the main ebb channel) would be entrained and moved through the channel and most likely deposited on the western portion like a point bar (Sylvester et al., 2019; Zulkifli et al., 2024). However, the deposition on the western portion of the ebb channel can also be a function of wave action as the bores break over the shallow ebb delta shoals in the middle of the inlet and obliquely transport sand further into the inlet. More than likely, it was a combination of both processes due to light shades of purple (representing small amounts of deposition) recorded in the thalweg and the darkest shades of purple (representing large amounts of deposition) recorded to the west of the channel thalweg, on the shoal platform labeled in (Figure 42). The bathymetric data in the summer of 2016 shows that the mouth of the ebb channel starts to rotate as the channel tries to become perpendicular to the dominant back-barrier tidal channel. However, after the passing of Hurricane Matthew in the fall of 2016, the bathymetric data shows that the mouth of the ebb channel has been redirected back to the west (Appendix B). This is due to the along-shore currents in the near-shore environment mirroring the direction of the wind from the hurricane. This interconnection in the near shore between the subtidal, mean currents, and atmospheric forcing was reported in (Wright et al., 1991; Wright et al., 1993; Marshall, 2004) and is also represented in the hydrodynamic data (Figure 41). Hurricane Matthew's winds drove the longshore current to the SW as the current interacted with wave action coming onshore. This would have created a net along-shore transport direction to the southwest. The longshore current would have interacted with the ebb jet flowing back through the inlet, blunting the ebb jet combined with onshore wave direction, creating parameters that led to the deposition seen in the bathymetric data and the elevation raster (Appendix C and Figure 42).

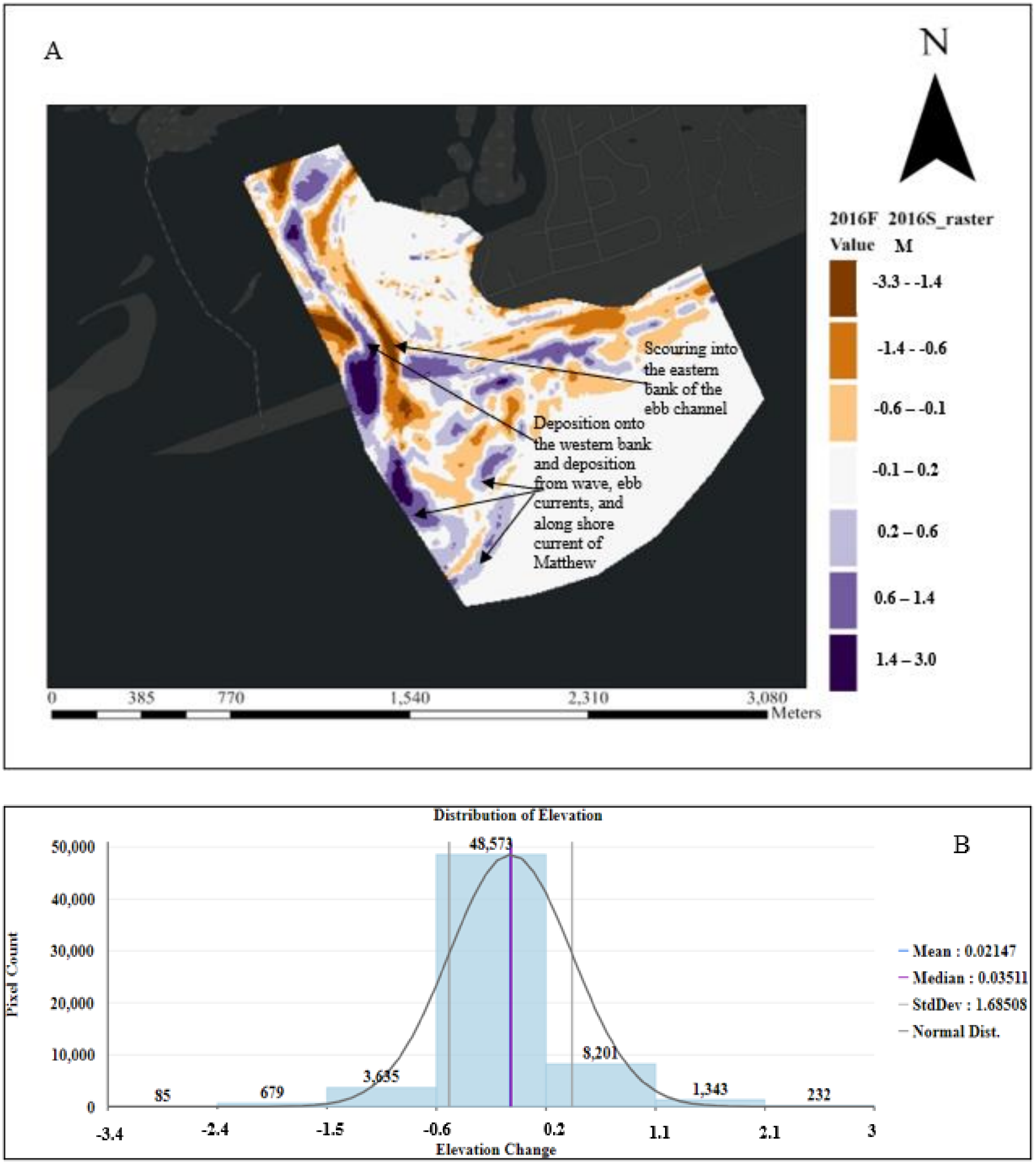

Figure 42. **A)** The raster output from summer 2016 to fall 2016, when Hurricane Matthew passed through Onslow Bay, using the DEM of difference method, showing deposition in shades of purple and shades of brown erosion. Deposition and erosion are recorded in ft datum NAVD 88. **B)** is a histogram showing elevation change on the x-axis and pixel count on the y-axis. This was used in the estimated volumetric calculations presented in Table 3. The y-axis is the number of pixels (6 m x 6 m per pixel) that fall within a range of elevation change. The x-axis represents the range of elevation change measured in feet. The range of elevation change is averaged. Then, the perimeter of a pixel is calculated (6 m x 6 m) and multiplied by the number of pixels in the specific range of elevation change to find the total perimeter of those pixels. Lastly, the range of elevation change is multiplied by the

total perimeter of the pixels that fell within the averaged elevation change, giving an estimate of the volume of the specific perimeter of the pixels in that range.

In the summer of 2017 to the fall of 2017, the bathymetric data recorded a breach of the outer ebb-tidal delta (Appendix C), more than likely starting through a trough along the ebb shoal that is evident in the bathymetric survey, labeled in the summer of 2017. Ebb tidal breaching is thought to be typically caused by tidal currents finding a more direct route over the ebb shoal. However, Lenstra et al. (2019) concluded with the help of Delft3D numerical morphologic modeling that there is a specific wave height that has to be met to first entrain the sediment for the tidal currents to move more sediment over the shoals for the mean flow to breach the outer shoal. Significant wave heights that are too great would aid in the inlet migration in the down drift direction and not cause the breaching and rotation effect Lenstra et al. (2019). In the period between the summer of 2017 to the fall of 2017, there were only two atmospheric events: one tropical storm that passed in very close proximity to Bogue Inlet and another event of no name that is recorded (Figure 46).

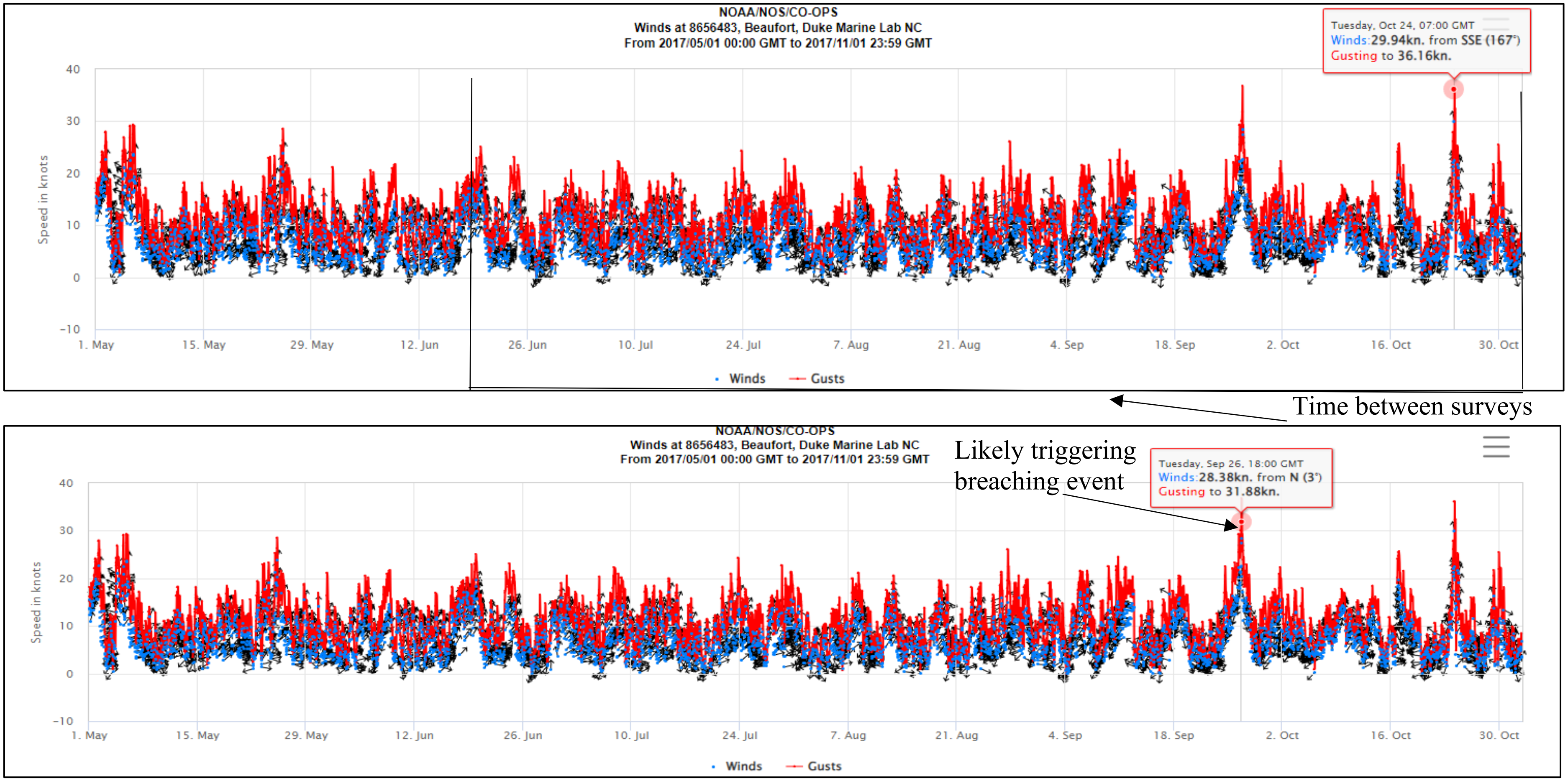

Figure 43. The wind speed graph from 05/01/2017 to 11/01/2017 shows atmospheric events that could have contributed to heightened sea states leading to sediment entrainment, transport, and outer ebb breaching. Note that only two events surpass 30 knots, representing the two most likely events to first trigger the breach and the second to fill in the channel mouth—source: https://tidesandcurrents.noaa.gov/.

Both events would have met the criteria of not being too energetic to continue forcing the inlet to migrate to the east but would have had significant wave heights enough to have caused high enough bed shear stresses to entrain fine grain sediment to have initiated the outer ebb shoal breach visible in (Appendix C), (bathymetric survey 2017 S to 2017 F). Furthermore, throughout the year 2017, these were the most energetic events. Marshall (2004) reported that atmospheric events comparable in strength and similar wind direction created significant wave heights of 0.6-1.8 m and an along-shore transport direction to the north and southwest with an across-shore transport onshore. Also, evident in the bathymetric surveys of 2017 S to 2017 F (Appendix C), the mouth of the main ebb channel quickly fills in from the 2017 S to 2017 F. Pointing to the first boxed atmospheric event in (Figure 43) being the trigger event of the breaching and channel mouth rotation and the second circled event to be what more than likely caused the infilling of the main channel mouth and further defection to the east. As Lenstra et al. (2019) alluded, breaches are accelerated significantly by wave-induced bed shear stress. However, the maximum erosion rate is found for moderate wave height because, for Hs = 2.5 m, the tidal flow is deflected by relatively strong wave-induced forces. In this case, channel deflection continues, and the breach is postponed.

From the fall of 2017 to the summer of 2018, the channel continued to become almost shore-normal; as the ebb-tidal delta migrated to the northeast (Appendix A), the storage volume (water column above the ebb-tidal delta) was reduced over time. This action is a function of sediment deposition onto the ebb-tidal delta's swash platform as it migrates. Deposition is also captured in the DEM of volumetric change raster, indicating substantial sediment deposition on the distal portion of the ebb-tidal delta (Figure 26) and throughout the whole survey extent (Figure 26). However, the DEM of difference raster of 2018 S-2018 F, the time that encompasses

Hurricane Florence, shows a very small net sediment gain and a portion of deposition near the middle of the ebb-tidal delta swash platform where the main inlet channel is located, indicating deposition from the ebb tidal jet (Figure 44).

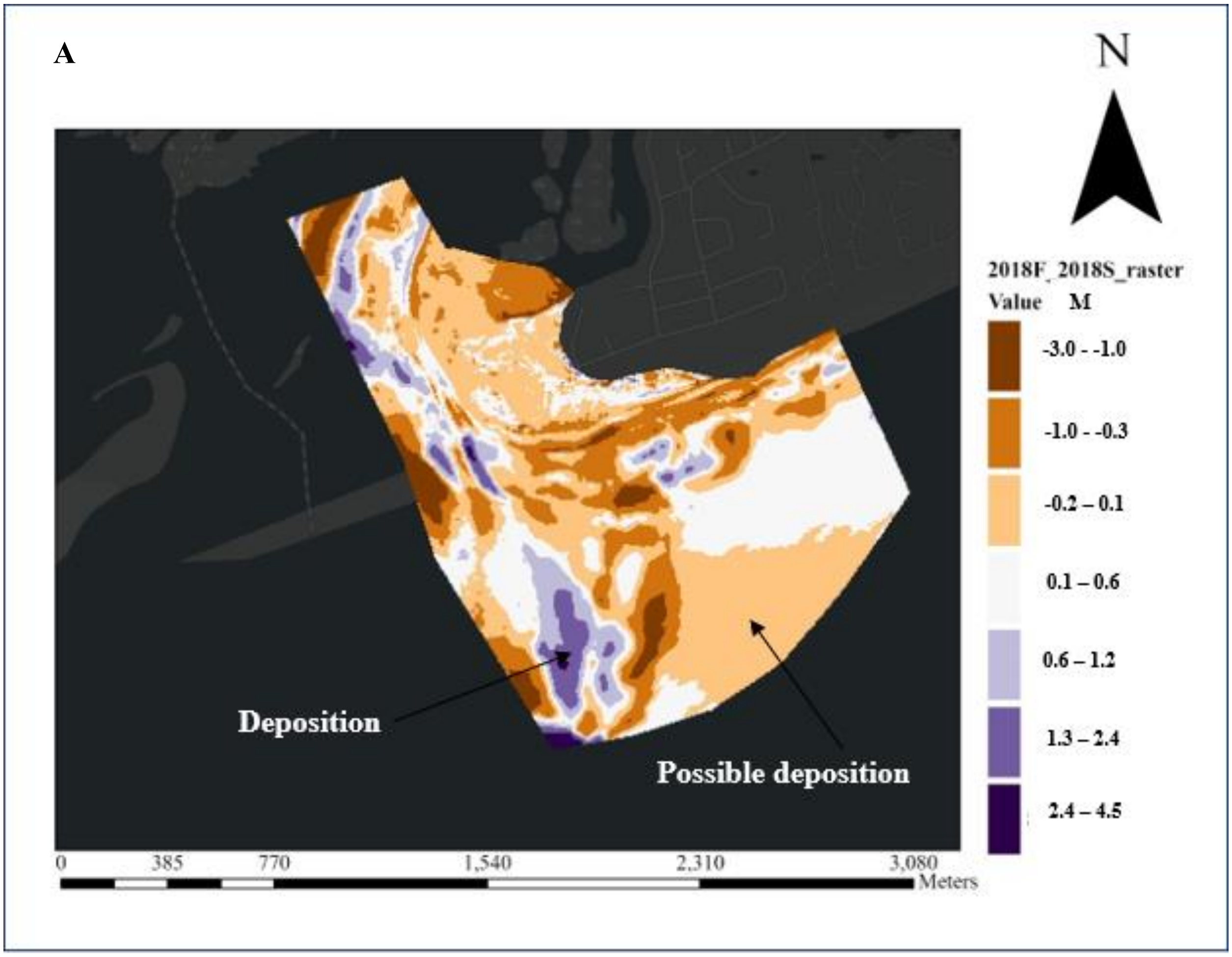

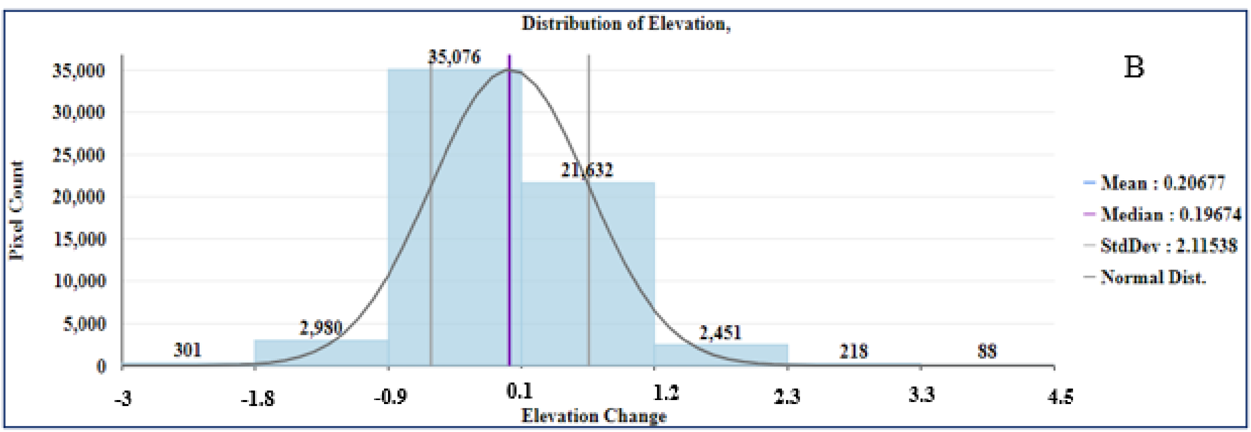

Figure 44. **A)** Raster map output from summer 2018 to fall 2018, when Hurricane Florence passed through Onslow Bay, using the DEM of difference method, showing deposition in shades of purple and shades of brown erosion. Deposition and erosion are recorded in ft datum NAVD 88. **B)** is a histogram showing elevation change on the x-axis and pixel count on the y-axis. This was used in the estimated volumetric calculations presented in Table 3. The y-axis is the number of pixels (6 m x 6 m per pixel) that fall within a range of elevation change. The x-axis represents the range of elevation change measured in feet. The range of elevation change is averaged. Then, the perimeter of a pixel is calculated (6 m x 6 m) and multiplied by the number of pixels in the specific range of elevation change to find the total perimeter of those pixels. Lastly, the range of elevation change is multiplied by the total perimeter of the pixels that fell within the averaged elevation change, giving an estimate of the volume of the specific perimeter of the pixels in that range. Note that the light shade of brown does not outright represent a negative elevation change (erosion); it ranges from -0.2 to 0.1 m, so some light shades of brown have a positive elevation change (deposition).

Hurricane Florence (Sept. 2018) exhibited a vastly different track than Hurricane Matthew and was the only storm to make landfall in Onslow Bay, south of Bogue Inlet (near Wrightsville Beach). However, it was not the strongest category storm when it passed through the embayment. As the storm approached landfall, it had wind speeds of 85 knots (a weak Category 2), weakening to a Category 1 storm as it interacted with friction from the land (Figure 9 and Appendix D). The winds would have been fetch limited, but the forward momentum of the hurricane as it traveled southwest through the embayment towards Wrightsville Beach would have made up for the fetch limited wind direction, pushing water into the bay and onshore as the storm made landfall (Appendix D).

Model simulations show that Hurricane Florence produced the most significant values of volumetric flow through the inlet, cross-sectional area growth, and fluid velocities (Figures 45, 46, and 47). As the hurricane first entered the northeastern section of the embayment, the wind field was producing an offshore wind direction. It resulted in, first, a significant ebb flow out of Bogue Inlet, at 1,700 m^3 per second (Figure 48), before the storm tracked across the embayment, to the southwest, and wind direction and magnitude changed, producing the highest recorded values of inflow of all the simulations. The highest volumetric flow value was observed in the inflow of 1,900 m^3 per second as Florence tracked into the middle of Onslow Bay, and onshore winds of the northeastern quadrant of the hurricane, where wind magnitudes are the strongest (Appendix D) were focused onshore and pushed the most significant amount of storm surge into Bogue Inlet (Figure 46).

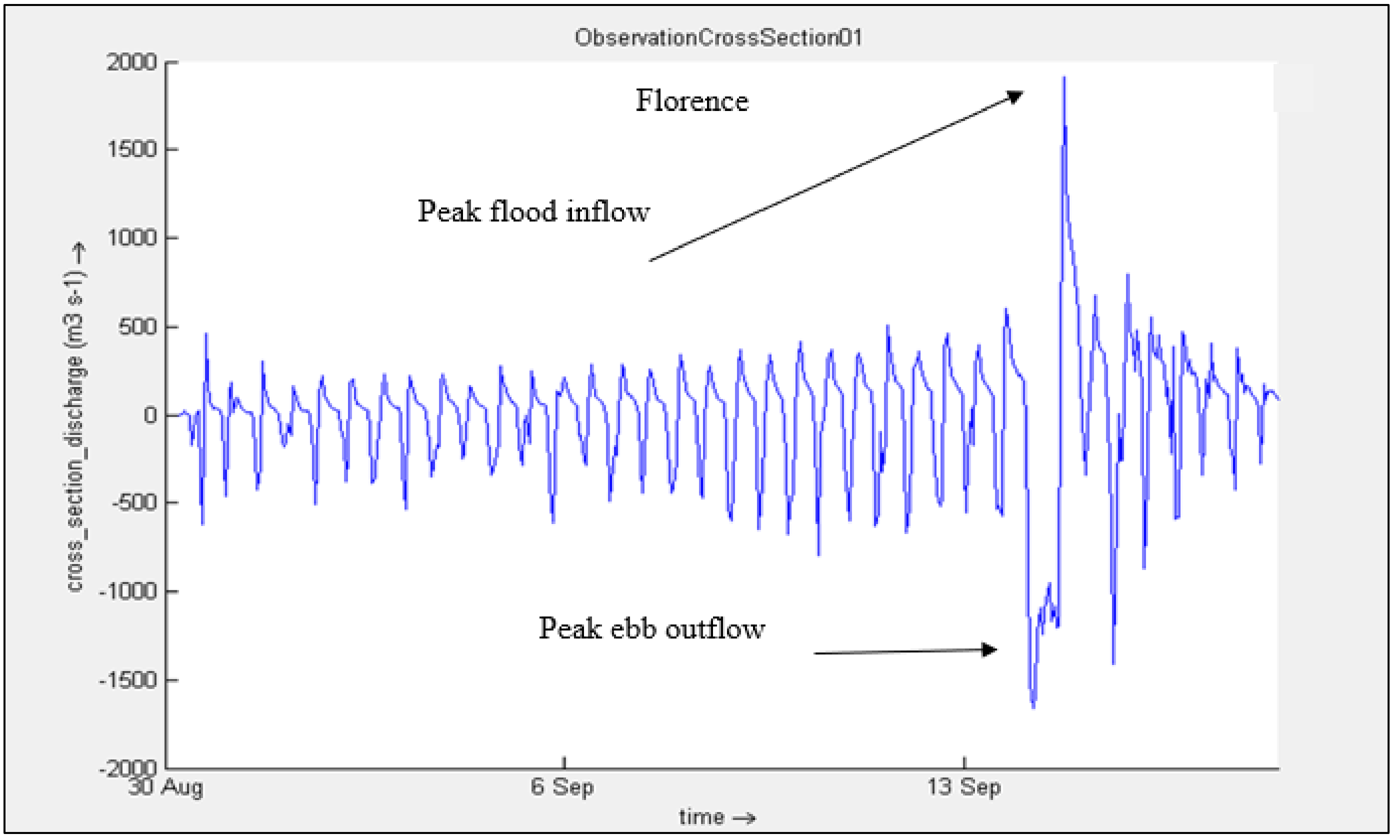

Figure 45. Data was produced from the model simulation of Hurricane Florence in Delft3D. The graph shows the cross-sectional discharge through Bogue Inlet, cubic meters per second, during the landfall of Hurricane Florence.

The highest cross-sectional growth of water in the inlet from a background value of 1,500 m^2 to over 3,600 m^3 (Figure 46) is a result of storm surge and was observed when the storm was in the middle of the bay (Appendix D). Note that in (Figure 46), there are two peaks in cross-sectional growth and no outflow in the cross-section as the hurricane made landfall. This is a function of the hurricane's track and wind field size. When the large peak inflow was recorded (Figure 46), wave propagation from the eye would have sent large, long-period swells into the coast, causing a prolonged period of water rise. Even after the Hurricane made landfall, the wind direction would have been coming out of the south, continuing to force water and waves from the south into Bogue Inlet, as evident in (Figure 46 and Appendix D). Furthermore, in Hurricane Matthew, the prolonged storm surge was not recorded, pointing to a hurricane's track as one of the most important factors that force wave direction and wind-driven currents that cause morphologic change.

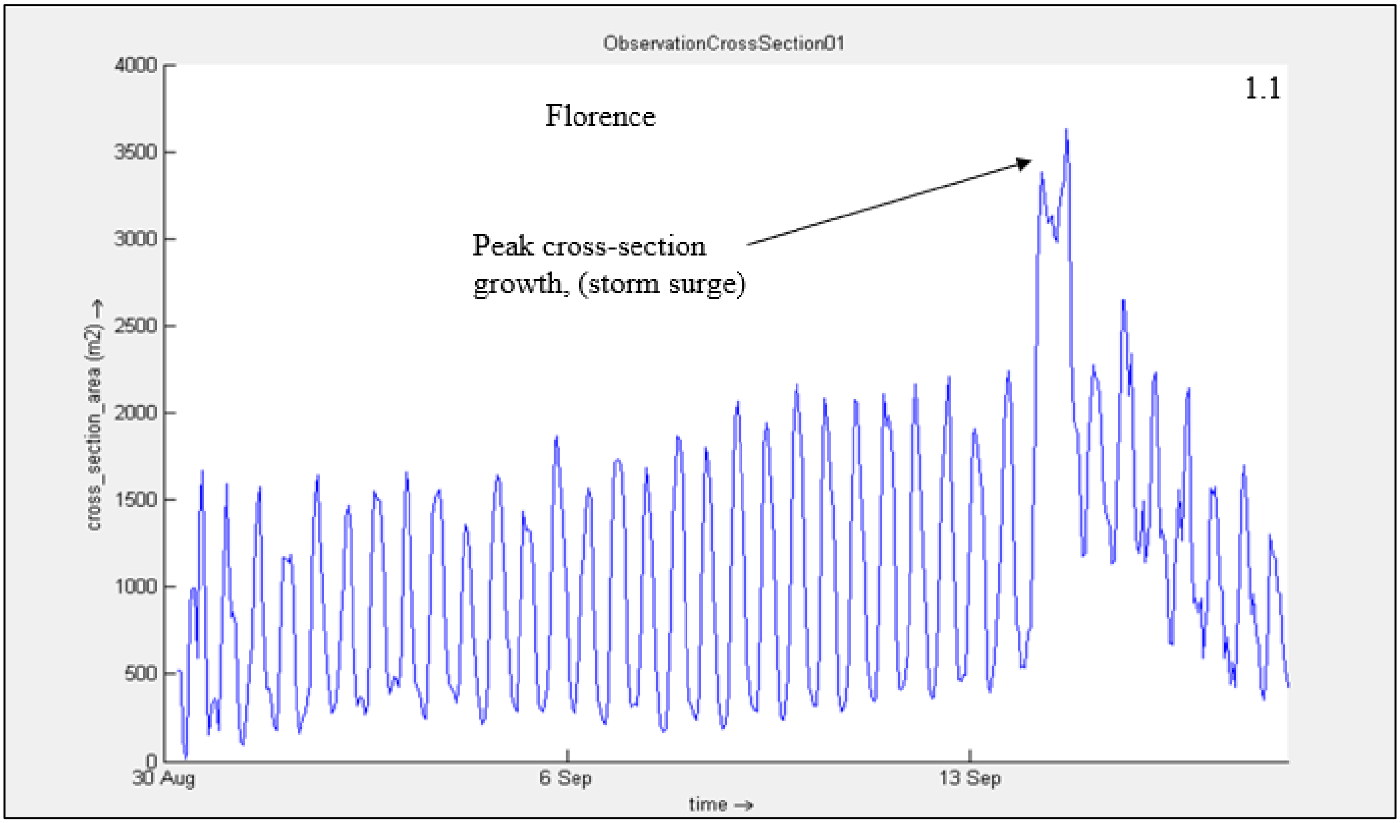

Figure 46. Data was produced from the model simulation of Hurricane Florence in Delft3D. The graph shows Bogue Inlets' cross-sectional growth of the water in the inlet or the storm surge that passed through the inlet when Hurricane Florence made landfall. The x-axis is presented in square meters, and the y-axis is time.

The largest fluid velocities were recorded on September 14 between 05:00 and 07:00 GMT, at the peak of astronomically high tide. Peak velocities in the inlet ranged from 1.19 to 1.93 meters per second and were observed in the hydrodynamic outputs (Figure 47). The velocities recorded are a function of the difference in hydrostatic head between the water in front of the hurricane, raising the elevation of the oceanfront from the back-barrier region. This is caused mainly by the direction of wind forcing, but the forward momentum of the storm plays a role, as well as the slope of the continental shelf and the time of astronomical tide that coincides with landfall.

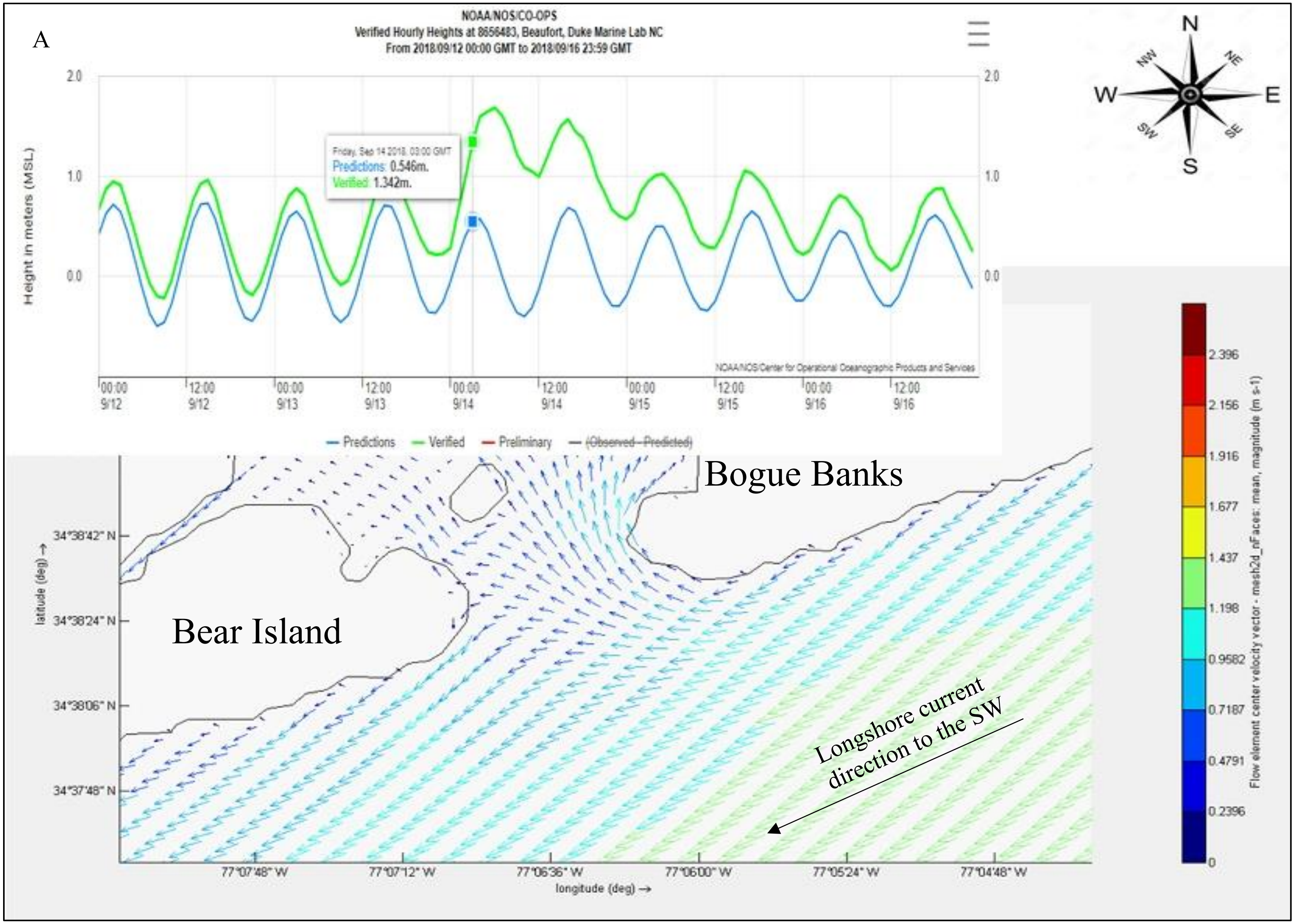
A
NOAA/NOS/CO-OPS
Verified Hourly Heights at 8656483, Beaufort, Duke Marine Lab NC
From 2018/09/12 00:00 GMT to 2018/09/16 23:59 GMT
Height in meters (MSL)
Friday, Sep 14 2018, 03:00 GMT
Predictions: 0.546m.
Verified: 1.342m.
NOAA/NOS/Center for Operational Oceanographic Products and Services
Predictions
Verified
Preliminary
(Observed - Predicted)
N
S
E
W
NW
NE
SW
SE
Bogue Banks
Bear Island
Longshore current direction to the SW
latitude (deg)
longitude (deg)
Flow element center velocity vector - mesh2d_nFaces: mean, magnitude (m s-1)

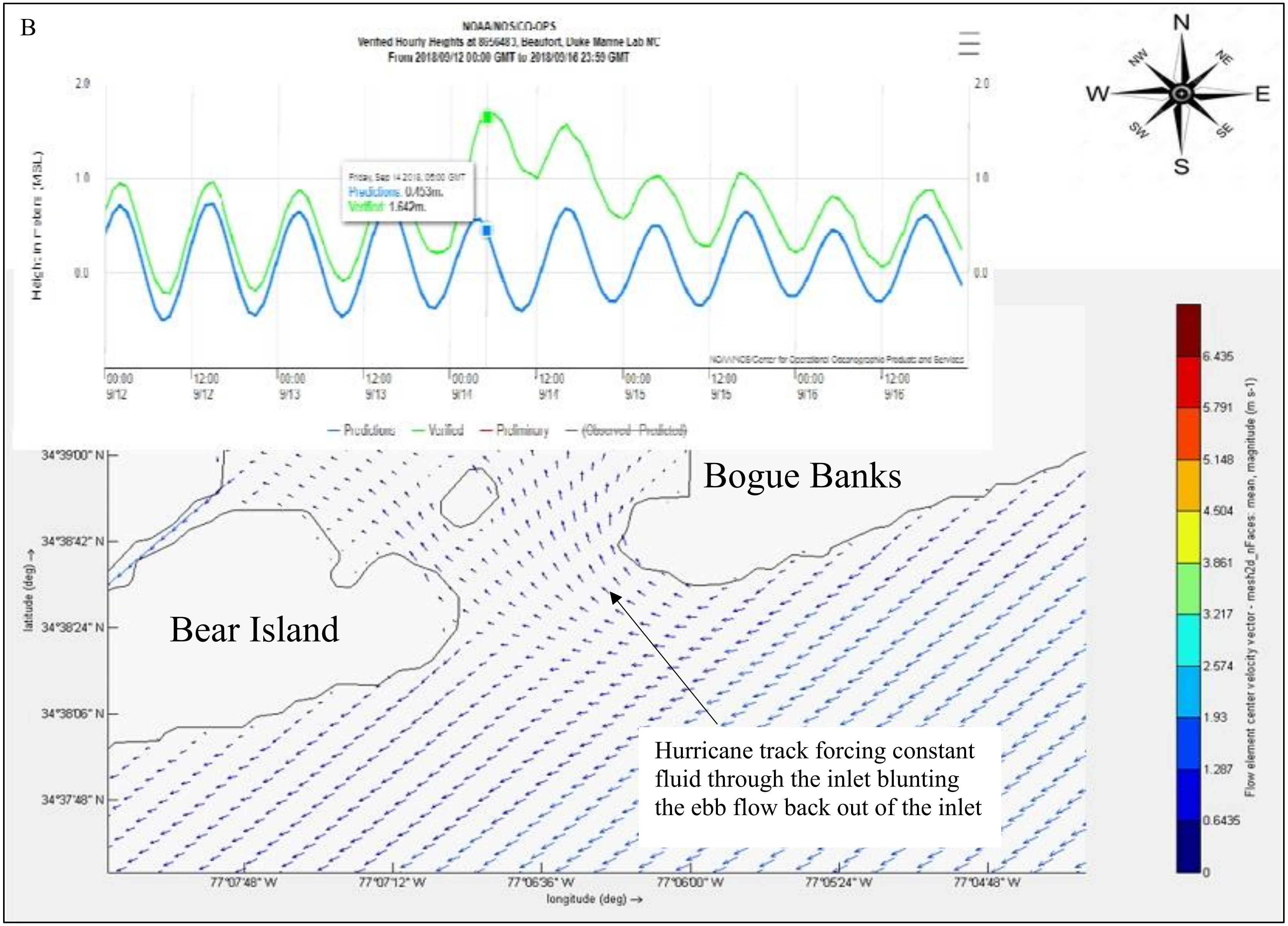
B
NOAA/NOS/CO-OPS
Verified Hourly Heights at 8656483, Beaufort, Duke Marine Lab NC
From 2018/09/12 00:00 GMT to 2018/09/16 23:59 GMT
Height in meters (MSL)
Predictions
Verified
Preliminary
N
S
E
W
Bogue Banks
Bear Island
Hurricane track forcing constant fluid through the inlet blunting the ebb flow back out of the inlet
latitude (deg)
longitude (deg)
Flow element center velocity vector - mesh2d_nFaces: mean, magnitude (m s-1)

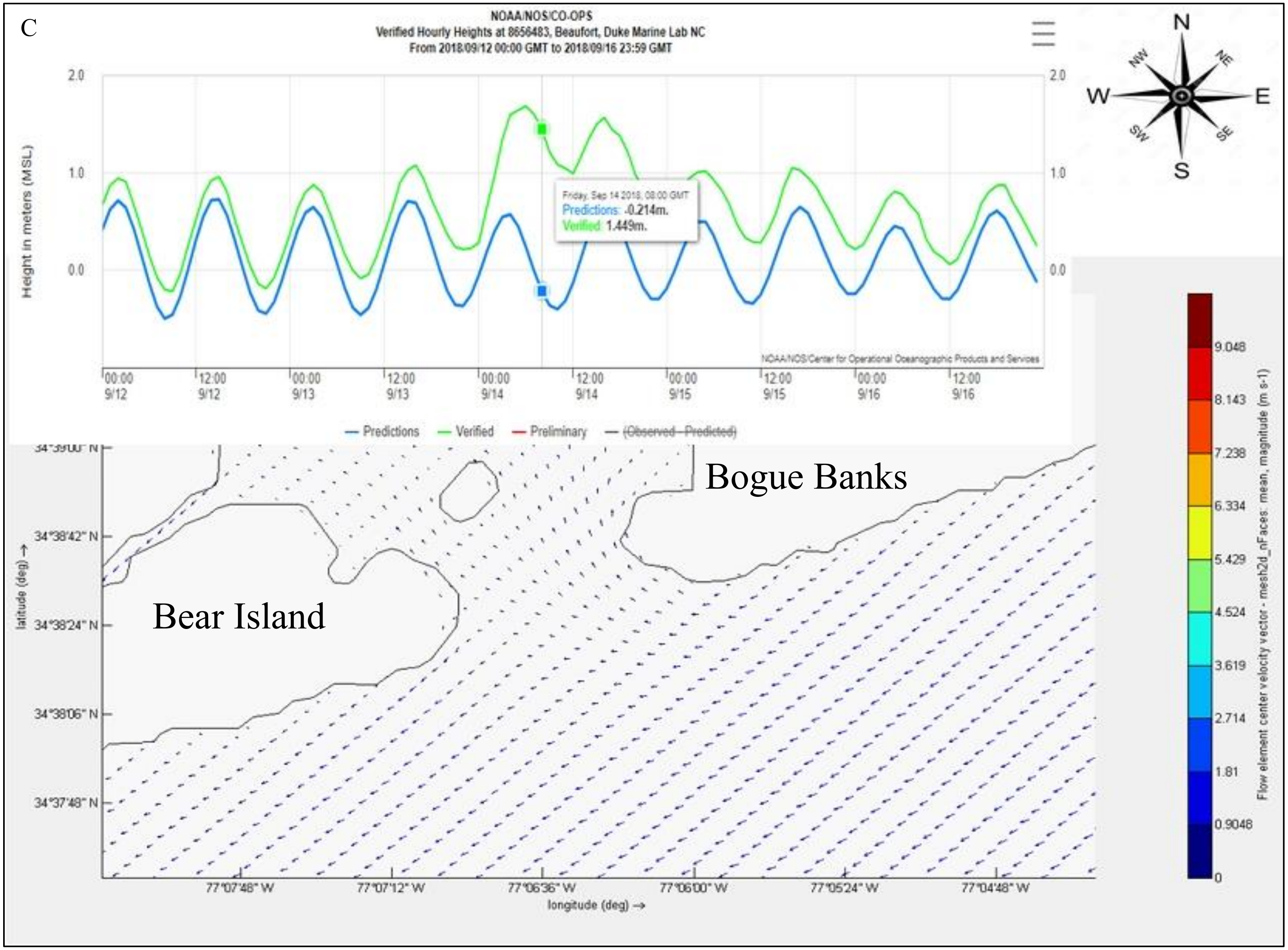
C
NOAA/NOS/CO-OPS
Verified Hourly Heights at 8656483, Beaufort, Duke Marine Lab NC
From 2018/09/12 00:00 GMT to 2018/09/16 23:59 GMT
Height in meters (MSL)
Friday, Sep 14 2018, 08:00 GMT
Predictions: -0.214m.
Verified: 1.449m.
NOAA/NOS/Center for Operational Oceanographic Products and Services
Predictions
Verified
Preliminary
(Observed - Predicted)
N
S
E
W
Bogue Banks
Bear Island
latitude (deg)
longitude (deg)
Flow element center velocity vector - mesh2d_nFaces: mean, magnitude (m s-1)

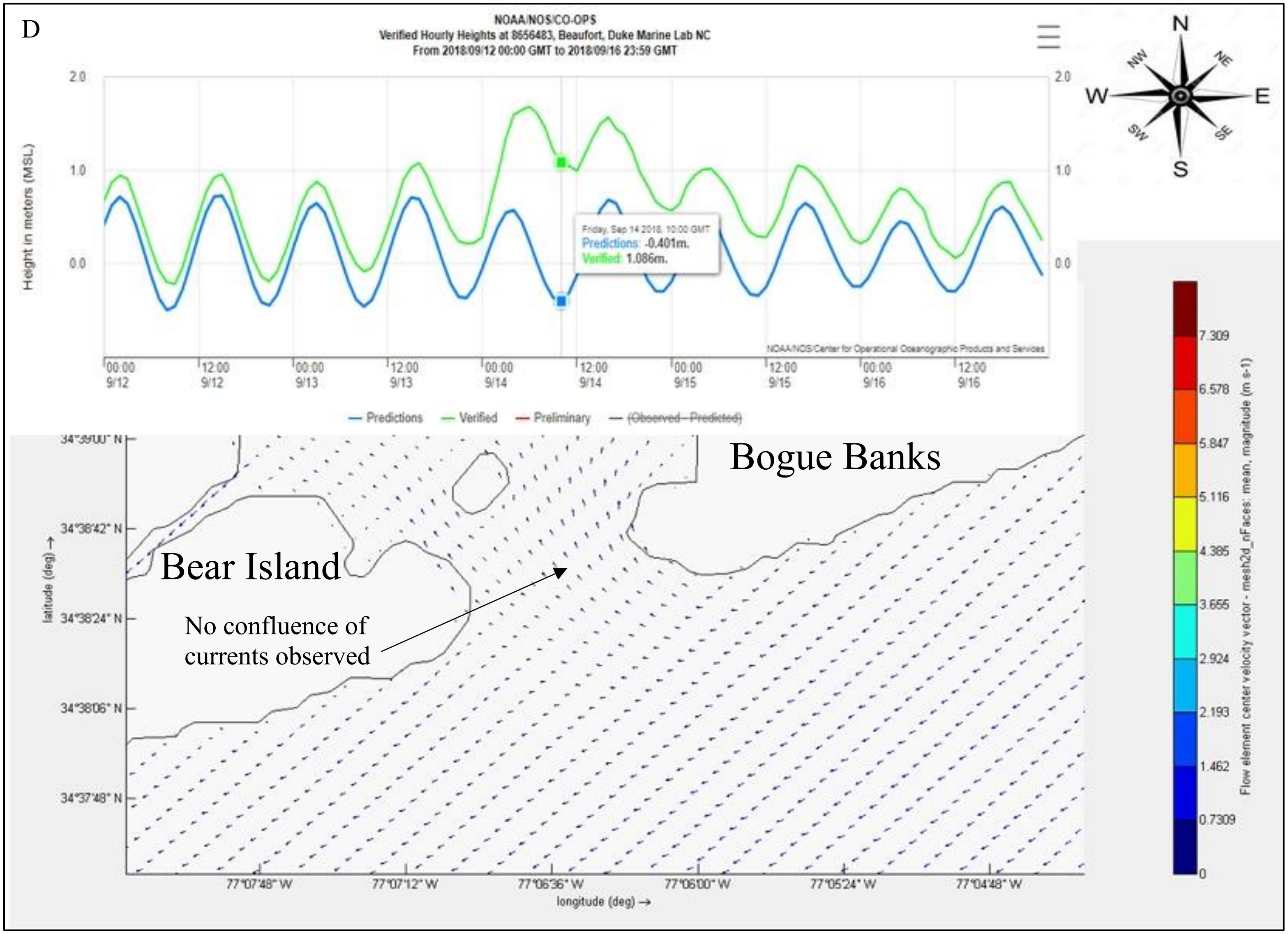

Figure 47. Hurricane Florence's varying current vectors and magnitudes within Bogue Inlet and the foreshore of Bogue Banks and Bear Island. Time steps from September 14th, 2018, at 03:00 GMT, to September 14th, 2018, 10:00 GMT, recorded at two-hour intervals. The y-axis represents latitude, and the x-axis

represents longitude; the color bar to the figure's right is presented in meters per second. The additional water levels, blue and green lines in the central portion of the figure, are data taken from Duke Marine Lab to show the specific time within the tidal cycle when the varying current vectors and magnitudes occur. The x-axis represents the water levels in feet above and below mean sea level, and the y-axis is time. Time steps are labeled (A-D), Source; https://tidesandcurrents.noaa.gov/.

From the summer of 2018 to the fall of 2018, the upper shoreface profile suggests the onshore transport of a longshore bar, starting approximately 500 m from the dune crest and accreting to the beach face (Appendix A). Furthermore, in (Appendix C) the bathymetric surveys from the summer of 2018 to the fall of 2018 (the time that encompassed the landfall of Hurricane Florence) show shoreline progradation and an increase in elevation on the eastern shoal platform, suggesting deposition and onshore transport. Both morphological changes could be the cause of wave-current interaction caused by the hurricane track, as the wind direction and forward momentum created the most significant value of storm surge. As the storm tracked through the embayment, winds started from the NE and switched to the E and SE. After landfall, the wind direction would still have been coming from the S, and wave action would have been directed up into the inlet. For almost the entire duration of the hurricane, there would have been an onshore transport direction and an alongshore transport direction to the SW, as suggested by the hydrodynamic model outputs (Figure 47). (Marshall, 2004; Wren and Leonard, 2005) also reported this across-shore along-shore transport direction as Hurricane Isabel made landfall in Onslow Bay. Additionally, in the inlet profiles (Appendix B), the bathymetric surveys (Appendix C), and the DEM of volumetric change raster (Figure 44), the middle shoal platform on the western bank of the main channel near the start of the flood-tidal delta ramp shows erosion. This would be a function of the back of the inlet channel migrating to the west to make the main channel as straight (most hydraulically efficient) as possible, connecting to the back-barrier tidal creek Seminack and McBride (2018). As the fluid discharge exceeded the maximum cross-sectional area that this portion of the channel could handle (caused by storm surge), scouring of the west bank would occur Huges (2002), transporting sediment to be deposited on the FTD and FTD ramp. Furthermore, wave action, superimposed on the storm surge, could have propagated further into the middle of the inlet onto the middle shoals due to the lack of ebb flow, adding in high enough bed shear stresses to entrain this fine to medium grain material to be then transported by the surge currents to the back-barrier region. The DEM of volumetric change raster from the summer of 2018 to the fall of 2018 is also skewed positively, with a net gain of 148,464 m^3, suggesting a net gain of sediment for the whole survey extent (Figure 44).

From the fall of 2018 to the summer of 2019, the shoreface profile started to show a relatively flat shoal platform as the ebb-tidal delta continued to migrate eastward, and the channel mouth continued to rotate slightly to the east (Appendix A and C). The summer of 2019 bathymetric survey shows a narrow longshore bar with an oblique shore orientation, and the slip face of this feature points to NNE. The slip face shows the onshore wave transport direction, which corroborates with the migration and rotation direction of the main inlet channel (Appendix C). At this time, little to no morphologic change is observed in the inlet profiles.

The last numerically modeled storm, Hurricane Dorian, occurred between the summer and fall of 2019. Hurricane Dorian tracked from the SW to the NE through the embayment before making landfall on Cape Hatteras in the Outer Banks. The storm had a relatively similar track to Hurricane Matthew, but Matthew's wind field was relatively larger (Appendix D). Onshore winds from Dorian started from the E, rotated to the NE, and then wrapped around, blowing out of the N as the storm exited the bay, blowing in the offshore direction (Appendix D). Even though the hurricane was strongest as it passed through Onslow Bay, the strongest wind field of the hurricane did not interact with Bogue Inlet (Appendix D). The model outputs for Hurricane Dorian show a calculated volumetric discharge value of 700 m^3 per second during the most significant inflow through the inlet and two peaks at 900 m^3 per second and 950 m^3 per second for the outflow (Figure 48). The largest volumetric discharge 950 m^3 is roughly 34 % larger than the discharged through the inlet in fair weather conditions measured by CSE (2005) at 624 m^3. The difference shows that even a hurricane with these parameters can create discharge values capable of morphologic change within the inlet channel and adjacent sub-environments.

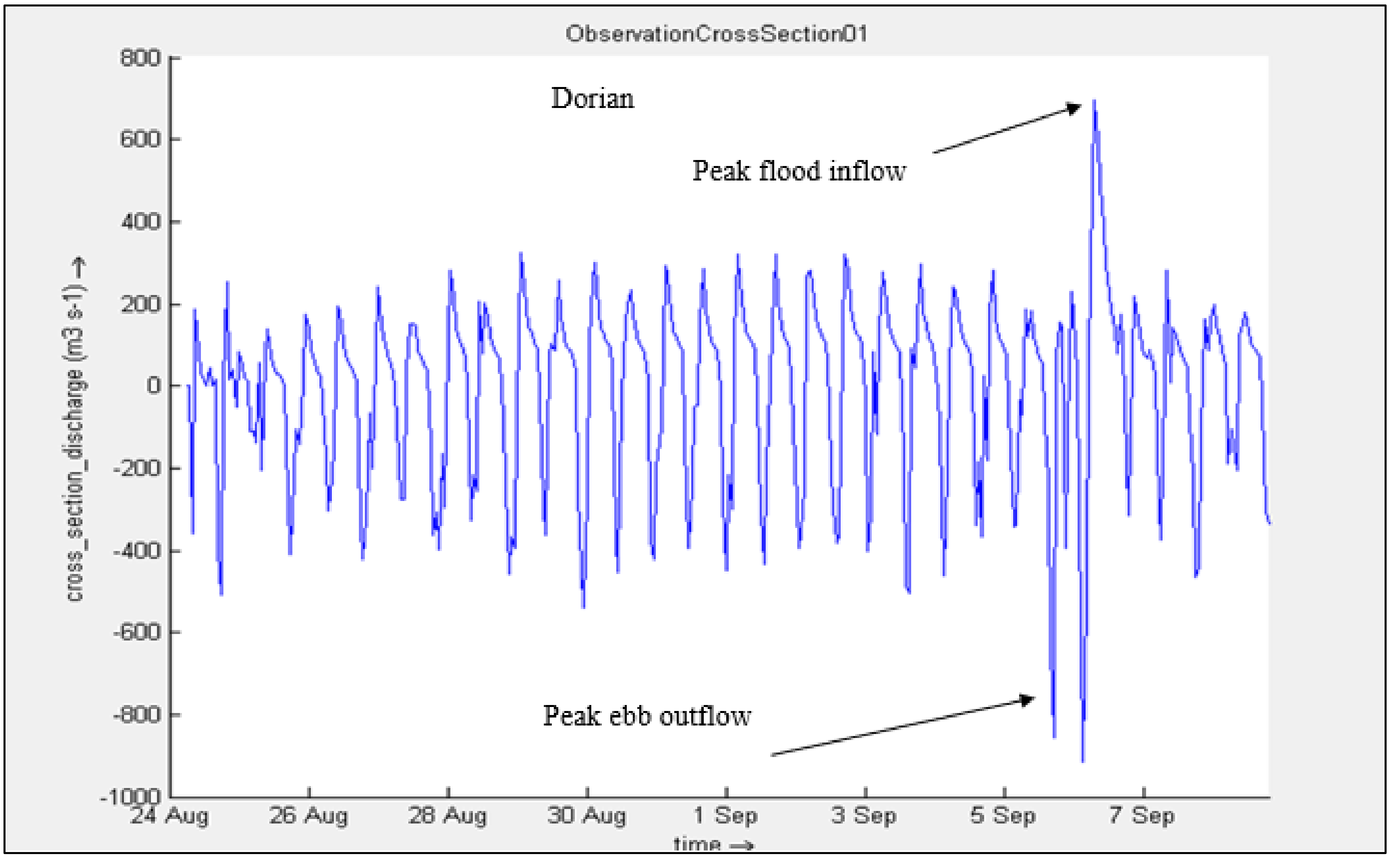

Figure 48. Data was produced from the model simulation of Hurricane Dorian in Delft3D. The graph shows the cross-sectional discharge through Bogue Inlet, in cubic meters per second, during Hurricane Dorian's landfall. The y-axis is presented in cubic meters per second, and the x-axis is presented as time.

Note that the two outflow peaks are larger in volume than the peak in inflow and occur before the inflow is recorded. Also, Dorian produced a cross-sectional growth of water in the inlet (storm surge) of 2,250 m^2 (Figure 49), which was relatively not larger than background values of 1,700 to 1,800 m^2. Furthermore, the storm surge produced two peaks of approximately the same value (Figure 49). It blunted the water residence until the storm passed, and the wind directions blew completely offshore from the north (Appendix D). These data are a function of the storm track, wind field size, and intensity of the winds. Even though there was an onshore push of water and wave action from the SE caused by the strongest winds closest to the eye of the hurricane (Appendix D), winds of this magnitude and direction never interacted with the inlet. Winds blowing from the NE, at approximately 26-29 meters per second (Appendix D), were forcing water out of the inlet as wave action and storm surge were directed up into the portion of the bay where Bogue Inlet is located. This is why the data would show two peak ebb discharges, as the overall water level was higher due to the relatively weak storm surge. As reported by (Wright et al., 1993; Marshall, 2004; Wren and Lenord, 2005), mean currents in the nearshore and shoreface mirror atmospheric wind direction in energetic enough events.

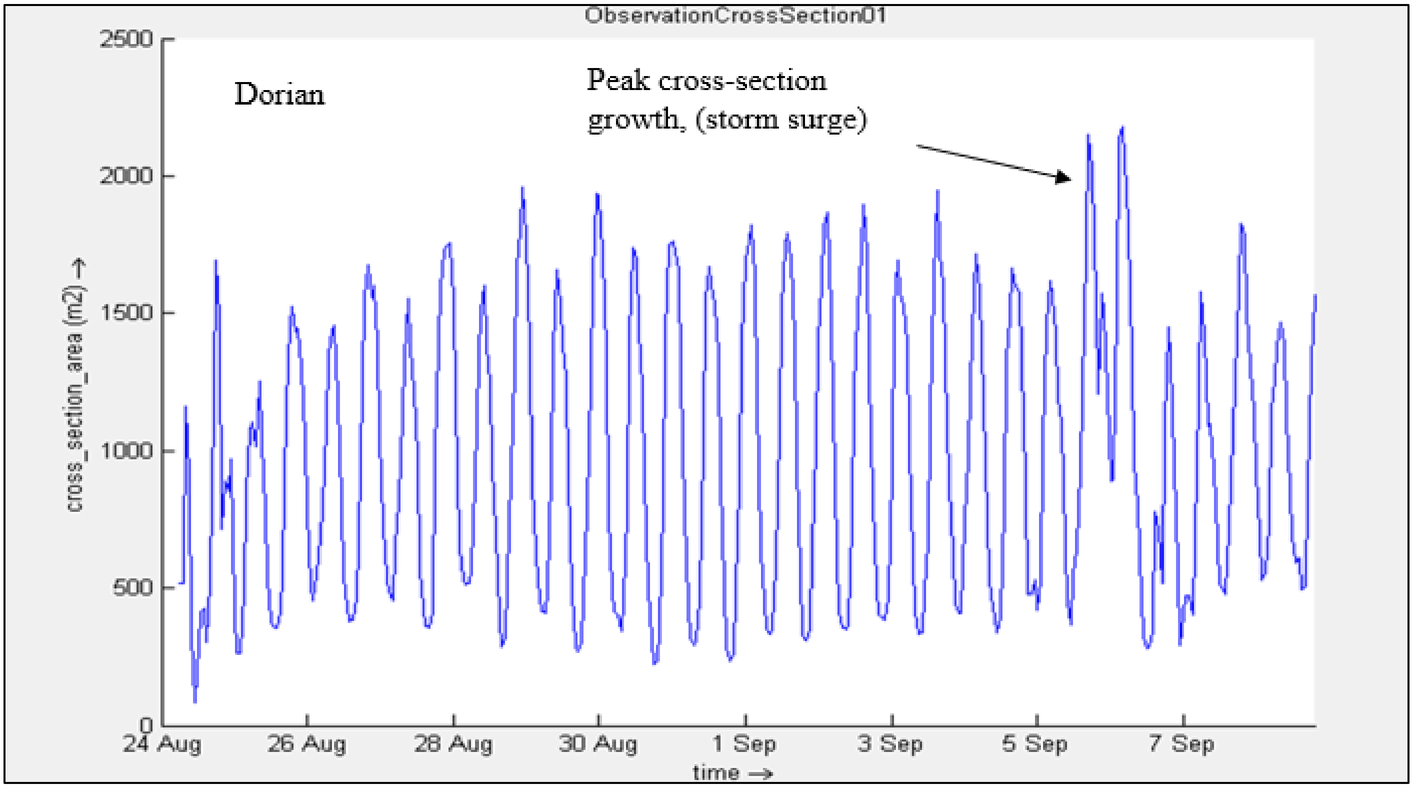

Figure 49. Data was produced from the model simulation of Hurricane Dorian in Delft3D. The graph shows Bogue Inlets' cross-sectional growth of water in the inlet (storm surge) that passed through the inlet when Hurricane Dorian passed through Onslow Bay. The y-axis is presented in square meters, and the x-axis is time.

A peak fluid velocity of 1.5-1.7 meters per second was recorded on September 6th, 2019, at 10:00 GMT, approaching low tide, located on the eastern margin of the inlet in the main inlet channel. At this time, winds were blowing offshore from the north (Figure 50, Appendix D).

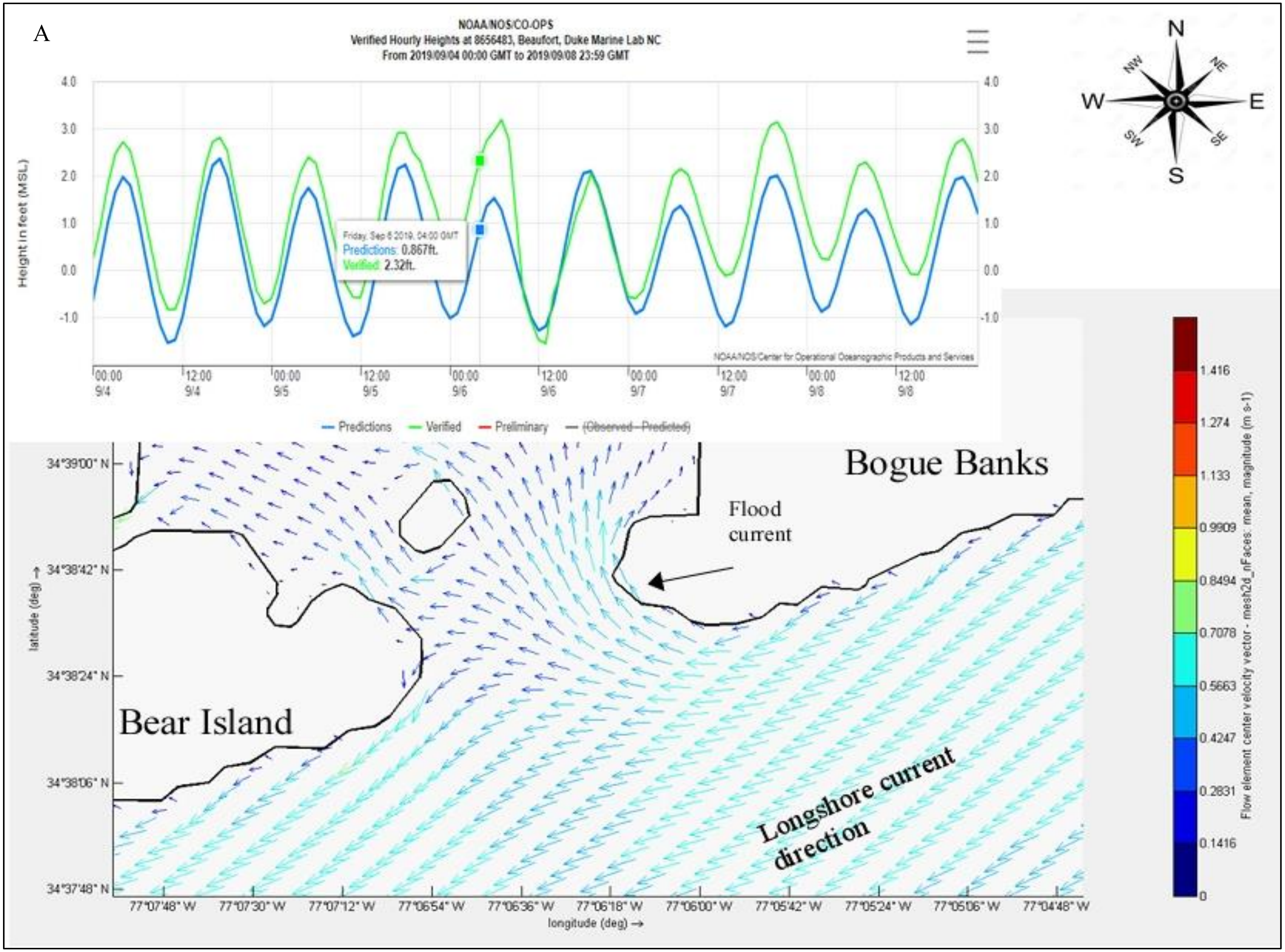
A
NOAA/NOS/CO-OPS
Verified Hourly Heights at 8656483, Beaufort, Duke Marine Lab NC
From 2019/09/04 00:00 GMT to 2019/09/08 23:59 GMT
Height in feet (MSL)
Friday, Sep 6 2019, 04:00 GMT
Predictions: 0.867ft.
Verified: 2.32ft.
NOAA/NOS/Center for Operational Oceanographic Products and Services
Predictions
Verified
Preliminary
(Observed - Predicted)
N
E
S
W
Bogue Banks
Flood current
Bear Island
Longshore current direction
latitude (deg)
longitude (deg)
Flow element center velocity vector - mesh2d_nFaces: mean, magnitude (m s-1)

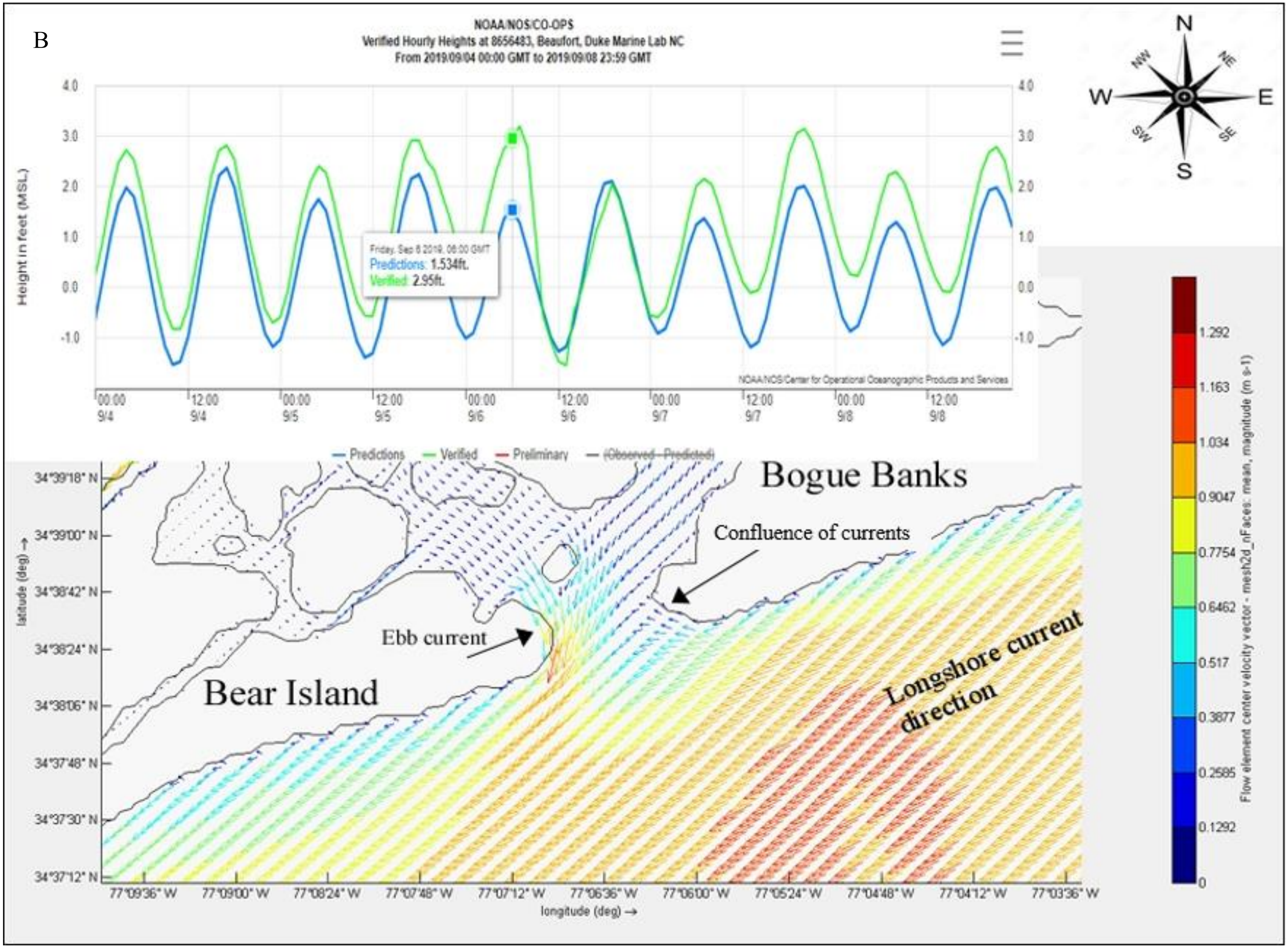
B
NOAA/NOS/CO-OPS
Verified Hourly Heights at 8656483, Beaufort, Duke Marine Lab NC
From 2019/09/04 00:00 GMT to 2019/09/08 23:59 GMT
Height in feet (MSL)
Friday, Sep 6 2019, 06:00 GMT
Predictions: 1.534ft.
Verified: 2.95ft.
NOAA/NOS/Center for Operational Oceanographic Products and Services
Predictions
Verified
Preliminary
(Observed - Predicted)
N
S
E
W
NW
NE
SW
SE
Bogue Banks
Confluence of currents
Ebb current
Bear Island
Longshore current direction
latitude (deg) →
longitude (deg) →
Flow element center velocity vector - mesh2d_nFaces: mean, magnitude (m s-1)

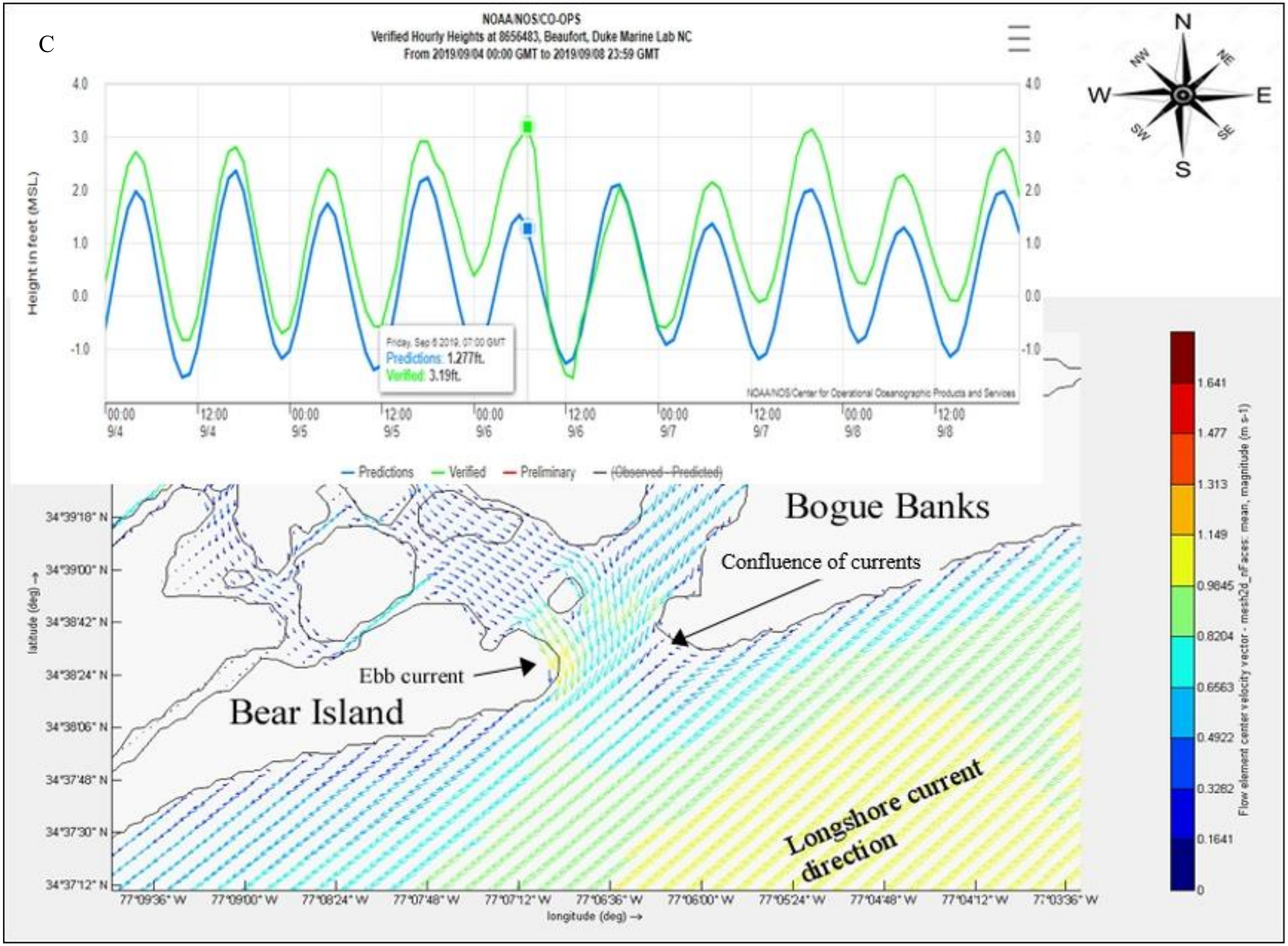
C
NOAA/NOS/CO-OPS
Verified Hourly Heights at 8656483, Beaufort, Duke Marine Lab NC
From 2019/09/04 00:00 GMT to 2019/09/08 23:59 GMT
Height in feet (MSL)
Friday, Sep 6 2019, 07:00 GMT
Predictions: 1.277ft.
Verified: 3.19ft.
NOAA/NOS/Center for Operational Oceanographic Products and Services
Predictions
Verified
Preliminary
(Observed - Predicted)
N
S
E
W
Bogue Banks
Confluence of currents
Ebb current
Bear Island
Longshore current direction
latitude (deg)
longitude (deg)
Flow element center velocity vector - mesh2d_nFaces: mean, magnitude (m s-1)

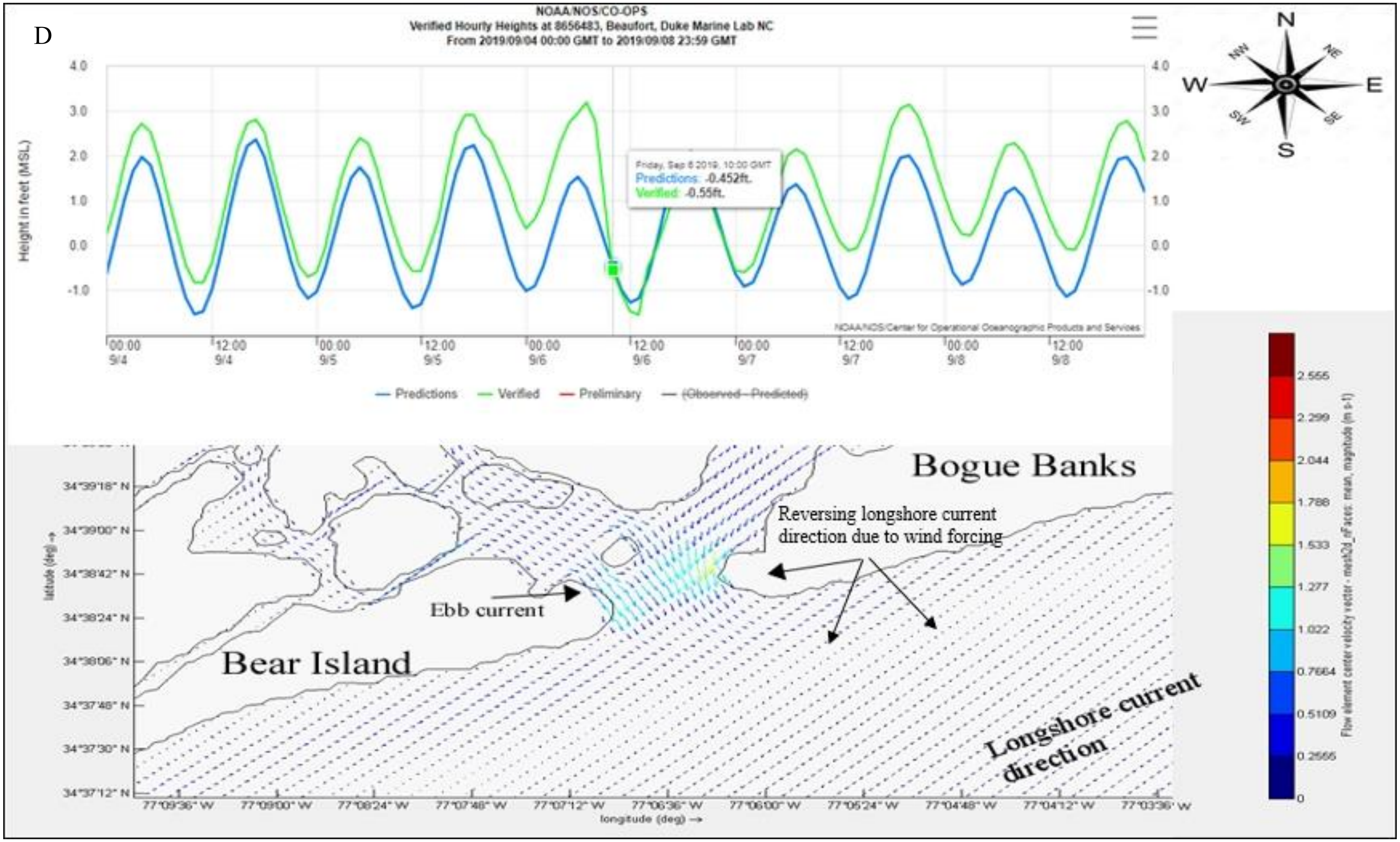

Figure 50. Hurricane Dorian's varying current vectors and magnitudes within Bogue Inlet and the foreshore of Bogue Banks and Bear Island. Time steps from September 6th, 2019, at 04:00 GMT, to September 6th, 2019, 10:00 GMT, recorded at two-hour intervals. The y-axis represents latitude, and the x-axis represents longitude; the color bar to the figure's right is presented in meters per second. The additional water levels, blue and green lines in the central portion of the figure, are data taken from Duke Marine Lab to show the specific time within the tidal cycle when the varying current vectors and magnitudes occur. The x-axis represents the water levels in feet above and below mean sea level, and the y-axis is time. Time steps are labeled (A-D), source; https://tidesandcurrents.noaa.gov

Note that even approaching high tide, at 06:00 GMT (Figure 50), when the food tidal flow should still propagate into the inlet, fluid vectors show water being forcefully pushed out of the inlet. This is due to wind forcing, which results in the phenomenon of the confluence of currents, also observed in Hurricane Matthew. However, the confluence of current phenomena is not recorded in the modeled simulation of Hurricane Florence. This is a direct function of wind-forced currents interaction with the M2 semidiurnal tidal currents. Additionally, this phenomenon slows surface currents near the eastern margin of the inlet from 06:00 to 07:00 GMT (Figure 50). It deflects the strongest flow in the direction of winds out of the western margin of the inlet, where the large marginal flood channel is located. Only when the wind direction is blowing directly from the N and the tidal cycle is approaching low tide at 10:00 GMT (Figure 50) is the confluence of currents not recorded. The model exhibits a more homogenous ebb flow through the inlet, and the strongest fluid velocities are recorded on the eastern margin where the main channel resides. Furthermore, from 04:00 to 06:00 GMT, the along-shore's current direction is to the SW (Figure 50) as the Winds shift to the north at 10:00 GMT, an observed, weak longshore current reversal is recorded in the NW direction (Figure 50). Again, this is a function of the mean current direction being forced by the direction of winds in the nearshore and shoreface (Wright et al., 1993; Marshall, 2004; Wren and Lenoard, 2005).

In the fall of 2019, the longshore bar observed in the summer survey 2019 (Appendix D) was almost completely welded to the shoreface of Bogue Banks. This action is also caught in the beach face profile, where the longshore bar trough is filled in, and the beach face exhibits a step-like profile (Appendix A). Furthermore, at the -3m contour on the distal portion of the ebb-tidal delta, the delta prograde basinward roughly 50 m (Appendix A). Additionally, the inlet channel mouth has rotated more to the east as the back portion of the channel visible in the western portion of the survey deepens to the west and continues to become straight (Appendix C). The only notable morphologic change in the inlet profile is scouring into the bank of Bogue Banks. These morphological changes can be explained In a few ways. Wave action coming from the S and SSE would have transported sediment in the onshore direction between the summer of 2019 and the fall of 2019 and the beginning of when Hurricane Dorian entered the embayment (Figure 51). The onshore transport direction would have caused the distal portion of the ebb-tidal delta to prograde basinward and as wave bores broke over the ebb delta, possibly welding the longshore bar to the foreshore (Appendix C).

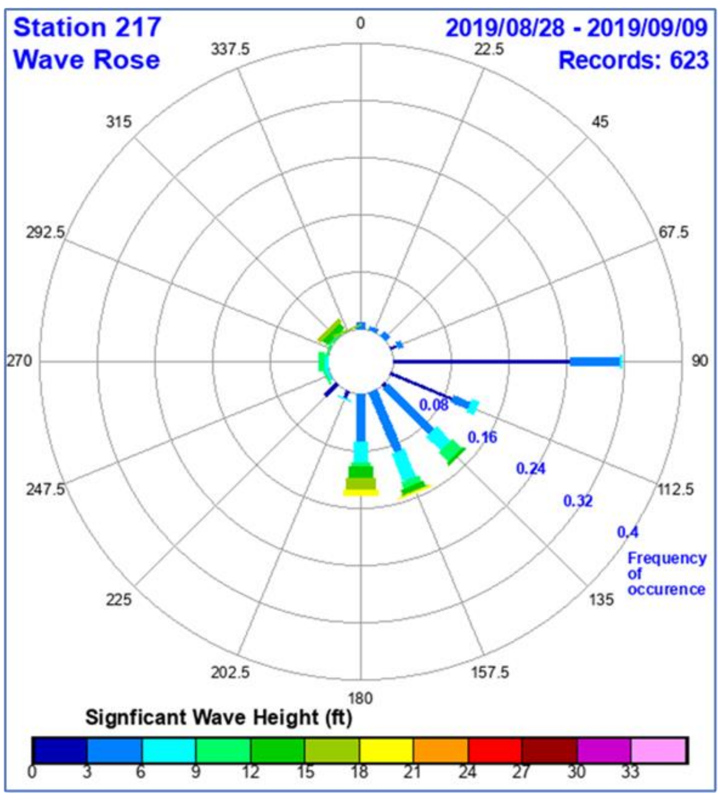

Figure 51. A wave rose diagram from the buoy station 217 (outer Onslow Bay), source https://cdip.ucsd.edu/. The color bar on the bottom represents significant wave height in feet (Hs) and frequency in the concentric rings starting from the center and radiating out. The time period is from 08/28/2019 to 09/09/2019, the time as Hurricane Dorian passed through Onslow Bay.

The further rotation of the back portion of the channel and the front of the channel mouth would have most likely occurred as the Hurricane's storm surge exceeded the maximum cross-sectional area of volumetric discharge that the channel could have held when peak discharges were recorded as well as the strongest wave direction from the south. The channel would have scoured to the east more than vertically due to the channel dimension being wider and exhibiting almost no western bank as the back portion counties to connect to the back-barrier tidal channel, migrating westward. The confluence of tidal currents would have played a role, too, in the eastward scouring into Bogue Banks, as observed in Hurricane Matthew's modeled outputs. The DEM of volumetric changes (Figure 52) also captures these morphologic changes. On the foreshore of the westernmost edge of Bogue Banks, flanking the main inlet channel, the beach face shows a region of accretion that matches precisely the extent of the shoreline migration from summer 2019 to fall 2019 (Figure 30). Large deposition values are shown along the ebb-tidal delta's terminal edge and on the main channel's western margin on the swash platform and shoals in the DEM of volumetric change raster (Figure 52). This is most likely a function of the longshore transport direction to the SW, as depicted in the hydrodynamic modeling (Figure 53). As the wind forced the bottom boundary mean currents to interact with the semidiurnal current to transport sediment onshore and into the inlet, the alongshore mean currents would have aided in deposition onto the leading edge of the ebb-tidal delta. (Figure 52). Furthermore, the volumetric change raster was skewed net positive at 328,568 m^3, suggesting large amounts of deposition through the survey extent. However, erosion values are shown where the main inlet channel is located, pointing to when the winds switched to blowing from the north, the peak ebb flow velocities would have exhibited enough bed shear stress to cause flushing of the main channel.

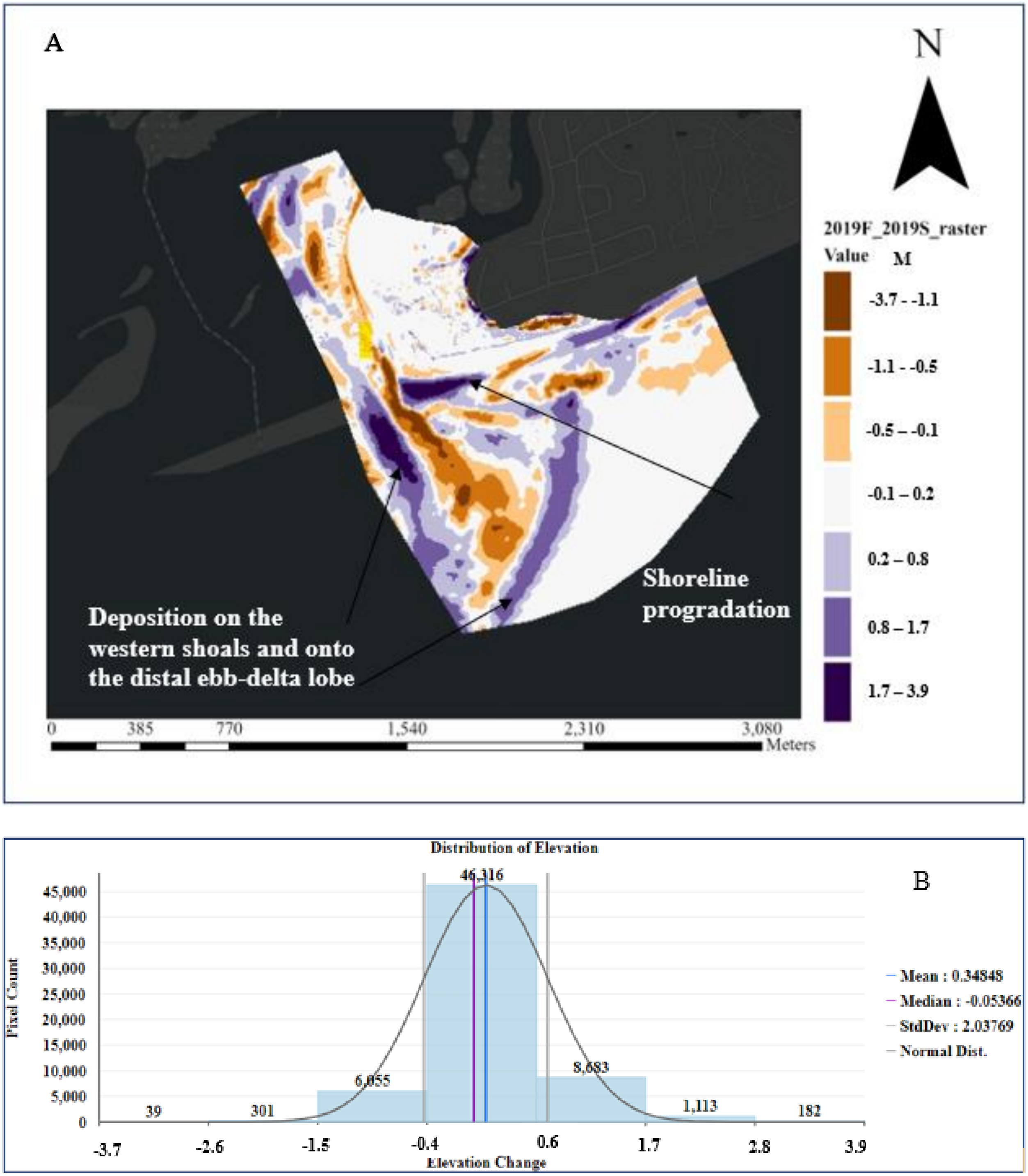

Figure 52. A) Is the raster output from summer 2019 to fall 2019, when Hurricane Dorian passed through Onslow Bay, using the DEM of difference method, showing deposition in shades of purple and shades of brown erosion. Deposition and erosion are recorded in ft datum NAVD88. **B)** is a histogram showing elevation change on the x-axis and pixel count on the y-axis. This was used in the estimated volumetric calculations presented in Table 3. The y-axis is the number of pixels (6 m x 6 m per pixel) that fall within a range of elevation change. The x-axis represents the range of elevation change measured in feet. The range of elevation change is averaged. Then, the perimeter of a pixel is calculated (6 m x 6 m) and multiplied by the number of pixels in the specific range of elevation change to

find the total perimeter of those pixels. Lastly, the range of elevation change is multiplied by the total perimeter of the pixels that fell within the averaged elevation change, giving an estimate of the volume of the specific perimeter of the pixels in that range.

The last period simulated using the Delft3D numerical modeling was the month of January 2018, with no reported tropical or extratropical storms. The first-time stamp was on January 13th, 2018, at 23:00 GMT (Figure 53), where the second semi-diurnal high tide was switching from flood to ebb flow. Note that at the start of the ebb tide, the longshore current vectors flow in the alongshore direction to the NW (Figure 53). This could be a function of the wave-current interaction in the shoreface from winds caused by a high-pressure system blowing from the SW or the S, directing waves from the S-SE. The wind direction would be caused by the clockwise rotation of an anticyclone (high-pressure system) that rotates in this direction in the northern hemisphere. However, a frontal boundary could also produce a wind direction from the SW-S Marshall (2004). The second time stamp was from January 14th at 02:00 GMT. This was two hours into the ebb flow. The offshore direction of the fluid vectors off Bear Island and a continued alongshore flow direction to the NW suggest that winds could have changed, blowing from the W. However, on Jan 14th at 04:00 GMT, data shows a reversal of the current direction of the longshore to the SW (Figure 53). Most likely, the wind direction is now blowing from the NNE, forcing the foreshore and nearshore currents to the SW. This current direction is reflected in the last time stamp on January 15th at 07:00 GMT. Note that in the last two-time stamps, the suggested change in wind direction, implied by the change in the longshore current direction, shows the phenomenon of the confluence of currents in the inlet again. As mentioned, this is a function of wind-forced mean current direction interacting with the semi-diurnal tidal current when low tide is reached. The confluence of currents can cause erosion and deposition depending on the location in the inlet; refer to the prior discussion on the explanation of erosion and deposition of the confluence of currents. Furthermore, the time lag CSE (2005) reported is observed as the ebb currents continue after the tides reverse and start the flood tidal phase (Figure 53).

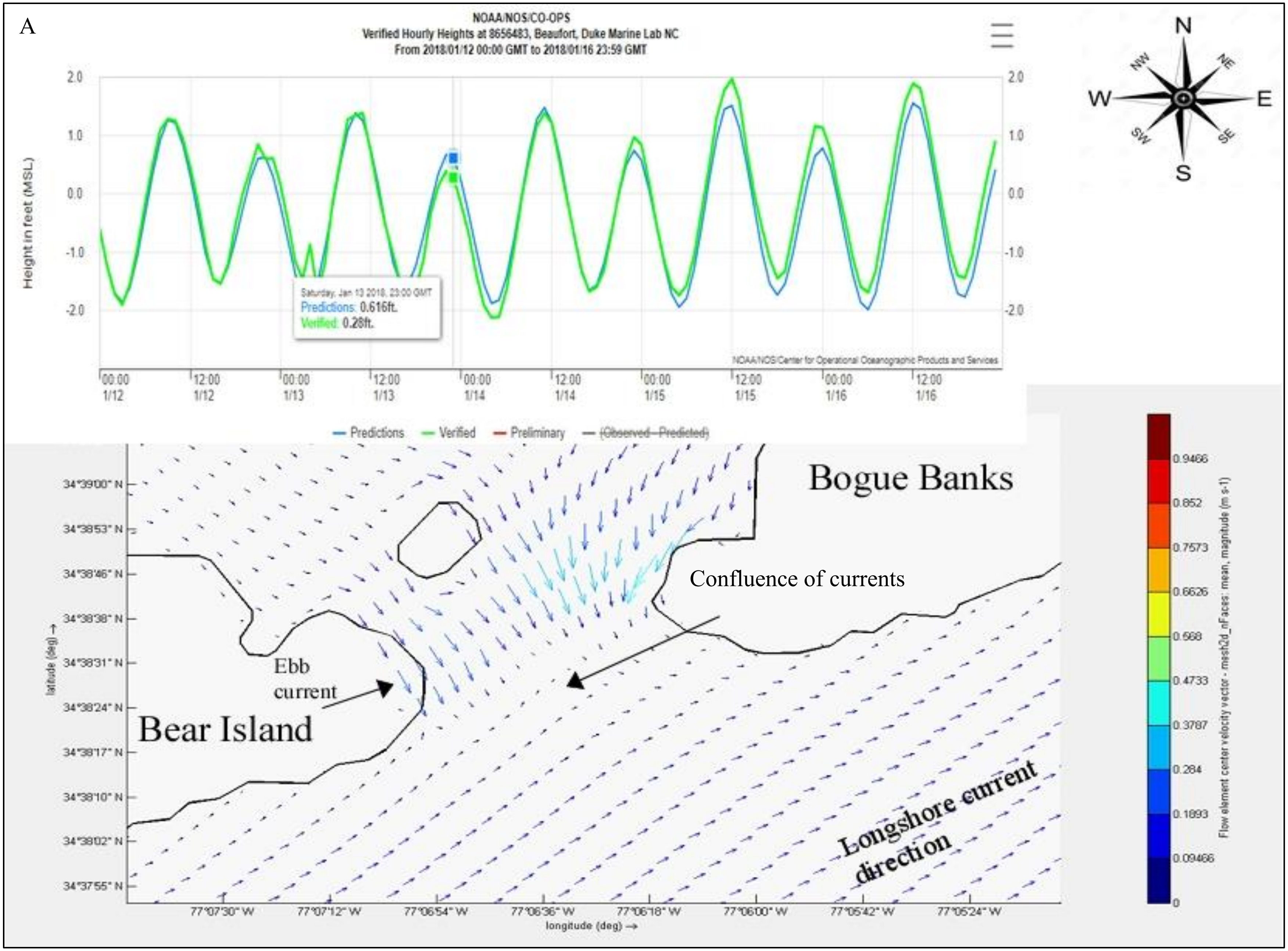
A
NOAA/NOS/CO-OPS
Verified Hourly Heights at 8656483, Beaufort, Duke Marine Lab NC
From 2018/01/12 00:00 GMT to 2018/01/16 23:59 GMT
Height in feet (MSL)
Saturday, Jan 13 2018, 23:00 GMT
Predictions: 0.616ft.
Verified: 0.28ft.
NOAA/NOS/Center for Operational Oceanographic Products and Services
Predictions
Verified
Preliminary
(Observed - Predicted)
N
S
E
W
NW
NE
SW
SE
Bogue Banks
Confluence of currents
Ebb current
Bear Island
Longshore current direction
latitude (deg) →
longitude (deg) →
Flow element center velocity vector - mesh2d_nFaces: mean, magnitude (m s-1)

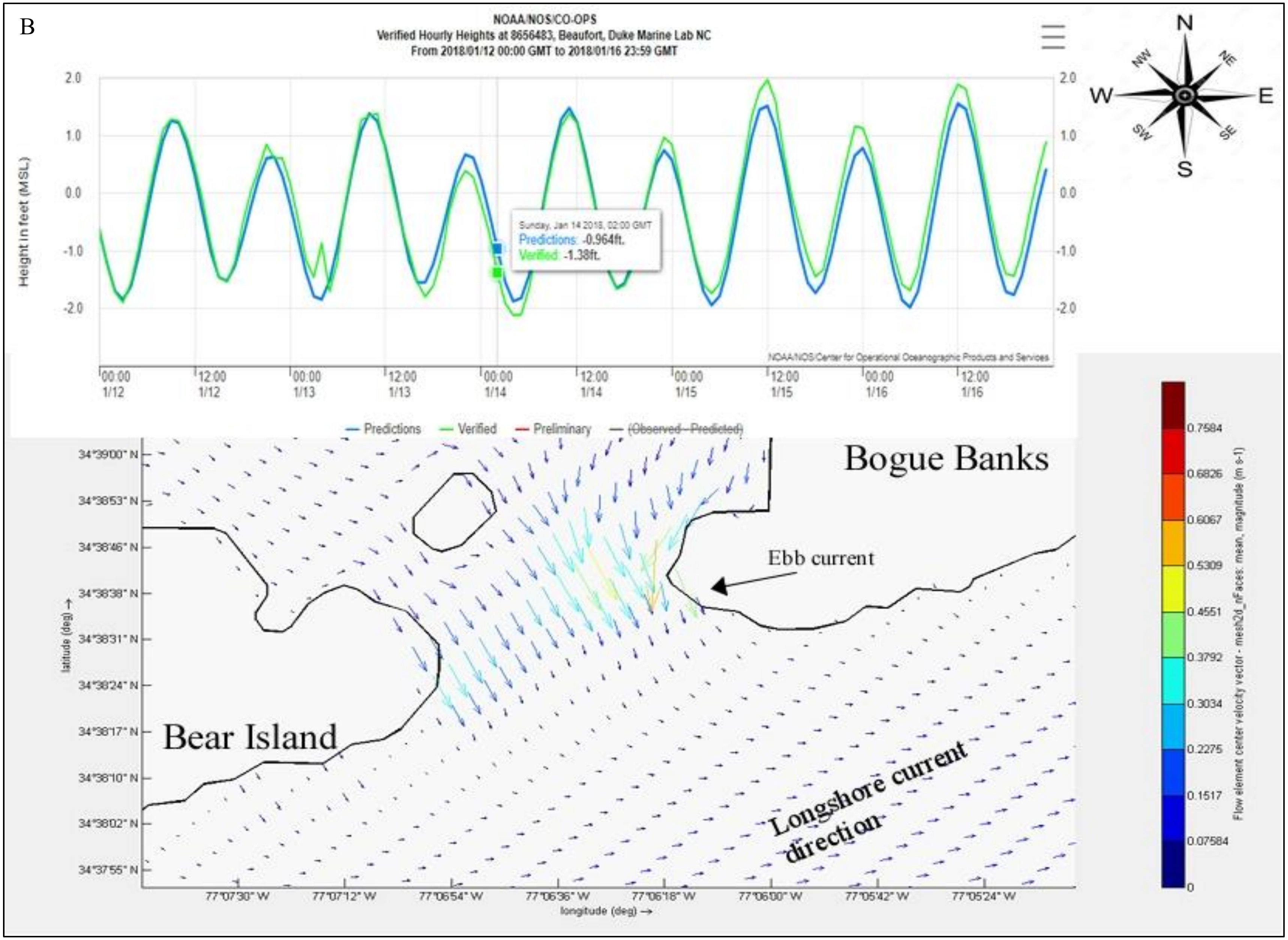

B
NOAA/NOS/CO-OPS
Verified Hourly Heights at 8656483, Beaufort, Duke Marine Lab NC
From 2018/01/12 00:00 GMT to 2018/01/16 23:59 GMT
Height in feet (MSL)
Sunday, Jan 14 2018, 02:00 GMT
Predictions: -0.964ft.
Verified: -1.38ft.
NOAA/NOS/Center for Operational Oceanographic Products and Services
Predictions
Verified
Preliminary
(Observed - Predicted)
N
S
E
W
NE
NW
SE
SW
Bogue Banks
Ebb current
Bear Island
Longshore current direction
latitude (deg)
longitude (deg)
Flow element center velocity vector - mesh2d_nFaces: mean, magnitude (m s-1)

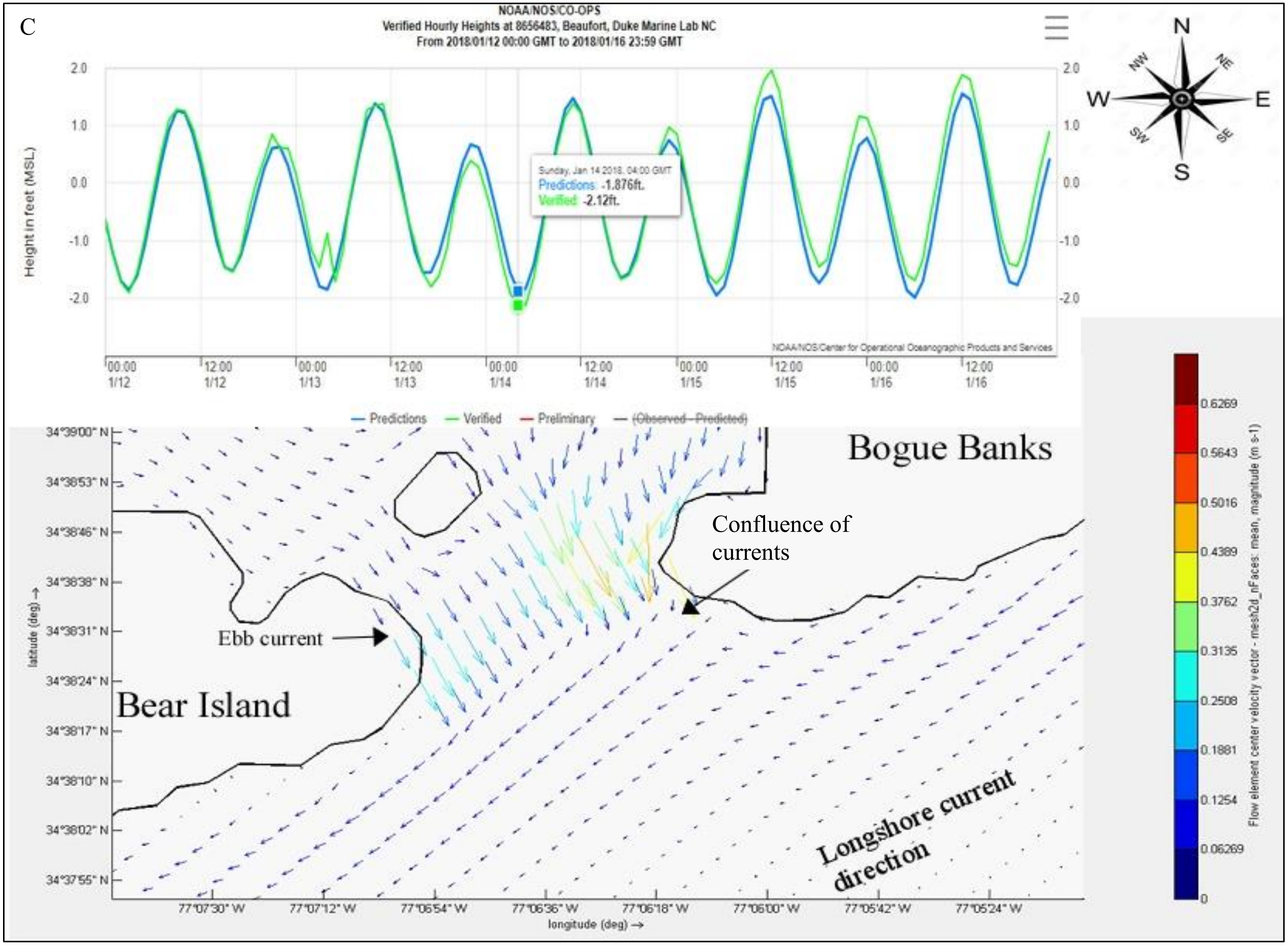
C
NOAA/NOS/CO-OPS
Verified Hourly Heights at 8656483, Beaufort, Duke Marine Lab NC
From 2018/01/12 00:00 GMT to 2018/01/16 23:59 GMT
Height in feet (MSL)
Sunday, Jan 14 2018, 04:00 GMT
Predictions: -1.876ft.
Verified: -2.12ft.
NOAA/NOS/Center for Operational Oceanographic Products and Services
Predictions
Verified
Preliminary
(Observed - Predicted)
N
S
E
W
Bogue Banks
Confluence of currents
Ebb current
Bear Island
Longshore current direction
latitude (deg)
longitude (deg)
Flow element center velocity vector - mesh2d_nFaces: mean, magnitude (m s-1)

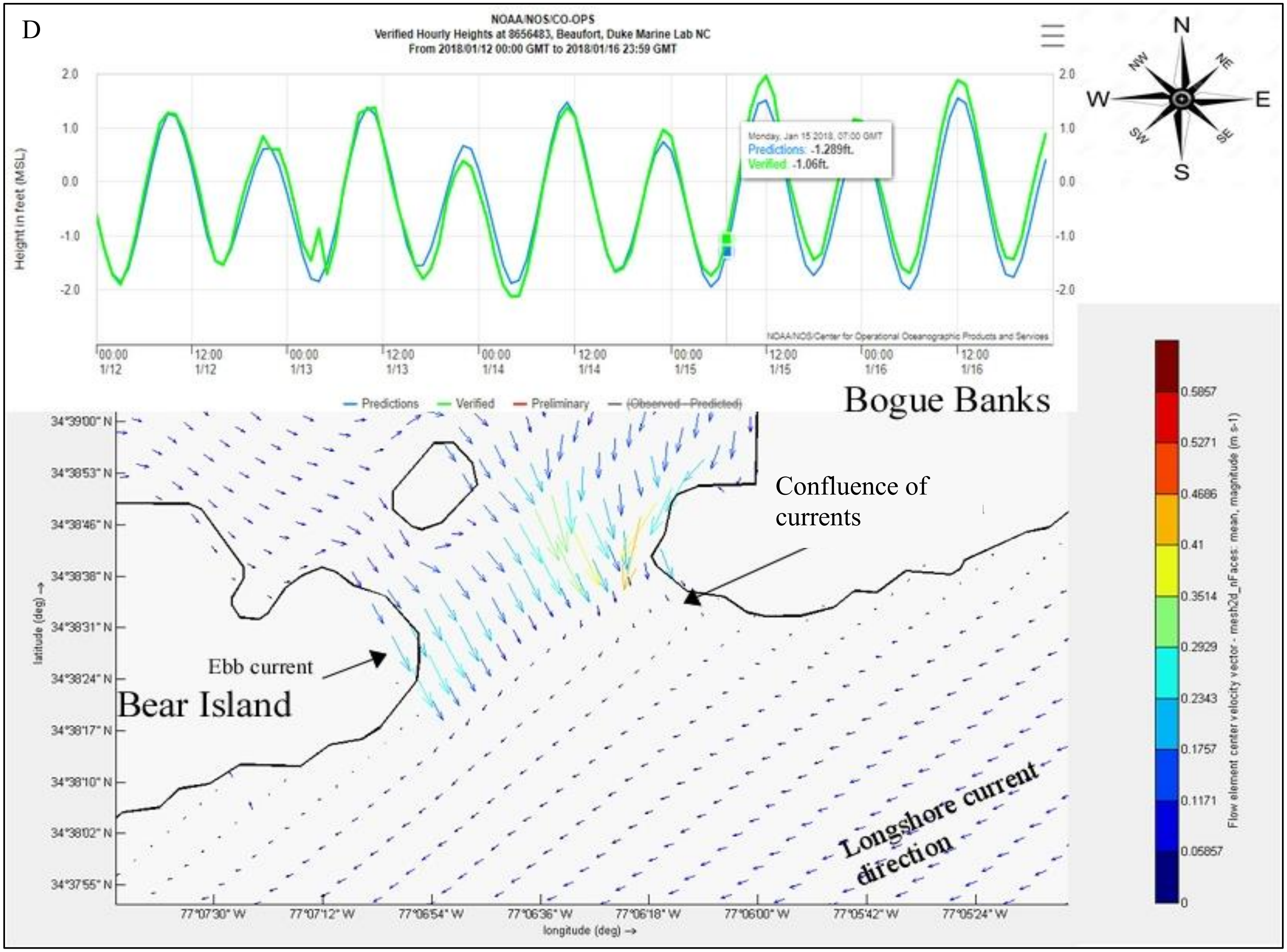

Figure 53. January 01/01/2018 through 12/31/2018, varying current vectors and magnitudes within Bogue Inlet and the foreshore of Bogue Banks and Bear Island. Time steps from January 13th, 2018, at 23:00 GMT, to January 15th, 2018, 07:00 GMT. The y-axis represents latitude, and the x-axis represents longitude;

the color bar to the figure's right is presented in meters per second. The additional water levels, blue and green lines in the central portion of the figure, are data taken from Duke Marine Lab to show the specific time within the tidal cycle when the varying current vectors and magnitudes occur. The x-axis represents the water levels in feet above and below mean sea level, and the y-axis is time. The time steps are labeled (A-D), source; https://tidesandcurrents.noaa.gov/.

In the last bathymetric surveys obtained from Geodynamics, from the fall of 2019 until the summer of 2022, some notable morphological changes were observed to conclude the most extensive understanding of the evolution of the inlet system. From the fall of 2019 to the spring of 2020, the inlet profile shows approximately 1.5 meters of deposition on the western bank of the main channel (Appendix B). The elevation changes on the western bank cause the dimensions of the channel to narrow. In the same period, the bathymetric survey depicts further rotation of the main channel in the back portion of the inlet westward (Appendix C). Also, the mouth of the channel continues to rotate slightly to the east (counterclockwise rotation). From 2020 S to 2020 F, vertical scouring of the channel is observed from -8 m to -8.5 m in the inlet profile (Appendix B). The bathymetric survey shows that the channel mouth has stopped rotating to the east but continues scouring in the region near the FTD ramp as the back-barrier tidal channel is completely in line with the main channel. The foreshore profiles show a continuous building of the ETD basinward from 2019 F to 2020 F to roughly 1,300 m from the dune ridge. Note that as the inlet channel's rotation slows, the channel starts vertically scouring once again. This is most likely due to the orientation of the channel and dimension of the channel narrowing, connecting to the back-barrier channel, where any changes in volumetric discharge (increase in the tidal prism) would cause vertical scouring instead of lateral scouring because the inlet is transitioning back to being less hydraulically efficient as it narrows (Hudson and Kesel, 2000; Seminack and McBride, 2018). There is more of a western bank to funnel the volume of water through a narrower channel (Appendix B). The seaward building of the shoreline is both a function of onshore wave direction and a time of a few storms where only one Category 1 storm made landfall to the south of Onslow Bay along the SC/NC state line in late July.

In the last three bathymetric surveys, 2021 S, 2021 F, and the summer of 2022 profiles, the shoreline was observed to accrete to 370 m until the summer of 2021 from the start of the beach profile (Appendix A). Additionally, from 2021 S until 2020 S, the shoal platform of the ETD deflates to a depth of -3.5 m from -2 m at approximately 750 m from the beginning of the beach profile (Appendix A). The bathymetric surveys capture this action as well. From 2021 S to 2021 F, the shoreline at Bogue Point prograde seaward, and the western bank of the channel mouth shows deposition (Appendix D). These morphological changes are accompanied by the observation of large sand waves in the broad mouth of the channel as it reaches its final orientation in the summer of 2022, the last bathymetric survey that was analyzed. The continued building seaward of the shoreline is accompanied by the lowest number of tropical and extratropical storms recorded, one tropical storm in 2021 that stays on land and no recorded storms into 2022. At this time, small amounts of deposition are observed on the western channel bank as the channel profile exhibits its most symmetrical dimension throughout the whole duration of the data obtained (Appendix B). The channel cross-sectional area is estimated again, measured from the -1.5 m contour at 1,318 m^2. The cross-sectional area is only 46 m^2 smaller than the cross-section measured in 2016. However, the main channel is in a linear geometry, connecting to the most dominant tidal creek. This indicates that the inlet channel has evolved into a state of dynamic equilibrium. Where the portion of the tidal prism that travels through the inlet, void of any energetic events, is within the channel's maximum cross-sectional width Hughes (2002). It is evident that no further scouring is obvious from 2021 S to 2022 S. Furthermore, large bedforms and basinward-facing sand waves are now present, at least to the extent of the data available throughout the study duration. This would be a function of a relatively quiet time with no significant atmospheric events where the volumetric discharge of the inlet would increase to an extent where it would exceed the maximum cross-sectional area of the inlet, causing morphological changes within the channel.

5.2 Hydrodynamic and stratigraphic controls on sediment and micropaleontology distribution

The grain size distribution throughout the inlet system is a function of fluid velocity and interactions with the morphological features that encounter the differentiating flow. To better understand the fluid dynamics, constrain sediment transport, and ground truth, both the hydrodynamic models and geospatial analysis, grain size sample locations were collected across the inlet, from the adjacent shoreline of Bear Island's spit to the West side of Emerald Isle's shoreline.

Grain size distribution in any subaqueous environment is dictated by the fluid velocities and the fluid dynamics, which are controlled mainly by atmospheric conditions (wind direction/ magnitude) and the characteristics of the sediment itself, size, lithologic makeup, and source (Wright et al., 1993; Marshall, 2004; Wren and Leonard, 2005). The sources of the samples collected in this study have only a few provenances: shoreface bypassing, the inner to the middle shelf, and adjacent sub-environments, i.e., subaerial siliciclastic barriers and subaqueous back-barrier estuary/sound (Riggs et al., 1996; Culver et al. in review). Postulates of sediments derived from various provenances are described in (Shmorhun et al., 2022; Culver et al., in review) in an adjacent inlet to the southwest, Bear Inlet. By comparing the divergence in grain size, one can better understand the energy, deposition parameters, and the sediment's probable provenance.

Samples collected for sedimentological data are shown in Figure 36. However, it must be noted that the aerial photos on which the grain size GPS locations are superimposed are not perfect photographic representations of the sub-environments where the samples were collected; they are generalized representations. This is due to not having aerial photographs of the exact dates and times of collection (BI-23) 07/13/23, (BI-ATS) 09/25/23, and (Shipek) 11/06/23 compared to the photos taken from open-source data (i.e., Google Earth) on 09/2024.

Throughout the inlet's sub-environments, sediment characteristics differ due to how the morphology interacts with the fluid velocities controlled by the tides and the atmosphere. Usually, in a main ebb channel, sediments will be gravelly sand, coarse sand, and medium sand, depending on the samples' location in the channel, the inlet's geography, and the current velocities of the flood and ebb flow. The sorting of these sediments can range from poorly sorted to moderately sorted. The sorting of sediments is a function of settling velocity (the time it takes a sediment grain to settle out of suspension). In Bogue Inlet, this is a function of wave action superimposed on the duration of the semi-diurnal tidal currents through the main channel. Furthermore, sorting would be a factor of storm parameters (i.e. duration of storm surge, wind direction, and discharge from inland precipitation). As mentioned in CSE (2005) and suggested in the hydrodynamic modeling of the hurricanes chosen in this study, Bogue Inlet is ebb-dominated. This means that the flood currents last relatively longer than ebb currents, and this asymmetry in duration causes the ebb flow to be more powerful than the flood flow. The tidal asymmetry would cause different sediment characteristics in specific channels. The marginal flood channels should have better-sorted finer sand due to the lower fluid velocities, and the main ebb channel should have more poorly sorted coarser sand due to the higher fluid velocities in these regions Kwoll and Winter (2011). In the main channel, BI-23-04, and BI-23-05, near the back portion of the main channel, the characteristics show moderately well-sorted coarse sand and moderately well-sorted medium sand. Further seaward towards the mouth of the main ebb channel, Shipek-106 and 105 both show a texture of poorly sorted gravelly sand.

Generally, a flood-tidal delta/ FTD ramp would exhibit sediment characteristics of fine grain size, well sorted, and the FTD ramp medium grain size and moderately well sorted (depending on location in that particular sub-environment) (Svenson et al., 2009; Kwoll and Winter, 2011; Wang et al., 2011). An ebb-tidal delta (ETD) would show a finer grain size and be well sorted, but it depends on whether the inlet system is wave-dominated, intermediate, or tidally dominated. Further, long-period waves would have a higher potential to transport a finer-grained material from the inner to middle shelf due to proximity to the fine-grained source. However, the tidal asymmetry of Bogue Inlet would cause relatively better sorting on the distal portion of the ETD than the proximal portion of the ETD and moderately well sorting on the FTD ramp and well sorting on the FTD itself in a low energy normal tidal cycle Kwoll and Winter (2011). In addition, when imposing a cyclonic system on the inlet, sorting and grain size characteristics would change in any subaqueous environment depending on the storm surge and intensity of the event (Marshal, 2004; Wern and Lenard, 2005). The shoals within an inlet system would exhibit characteristics similar to those of the ebb-tidal delta and somewhat of the flood-tidal delta. This is because current and wave action, depending on the sea state, would interact with the morphological features similarly to Kwoll and Winter (2011). For example, large shoaling bodies (longshore and marginal channel sand bars) will constantly interact with wave and current energy. This constant regime of energy will entrain grains with low densities to be transported to regions with lower energy and only periodically transport larger grains into these sub-environments when energetic sea states are created. This process leads to characteristics exhibiting well sorting with grain sizes dependent on the velocities that transport the material to these regions.

The first sediment samples (BI-23-00) were collected on 07/13/23, the second samples (BI-ATS-00) on 09/25/23, and the third sample (Shipek-00) were collected on 11/06/23. Tropical Storm Idalia occurred between the first two sample dates from 08/31/23 at 1:00 am EST to 08/31/23 at 7:00 am EST, passing through the embayment approximately 55 NM south of Bogue Inlet (Figure 54). Figure 35 shows a change in grain size (discussed below) shortly after Tropical Storm Idalia passed. A sediment characteristic change was also reported in Bear Inlet by (Shmorhun et al., 2022; Culver et al., in review) shortly after Hurricane Florence made landfall southwest of Bogue Inlet. Tropical Storm Idalia had peak winds of 51 MPH, which occurred roughly two weeks before samples labeled ATS (after tropical storm) were collected on 9/25/23.

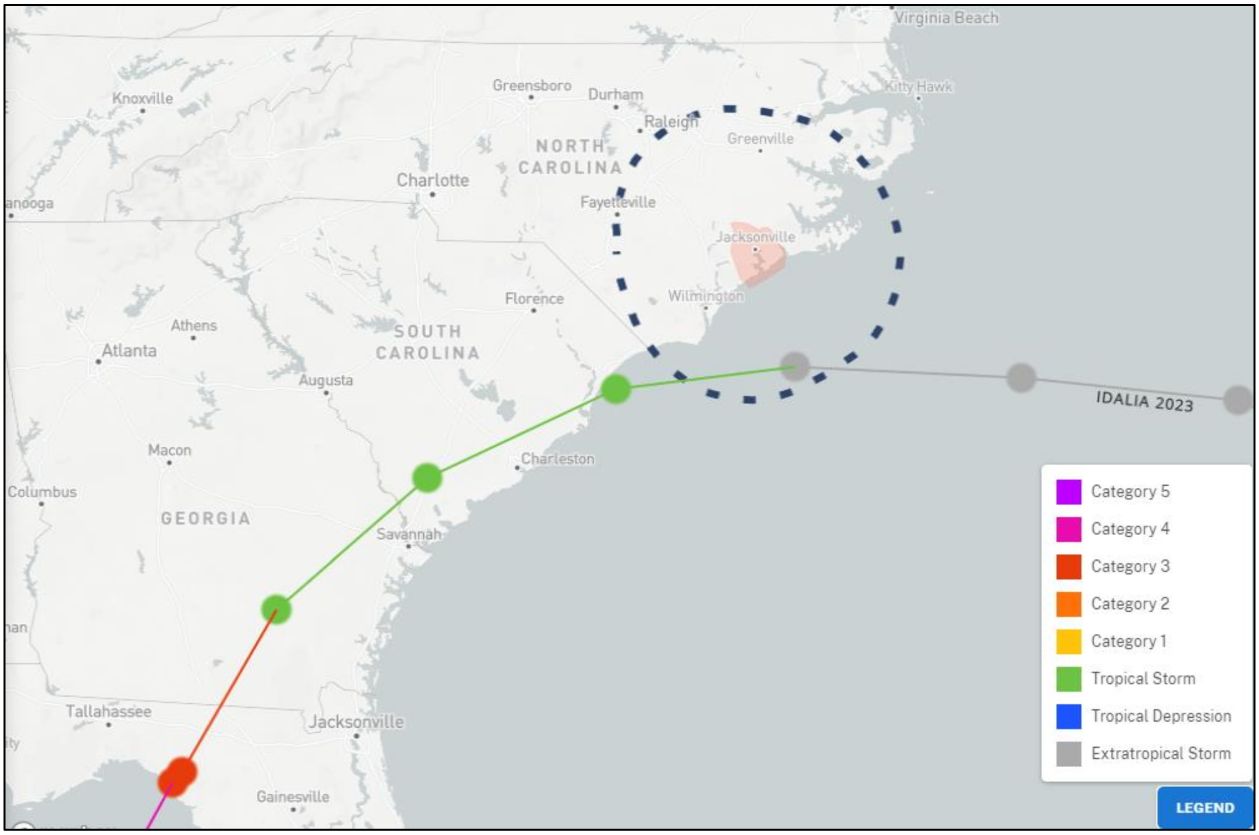

Figure 54. Shows the track of tropical storm Idalia; it passes on the outskirts of Onslow Bay from 08/31/23 06Z to 08/31/23 12Z, where the eye of the storm enters and exists the blue dashed line, which has a circumference of 60 nautical miles with the center as the red area near Jacksonville NC. Source: https://coast.noaa.gov/hurricanes

The two samples in closest proximity to one another that were collected before and after the storm (BI-23-07 roughly 101 meters north of BI-ATS-02) show a slight change in texture (Figure 35 and Appendix E). Both samples are in the large marginal flood channel on the east side of the inlet, and the marginal channel did not change much in morphology after the passing of the tropical storm. BI-23-07 recorded a mean grain size of -0.77Φ to BI-ATS-02's mean grain size of 1.40 Φ (the grain size got finer) (Figure 35 and Table 6). The sorting value of BI-23-07 was 0.91 to BI-ATS-02's value of 0.86, meaning the sorting improved. However, as reported by (Shmorhun et al., 2022; Culver et al., in review), the change in sediment character could represent transport from the adjacent dunes on Emerald Ilse, where there is a well-sorted aeolian source or the source of finer sediment could be from offshore. Most likely due to the track and intensity of the storm, the change in the sediment characteristic in this location was due to the offshore to onshore wind forcing waves on shore from a non-fetch limited wind direction. During this time, the bed shear stress caused by the heightened near-bed wave orbital energy was enough to entrain sediment and cause an across-shore on-shore sediment direction of fine sediment on the inner shelf. An extratropical storm similar in magnitude in Onslow Bay, reported by Marshall (2004) and Wren and Lenard (2005), created the mobilization of fine sand as bedload from wave orbital velocities ranging from 9.9 cm per second to 37 cm per second throughout the event. As the subtidal across-shelf current component increased to more than 15 cm per second, suspended sediments were driven in the onshore direction. Simultaneously, sediment was still being moved to the north as bedload by waves approaching from the south Marshall (2004). This scenario suggests that an event with a similar strength could direct transport under the maximum conditions in the across-shelf onshore direction. Furthermore, the hydrodynamic data show that hurricanes Matthew and Dorian, relatively like the extratropical storm but stronger, created the largest velocities of the flood tide in the marginal flood channel on the eastern side of the inlet, pointing to the potential transport of sediment from the foreshore and nearshore, that had been driven on shore by the longer period swells. It should be noted that this was the only sample to show enough notable change and that it was close enough to make a comparison. Samples BI-23-03 and BI-ATS-03, located approximately near the main inlet channel, were the same. Sample BI-23-04 is just as close but exhibits a coarser grain size; this is most likely a function of the sample depth being collected 1.2 meter deeper than both BI-23-03 and BI-ATS-03 (Table 7) and would encounter more constant higher fluid velocities being closer to the channel thalweg. This could have been a function of the moderate intensity of the storm, or enough time had passed for the regular mechanism of the ebb flow to redistribute any sediment that could have been deposited in the region.

The six most abundant foraminifera species by relative percent in this study, in order of decreasing percent, are *Elphidium excavatum* (47 %), *Quinqueloculina seminula* (10 %), *Quinqueloculina lamarckiana* (9 %), *Ammonia parkinsoniana* (6%), *Eponides repandus* (5 %), and *Cibicides* sp. (1 %) (Table 9). These data are similar to data from (Shmorhun et al., 2022; Culver et al. in review), who analyzed samples from Bear Island and Bear Inlet southwest of Bogue Inlet (Figure 38). In Shmorhun et al. (2022), the six most abundant species in relative percent were *Elphidium excavatum* (35%), *Quinqueloculina lamarckiana* (19%), *Ammonia parkinsoniana* (18%), *Eponides repandus* (5.7%), *Quinqueloculina seminula* (5.2%), and *Ammonia tepida* (2.1%). Furthermore, the spatial distribution of varying species throughout Bogue Inlet is similar to the analysis of Bear Inlet before Bogue Inlet experienced the passing of Tropical Strom Idalia. In this study and Shmorhun et al. (2022), the highest relative percent of *Quinqueloculina lamarckiana* was recorded in the marginal flood channels, the main inlet channel, the flood-tidal delta, and the FTD ramp (Appendix F). Shmorhun et al. (2022) recorded the highest abundance of *Eponides repandus* in inlet channel environments (marginal flood channel, ebb channel), and the highest relative percent of *E. repandus* was found in the large marginal flood channel on the eastern margin of Bogue Inlet, (Appendix F); it also occurs on the marginal linear bar complexes adjacent from the main channel. The highest relative abundance of *Ammonia parkinsoniana* was found in the (barrier combined) environmental supergroup, including foreshore, washover, dune, sand flat, spit, longshore bar, and as well as the ETD Shmorhun et al. (2022). In the current study, the highest relative abundance of *Ammonia parkinsoniana* is closest to the marginal flood channels, the margin of the main inlet channel, and the flood tidal delta ramp (Appendix F). The corroboration in the above recordings could be a function of the proximity to the sub-environments labeled in the super group (barrier combined) (Shmorhun et al., 2022; Culver et al., in review). It would be most probable that in the right conditions (storm track, size, and intensity), as a low-pressure system passed, there would be transport from the inner-shelf, foreshore, and lateral variability within the inlet system (dunes, marginal channels, and shoals). Furthermore, as mentioned in the hydrodynamic and morphology discussion section and the previous sedimentology section, the hydrodynamic model output data shows that the most prominent ebb and flood flows are on the margins of Bogue Inlet, directed through the mouth of the ebb channel on the eastern side of the inlet and in the relatively large flood channel on the western margin from the nearshore (Appendix F). This action would result in transport from sub-environments like the nearshore to where the species' highest relative percentage is recorded in this study.

Fossil foraminifera are found in every sample in this study, but six of the 12 samples are barren of sugary fossil specimens (Figures 58–60). Culver et al. (in review) state that fossil foraminifera, either phosphatic or sugary, are more resistant to breakage and destruction than empty modern foraminiferal tests and have higher residence times in modern sediments than modern foraminiferal tests. This statement is supported by phosphatic specimens, seven of the twelve samples being more abundant than modern species (Tables 8 and 9).

Figure 55. The figure presents the distribution of the total relative percentage of phosphatic and sugary fossil foraminifera. The symbols are the location*s* from both surface sampling methods, the Ponar and the Shipek grab sampler. Samples labeled BI-23 were collected on 07/13/23*,* red boxes; samples labeled BI-ATS were collected on 09/25/23*,* green triangles; and samples labeled Shipek were collected on 11/06/23*,* the white stars.

Figure 56. The figure presents the distribution of the relative percentage of fossil, sugary foraminifera. The symbols are the location*s* from both surface sampling methods, the Ponar and the Shipek grab sampler. Samples labeled BI-23 were collected on 07/13/23*,* red boxes; samples labeled BI-ATS were collected on 09/25/23*,* green triangles; and samples labeled Shipek were collected on 11/06/23*,* the white stars.

Figure 57. The figure presents the distribution of the relative percentage of fossil, phosphatic foraminifera. The symbols are the location*s* from both surface sampling methods, the Ponar and the Shipek grab sampler. Samples labeled BI-23 were collected on 07/13/23*,* red boxes; samples labeled BI-ATS were collected on 09/25/23*,* green triangles; and samples labeled Shipek were collected on 11/06/23*,* the white stars.

Table 8. Foraminifera modern relative percentage

The relative percentage of modern foraminifera picked throughout the sample locations in Bogue Inlet.

	BI-23-01	BI-23-02	BI-23-03	BI-23-04	BI-23-05	BI-23-06	BI-23-07	BI-ATS-04	BI-ATS-05	Shipek-104	Shipek-105	Shipek-106	Total # Count, all Samples
Ammonia parkinsoniana	15 (10.9%)	5 (4.3 %)	17 (13.9%)	1 (1.1%)	1 (1 %)	7 (6.4%)	4 (4.7%)	9 (9.4 %)	11 (12.6 %)	8 (7.8%)	4 (3.6%)		82 (7.2%)
Buccella inusitata	4 (2.9%)		1 (0.8%)	1 (1.1%)		2 (1.8%)		1(1.0%)	1 (1.1 %)				10
Cibicides americanus										1 (0.9%)			1
Cibicides lobatulus	1 (0.7%)						1(1.1%)			1 (0.9%)			3
Cibicides sp.	2 (1.4%)	1 (0.8%)	6 (4.9%)					5 (5.2 %)	1 (1.1 %)	3 (2.9%)	2 (1.8%)		20 (1.7%)
Elphidium excavatum	55 (40.1%)	58 (50.0%)	72 (59.0%)	56 (64.3%)	56 (72.7%)	64 (59.2%)	59 (69.64%)	39 (41.0%)	58 (66.6%)	53 (51.9%)	54 (49.5%)	2 (25 %)	626 (55.2%)
Elphidium galvestonensis		1 (0.8 %)				2 (1.8%)						1 (12.5 %)	4
Elphidium macellum						2 (1.8%)							2
Elphidium mexicanum	1 (0.7%)		1 (0.8%)					2 (2.1%)					4
Elphidium sp.													
Eponides repandus	6 (4.3%)	12 (10.3%)	2 (1.6%)	7 (8.0%)		10 (9.2%)	4 (4.7%)	5 (5.2%)	4 (4.5 %)	10 (9.8%)	12 (11.0%)	1 (12.5 %)	73 (6.6%)
Hanzawaia strattoni		2 (1.7 %)	3 (2.4%)		1 (1.2%)	4 (3.7%)			1 (1.1%)		3 (2.7%)		14
Indeterminate rotaliids			3 (2.4%)	3 (34.0%)			1 (1.1%)	2 (2.1%)					9
Nonionella atlantica	2 (1.4%)								1 (1.1%)				3
Nonionella sp.			1 (0.8%)										1
Planktonic	5 (3.6%)		1 (0.8%)				1 (1.1%)						7
Poroeponides lateralis	1 (0.7%)							1 (1.0%)			3 (2.7%)		5
Quinqueloculina jugosa	4 (2.9%)		1 (0.8%)					2 (2.1%)	1 (1.1%)				8
Quinqueloculina lamarckiana	15 (10.9%)	1 (0.8 %)	5 (4.0%)	6 (6.8%)	10 (12.9%)	12 (11.1%)	9 (10.5%)	22 (23.1%)	6 (6.8%)	13 (12.7%)	22 (20.1%)	2 (25 %)	123 (11.3%)
Quinqueloculina seminula	27 (19.7%)	36 (31.0%)	8 (6.5%)	13 (14.9%)	9 (11.6%)	4 (3.7%)	6 (7.0%)	6 (6.3 %)	3 (3.4 %)	13 (12.7%)	9 (8.2%)	1 (12.5 %)	135 (11.9%)
Rosalina floridana								1 (1.0 %)					1
Uvigerina sp.			1 (0.8%)										1

Total # count per sample	148	129	129	109	100	121	110	114	104	119	118	8	1310
Total # modern	137	116	122	87	77	108	85	95	87	102	109	7	1133
Calculated no. modern foraminifera, 50g sediment	545	510	395	121.5	190	385	270	334.6	198.8	344	367	17.5	
Calculated no. fossil foraminifera, 50g sediment	47.7	57.4	22.8	30.7	57.6	46.4	75.6	66.9	38.8	57.4	30.2	2.5	

Table 9. The relative percentage of the total fossil foraminifera picked throughout the sample locations in Bogue Inlet.

Species name	BI-23-01	BI-23-02	BI-23-03	BI-23-04	BI-23-05	BI-23-06	BI-23-07	BI-ATS-04	BI-ATS-05	Shipek-104	Shipek-105	Shipek-106	Total Count, all Samples	Percent Fossil
Ammonia parkinsoniana phos	1 (0.7%)	1 (0.8%)	1 (0.8%)	1 (0.9%)	1 (1%)	1 (0.8%)	3 (2.7%)	1 (0.9%)	1 (0.9%)	3 (2.5%)				
Buccella anderseni phos						1 (0.8%)								
Buccella inusitata phos										1 (0.8%)				
Buccella inusitata sugary					1 (1%)					1 (0.8%)				
Cibicides americanus phos									1 (0.9%)					
Cibicides sp. sugary								1(0.9%)						
Cibicides sp. phos	1 (0.7%)									1(0.8%)				
Elphidium excavatum phos	7 (4.7%)	9 (6.9%)	4 (3.1%)	13 (11.92%)	16 (16%)	5 (4.1%)	19 (17.2%)	10 (8.8%)	15 (14.4%)	8 (6.7%)	7 (5.9 %)	1 (12.5%)		
Elphidium excavatum sugary		1 (0.8%)			1 (1%)		1 (0.9%)							
Elphidium galvestonensis phos								1(0.9%)						
Elphidium macellum sugary						1 (0.8%)								
Elphidium sp. sugary		2 (1.6%)												
Eponides repandus sugary					1 (1%)									
Hanzawaia strattoni phos	1 (0.7%)		1 (0.8%)		1 (1%)			3 (2.6%)		3 (2.5%)	1 (0.8 %)			
Hanzawaia strattoni sugary								2 (1.8%)						
Indeterminate rotaliids phos			1 (0.8%)	1 (0.9%)										
Planulina sp. phos											1 (0.8 %)			
Quinqueloculina lamarckiana phos				3 (2.8%)	2 (2%)	3 (2.5%)	2 (1.8%)							
Quinqueloculina seminula phos	1 (0.7%)			4 (3.7%)		2 (1.7%)		1 (0.9%)						

Total # count per sample	148	129	129	109	100	121	110	114	104	119	118	8	1310	
Total # modern	137	116	122	87	77	108	85	95	87	102	109	7	1133	
Total # fossil	11 (7.4%)	13 (10.1%)	7 (5.4%)	22 (20.2%)	23 (23%)	13 (10.7%)	25 (22.7%)	19 (16.7%)	17 (16.3%)	17 (14.3%)	9 (7.6 %)	1 (12.5%)	177 (13.5%)	13.50%
Total # fossil phosphatic	11 (7.4%)	10 (7.8%)	7 (5.4%)	22 (20.2%)	20 (20%)	12 (9.9%)	24 (21.8%)	16 (14%)	17 (16.3%)	16 (13.4%)	9 (7.6 %)	1 (12.5%)	165 (12.6%)	12.60%
Total # fossil sugary	0	3 (2.3%)	0	0	3 (3%)	1 (0.8%)	1 (0.9%)	3 (2.6%)	0	1 (0.8%)	0	0	12 (0.9 %)	0.90%
Calculated no. modern foraminifera, 50g sediment	545	510	395	121.5	190	385	270	334.6	198.9	344	367	17.5		
Calculated no. fossil foraminifera, 50g sediment	47.7	57.4	22.8	30.7	57.6	46.4	75.6	66.9	38.8	57.4	30.2	2.5		

No true patterns were observed in samples labeled ATS (after the tropical storm). The total number of phosphatic specimens picked in samples ATS-04 and ATS-05 decreased (Tables 8 and 9). However, in total relative percentage compared to samples collected before the storm, the relative percents were similar, only varying by one or two specimens (Tables 8 and 9). This could be due to the samples being located near the FTD ramp, closest to the flood tidal delta, or due to the very few numbers of samples taken in this study compared to (Shmorhun et al., 2022; Culver et al. in review).

The highest total relative percent of fossil specimens correspond to the samples with moderate to moderately well sorting and coarse to medium sand. The lowest relative percentages are found in the samples with very well sorting and fine sand. Samples BI-23-04, 05, and 07 show the highest total relative percentage in decreasing percentage, 05 (23%), 07 (22.7%), and 04 (20.2%). BI-ATS-04 and 05 have intermediate relative percentages at BI-ATS-04 (16.7%) and BI-ATS-05 (16.3%). BI-23-03 has the lowest relative percentage at (5.2%). The distribution of the total relative percent of fossil specimens is a function of the fluid velocities in the time and location of deposition controlled mostly by the interaction with the morphology of the inlet. For example, sample BI-23-05 is located approximately in the back portion of the main channel. In this location, there would be large fluxes in energy as the tidal cycle went through the flood and ebb flows. There would be high enough velocities in scenarios when the inlet encountered heightened sea states for the fossil specimen to be transported by wave and current interaction to the middle and back of the inlet. As the currents transporting the specimens interacted with the inlet morphology (channel banks, inlet shoals, linear channel bars), the velocity would slow quickly enough for the deposition of the specimens. Furthermore, the highest relative percentage of fossil phosphatic specimens are located in samples BI-23-04, BI-23-05, and BI-23-07. From 04 to 07, these sample locations are near the back portion, in the (main channel), in the middle of the inlet (main channel), and in the large eastern marginal flood channel where the likely highest fluid velocities and current confluences occur. This is why higher relative percentages are found in samples with moderate sorting. Because sorting is a function of the time it takes for a sediment grain to be deposited and how frequently the changing energy regime occurs.

Other factors to consider would be the changing wind directions and tidal current reversal/interactions. In specific parts of the inlet (i.e., marginal flood channel), differing current velocities and vectors could create eddies where velocities are slow enough for deposition, as in the region where the hydrodynamic data show a confluence of currents. Depending on the confluence angle, the differing velocities of the currents create a shear layer where greater velocities are separated from a zone called the separation zone, where velocities are slower Shaheed et al. (2021). In these regions of the inlet, deposition could occur, and the hydrodynamic data shows a region where the confluence of flow occurs, which is in the marginal flood channel on the eastern side of the inlet where the second highest relative percentage of specimens are recorded and shows moderately well sorting of coarse sand, BI-23-07. Additionally, as mentioned above, the lowest relative percents were recorded in a sample that was very well sorted and exhibited fine sand, BI-23-03. This sample is located approximately on what can be interpreted as a linear channel bar or the bank of the main channel in the inner portion of the inlet. This region encounters constant wave bores as they break and slow after interacting with portions of the ebb shield seaward, where velocities would be slow enough in low energy conditions to only transport fine-grained sediment to be deposited. However, in scenarios of higher energy like storm surge most of this material would be transported back into the back-barrier portion of the inlet, also possibly contributing to the low relative percentage values.

Comparing the data to other foraminiferal studies at other geographic locations along North Carolina's barrier islands and stretching up to the southern Delmarva Peninsula, Virginia, there are some similarities in the data. As presented in (Schnitker, 1971; Culver et al., 1996, 2006; Collins et al., 1999; Hippentsteel and Martin, 1999; Scott et al., 2003; Smith, 2006), *Elphidium excavatum*, *Elphidium galvestonense*, *Elphidium mexicanum*, *Hanzawaia strattoni*, *Ammonia parkinsoniana*, *Buccella inusitata* and *Eponides repandus* commonly occur on the open shelf. Culver et al. (1996), on the eastern shore of Virginia; Robinson and McBride (2006), in the northern Outer Banks; Moran et al. (2012) Currituck Sound; Smith et al. (2009) Oregon Inlet to Cape Hatteras; Smith et al. (2006) Oregon, Hatteras, and Ocracoke Inlets, all show that the most dominant specimen of all normal marine salinity environments consists of *Elphidium excavatum*. However, there is some variability in species abundance concerning spatial distribution in the context of salinity-related environments. Culver et al. (2006) mention the variability in species abundance in the back-barrier near-shore estuary sands of Pamlico Sound, showing a low assemblage diversity and is a function of salinity. However, the calcareous benthic species *Elphidium excavatum* dominates normal salinity, inlet, shoreface, nearshore, and inner shelf environments north and south of Cape Hatteras (Schnitker, 1971; Vance et al., 2006; Abbene et al., 2006; Shmorhun et al., 2022; Culver et al., in review) (Figure 55). This study's relative percentage of Elphidium excavatum corroborates with the literature above, as the species is the most dominant in Bogue Inlet. Furthermore, species such as *Quinqueloculina semin*ula (10.3%), *Quinqueloculina lamarckiana* (9.3%), *Ammonia parkinsonian* (6.2%), the second-third and fourth most abundant species in this study (Table 8), are also relatively the second, third, and fourth most abundant species of inlet environments (Culver et al., 1996; Robinson and McBride, 2006; Smith et al., 2006; Smith et al., 2009). It should also be noted that not all the studies mentioned above used the same sampling methods as the data presented in this study; most were down-core samples.

Elphidium excavatum, *Elphidium galvestonense*, *Elphidium mexicanum*, *Hanzawaia strattoni*, *Ammonia parkinsoniana*, and *Buccella inusitata* are all species identified in samples from Bogue Inlet. However, *Elphidium galvestonense* (0.3%), *Elphidium mexicanum* (0.3%), *Hanzawaia strattoni* (1.06%), and *Buccella inusitata* (0.76%) are recorded in low relative percentages of total picked (Table 8). Furthermore, the presence of *Eponides repandus* (5.5%) identified from 95 m to 25 m, respectively, on the shelf of Onslow Bay Schnitker (1971), and the presence of seven modern planktonic specimens consisting of (0.53%) of total picked specimens point to onshore transport of shelf sediments from open marine water masses. This would coincide with the general trend of more frequent and stronger storms, as presented in (Table 1) in this geographic region of the Atlantic basin.

5.3 Geophysics and the stratigraphic model

The geophysical data exhibit various levels of agreement with the stratigraphic model outputs developed using the model of Pearson et al. (2022). In the stratigraphic model along profile D to D’ (Figure 32) (orientated west to east), there is some agreement with medium amplitude reflections that gently dip to the west, which could be interpreted as relic sand bars, R1 (refection surface one) located on the western portion swash platform (Figures 31 and 32). As waves break over this portion of the swash platform, entraining fine-grained sand, slower ebb currents could transport fine-grained material and then deposit this material in this orientation to create these reflection surfaces. The second prominent feature is a high amplitude continuous sub-horizontal reflection (R2) (Figure 32), interpreted as an erosional surface in the middle of the inlet channel throat (Figures 31 and 32); it is highly probable to have a high amplitude refection in this region. A change in grain size (coarse-grained channel lag) would create a high amplitude reflection due to more acoustic energy being reflected off a large surface area of the grains deposited in this region possibly from onshore wave-current interaction or lateral transport from other coarse grain regions of the inlet and foreshore.

However, there is a sand envelope that the model predicts and is represented in the acoustic data above all the reflection surfaces, but the depth of this envelope is not well known. It should be noted that complete agreement between the stratigraphic model outputs and the sub-bottom acoustic data is not expected because there is one year, five months, and five days in the time between when the bathymetric data used in the model was collected, summer of 2022, and when the acoustic data was collected, in 2023. Under the eastern portion of R2 (R3), a low amplitude parabolic reflection is observed at approximately 350 m and ends at 500 m. Continuing eastward, the model shows a shoal complex near the terminal delta lobe characterized by basinward (east) dipping foresets associated with the distal ebb-tidal delta. The sub-bottom data show medium amplitude eastward dipping beds interpreted as foresets as predicted in the model. It is realistic to suggest that due to Bogue Inlet being ebb-dominated, the ebb current could propagate over these shoals and deposit coarser material being flushed out of the inlet to create these reflection surfaces.

The stratigraphic model also agreed moderately well with the sub-bottom data in the survey line E'-E. However, there has been substantial change to the seafloor morphology since the model data were acquired. Beginning in the southwest, at E' (Figures 31 and 33), the model shows south-dipping units at the distal edge of the ebb-tidal delta. The sub-bottom data does not pick up these units with any confidence. The first reflection surface, R1, a low-amplitude sub-parallel discontinuous reflection, is faintly picked up in the acoustic data and labeled in the stratigraphic model (Figure 33). As the survey track passes over the inlet channel, a medium amplitude reflection is captured in the acoustic data and interpreted to be another erosional surface, R2, which shows up in both the predictive stratigraphic model and the sub-bottom data (Figure 33). From approximately 750 m to 870 m, a low-amplitude sub-horizontal reflection is picked up in the sub-bottom data. This feature is labeled R3 in the raw acoustic data and the stratigraphic model. It is possible that this reflection could be a marginal flood channel due to its location within the inlet system, and its low amplitude reflection suggests a well-sorted medium grain size that would be present in a marginal flood channel in the foreshore. As the survey line proceeds onto the adjacent (eastern) swash platform, traveling to the NE and changing direction to the east basinward (Figure 31), the stratigraphic model shows a series of possible swash bars dipping basinward. These features are picked up as medium amplitude, eastward, gently dipping clinoforms, faintly present in the sub-bottom data, and can be interpreted as low relief sand bars. The medium to low amplitude reflections here makes interpretations difficult in this location (Figure 33).

Overall, the stratigraphic model agrees moderately well with the acoustic data. The most prominent high-amplitude reflections were captured in both data sets to varying degrees. Suppose the bathymetric data were entirely up to date, and the geophysical survey occurred simultaneously with the bathymetric survey that produced the models. In that case, there may have been better agreement between the model outputs and sub-bottom data. Furthermore, this novel method of possibly interpreting how a region has stratigraphically evolved could be used in similar fluvial settings and possibly aeolian. With the cost-effective way of collecting lidar-based topographic data, this code could be implemented in similar or related geomorphic settings.

6.0 SYNTHESIS

The stratigraphic model and geophysics moderately agree on defining the units that could reflect the inlet's long-term morphological evolution based on the almost two decades of morphologic data analyzed coupled with data from the hydrodynamic models. Compared to the sub-bottom data, the stratigraphic model does not completely constrain the location of units that would form at different times but does suggest different energy regimes. This is most likely a function of the period between the last bathymetric survey and when the sub-bottom data was collected. Over a year of morphologic change makes defining the unit's absolute time and location impossible without data collected simultaneously. However, the hydrodynamic models constrain most mechanisms that govern morphologic and volumetric change. Furthermore, in high and relatively low energy conditions, the hydrodynamic models suggest processes forced by wind directions as currents interact, which could create the bed shear and critical shear stresses that would entrain and transport material. Sedimentological characteristics and microfossil assemblages can be corroborated with the velocity data from the hydrodynamic models. This suggests the best fit where fluid velocities with enough energy exist where specific grain sizes occur. For example, locations of the highest velocities occur where the coarsest grains are found. In specific locations within the inlet, microfossil assemblages occur where the hydrodynamic data suggest the most probable transport pathways, and then deposition would occur.

7.0 CONCLUSION

Overall, geospatial, geophysical, hydrodynamic, sedimentologic and micropaleontological data show that wind-driven reversal of longshore currents, wave energy/direction, and sediment supply (human-induced or natural) are the significant factors in Bogue Inlet's migration and evolution (Wren and Lenoard, 2005; Nienhuis and Ashton, 2016; Seminack and McBride, 2017; Lenstra et al., 2019). Wind forcing significantly influences the reversal of longshore currents, wave-current interaction, and the confluence of currents within the inlet. Specific atmospheric events (hurricanes, extra-tropical storms, frontal boundaries, and extended wind events) can meet the parameters to transport material in the onshore, offshore, and along-shore directions to force morphologic change (Wright et al., 1993; Thieler, 2001; Marshall, 2004; Wren and Lenoard, 2005). Furthermore, geospatial data suggest that Bogue Inlets migration is dictated by the inlet channel's geometry and the migration westward of the flood-tidal delta and the hydraulically dominant back-barrier tidal creek, as the back-barrier region and the whole survey extent gains material as it evolves, filling of the low accommodation space behind the inlet. Additionally, the lateral migration to the northeast and inlet channels' rotation is a function of wave direction, significant wave height, current interactions, and sediment transport, destabilizing the system (Hayes and FitzGerald, 2013; Seminack and McBride, 2017). Additionally, as the inlet's cross-sectional area and tidal prism fluctuate in response to sediment input and significant discharge events, the inlet tries to reach a state of dynamic equilibrium. An equilibrium state is where the tidal prism has enough energy to keep the inlet open, handling any input of sediment into the system and being able to withstand discharge events from storms where the equilibrium cross-sectional area of the channel is larger than the minimum area needed to hold major discharges without creating morphological change of the inlet channel (Jarrett, 1976; Hughes, 2002). Sedimentological and microfossil assemblages suggest transport from the foreshore and inner-shelf in energetic events, which further constrains the parameters needed for morphologic evolution. Furthermore, additional novel analysis methods can support other methodologies to gain a more complex understanding of dynamic systems.

As more frequent and stronger storms interact with this portion of North Carolina's coast, studying the morphodynamics of inlets like Bogue Inlet in the context of interactions with storms using a multi-faceted approach that utilizes foraminiferal, sedimentological, geospatial, geophysical, and hydrodynamic methods, coastal scientists and engineers alike can better understand how our coastlines will evolve in the future. This knowledge can also give better analogs to downcore studies to constrain how coastal environments have evolved in the past. By constraining how our coastlines could change, we can better mitigate and adapt to the changes we observe now and in future generations to protect human assets and biodiversity.

REFERENCES

Abbene, I.J., Culver, S.J., Corbett, D.R., Buzas, M.A., and Tully, L.S., 2006. Distribution of foraminifera in Pamlico Sound, North Carolina, over the past century: Journal of Foraminiferal Research, v. 36, 2006 p. 135–151, http://pubs.geoscienceworld.org/cushmanfoundation/jfr/article-pdf/36/2/135/3024653/135.pdf.

Atkinson, L.P., Singer, J.J., Pietrafesa, L.J., 1980. The volume of summer subsurface intrusions into Onslow Bay, North Carolina. *Deep Sea Research Part A. Oceanographic Research Papers*, vol. 27, no. 6, June 1980, pp. 421–434, https://doi.org/10.1016/0198-0149(80)90053-9.

Ar6 synthesis report: Climate change 2023. IPCC. (n.d.). Retrieved April 3, 2023, from https://www.ipcc.ch/report/sixth-assessment-report-cycle/.

Avila, L.A., Stewart, S.R., Berg, R., Hagen, A.B., Hurricane Dorian. *National Hurricane Center Tropical Cyclone Report.* www.nhc.noaa.gov/data/tcr/AL052019_Dorian.pdf. Accessed 28 May 2024.

Beach Preservation Plan. *Beach Preservation Plan, Carteret County, NC - Official Website*, www.carteretcountync.gov/313/Preservation-Plan. Accessed 29 Oct. 2024.

Bergstrom, E., Silva, J., Martins, C., Horta, P.A., 2019. Seagrass can mitigate negative ocean acidification effects on calcifying algae: Scientific *Reports*, vol. 9, no. 1, 13 Feb. 2019, https://doi.org/10.1038/s41598-018-35670-3.

Burningham, H., and French, J.R., 2007. Morphodynamics and sedimentology of mixed-sediment inlets. *Journal of Coastal Research*, vol. 50, no. sp1, 30 June 2007, https://doi.org/10.2112/jcr-si50-134.1.

Blott, S.J., and Pye, k., 2001. Gradistat: A grain size distribution and statistics package for the analysis of unconsolidated sediments. *Earth Surface Processes and Landforms*, vol. 26, no. 11, 28 Sept. 2001, pp. 1237–1248, https://doi.org/10.1002/esp.261.

Bogue Inlet AIWW Crossing. *Bogue Inlet AIWW Crossing, Carteret County, NC - Official Website*, www.carteretcountync.gov/655/Bogue-Inlet-AIWW-Crossing. Accessed 29 Oct. 2024.

Bogue Inlet Channel Relocation Project. Bogue Inlet Channel Relocation Project, Carteret County, NC - Official Website. (n.d.). Retrieved April 10, 2023. https://www.carteretcountync.gov/659/Phase-III---Bogue-Inlet-2005.

Bogue Inlet. NCDOJ. (n.d.). Retrieved April 10, 2023, from https://ncdoj.gov/opinions/bogue-inlet/.

Bowen, A.J., 1980. Simple models of nearshore sedimentation: beach profiles and longshore bars. In McCann S. (ed.), The Coastline of Canada. Geological Survey of Canada. Paper 80–10, pp. 1–11.

Buzas, M.A., 1969. Foraminiferal species densities and environmental variables in an estuary. *Limnology and Oceanography*, vol. 14, no. 3, May 1969, pp. 411–422, https://doi.org/10.4319/lo.1969.14.3.0411.

Buzas, M.A., Smith, R.K., and Beem, K.A., 1977. Ecology and systematics of foraminifera in two Thalassia habitats, Jamaica, West Indies: Smithsonian Contributions to Paleobiology, no. 31.

Buzas, M.A., Hayek, L.C., Reed, S.A., and Jett, J.A., 2002. Foraminiferal densities over five years in the Indian River Lagoon, Florida: A model of pulsating patches: Journal of Foraminiferal Research, v. 32, p. 68–92.

Castelle, B., and Gerd, M., 2022. Morphodynamics of wave-dominated beaches. *Cambridge Prisms: Coastal Futures*, vol. 1, 23 Aug. 2022, https://doi.org/10.1017/cft.2022.2.

Chakrabarti, S.K., 2005. *Handbook of Offshore Engineering*. Elsevier.

Cleary, W.J., Riggs, S.R., Marcy, D.C., & Snyder, S.W., 1996. The influence of inherited geological framework upon a hardbottom-dominated shoreface on a high-energy shelf: Onslow Bay, North Carolina, USA. Geological Society, London, Special Publications, 117(1), 249–266. https://doi.org/10.1144/gsl.sp.1996.117.01.15.

Cleary, W.J., 1996. Inlet induced shoreline changes: Cape Lookout to Cape Fear, NC, In Cleary, W.J., (Ed.) Carolina Geological Society Field Trip Guidebook, 1996, pp.49–59.

Cleary, W.J., and Marden. T.P., 2004. Second ed., NC, Sea Grant College Program, Wilmington, NC, 2004, pp. 1–53, *Shifting Shorelines: A Pictorial Atlas of North Carolina Inlets*.

Cleary, W.J., 2008. *Overview of Oceanfront Shorelines: Cape Lookout to Sunset Beach, NC*, 8 Aug. 2008.

Coastal Science & Engineering, (CSE), 2005. Flow Observations Bogue Inlet North Carolina, Memorandum Report, Carteret Co., Shore Protection Office, Emerald Isle, NC.

Coco, G., and Murray, A.B., 2007. Patterns in the sand: from forcing templates to self-organization. Geomorphology 91, 271–290.

Collins, E.S., Scott, D.B., and Gayes, P.T., 1999, Hurricane records on the South Carolina coast can be detected in the sediment record? Quaternary International, 56, 15–26.

Crowson, R.A., 1980, Nearshore rock exposures and their relationship to modern shelf sedimentation, Onslow Bay, North Carolina: Un-pub. M.S. Thesis, Dept. of Geology, East Carolina Univ., Greenville, 128 p.

Culver, S.J., and Buzas, M.A., 1981. Recent benthic foraminiferal provinces on the Atlantic continental margin of North America. *The Journal of Foraminiferal Research*, vol. 11, no. 3, 1 July 1981, pp. 217–240, https://doi.org/10.2113/gsjfr.11.3.217.

Culver, S.J., 1993. Foraminifera, in Lipps, J.H., ed., Fossil Prokaryotes and Protists, Boston, Blackwell scientific publication, p. 203–247.

Culver, S.J., Woo, H.J., Oertel, G.F., & Buzas, M.A., 1996. Foraminifera of coastal depositional environments, Virginia, U.S.A.: Distribution and taphonomy. *PALAIOS*, *11*(5), 459. https://doi.org/10.2307/3515213.

Culver, S.J., 1996. Interpreting paleoenvironments with microfossils. The Paleontological Society Papers, pp. 2, 283–293. https://doi.org/10.1017/s108933260000334x.

Culver, S.J., Ames, D.V., Corbett, D.R., Mallinson, D.J., Riggs, S.R., Smith, C.G., & Vance, D.J., 2006. Foraminiferal and sedimentary record of late Holocene barrier island evolution, Pea Island, North Carolina: The role of storm overwash, inlet processes, and anthropogenic modification. Journal of Coastal Research, pp. 224, 836–846. https://doi.org/10.2112/03-0103.1.

Culver, S.J., 2023. Micro-to macro-scale foraminiferal distributions: The contributions of Martin A. Buzas., *Journal of Foraminiferal Research*, vol. 53, no. 3, 1 July 2023, pp. 187–191, https://doi.org/10.2113/gsjfr.53.3.187.

Culver, S.J., Mallinson, D., Allen, C., Brown, C., Shmorhun, N., Buzas, M., (in review) The effects of two hurricanes on foraminiferal assemblages and sediments of a wave-dominated micro tidal barrier-island system, North Carolina, USA. *PALAIOS*.

Davis, R. E., and Robert, D., 1993. Nor'easters. *American Scientist*, vol. 81, no. 5, 1993, pp. 428–39. *JSTOR*, http://www.jstor.org/stable/29775010. Accessed 19 Apr. 2023.

Delft Hydraulics, 2021. Delft3D-FLOW Flexible Mesh, Computational Cores and User Interface, User Manual. Version 0.9.1, Deltares, Delft, The Netherlands.

Folk R.L., 1968. Petrology of Sedimentary Rocks: Austin, HemphiU's 102 p.

Fitzgerald, D.M., 1976. Ebb-tidal delta of Price Inlet, South Carolina: Geomorphology, physical processes, and associated inlet changes. In: Hayes, M.O., and Kana, T.W., (eds.), Terrigenous Clastic Depositional Environments. Columbia, South Carolina: Geology Department, University of South Carolina, Technical Report 11- CRD, pp. II143–II157.

Fitzgerald, D.M., Rosen, P.S., and Van Heteren, S., 1994. New England barriers. In: Davis, R.A., (ed.), Geology of Holocene Barrier Island Systems. New York: Springer-Verlag, pp. 305–394.

FitzGerald, D.M., 1996. Geomorphic Variability and Morphologic and Sedimentologic Controls on Tidal Inlets. *Journal of Coastal Research*, no. Special Issue, 1996, pp. 47–71. *23*.

FitzGerald, D.M., Fenster, M.S., Argow, B.A., & amp; Buynevich, I.V., 2008. Coastal impacts due to sea-level rise. Annual Review of Earth and Planetary Sciences, 36(1), 601–647. https://doi.org/10.1146/annurev.earth.35.031306.140139.

FitzGerald, D., Buynevich, I., & amp; Hein, C., 2011. Morphodynamics and facies architecture of tidal inlets and tidal deltas. Principles of Tidal Sedimentology, 301–333. https://doi.org/10.1007/978-94-007-0123-6_12.

Geodynamics, LLC., 2017. Mean High Water Contour Determination for the Beaches of the Carteret Co., Shore Protection Surveys, report, Shore Protection Office, Emerald Isle, NC.

Hayes, M.O., and FitzGerald, D.M., 2013. Origin, evolution, and classification of tidal inlets. *Journal of Coastal Research*, vol. 69, Sept. 2013, pp. 14–33, https://doi.org/10.2112/si_69_3.

Hawkes, A.D., and Horton, B.P., 2012. Sedimentary record of storm deposits from Hurricane Ike, Galveston and San Luis Islands, Texas: Geomorphology, v. 171-172, p. 180–189.

Hine, A.C., and Stephen W. S., 1985. Coastal lithosome preservation: Evidence from the Shoreface and inner continental shelf off Bogue Banks, North Carolina. *Marine Geology*, vol. 63, no. 1–4, Feb. 1985, pp. 307–330, https://doi.org/10.1016/0025-3227(85)90088-x.

Hippensteel, S.P., and Martin R.E., 1999. Foraminifera as an indicator of overwash deposits, barrier-island sediment supply, and barrier-island evolution: Folly Island, South Carolina: 33 Palaeogeography, Palaeoclimatology, Paleoecology, v. 149, p. 115–125.

Hippensteel, S.P., Eastin, M.D., and Garcia, W.J., 2013. The geological legacy of Hurricane Irene: implications for the fidelity of the paleo-storm record: GSA Today, 23 (12), 4–10.

Hippensteel, S.P. and Garcia, W.J., 2014. Micropaleontological evidence of prehistoric 34 hurricane strikes from southeastern North Carolina: Journal of Coastal Research, v. 30, p. 1157–1172.

Historical hurricane tracks. (n.d.). Retrieved March 11, 2023, from https://coast.noaa.gov/hurricanes/#map=4/32/-80.

Hjulström, F., 1939. Transportation of detritus by moving water: Part 1. Transportation. In P. D. Trask (Ed.), Recent marine sediments. A Symposium: Tulsa, Oklahoma (pp. 5–31). Tulsa, OK: AAPG.

Horton, B.P., Sawai, Y., Hawkes, A.D., and Witter, R.C., 2011. Sedimentology and paleontology of a tsunami deposit accompanying the great Chilean earthquake of February 2010: Marine Micropaleontology, v. 79, p. 132–138.

Hughes, S.A., 2002. Equilibrium Cross Sectional Area at Tidal Inlets. *Journal of Coastal Research*, Vol. 18, no. No. 1, 2002, pp. 160–174. *(Winter, 2002)*.

Hudson, P.F., Kesel, R.H., 2000. Channel migration and meander-bend curvature in the lower Mississippi River prior to major human modification. Geology 28:531–534. https://doi.org/10.1130/0091-7613(2000)28.

Hurricane Matthew. (n.d.). Retrieved March 11, 2023, from https://www.nhc.noaa.gov/archive/2016/al14/al142016.discus.033.shtml.

Allan, J.L., Hodgson, M., Ghoshal, S., Latiolais, M.M., 2012. Geomorphic change detection using historic maps and DEM differencing: The temporal dimension of geospatial analysis. *Geomorphology*, vol. 137, no. 1, Jan. 2012, pp. 181–198, https://doi.org/10.1016/j.geomorph.2010.10.039.

James, M.R., Robson, S., Smith, M.W., 2017. 3-D uncertainty-based topographic change detection with structure-from-motion photogrammetry: Precision maps for ground control and directly georeferenced surveys. Earth Surf. Process. 2017, 42, 1769–1788.

Jarrett, J.T., 1976. Tidal Prism-Inlet Area Relationships. GITI Report 3, US Army Engineer Waterways Experiment Station, Vicksburg, Mississippi.

Kaliraj, S., Chandrasekar, N., & Ramachandran, K.K., 2017. Mapping of coastal landforms and volumetric change analysis in the southwest coast of Kanyakumari, South India, using remote sensing and GIS techniques. The Egyptian Journal of Remote Sensing and Space Science, 20(2), 265–282. https://doi.org/10.1016/j.ejrs.2016.12.006.

Kemp, A.C., Kegel, J.J., Culver, S.J., Barber, D.C., Mallinson D.J., Leorri, E., Bernhardt, C.E., Cahill, N., Riggs, S.R., Woodson, A.l., Mulligan, R.P., Horton B.P., 2017. Extended late holocene relative sea-level histories for North Carolina, USA. *Quaternary Science Reviews*, vol. 160, Mar. 2017, pp. 13–30, https://doi.org/10.1016/j.quascirev.2017.01.012.

Komar, P.D., 2018. Handbook of Coastal Processes and Erosion. CRC Press.

Komar, P.D., 1998. Beach processes and sedimentation. Prentice-Hall.

Komar P.D., 1996. Tidal-Inlet Processes and Morphology Related to the Transport of Sediments. Journal of Coastal Research, Special Issue No. 23, 23–45. Fort Lauderdale (Florida). ISSN 0749-0208.

Kwoll, E., and Winter, C., 2011. Determination of the initial grain size distribution in a tidal inlet by means of numerical modeling. Journal of Coastal Research, SI 64 (Proceedings of the 11th International Coastal Symposium), 1081 – 1085. Szczecin, Poland, ISSN 0749-0208.

Langfelder, J., Stafford, D., and Amein, M., 1968. A Reconnaissance of Coastal Erosion in North Carolina. Raleigh, North Carolina: North Carolina State University, North Carolina Department of Civil Engineering Technical Report, Project ERD-238, 126p.

Lane, S.N., Chandler, J.H., Richards, K.S., 1994. Developments in monitoring and modeling small-scale river-bed topography. Earth Surf. Process. Landforms. 1994, 19, 349–368.

Lenstra, K. J., Ridderinkhof, Wim, & Vegt, M. van der, 2019. Unraveling the mechanisms that cause cyclic channel-shoal dynamics of Ebb-Tidal Deltas: A numerical modeling study. *Journal of Geophysical Research: Earth Surface*, vol. 124, no. 12, Dec. 2019, pp. 2778–2797, https://doi.org/10.1029/2019jf005090.

Lesser, G.R., Roelvink, J.A., van Kester, G.A.T.M., and Stelling, G.S., 2004. Development and validation of a three-dimensional morphological model. *Coastal Engineering*, 51 (8-9), 883-915.

NASA. (2022, February 24). *NASA Sea Level Change Portal*. NASA. Retrieved April 20, 2023, from https://sealevel.nasa.gov/understanding-sea-level/global-sea-level/overview.

Mallinson, D.J., Culver, S.J., Riggs, S.R., Walsh, J.P., Ames, D., Smith, C.W., 2008. Past, present and future inlets of the Outer Banks Barrier Islands, North Carolina: A White Paper. East Carolina University.

Mallinson, D.J., Culver, S.J., Leorri, E., Mitra, S., Mulligan, R., & Riggs, S., 2018. Barrier Island and estuary co-evolution in response to Holocene climate and sea-level change: Pamlico sound and the Outer Banks Barrier Islands, North Carolina, USA. Barrier Dynamics and Response to Changing Climate, pp. 91–120. https://doi.org/10.1007/978-3-319-68086-6_3.

Manchia, C.M., and Mulligan, R.P., 2022. Hurricane wind-driven surface waves on a narrow continental shelf and exposed coast. Continental Shelf Research, 237, p.104681.

Manchia, C.M., Mulligan, R.P., Mallinson, D.J., Culver, S.J., 2023. Coastal response to the landfall of a hurricane on a series of inlets and narrow back-barrier waterways. *Estuaries and Coasts*, vol. 46, no. 7, 25 July 2023, pp. 1690–1708, https://doi.org/10.1007/s12237-023-01242-6.

Marshall, J.A., Event Driven Sediment Mobility on the Inner Continental Shelf of Onslow Bay, NC. *University of North Carolina at Wilmington*, 2004.

Masters, J., 2022, November 16. Why are there so many Atlantic-named storms? Five possible explanations. Yale climate connections. Yale Climate Connections. Retrieved March 11, 2023, from https://yaleclimateconnections.org/2021/05/why-are-there-so-many-atlantic-named-storms-five-possible-explanations/.

Mcbride, R.A., and Robinson, M.M., 2003. Geomorphic evolution and geology of Old Currituck Inlet and its flood tidal delta, Virginia/North Carolina (Part 1). Reston VA: American Society of Civil Engineers. Coastal Sediments '03, 14 pp.

McNinch, J.E., & Wells, J.T., 1999. Sedimentary processes and depositional history of a cape-associated shoal, Cape Lookout, North Carolina. Marine Geology, 158(1-4), 233–252. https://doi.org/10.1016/s0025-3227(98)00169-8.

Miller, K.G., Kominz, M.A., Browning, J.V., Wright, J.D., Mountain, G.S., Katz, M.E., Sugarman, P.J., Cramer, B.S., Christie-Blick, Nicholas, Pekar, S.F., 2005. The Phanerozoic record of global sea-level change. *Science*, vol. 310, no. 5752, 25 Nov. 2005, pp. 1293–1298, https://doi.org/10.1126/science.1116412.

Moffat & Nichol, Geodynamics, LLC., 2022. Bogue Banks Beach & Nearshore Mapping Program, Final Report, Carteret Co., Shore Protection Office, Emerald Isle, NC.

Moran, K.L., Mallinson, D.J., Culver, S.J., Leorri, Eduardo, Mulligan, R.P., 2015. Late Holocene evolution of Currituck Sound, North Carolina, USA: Environmental change driven by sea-level rise, storms, and barrier island morphology. *Journal of Coastal Research*, vol. 31, no. 4, 1 July 2015, p. 827, https://doi.org/10.2112/jcoastres-d-14-00069.1.

Munsterman, D., and Kerstholt, S., 1996. Sodium polytungstate, a new non-toxic alternative to bromoform in heavy liquid separation: Review of Palaeobotany and Palynology, v. 91, p 417–422.

Nienhuis, J.H., and Ashton, A.D., 2016. Mechanics and rates of tidal inlet migration: Modeling and application to natural examples. *Journal of Geophysical Research: Earth Surface*, vol. 121, no. 11, Nov. 2016, pp. 2118–2139, https://doi.org/10.1002/2016jf004035.

Nummedal, D., and Humphries, S.M., 1978. Hydraulics and dynamics of North Inlet, South Carolina, 1975-1976. GITI Report No 16, Coastal Eng Res Cntr, US Army Corps of Engineers, Ft Belvoir, VA, 214 pp.

Oertel, G.F., 1975. Ebb tidal deltas of Georgia estuaries. In: Cronin, L.E. (Ed.), Estuarine Research 2. Academic Press, New York, pp. 267–276.

Oertel, G.F., Weishar, 1988. Process of sediment exchange between tidal inlets, ebb deltas and barrier islands. In: Aubrey, D.G. (Ed.), Hydrodynamics and Sediment Dynamics of Tidal Inlets. Springer-Verlag, New York, pp. 297–318.

Olsen Associates, Inc., 2006. Regional sand transport study: Morehead City Harbor federal navigation project, summary report, Carteret Co., NC, 108 p.

Park, J.Y., & Wells, J.T., 2005. Longshore transport at Cape Lookout, North Carolina: Shoal evolution and the regional sediment budget. Journal of Coastal Research, pp. 211, 1–17. https://doi.org/10.2112/02051.1.

Pearson, S.G., Elias, E.P.L., van Prooijen, B.C., van der Vegt, H., van der Spek, A.J.F., & Wang, Z.B., 2022. A novel approach to mapping Ebb-Tidal Delta Morphodynamics and stratigraphy. Geomorphology, p. 405, 108185. https://doi.org/10.1016/j.geomorph.2022.108185.

Pearson, D.K., 1979. Surface and shallow subsurface sediment regime of the nearshore inner continental shelf, Nags Head and Wilmington areas, North Carolina: Unpublished. M.S. Thesis, Dept. of Geology, East Carolina Univ., Greenville, 120 p.

Peters, S.E., and Loss, D.P., 2012. Storm and fair-weather wave base: A relevant distinction? *Geology*, vol. 40, no. 6, June 2012, pp. 511–514, https://doi.org/10.1130/g32791.1.

Raff, J.L., Shawler, J.L., Ciarletta, D.J., Hein, E.A., Lorenzo-Trueba, J., & Hein, C.J., 2018. Insights into barrier-island stability derived from transgressive/regressive state changes of Parramore Island, Virginia. *Marine Geology*, *403*, 1–19. https://doi.org/10.1016/j.margeo.2018.04.007.

Rasmussen, T.L., Thomsen, E., Moros, M., 2016. North Atlantic warming during Dansgaard-Oeschger events is synchronous with Antarctic warming and out of phase with Greenland Climate: Scientific *Reports*, vol. 6, no. 1, 5 Feb. 2016, https://doi.org/10.1038/srep20535.

Renaud, P.E., Ambrose, W.G., Riggs, S.R., and Syster, D.A., 1996a. multi-level effects of severe storms on an offshore temperate hardbottom system: benthic sediments, macroalgae, and implications for fisheries: Marine Ecology, v. 17, p. 383–398.

Renaud, P.E., Riggs, S.R., Ambrose, W.G., Schmid, K.A., and Snyder, S.W., 1996b. Biological-geological interactions: storm effects on macroalgal communities and implications for fisheries resources: Continental Shelf Research, v. 17, p. 37–56.

Rodi, W., 1984. Numerical methods in aeronautical fluid dynamics. *Applied Mathematical Modelling*, vol. 8, no. 2, Apr. 1984, p. 141, https://doi.org/10.1016/0307-904x(84) 90069–6.

Riggs, S.R., 1979. A geologic profile of the North Carolina coastline continental shelf system, in Langfelder, J., Ocean Outfall Wastewater Disposal Feasibility and Planning: N.C. State Univ. Press, p. 90–113.

Riggs, S.R., Snyder, S.W., Mearns, D.L., and Hine, A.C., 1986. Hard bottoms: Their character and distribution, Onslow Bay, North Carolina continental shelf: University of North Carolina, Sea Grant College Publication UNC-SG-86-25, Raleigh, North Carolina, one plate.

Riggs, S.R., Cleary, W.J., & Snyder, S.W., 1995. Influence of inherited geologic framework on Barrier Shoreface Morphology and Dynamics. Marine Geology, 126(1-4), pp. 213–234. https://doi.org/10.1016/0025-3227(95)00079-e.

Riggs S.R., Stephen W.S., 1996. Hardbottom morphology and relationship to the Geologic Framework: Mid-Atlantic Continental Shelf. *SEPM Journal of Sedimentary Research*, *Vol. 66*. https://doi.org/10.1306/d4268419-2b26-11d7-8648000102c1865d.

Riggs, S.R., Cleary, W.J., Snyder, S.W., 1996. Morphology and Dynamics of Barrier and Headland Shorefaces in Onslow Bay, North Carolina. *Environmental Coastal Geology: Cape Lookout to Cape Fear, NC*, 10 Nov. 1996.

Riggs, S.R., Ambrose, W.G., Cook, J.W., Snyder, S.W., Snyder, S.W., 1998. Sediment production on sediment-starved continental margins; the interrelationship between hardbottoms, sedimentological and benthic community processes, and Storm Dynamics. *Journal of Sedimentary Research*, vol. 68, no. 1, 1 Jan. 1998, pp. 155–168, https://doi.org/10.2110/jsr.68.155.

Rich, B., 2017. May 8. *Geodynamics: Mapping beaches and inlets*. Coastal Review. Retrieved April 10, 2023, from https://coastalreview.org/2017/05/geodynamics-mapping-beaches-inlets/.

Robinson, M.M., and Mcbride, R.A., 2006. Benthic foraminifera from a relict flood tidal delta along the Virginia/North Carolina Outer Banks. Micropaleontology, 52: 67-80.

Ruessink, B., 1998. The temporal and spatial variability of infragravity energy in a barred nearshore zone. Continental Shelf Research 18, 585–605. https:// doi.org/10.1016/S0278-4343(97)00055-1.

Ruth, T. and Low, D., 1981. Marine Flora and Fauna of the North-Eastern United States. Protozoa: Sarcodina: Benthic Foraminifera. *The Journal of Foraminiferal Research,* National Oceanic and Atmospheric Administration Technical Report NMFS Circular 439, 1981. 51 pages. D822, User Services Branch, Environmental Sciences Information Center, NOAA, Rockville, MD 20852.

Schnitker, D.F., 1971. Distribution of Foraminifera on the North Carolina continental shelf: University of Illinois. Studies in Geology and Paleontology, v.8.

Scott, D.B., Collins, E.S., Gayes, P.T., & Wright, E., 2003. Records of Prehistoric Hurricanes on the South Carolina Coast Based on Micropaleontological and Sedimentological Evidence, with Comparison to Other Atlantic Coast Records. Geological Society of America Bulletin 115, 1027–1039.

Seafloor mapping. National Centers for Environmental Information (NCEI). (n.d.). Retrieved March 11, 2023, from https://www.ncei.noaa.gov/products/seafloor-mapping.

Seafloor sampling. Seafloor Sampling | National Oceanography Centre. (n.d.). Retrieved April 4, 2023, from https://noc.ac.uk/facilities/national-marine-equipment-pool/scientific-engineering/seafloor-sampling.

Seminack, C.T., and McBride, R.A., 2017. A life-cycle model for wave-dominated tidal inlets along passive margin coasts of North America. *Geomorphology*, vol. 304, Mar. 2018, pp. 141–158, https://doi.org/10.1016/j.geomorph. 2017.12.038.

Shaheed, R., Yan, X., & Mohammadian, A., 2021. Review and comparison of numerical simulations of secondary flow in river confluences. *Water*, vol. 13, no. 14, 11 July 2021, p. 1917, https://doi.org/10.3390/w13141917.

Shmorhun, N.M., Culver, S.J., Mallinson, D.J., Farrell, K.M., Cressman, A., Grove, A., Howie, L., Lynn, A., Sutton, S., Twarog, M., and Riggs, S.R., 2022. Characterizing modern and Holocene barrier island environments with foraminiferal assemblages: an example from a wave-dominated, microtidal barrier island, North Carolina, USA: Palaios, v. 37, p. 443–470.

Sirianni, H., Sirianni, M.J., Mallinson, D.J., Lindquist, N.L., Valdes-Weaver, L.M., Moody, M., Henry, B., Colli, C., Rubino, B., Peñalver, M.M., Henne, C., 2022. Quantifying recent storm-induced change on a small fetch-limited barrier island along North Carolina's Crystal Coast using aerial imagery and LIDAR. Coasts, vol. 2, no. 4, 14 Nov. 2022, pp. 302–322, https://doi.org/10.3390/coasts2040015.

Slatt, R.M., 2013. Nondeltaic, shallow marine deposits and reservoirs. *Developments in Petroleum Science*, 2013, pp. 441–473, https://doi.org/10.1016/b978-0-444-56365-1.00010-9.

Smith, C.W., 2006. Lithologic, geophysical, and paleoenvironmental framework of relict inlet channel-fill and adjacent facies: North Carolina Outer Banks. Masters Thesis, East Carolina University, Greenville, 296 pp.

Smith, C.G., Culver, S.J., Mallinson, D.J., Riggs, S.R., and Corbett, D.R., 2009. Recognizing former flood-tide deltas in the Holocene stratigraphic record from the Outer Banks, North Carolina, USA: Stratigraphy, v. 6, p. 61–78.

Smith, G., and Mocke, G., 2002. Interaction between breaking/broken waves and infragravity-scale phenomena to control sediment suspension transport in the surf zone. Marine Geology 187, 329–345. https://doi.org/10.1016/S0025- 3227(02)00385-7.

Stacy S.R., 2017. Hurricane Matthew. *National Hurricane Center Tropical Cyclone Report Hurricane Matthew*, 7 Apr. 2017, www.nhc.noaa.gov/data/tcr/AL142016_Matthew.pdf.

Stewart, S.R., Berg, Robbie, 2019. Hurricane Florence. *National Hurricane Center Tropical Cyclone Report*, www.nhc.noaa.gov/data/tcr/AL052019_Florence.pdf. Accessed 28 May 2024. 25 September 2019.

Skipp, G.L., & Brownfield, I.K., 1993. Improved density gradient separation techniques using sodium polytungstate and a comparison to the use of other heavy liquids. *Open-File Report*. https://doi.org/10.3133/ofr92386.

Svenson, C., Ernstsen, V.B., Winter, C., and Hebbeln, D., 2009. Tide-driven sediment variations on a large compound dune in the Jade tidal inlet channel, Southeastern North Sea. Journal of Coastal Research, SI 56 (Proceedings of the 10th International Coastal Symposium), 361-365. Lisbon, Portugal, ISSN 0749-0258.

Swift, D.J.P., 1976. Continental shelf sedimentation, in Stanley, D.J., and Swift, D.J.P., eds., Marine Sediment Transport and Environmental Management: New York, Wiley, p. 311–350.

Sylvester, Z., Durkin, P., & Covault, J.A., 2019. High curvatures drive river meandering. *Geology*, vol. 47, no. 3, 6 Feb. 2019, pp. 263–266, https://doi.org/10.1130/g45608.1.

Szczyrba, L., 2023. Nearshore Flow Dynamics over Shore-Oblique Bathymetric Features during Storm Wave Conditions, 14 Nov. 2023, https://doi.org/10.22541/essoar.170000362.26680833/v1.

The IPCC 2007 report. 2007. *Climate Change*, 480–481. https://doi.org/10.1017/cbo9780511803826.013.

Thieler, E.R., 1996. Shoreface processes in Onslow Bay. In W.J. Cleary (editor), Environmental Coastal Geology: Cape Lookout to Cape Fear, NC. Carolina Geological Society, 23–32.

Thieler, E.R., Schwab, W.C., Pilkey, O.H., and Cleary, W.J., 2001. Modern sedimentation on the shoreface and inner shelf at Wrightsville Beach, North Carolina. Journal of Sedimentary Research 71(6), 958-970.

USACE. 2001. Section 111 Report: Morehead City/Pine Knoll Shores, North Carolina. U.S. Army Corps of Engineers, Wilmington District. June 2001.

Valiela, I., Cole, M.L., Mcclelland, J., Hauxwell, J., Cebrian, J., Joye, S.B., 2002. Role of Salt Marshes as Part of Coastal Landscapes. In: Weinstein, M.P., Kreeger, D.A. (eds) Concepts and Controversies in Tidal Marsh Ecology. Springer, Dordrecht. https://doi.org/10.1007/0-306-47534-0_3.

Vance, D.J., Culver, S.J., Corbett, D.R., and Buzas, M.A., 2006. Foraminifera in the Albemarle estuarine system, North Carolina: distribution and recent environmental change. Journal of Foraminiferal Research, 36: 15–33.

Van Gaalen, J.F., Tebbens, S.F., & Barton, C.C., 2016. Longshore sediment transport directions and rates from northern Maine to Tampa Bay, Florida: Literature compilation and interpretation. Journal of Coastal Research, 322, 1277–1301. https://doi.org/10.2112/jcoastres-d-15-00002.1.

Wang, Y., Gao, S., Hebbeln, D., and Winter, C., 2011. Modeling Grain Size Distribution Patterns in the Backbarrier Tidal Basins, East Frisian Wadden Sea (Southern North Sea). Journal of Coastal Research, SI 64 (Proceedings of the 11th International Coastal Symposium). Szczecin, Poland, ISSN 0749-0208.

Water levels - NOAA tides and currents. Tides & Currents. (n.d.). Retrieved March 10, 2023, from https://tidesandcurrents.noaa.gov/waterlevels.html?id=8656483.

Waters, V.J., & Snyder, S.W., 1986. Planktonic foraminiferal biostratigraphy of the Pungo River Formation, southern Onslow Bay, North Carolina continental shelf. *The Journal of Foraminiferal Research*, *16*(1), 9–23. https://doi.org/10.2113/gsjfr.16.1.9.

Welcome to CDIP. Welcome to CDIP! Home. (n.d.). Retrieved March 11, 2023, from https://cdip.ucsd.edu/themes.

Webster, F., 1953. A description of Gulf Stream meanders off Onslow Bay. *Deep Sea Research (1953)*, vol. 8, no. 2, Sept. 1961, pp. 130–143, https://doi.org/10.1016/0146-6313(61)90005-3.

Wren, P.A., Lynn, A. L., 2005. Sediment transport on the mid-continental shelf in Onslow Bay, North Carolina during Hurricane Isabel. *Estuarine, Coastal and Shelf Science*, vol. 63, no. 1–2, Apr. 2005, pp. 43–56, https://doi.org/10.1016/j.ecss.2004.10.018.

Wright, L.D., and Short A.D., 1984. Morphodynamic variability of surf zones and beaches: a synthesis. Marine Geology 56, 93–118.

Wright, L.D., Boon, J.D., Kim, S.C., List J.H., 1991. Modes of cross-shore sediment transport on the shoreface of the Middle Atlantic Bight. Marine Geology, 96, 19–51.

Wright, L.D., 1993. Micromorphodynamics of the inner continental shelf: a Middle Atlantic Bight case study. Journal of Coastal Research (special issue), 15, 93–120.

Wright, L.D., 1995. Micromorphodynamics of inner continental shelves. CRC Press, Boca Raton, 241 pp.

Xu, J.P., Wright, L.D., 1998. Observations of wind-generated currents of Duck, North Carolina. Journal of Coastal Research 14, 610–619.

Zhong, X., and Zhong-Hai Li., 2021. Subduction initiation at Passive Continental Margins: A review based on Numerical Studies. *Solid Earth Sciences*, vol. 6, no. 3, Sept. 2021, pp. 249–267, https://doi.org/10.1016/j.sesci.2021.06.001.

Zulkifli, Z., Clare, M.A., Heijnen, M., Lintern, D., Gwyn, S., Cooper, T., Peter J.C., Matthieu, J.B., Minshull, T.A., Moreno, H.M., Peakall, J., Darby, S., 2024. A threshold in submarine channel curvature explains erosion rate and type. *Earth and Planetary Science Letters*, vol. 646, Nov. 2024, p. 118953, https://doi.org/10.1016/j.epsl.2024.118953.

Appendix A: Dune, beach, and shoreface cross-sectional profile 2005-2022

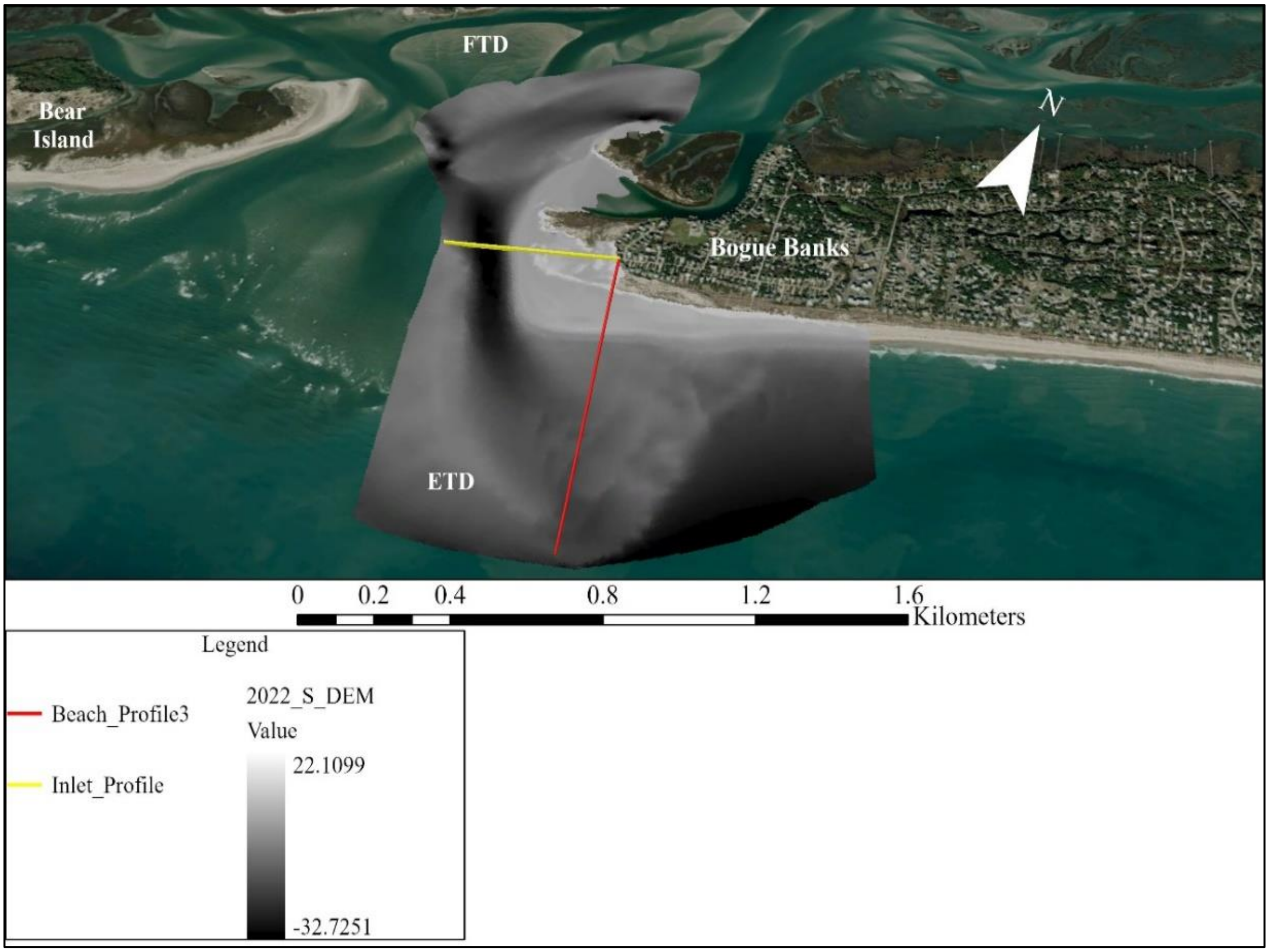

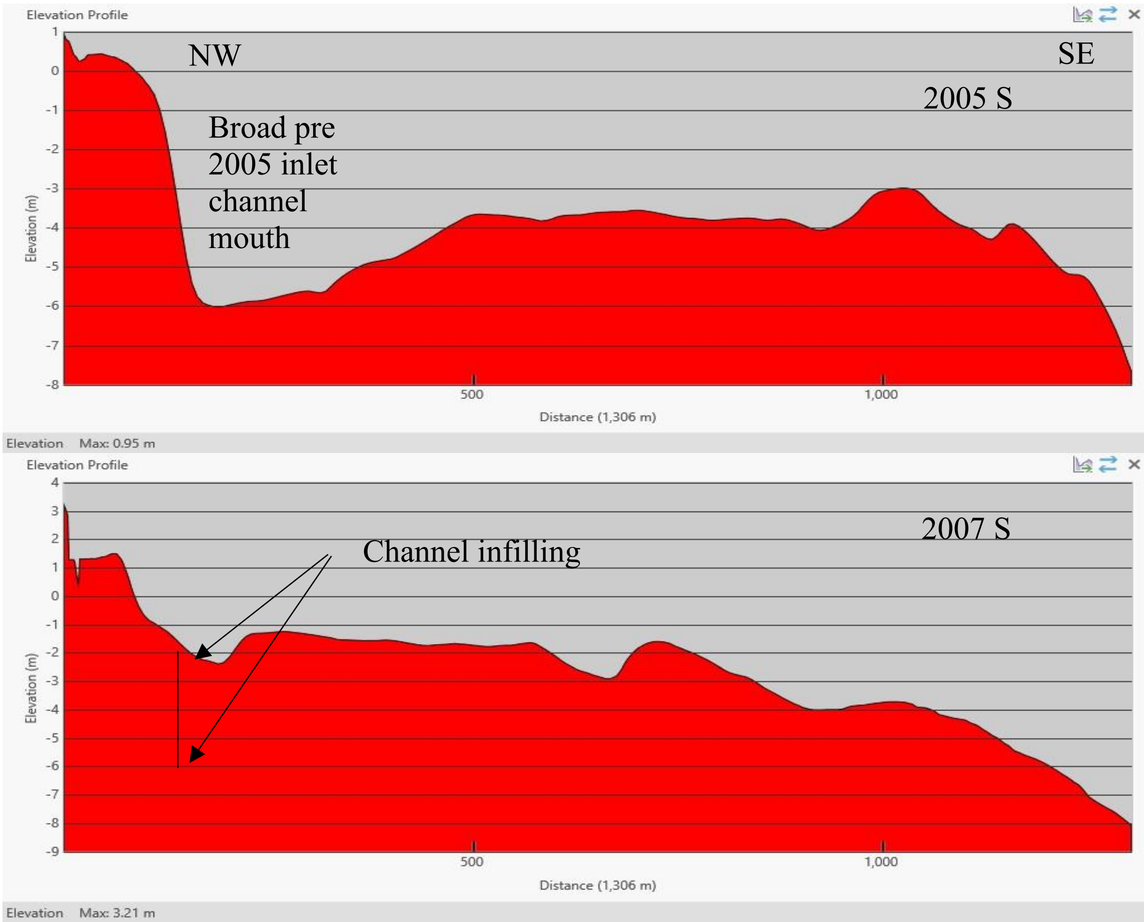
Elevation Profile
NW
SE
2005 S
Broad pre 2005 inlet channel mouth
Elevation (m)
500
1,000
Distance (1,306 m)
Elevation Max: 0.95 m
Elevation Profile
2007 S
Channel infilling
Elevation (m)
500
1,000
Distance (1,306 m)
Elevation Max: 3.21 m

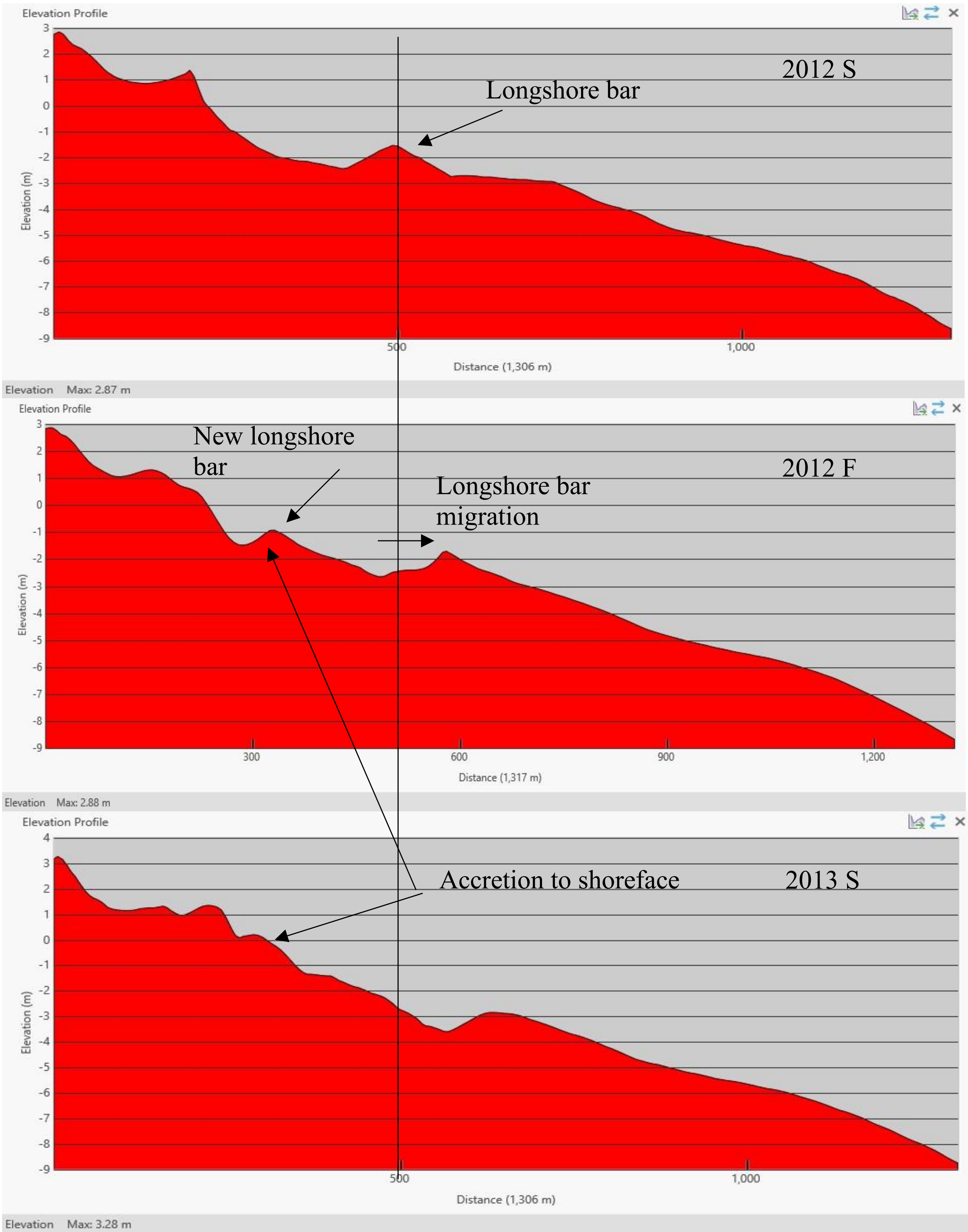

Elevation Profile
2012 S
Longshore bar
Elevation (m)
Distance (1,306 m)
Elevation Max: 2.87 m
Elevation Profile
New longshore bar
2012 F
Longshore bar migration
Distance (1,317 m)
Elevation Max: 2.88 m
Elevation Profile
Accretion to shoreface
2013 S
Distance (1,306 m)
Elevation Max: 3.28 m

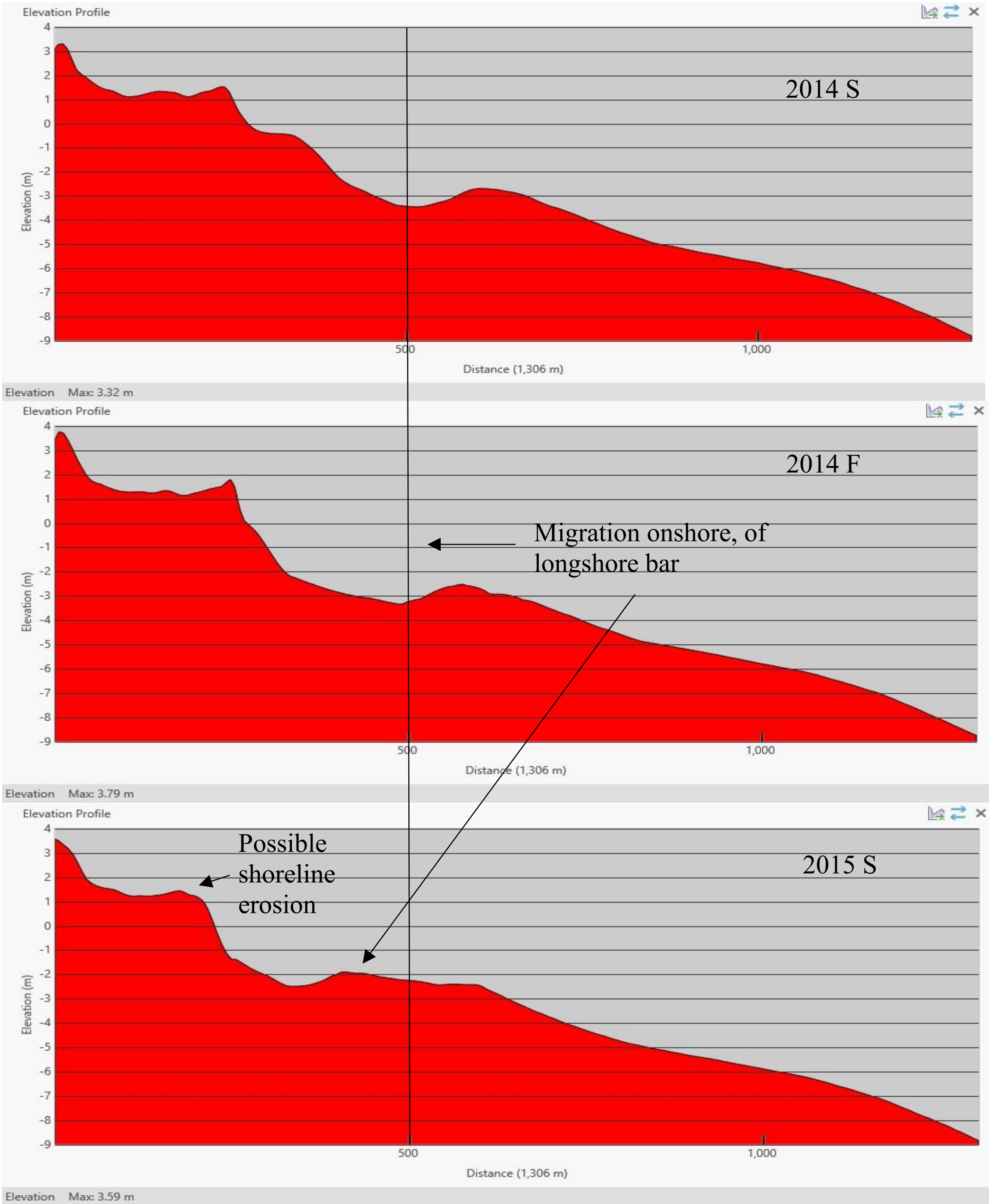

Elevation Profile
2014 S
Distance (1,306 m)
Elevation Max: 3.32 m
Elevation Profile
2014 F
Migration onshore, of longshore bar
Distance (1,306 m)
Elevation Max: 3.79 m
Elevation Profile
Possible shoreline erosion
2015 S
Distance (1,306 m)
Elevation Max: 3.59 m

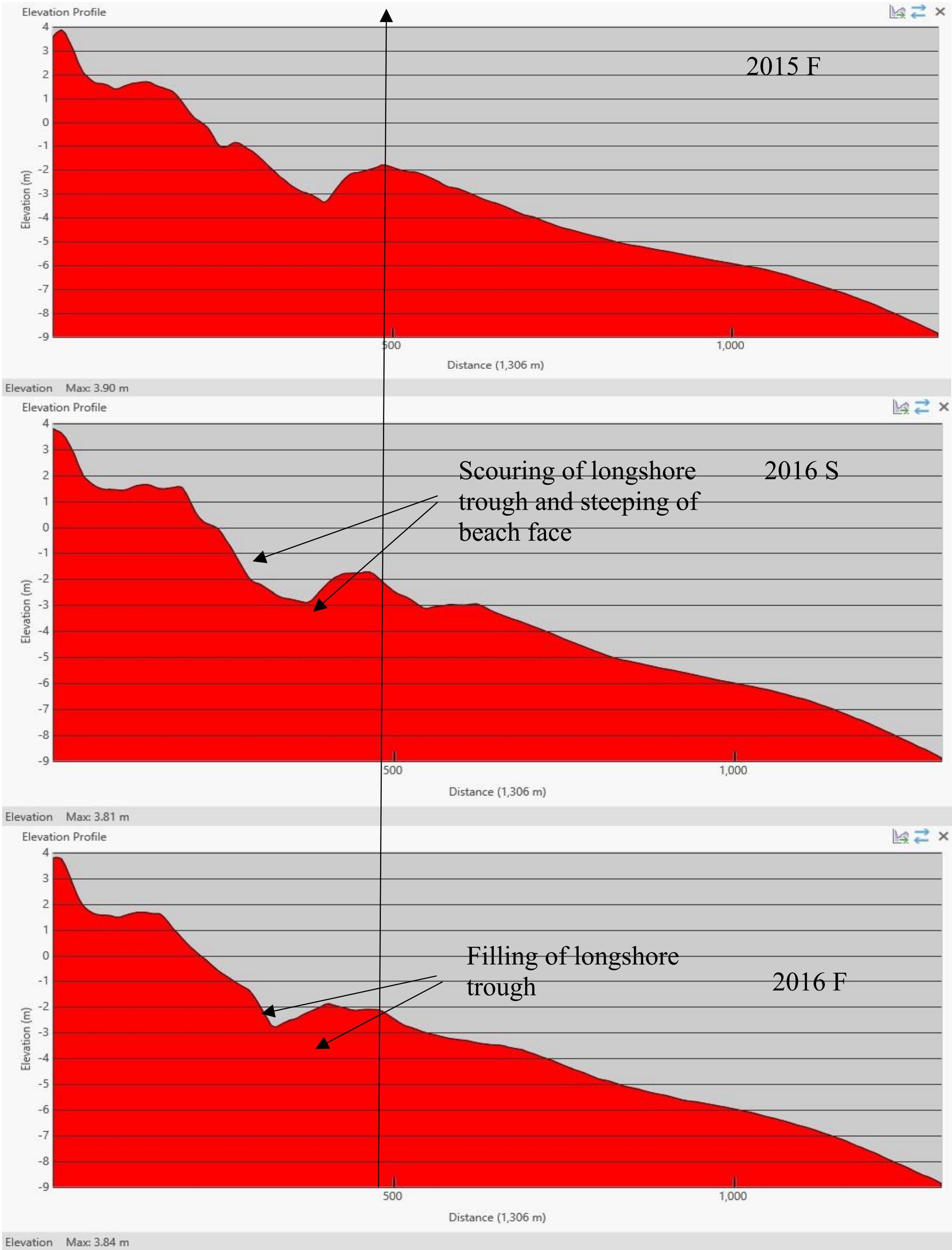

Elevation Profile
2015 F
Elevation (m)
Distance (1,306 m)
500
1,000
Elevation Max: 3.90 m
Elevation Profile
Scouring of longshore trough and steeping of beach face
2016 S
Elevation (m)
Distance (1,306 m)
500
1,000
Elevation Max: 3.81 m
Elevation Profile
Filling of longshore trough
2016 F
Elevation (m)
Distance (1,306 m)
500
1,000
Elevation Max: 3.84 m

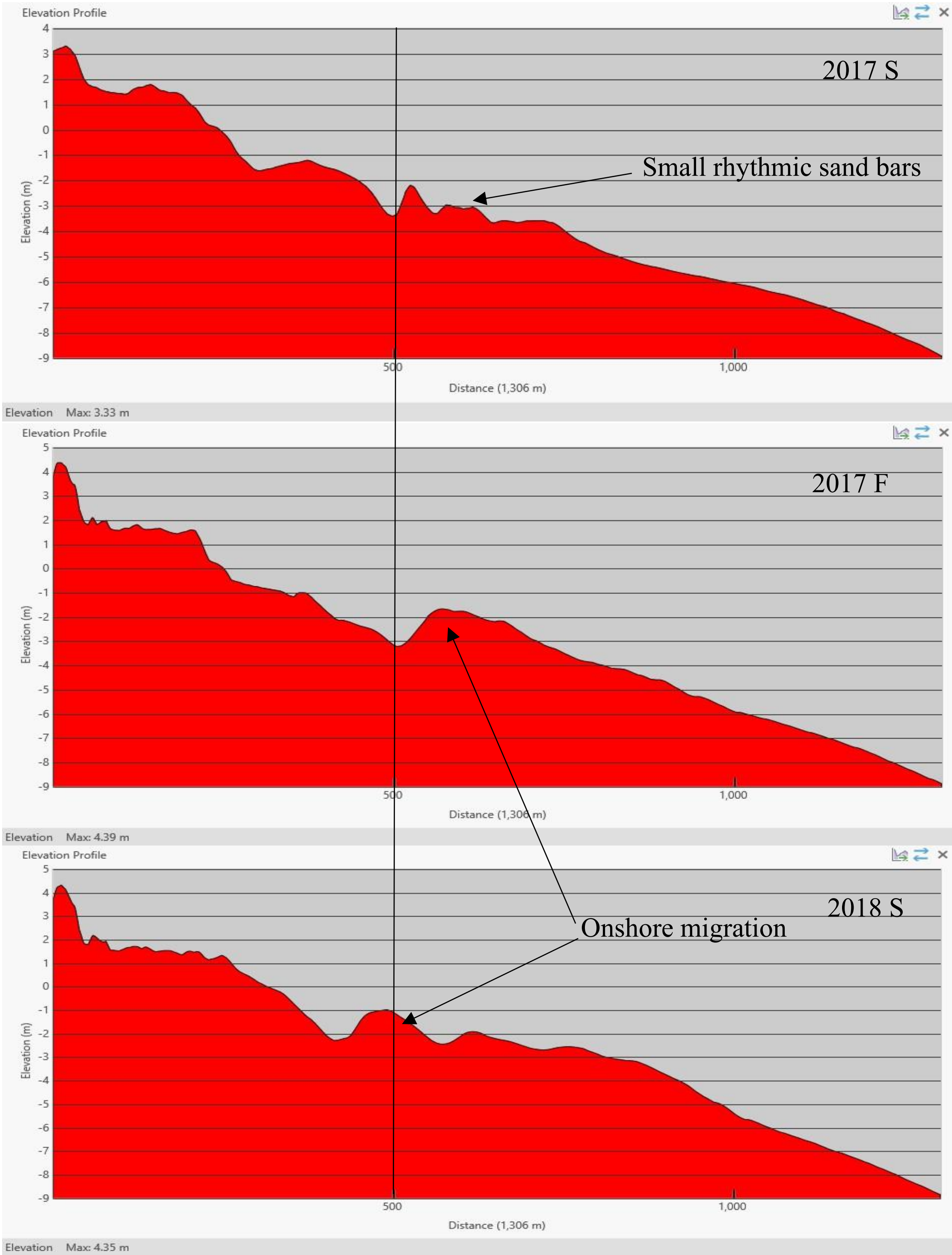
Elevation Profile
2017 S
Small rhythmic sand bars
Elevation (m)
Distance (1,306 m)
Elevation Max: 3.33 m
Elevation Profile
2017 F
Elevation (m)
Distance (1,306 m)
Elevation Max: 4.39 m
Elevation Profile
2018 S
Onshore migration
Elevation (m)
Distance (1,306 m)
Elevation Max: 4.35 m

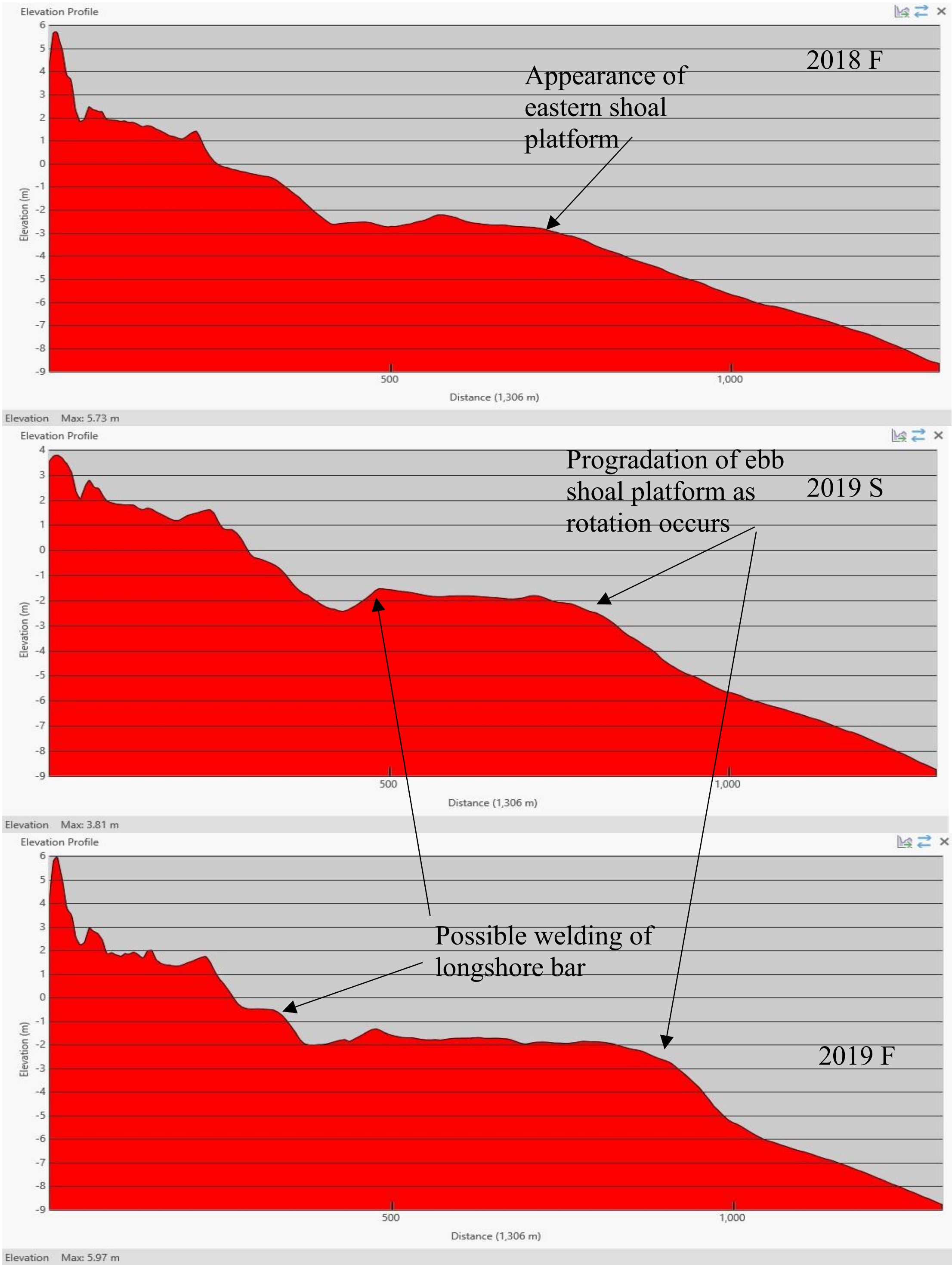
Elevation Profile
2018 F
Appearance of eastern shoal platform
Elevation (m)
Distance (1,306 m)
500
1,000
Elevation Max: 5.73 m
Elevation Profile
Progradation of ebb shoal platform as rotation occurs
2019 S
Elevation (m)
Distance (1,306 m)
500
1,000
Elevation Max: 3.81 m
Elevation Profile
Possible welding of longshore bar
2019 F
Elevation (m)
Distance (1,306 m)
500
1,000
Elevation Max: 5.97 m

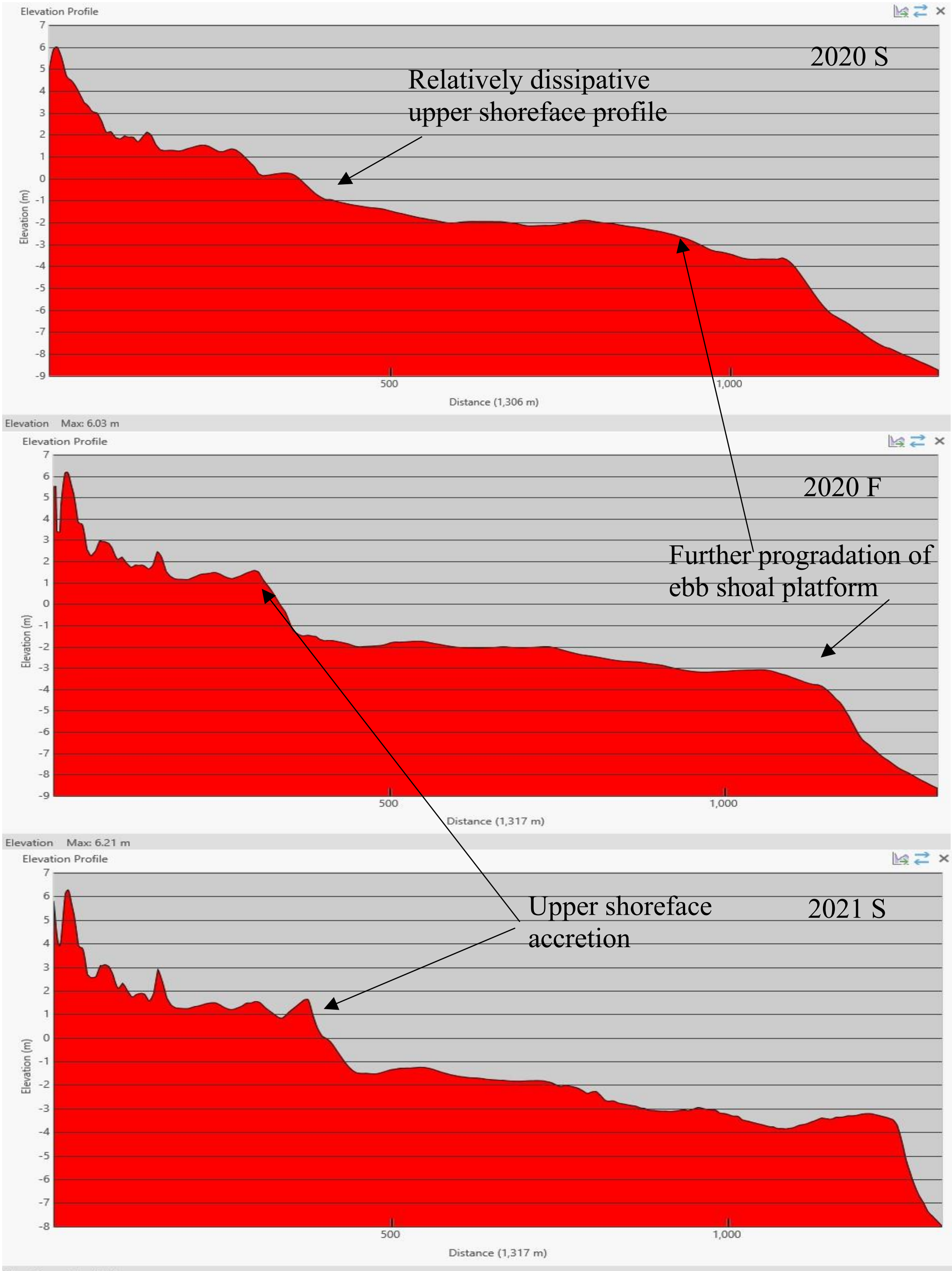

Elevation Profile
2020 S
Relatively dissipative upper shoreface profile
Elevation (m)
Distance (1,306 m)
Elevation Max: 6.03 m
Elevation Profile
2020 F
Further progradation of ebb shoal platform
Elevation (m)
Distance (1,317 m)
Elevation Max: 6.21 m
Elevation Profile
Upper shoreface accretion
2021 S
Elevation (m)
Distance (1,317 m)
Elevation Max: 6.29 m

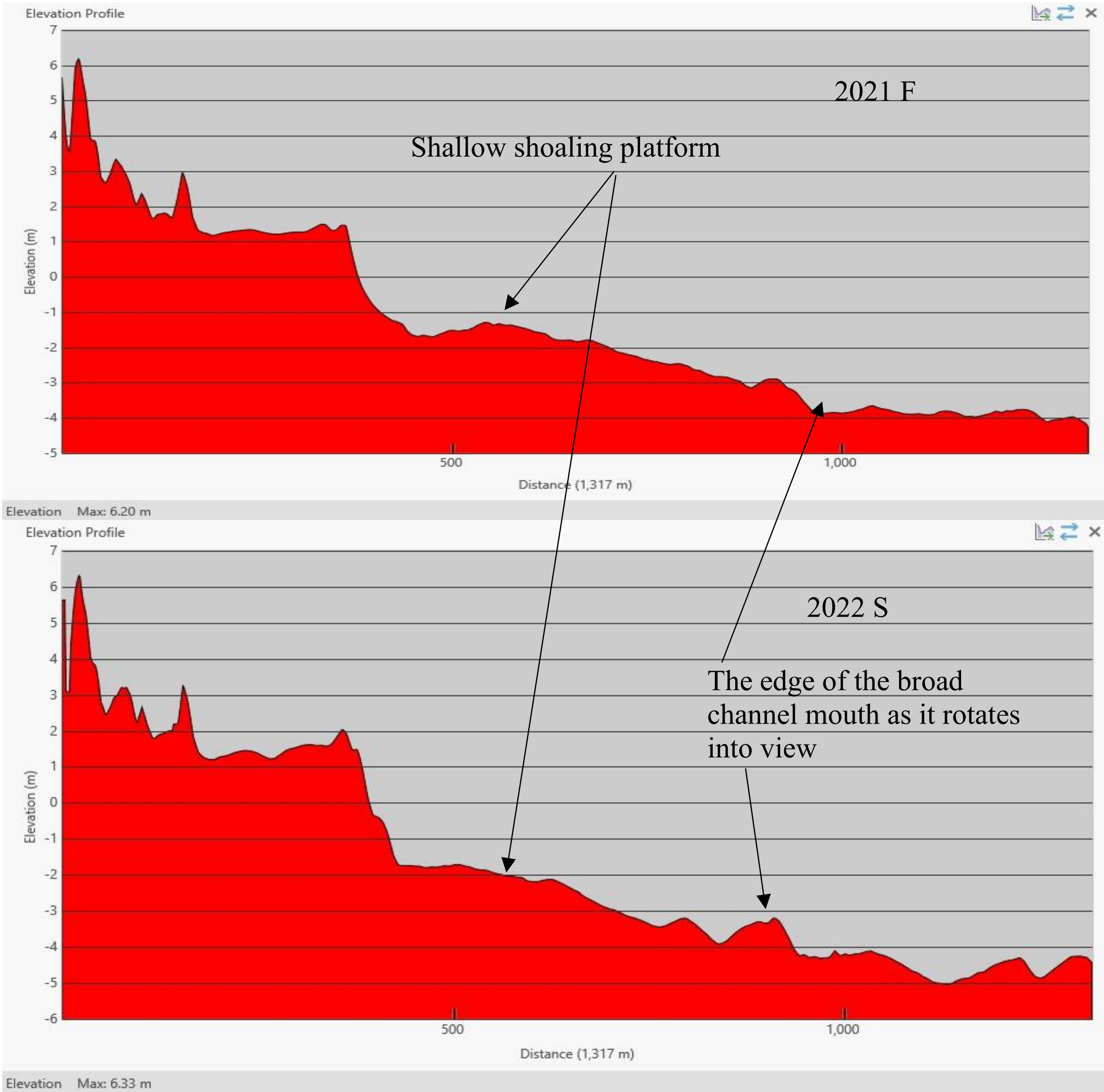
Elevation Profile
2021 F
Shallow shoaling platform
Elevation (m)
Distance (1,317 m)
Elevation Max: 6.20 m
Elevation Profile
2022 S
The edge of the broad channel mouth as it rotates into view
Elevation (m)
Distance (1,317 m)
Elevation Max: 6.33 m

Appendix B: Cross-sectional profiles of bogue inlet, main channel, 2005-202

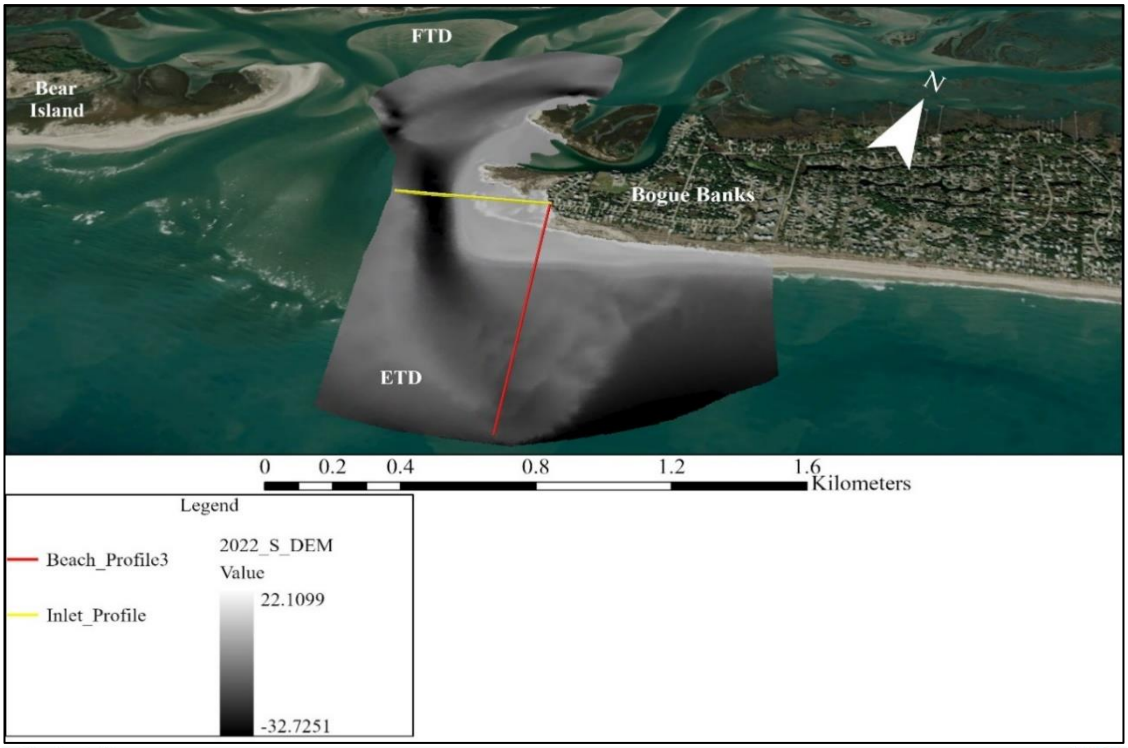

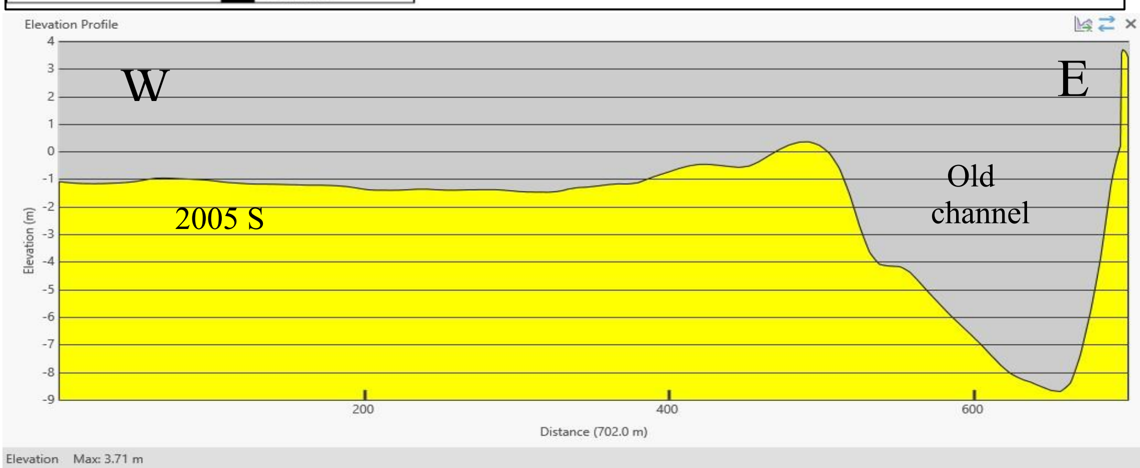

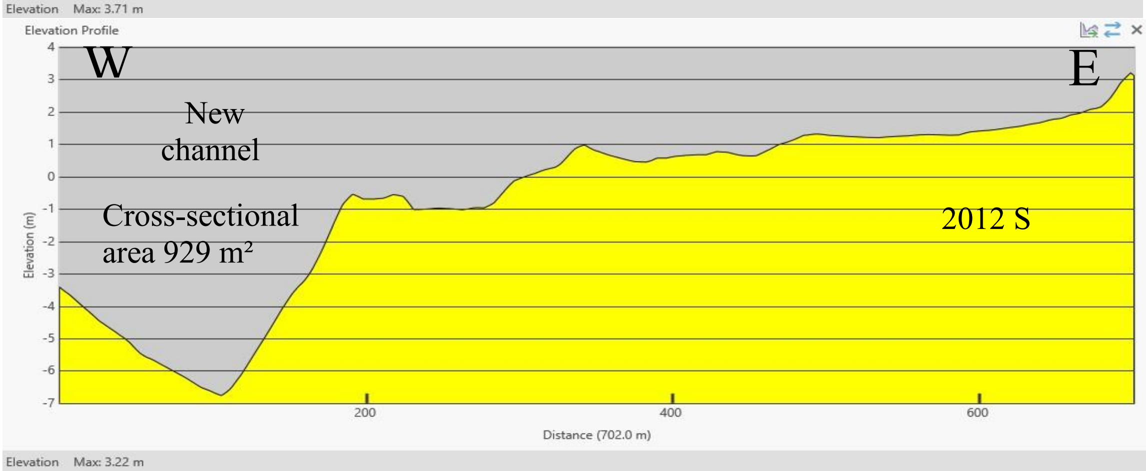

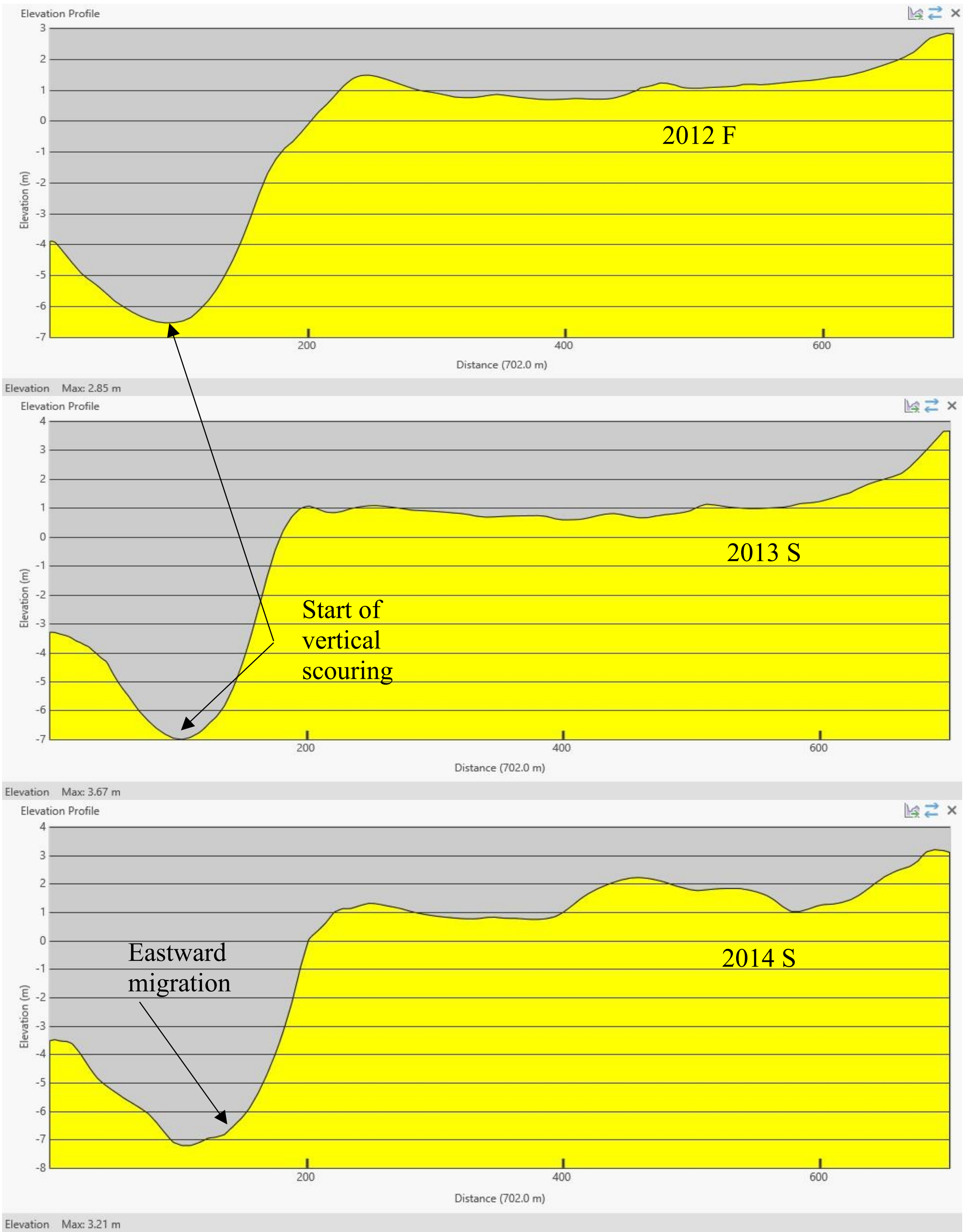
Elevation Profile
Elevation (m)
2012 F
Distance (702.0 m)
Elevation Max: 2.85 m
Elevation Profile
Elevation (m)
2013 S
Start of vertical scouring
Distance (702.0 m)
Elevation Max: 3.67 m
Elevation Profile
Elevation (m)
Eastward migration
2014 S
Distance (702.0 m)
Elevation Max: 3.21 m

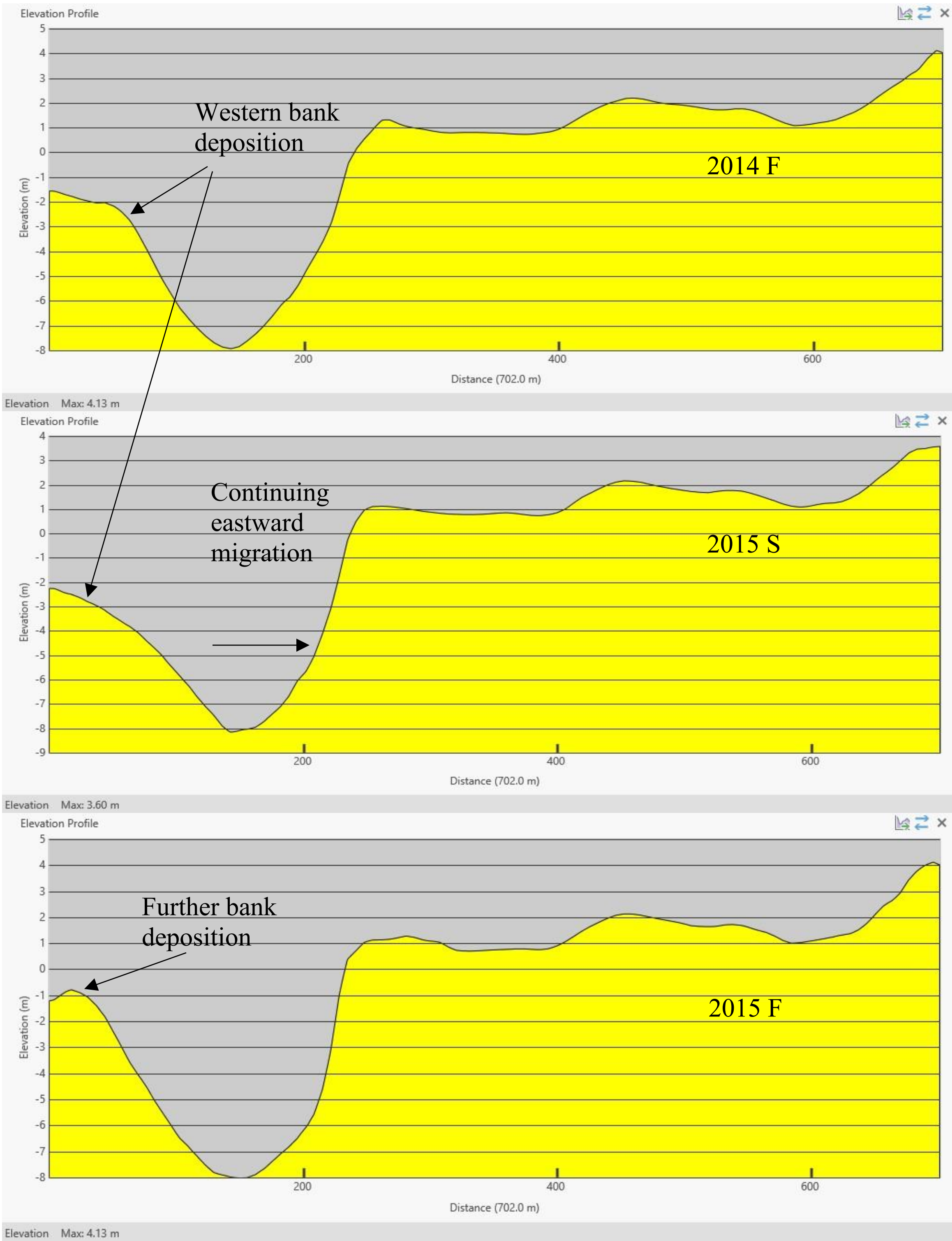
Elevation Profile
Elevation (m)
Distance (702.0 m)
Western bank deposition
2014 F
Elevation Max: 4.13 m
Elevation Profile
Continuing eastward migration
2015 S
Elevation Max: 3.60 m
Elevation Profile
Further bank deposition
2015 F
Elevation Max: 4.13 m

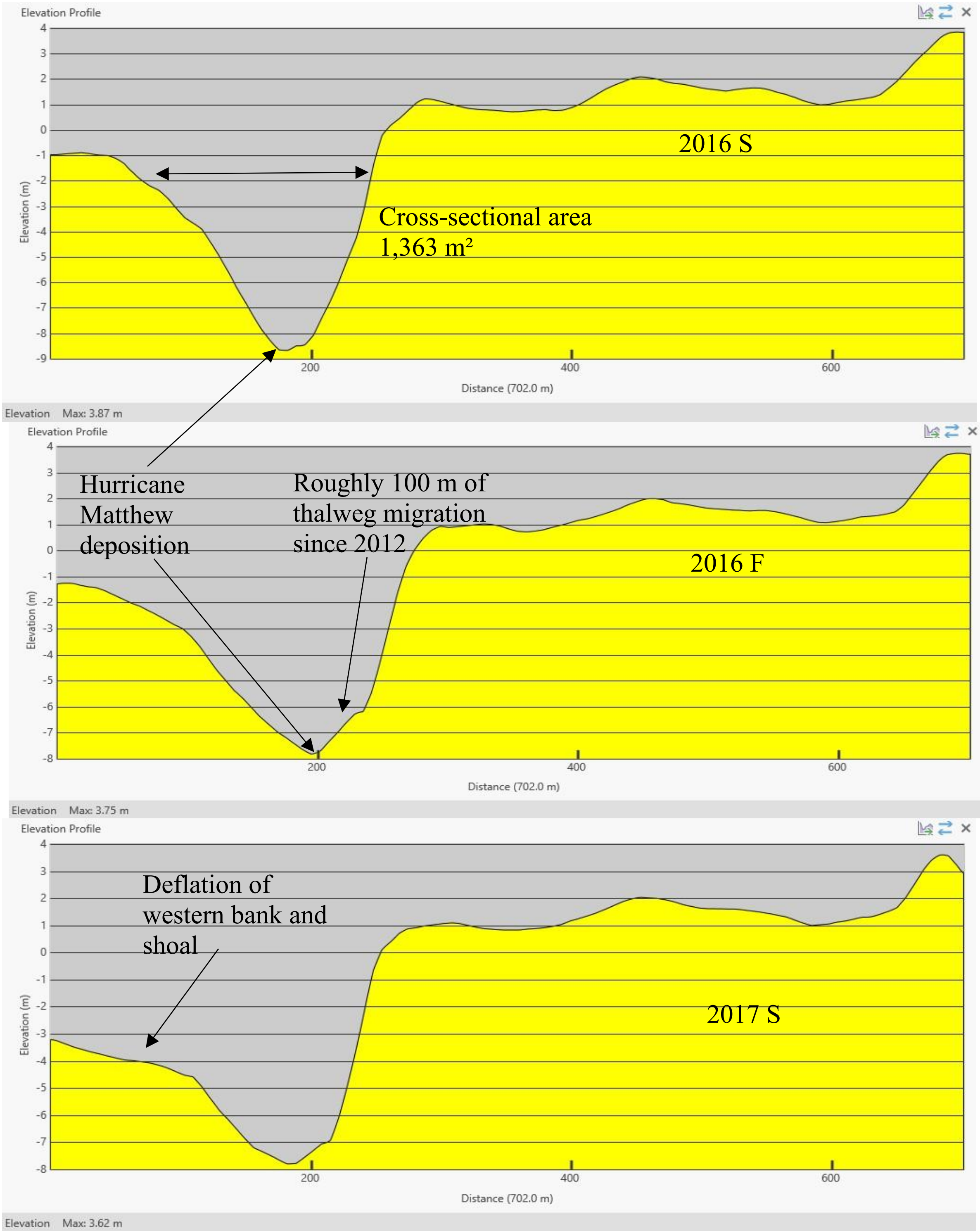

Elevation Profile
2016 S
Cross-sectional area
1,363 m²
Elevation (m)
Distance (702.0 m)
Elevation Max: 3.87 m
Elevation Profile
Hurricane
Matthew
deposition
Roughly 100 m of
thalweg migration
since 2012
2016 F
Elevation (m)
Distance (702.0 m)
Elevation Max: 3.75 m
Elevation Profile
Deflation of
western bank and
shoal
2017 S
Elevation (m)
Distance (702.0 m)
Elevation Max: 3.62 m

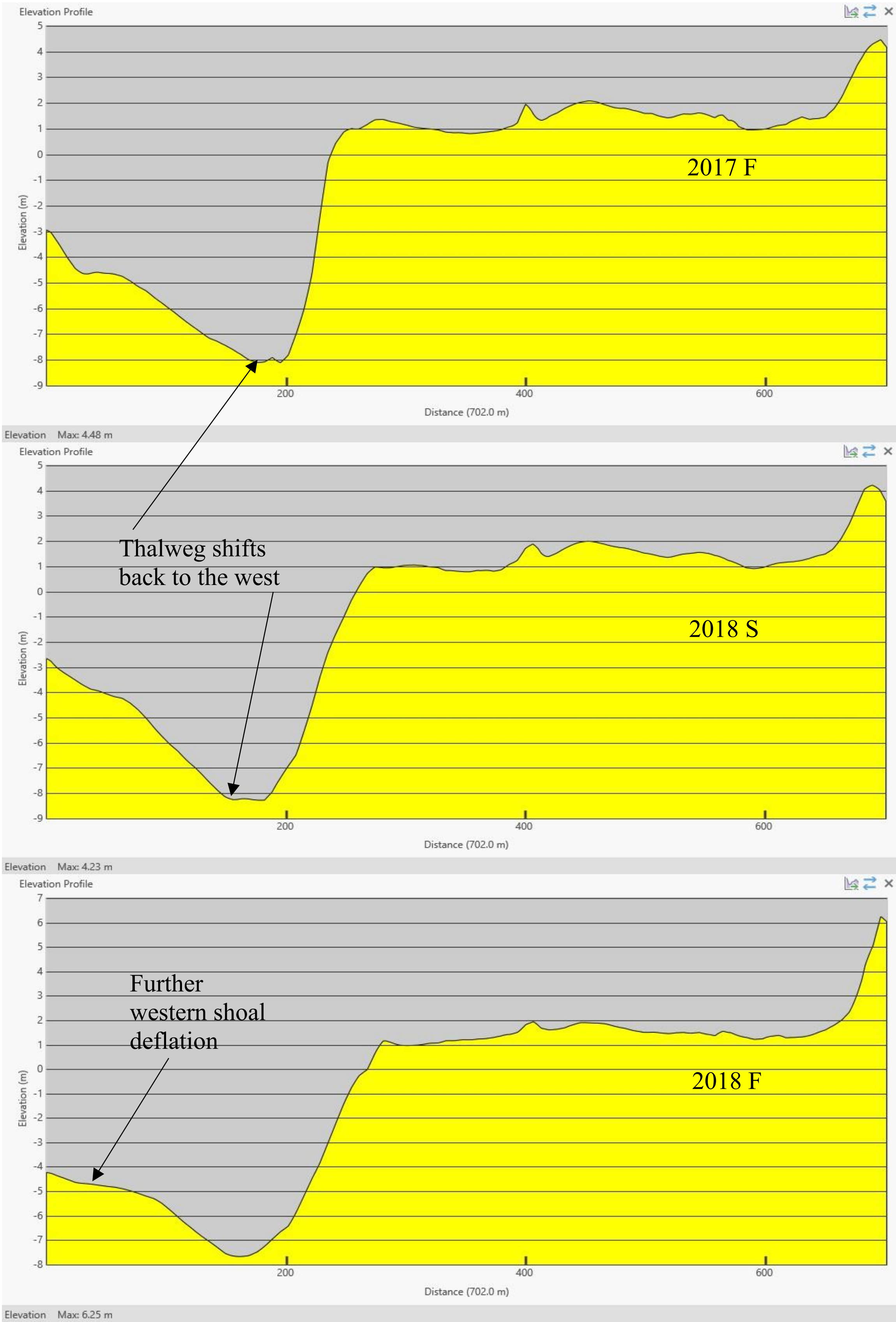
Elevation Profile
Elevation (m)
Distance (702.0 m)
2017 F
Elevation Max: 4.48 m
Elevation Profile
Thalweg shifts back to the west
2018 S
Elevation (m)
Distance (702.0 m)
Elevation Max: 4.23 m
Elevation Profile
Further western shoal deflation
2018 F
Elevation (m)
Distance (702.0 m)
Elevation Max: 6.25 m

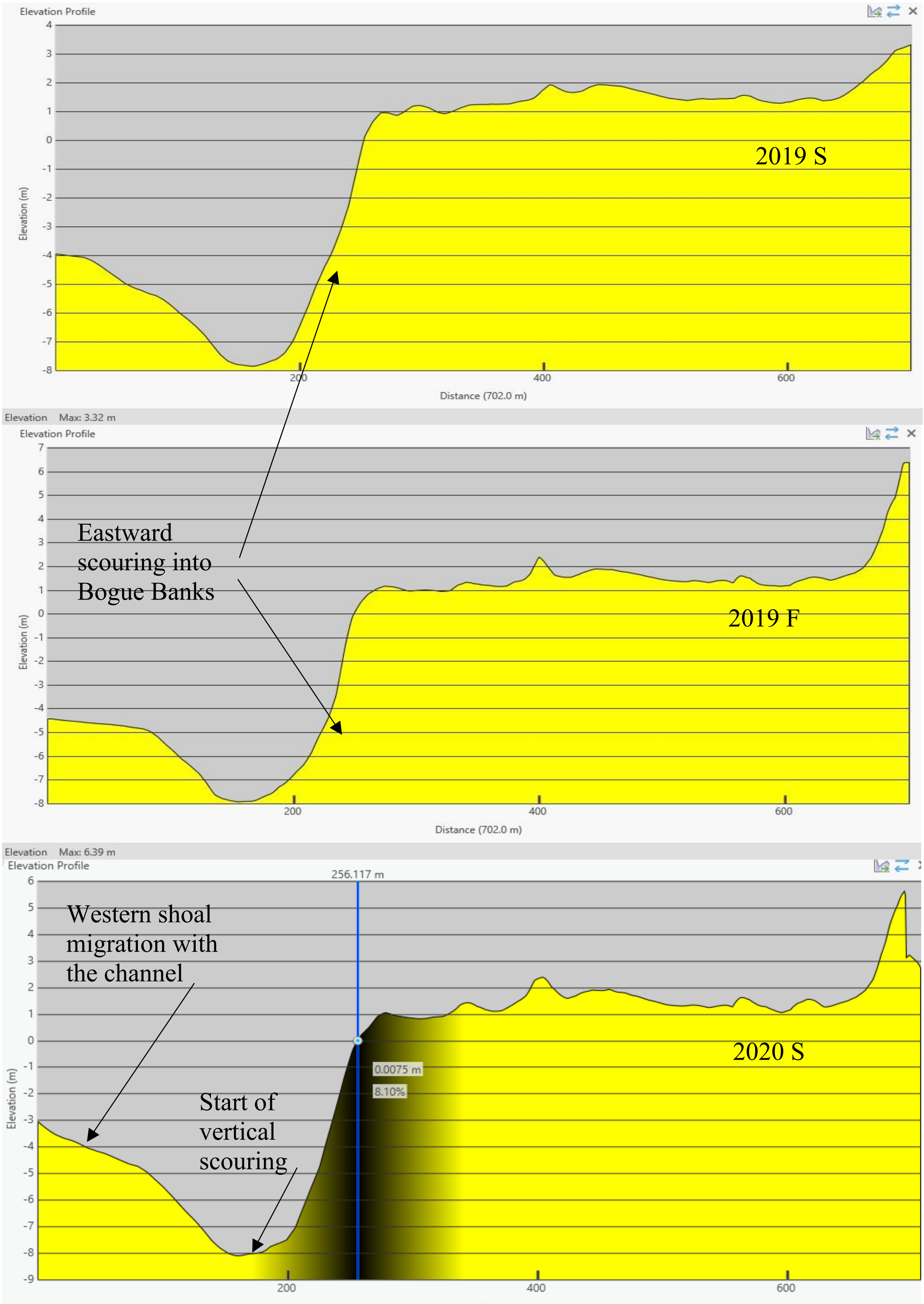
Elevation Profile
Elevation (m)
Distance (702.0 m)
2019 S
Elevation Max: 3.32 m
Elevation Profile
Eastward
scouring into
Bogue Banks
2019 F
Elevation Max: 6.39 m
Elevation Profile
256.117 m
Western shoal
migration with
the channel
Start of
vertical
scouring
0.0075 m
8.10%
2020 S
Distance (707.1 m)

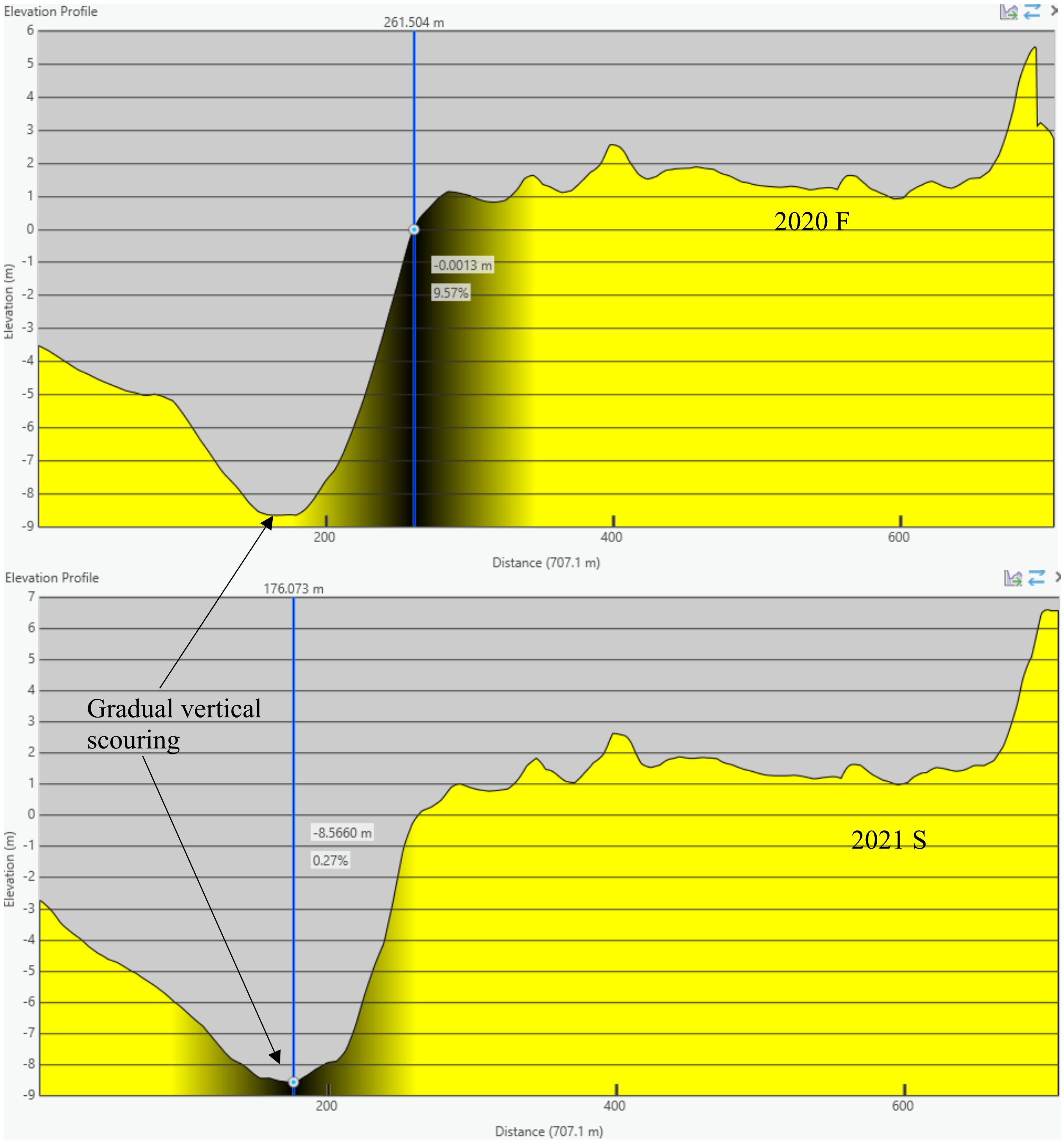
Elevation Profile
261.504 m
-0.0013 m
9.57%
2020 F
Elevation (m)
Distance (707.1 m)
Elevation Profile
176.073 m
-8.5660 m
0.27%
2021 S
Gradual vertical scouring
Elevation (m)
Distance (707.1 m)

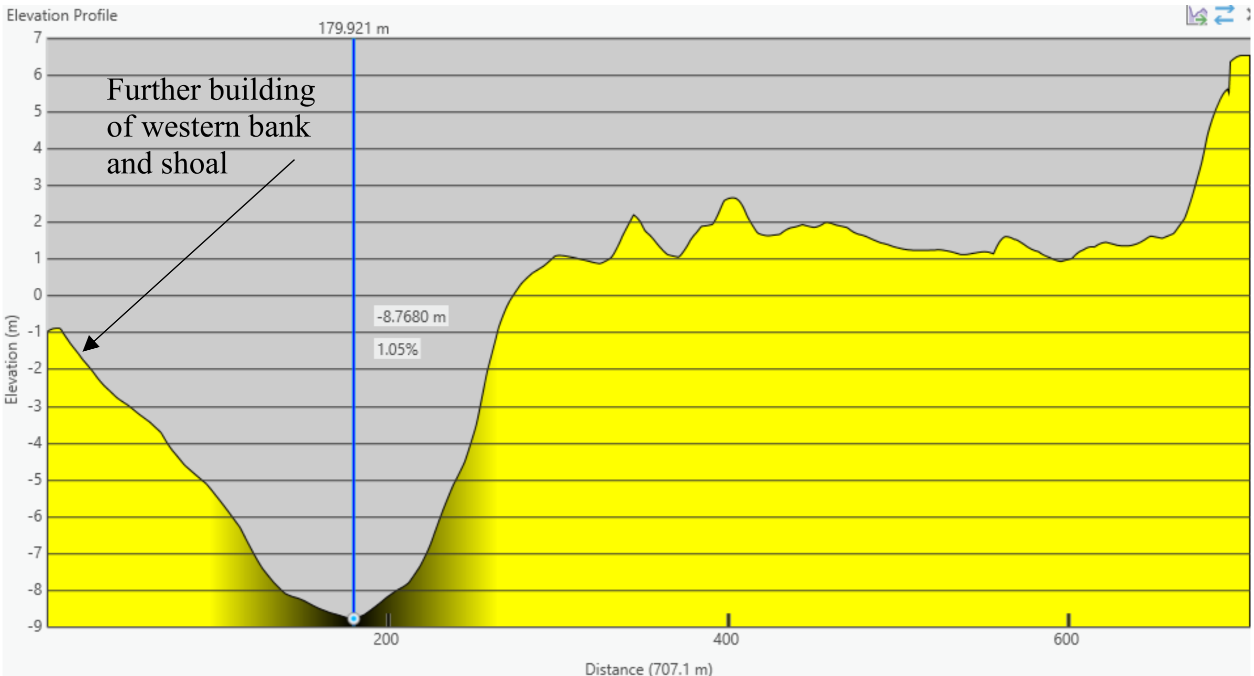
Elevation Profile
179.921 m
Further building of western bank and shoal
-8.7680 m
1.05%
Elevation (m)
7
6
5
4
3
2
1
0
-1
-2
-3
-4
-5
-6
-7
-8
-9
200
400
600
Distance (707.1 m)

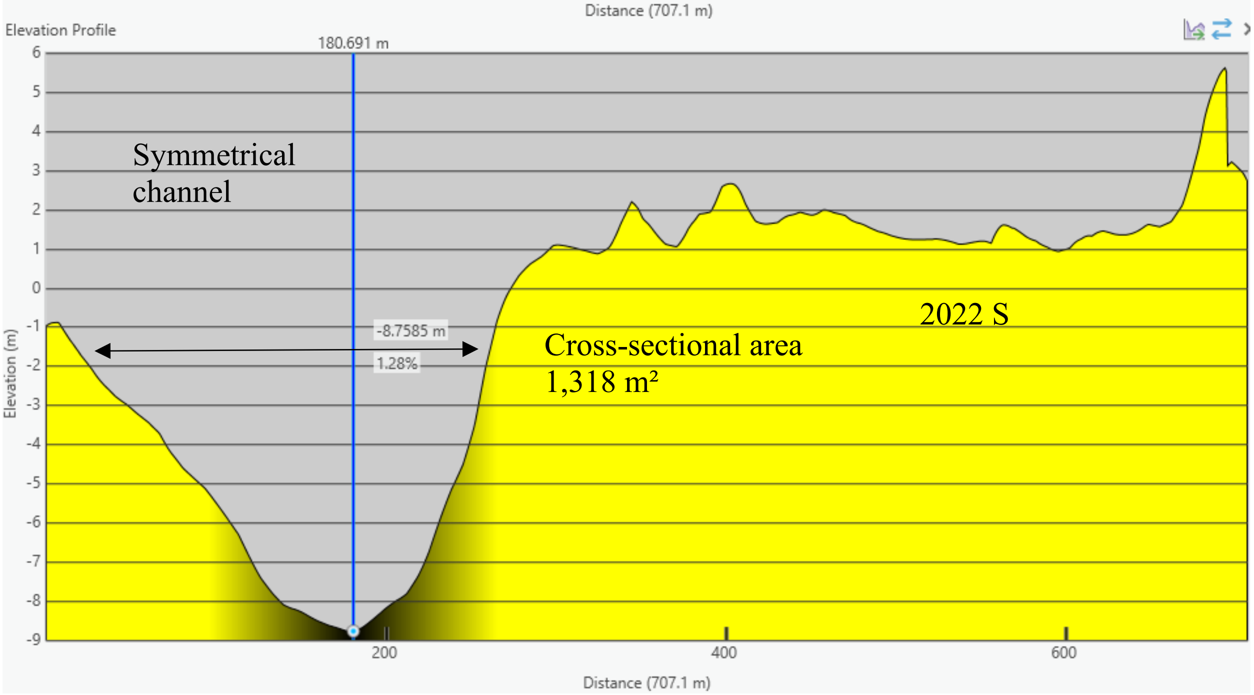
Elevation Profile
180.691 m
Symmetrical channel
-8.7585 m
1.28%
2022 S
Cross-sectional area 1,318 m²
Elevation (m)
6
5
4
3
2
1
0
-1
-2
-3
-4
-5
-6
-7
-8
-9
200
400
600
Distance (707.1 m)

Appendix C: Time series of the bathymetric surveys, Datum NAVD88; 2005-2022

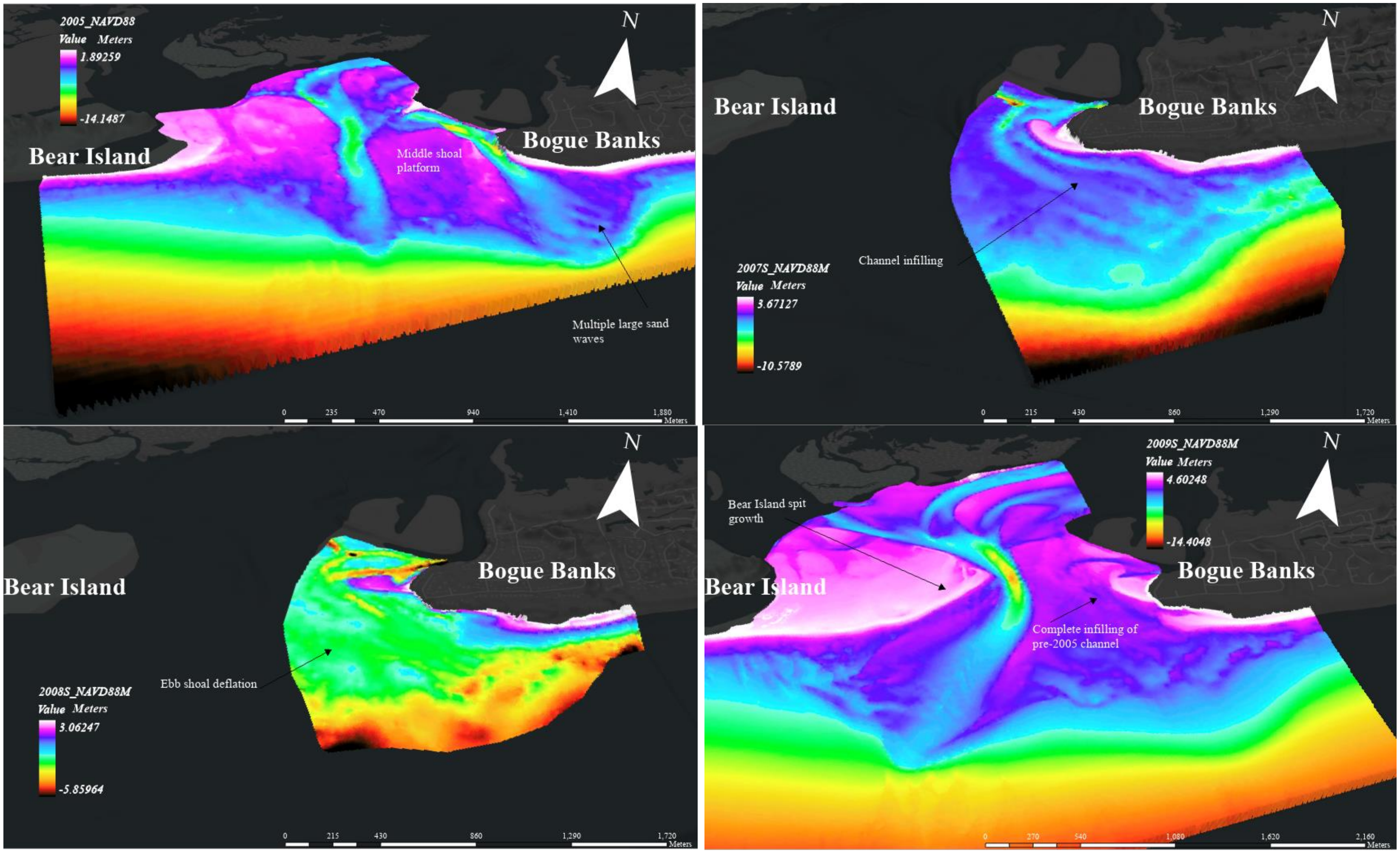

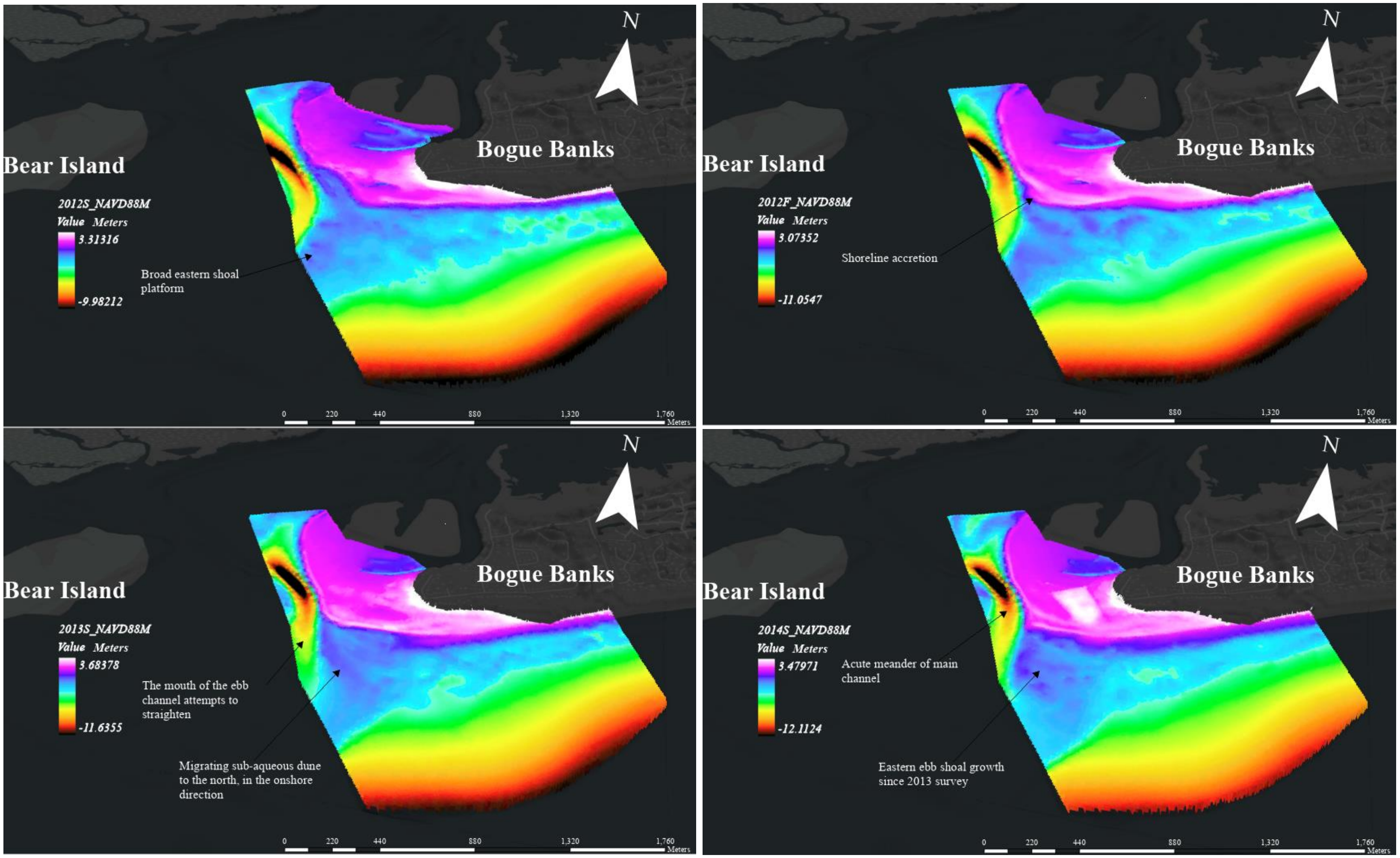
N
Bear Island
Bogue Banks
2012S_NAVD88M
Value Meters
3.31316
-9.98212
Broad eastern shoal platform
0 220 440 880 1,320 1,760 Meters
N
Bear Island
Bogue Banks
2012F_NAVD88M
Value Meters
3.07352
-11.0547
Shoreline accretion
0 220 440 880 1,320 1,760 Meters
N
Bear Island
Bogue Banks
2013S_NAVD88M
Value Meters
3.68378
-11.6355
The mouth of the ebb channel attempts to straighten
Migrating sub-aqueous dune to the north, in the onshore direction
0 220 440 880 1,320 1,760 Meters
N
Bear Island
Bogue Banks
2014S_NAVD88M
Value Meters
3.47971
-12.1124
Acute meander of main channel
Eastern ebb shoal growth since 2013 survey
0 220 440 880 1,320 1,760 Meters

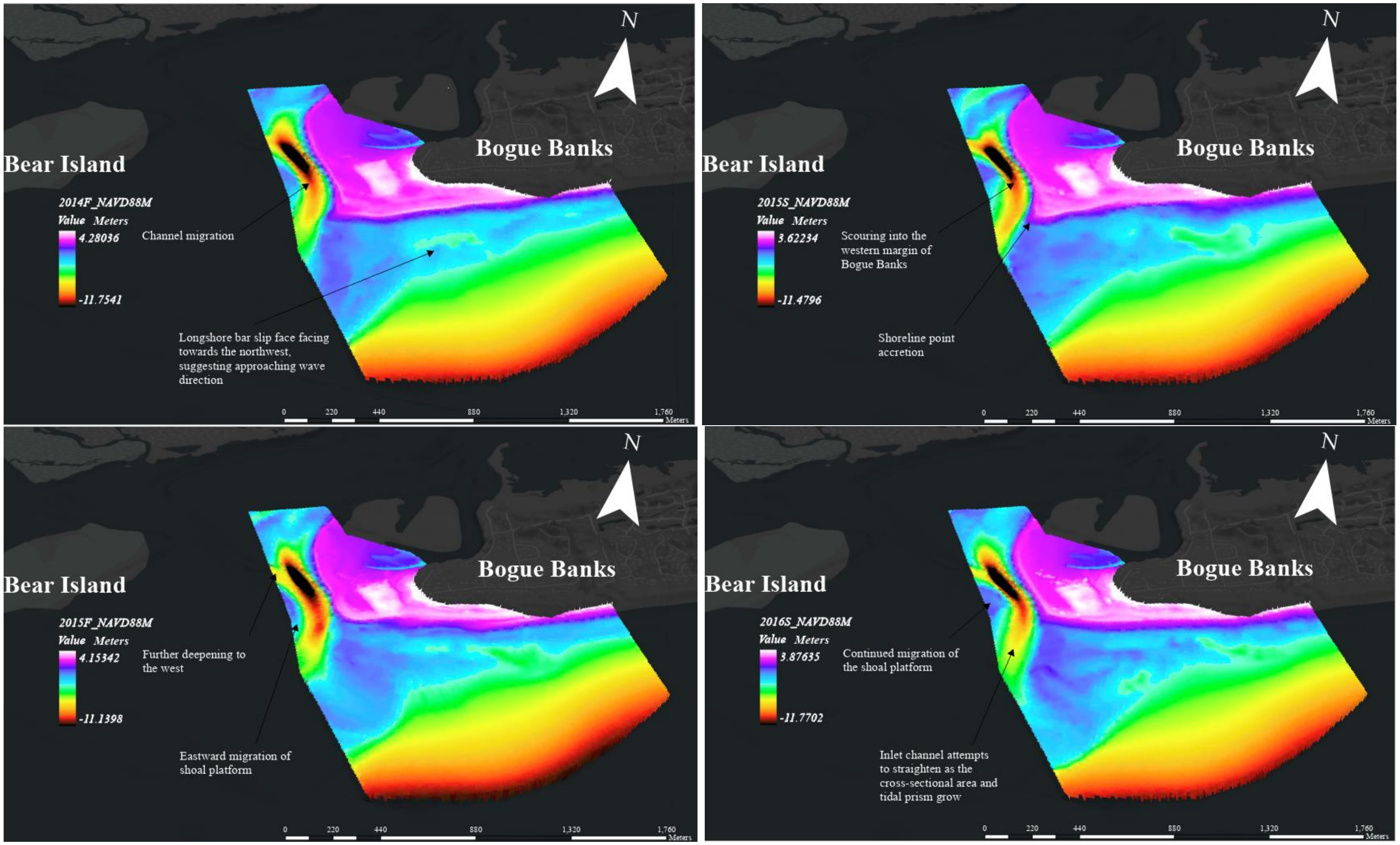
N
Bear Island
Bogue Banks
2014F_NAVD88M
Value Meters
4.28036
-11.7541
Channel migration
Longshore bar slip face facing towards the northwest, suggesting approaching wave direction
0 220 440 880 1,320 1,760 Meters
N
Bear Island
Bogue Banks
2015S_NAVD88M
Value Meters
3.62234
-11.4796
Scouring into the western margin of Bogue Banks
Shoreline point accretion
0 220 440 880 1,320 1,760 Meters
N
Bear Island
Bogue Banks
2015F_NAVD88M
Value Meters
4.15342
-11.1398
Further deepening to the west
Eastward migration of shoal platform
0 220 440 880 1,320 1,760 Meters
N
Bear Island
Bogue Banks
2016S_NAVD88M
Value Meters
3.87635
-11.7702
Continued migration of the shoal platform
Inlet channel attempts to straighten as the cross-sectional area and tidal prism grow
0 220 440 880 1,320 1,760 Meters

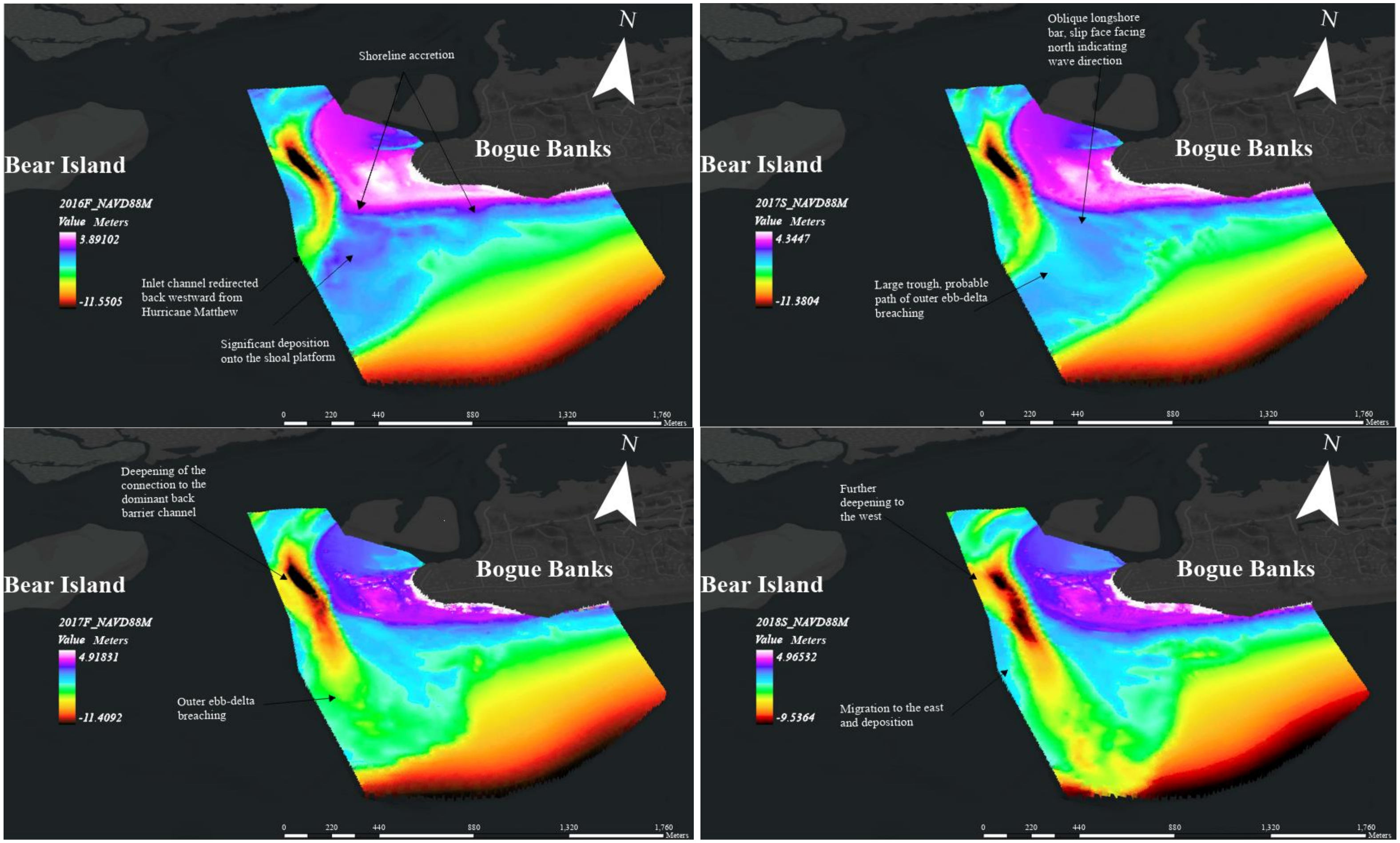

Shoreline accretion
N
Bear Island
Bogue Banks
2016F_NAVD88M
Value Meters
3.89102
-11.5505
Inlet channel redirected back westward from Hurricane Matthew
Significant deposition onto the shoal platform
Oblique longshore bar, slip face facing north indicating wave direction
N
Bear Island
Bogue Banks
2017S_NAVD88M
Value Meters
4.3447
-11.3804
Large trough, probable path of outer ebb-delta breaching
Deepening of the connection to the dominant back barrier channel
N
Bear Island
Bogue Banks
2017F_NAVD88M
Value Meters
4.91831
-11.4092
Outer ebb-delta breaching
Further deepening to the west
N
Bear Island
Bogue Banks
2018S_NAVD88M
Value Meters
4.96532
-9.5364
Migration to the east and deposition
0 220 440 880 1,320 1,760 Meters

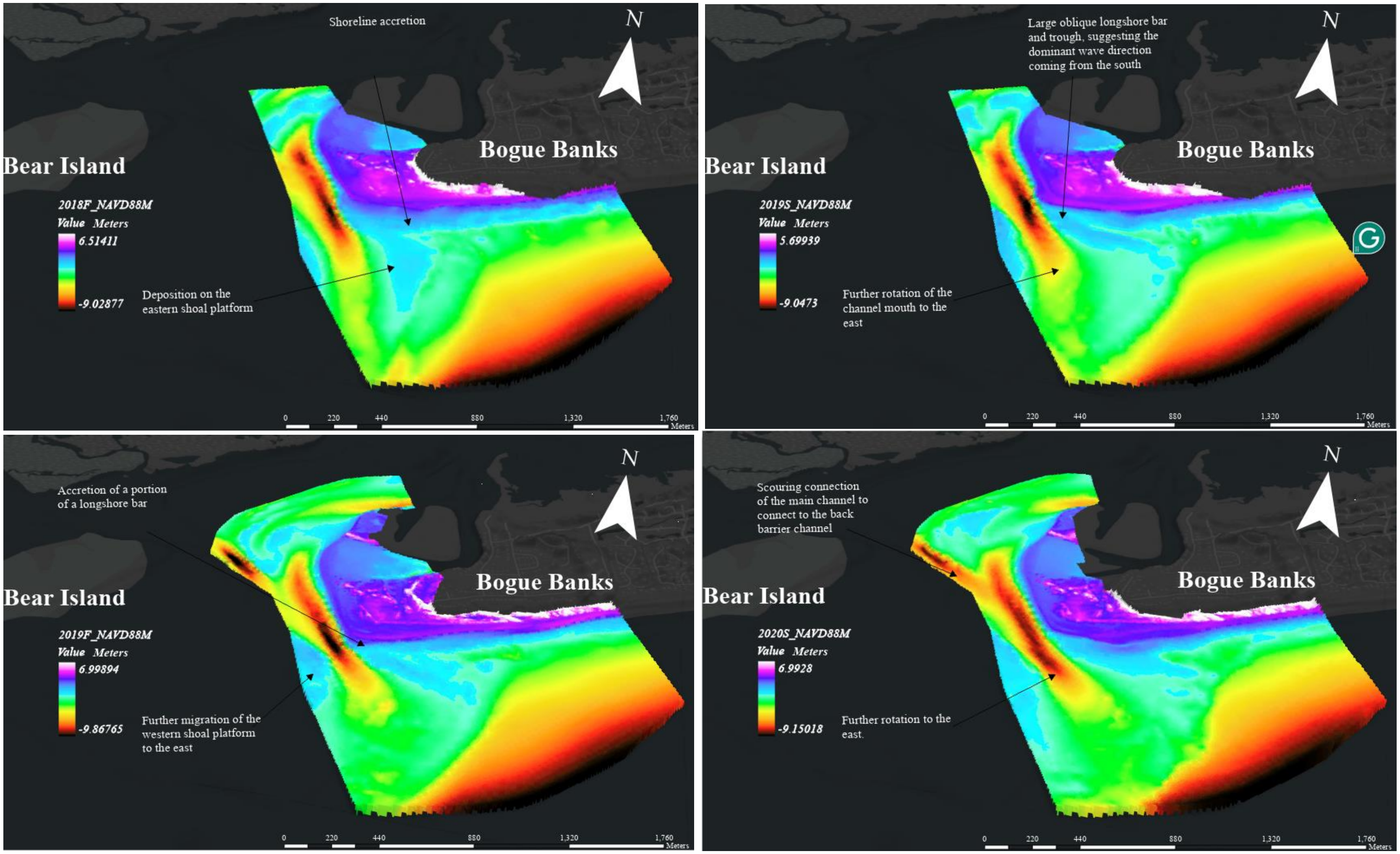

Shoreline accretion
N
Bear Island
Bogue Banks
2018F_NAVD88M
Value Meters
6.51411
-9.02877
Deposition on the eastern shoal platform
Large oblique longshore bar and trough, suggesting the dominant wave direction coming from the south
2019S_NAVD88M
5.69939
-9.0473
Further rotation of the channel mouth to the east
Accretion of a portion of a longshore bar
2019F_NAVD88M
6.99894
-9.86765
Further migration of the western shoal platform to the east
Scouring connection of the main channel to connect to the back barrier channel
2020S_NAVD88M
6.9928
-9.15018
Further rotation to the east.
0 220 440 880 1,320 1,760
Meters

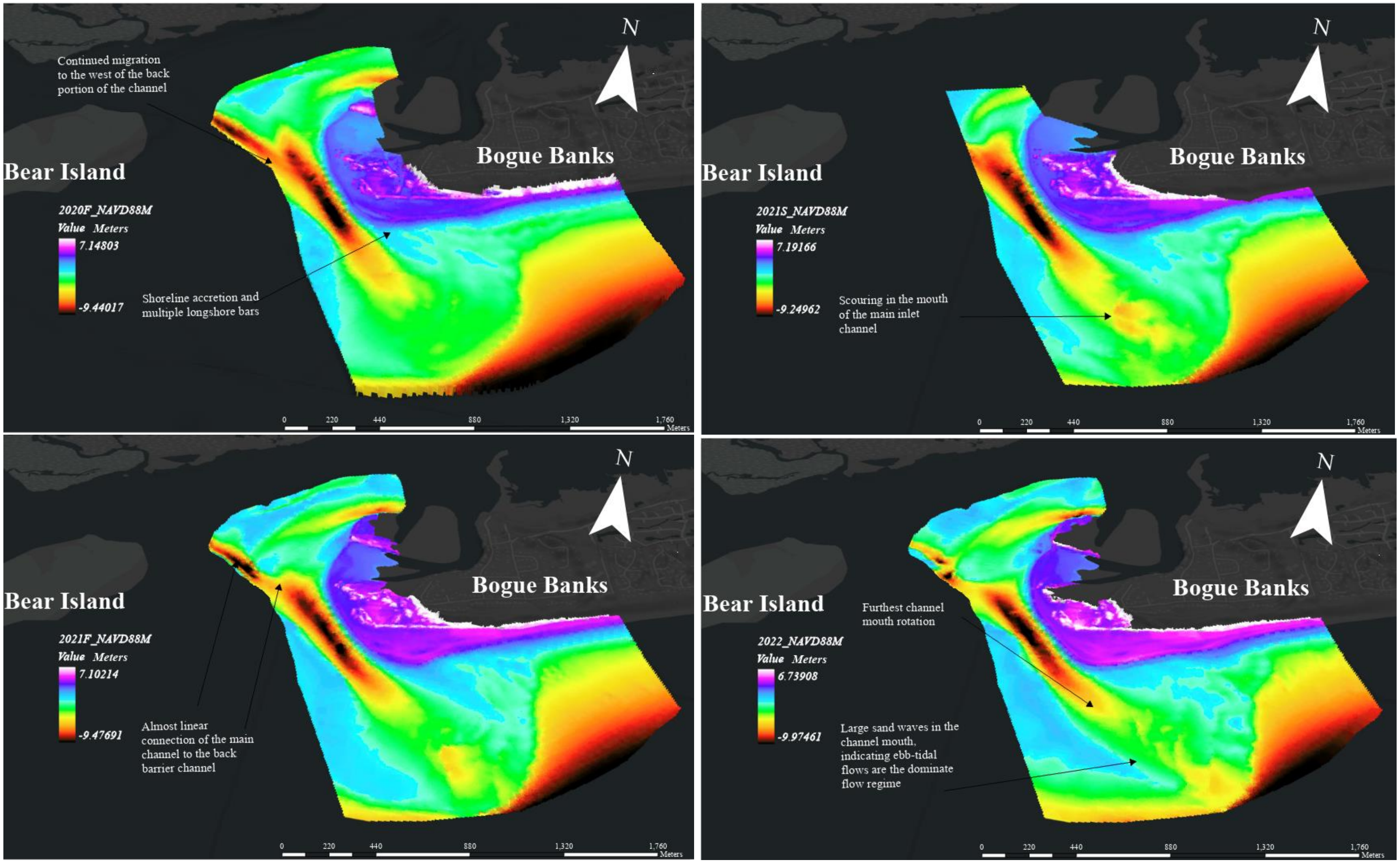
N
Continued migration to the west of the back portion of the channel
Bear Island
Bogue Banks
2020F_NAVD88M
Value Meters
7.14803
-9.44017
Shoreline accretion and multiple longshore bars
0
220
440
880
1,320
1,760
Meters
N
Bear Island
Bogue Banks
2021S_NAVD88M
Value Meters
7.19166
-9.24962
Scouring in the mouth of the main inlet channel
0
220
440
880
1,320
1,760
Meters
N
Bear Island
Bogue Banks
2021F_NAVD88M
Value Meters
7.10214
-9.47691
Almost linear connection of the main channel to the back barrier channel
0
220
440
880
1,320
1,760
Meters
N
Bear Island
Bogue Banks
Furthest channel mouth rotation
2022_NAVD88M
Value Meters
6.73908
-9.97461
Large sand waves in the channel mouth, indicating ebb-tidal flows are the dominate flow regime
0
220
440
880
1,320
1,760
Meters

Appendix D: Time stamps, Hurricane Matthew, Florence, and Dorian's varying wind fields, 1, 1.1, 1.2, and 1.3

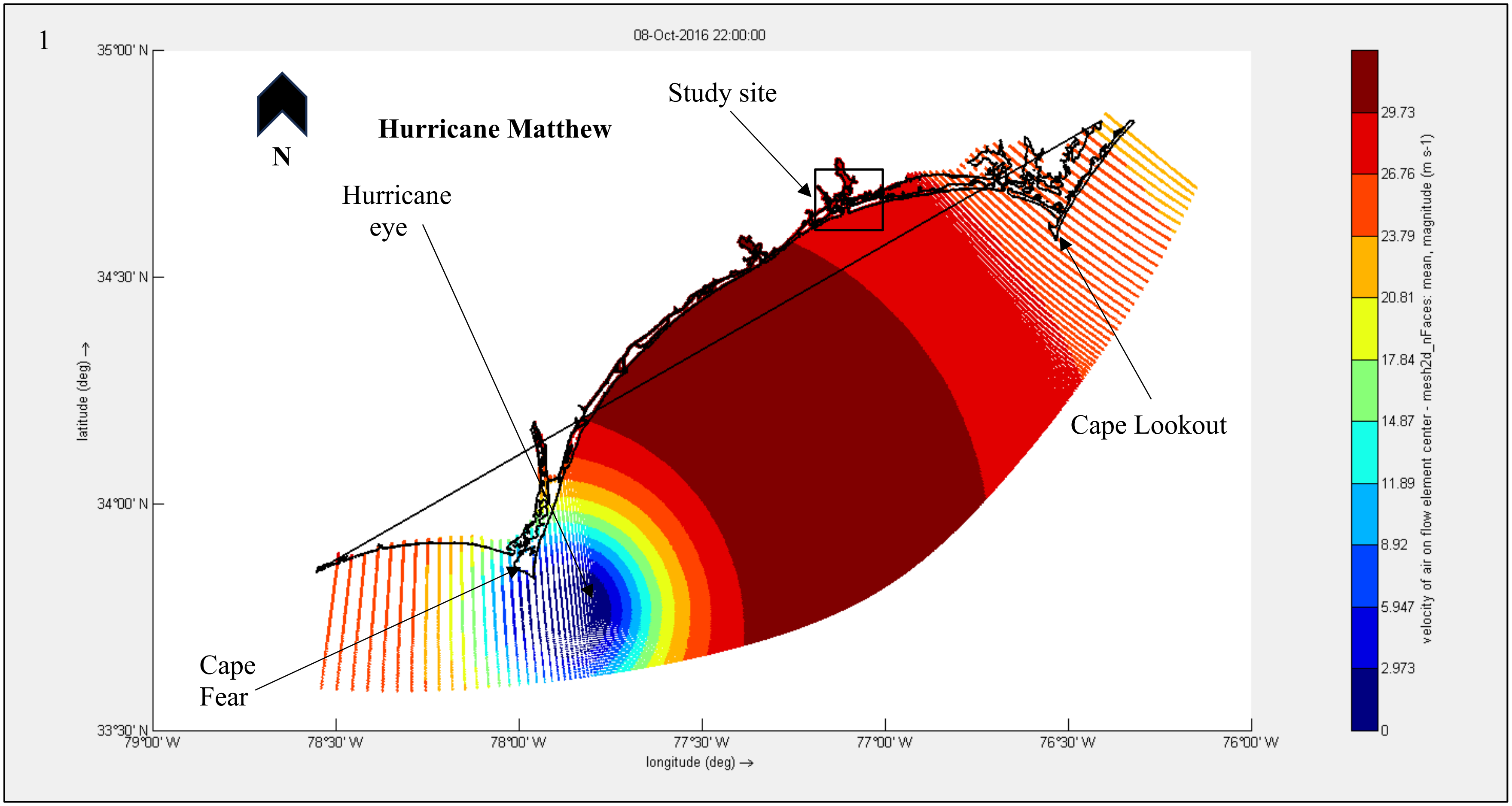

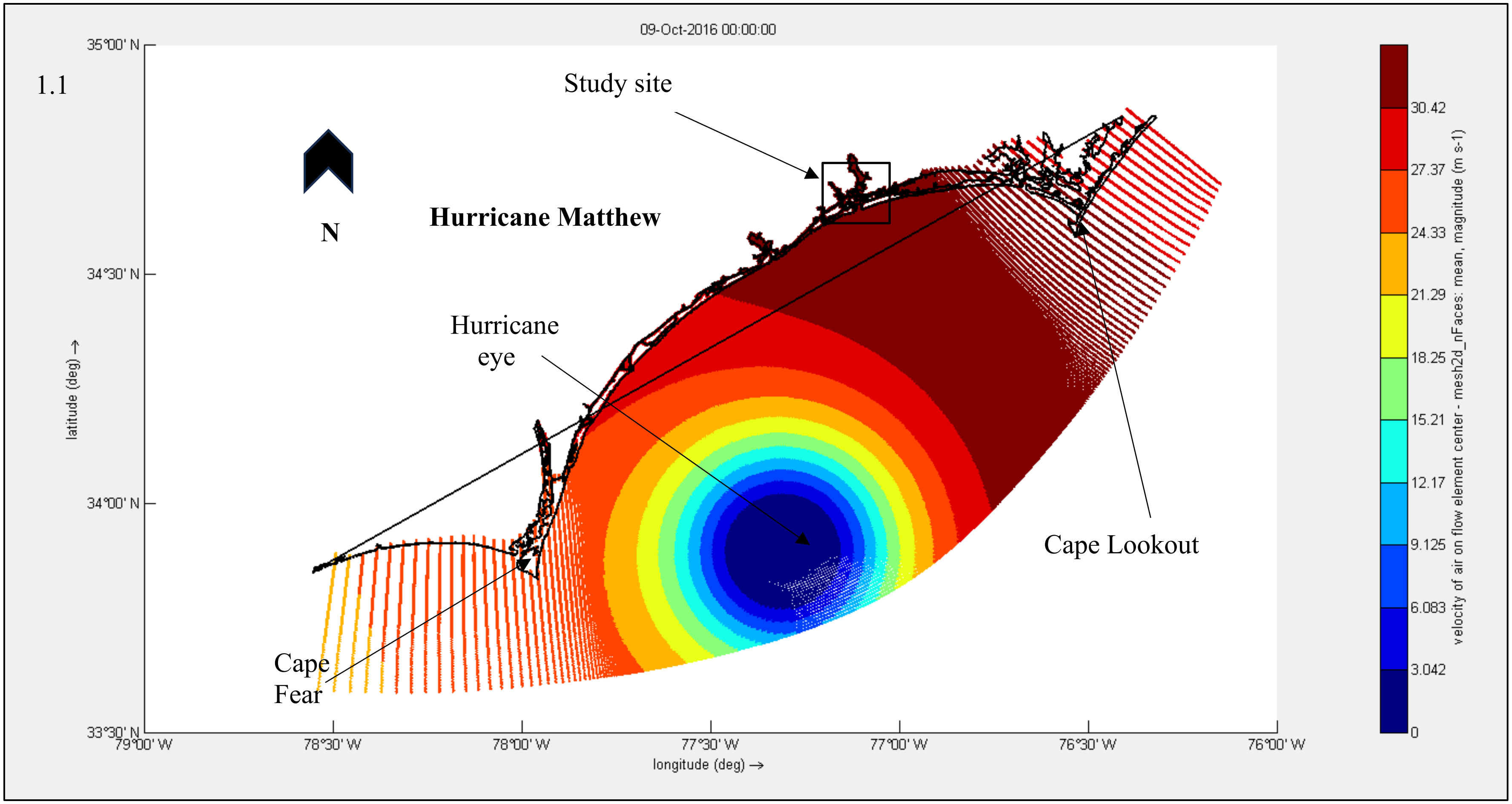
09-Oct-2016 00:00:00
1.1
N
Hurricane Matthew
Study site
Hurricane eye
Cape Lookout
Cape Fear
35°00' N
34°30' N
34°00' N
33°30' N
79°00' W
78°30' W
78°00' W
77°30' W
77°00' W
76°30' W
76°00' W
latitude (deg) →
longitude (deg) →
30.42
27.37
24.33
21.29
18.25
15.21
12.17
9.125
6.083
3.042
0
velocity of air on flow element center - mesh2d_nFaces: mean, magnitude (m s-1)

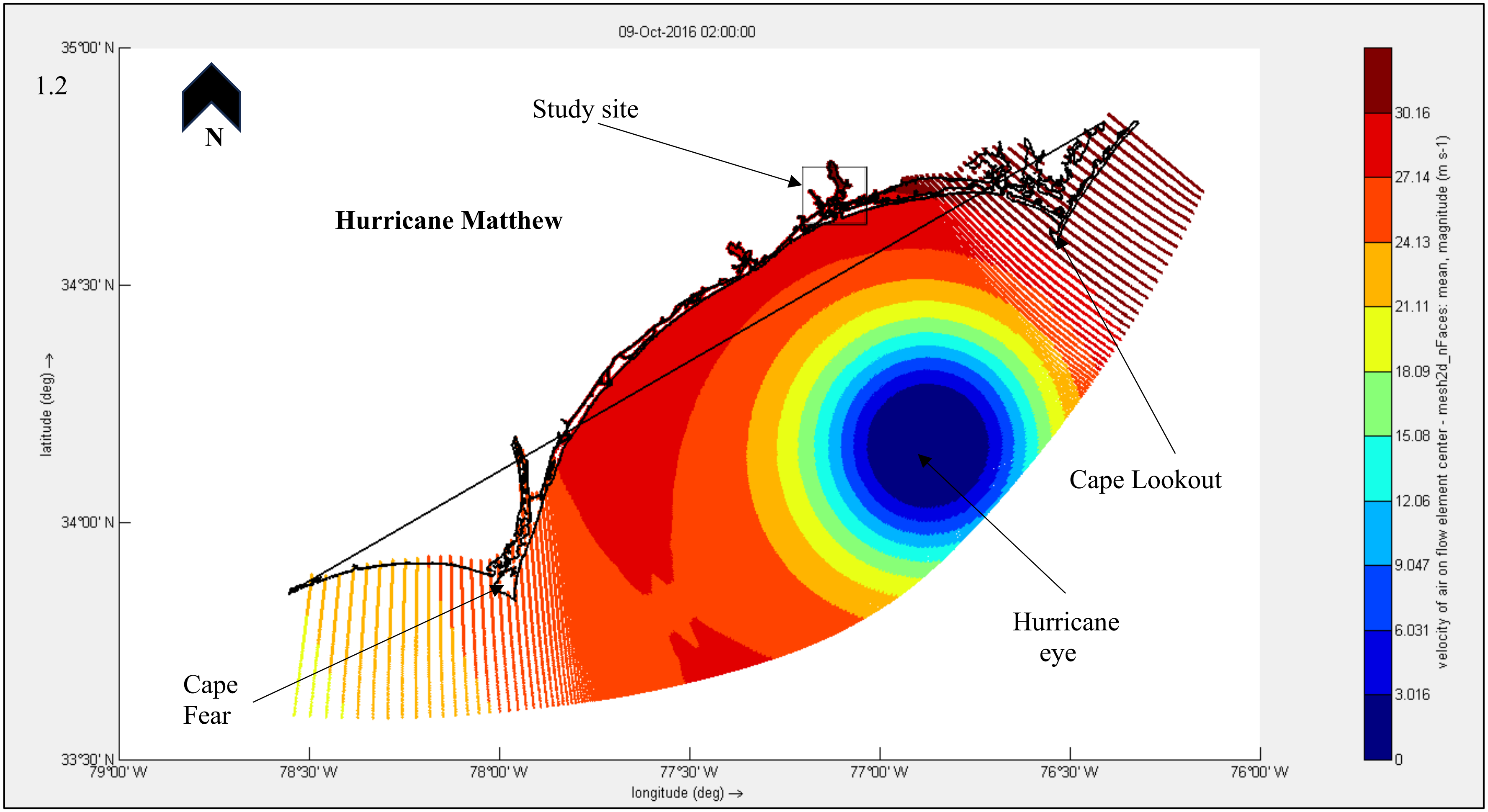

09-Oct-2016 02:00:00
1.2
N
Study site
Hurricane Matthew
Cape Lookout
Hurricane eye
Cape Fear
35°00' N
34°30' N
34°00' N
33°30' N
79°00' W
78°30' W
78°00' W
77°30' W
77°00' W
76°30' W
76°00' W
latitude (deg) →
longitude (deg) →
30.16
27.14
24.13
21.11
18.09
15.08
12.06
9.047
6.031
3.016
0
velocity of air on flow element center - mesh2d_nFaces: mean, magnitude (m s-1)

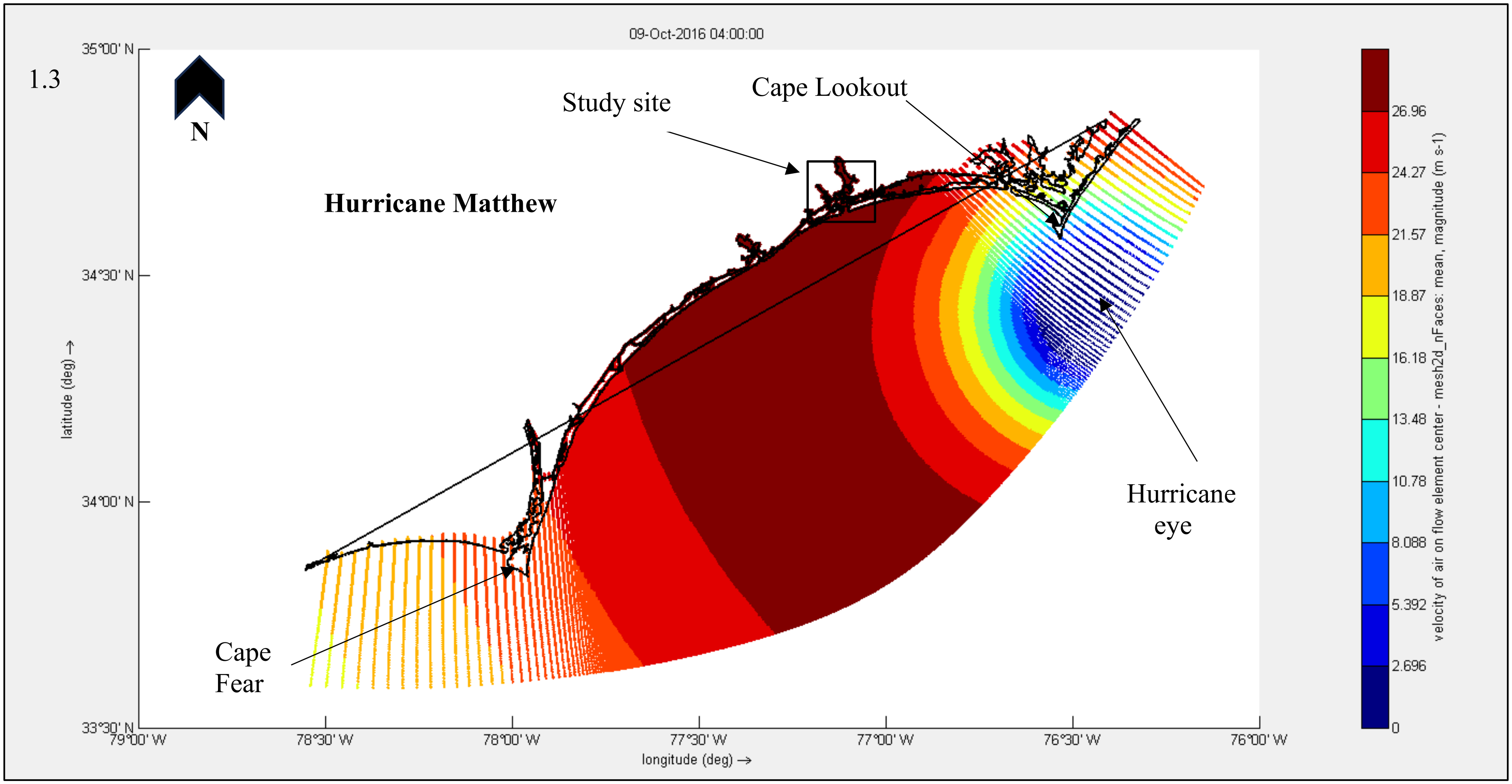

1.3
09-Oct-2016 04:00:00
N
Hurricane Matthew
Study site
Cape Lookout
Hurricane
eye
Cape
Fear
35°00' N
34°30' N
34°00' N
33°30' N
latitude (deg) →
79°00' W
78°30' W
78°00' W
77°30' W
77°00' W
76°30' W
76°00' W
longitude (deg) →
26.96
24.27
21.57
18.87
16.18
13.48
10.78
8.088
5.392
2.696
0
velocity of air on flow element center - mesh2d_nFaces: mean, magnitude (m s-1)

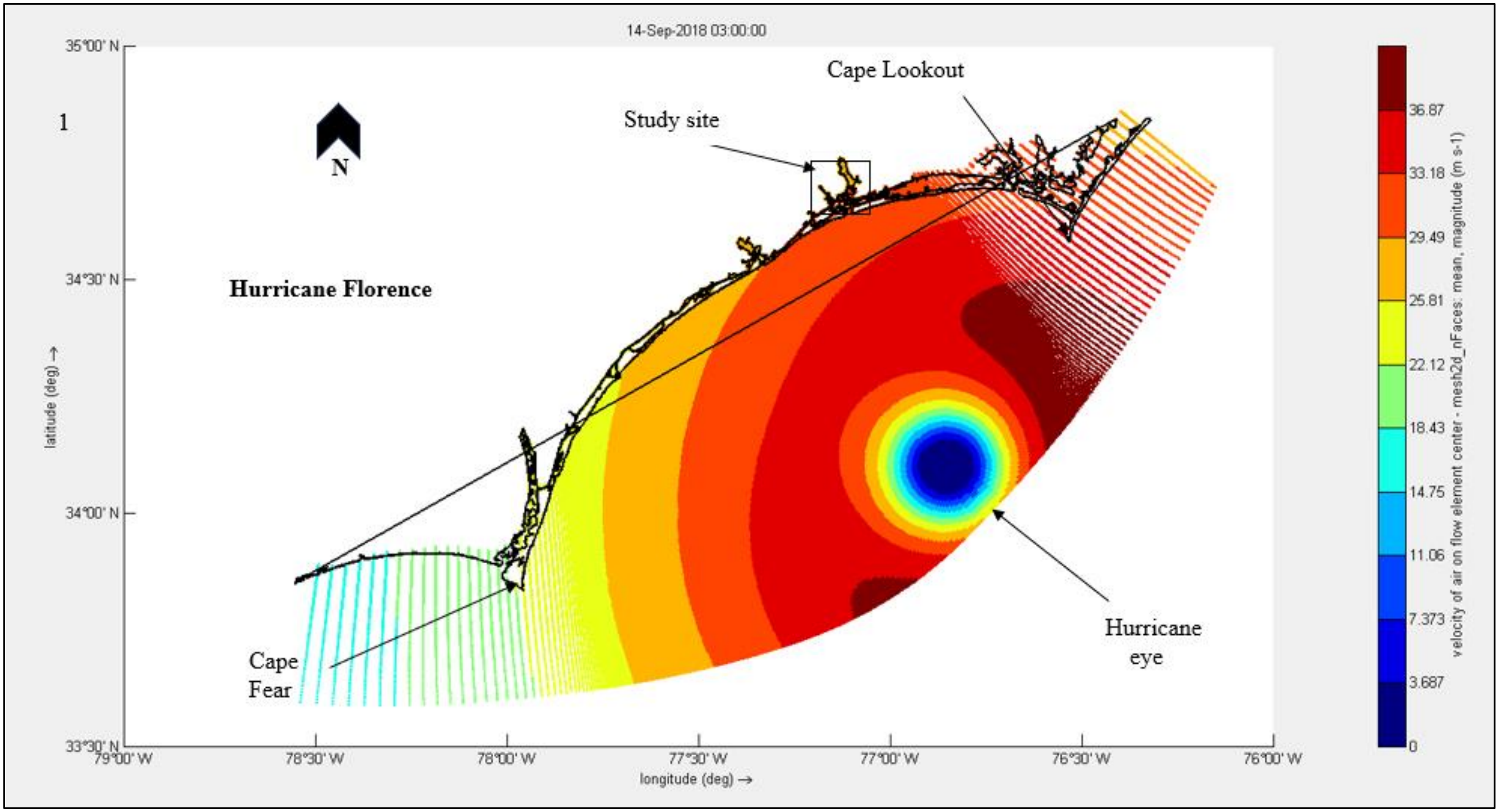
14-Sep-2018 03:00:00
1
N
Hurricane Florence
Study site
Cape Lookout
Cape Fear
Hurricane eye
35°00' N
34°30' N
34°00' N
33°30' N
latitude (deg) →
79°00' W
78°30' W
78°00' W
77°30' W
77°00' W
76°30' W
76°00' W
longitude (deg) →
velocity of air on flow element center - mesh2d_nFaces: mean, magnitude (m s-1)
36.87
33.18
29.49
25.81
22.12
18.43
14.75
11.06
7.373
3.687
0

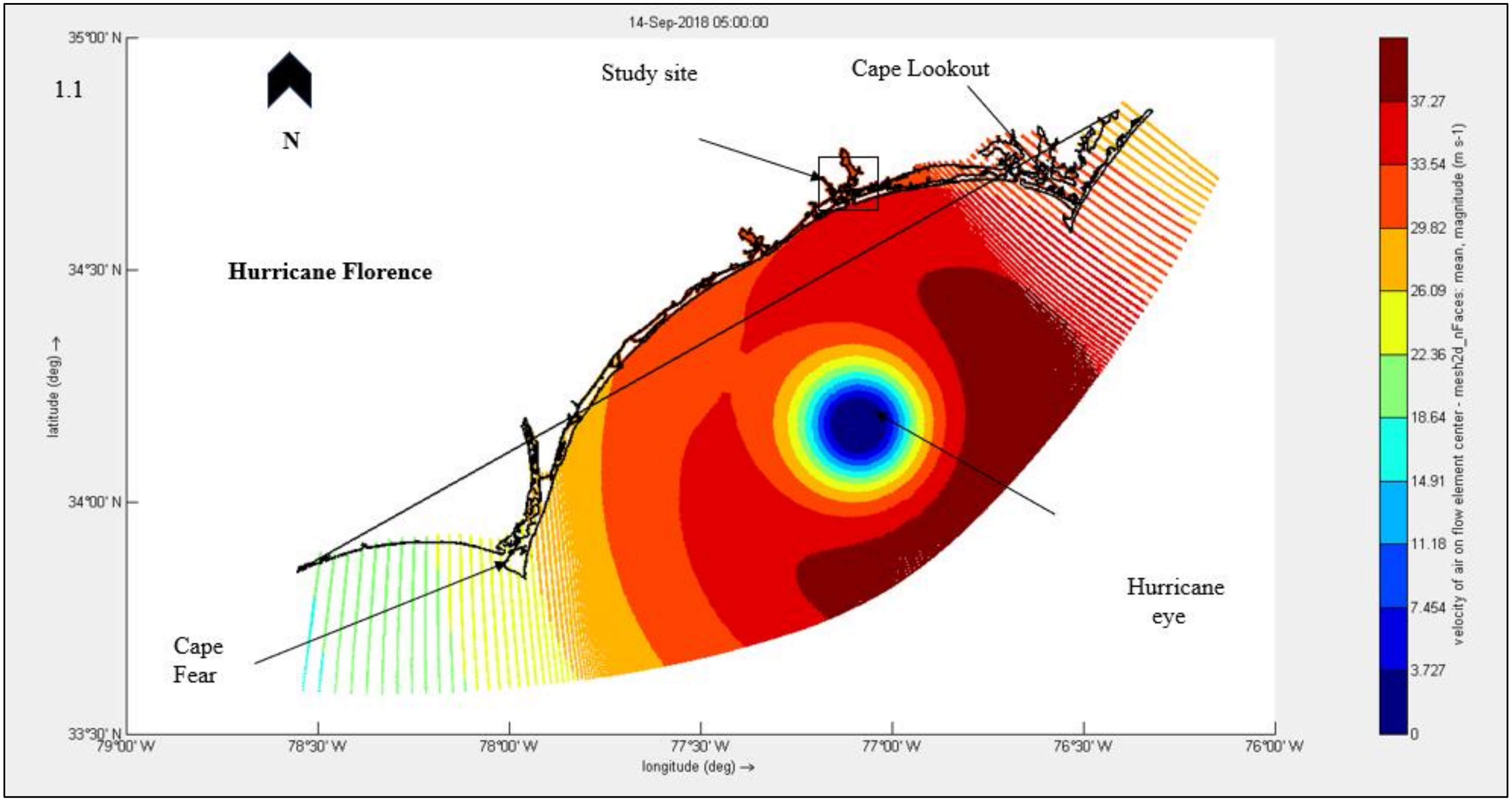
14-Sep-2018 05:00:00
1.1
N
Study site
Cape Lookout
Hurricane Florence
Cape
Fear
Hurricane
eye
35°00' N
34°30' N
34°00' N
33°30' N
79°00' W
78°30' W
78°00' W
77°30' W
77°00' W
76°30' W
76°00' W
latitude (deg) →
longitude (deg) →
37.27
33.54
29.82
26.09
22.36
18.64
14.91
11.18
7.454
3.727
0
velocity of air on flow element center - mesh2d_nFaces: mean, magnitude (m s-1)

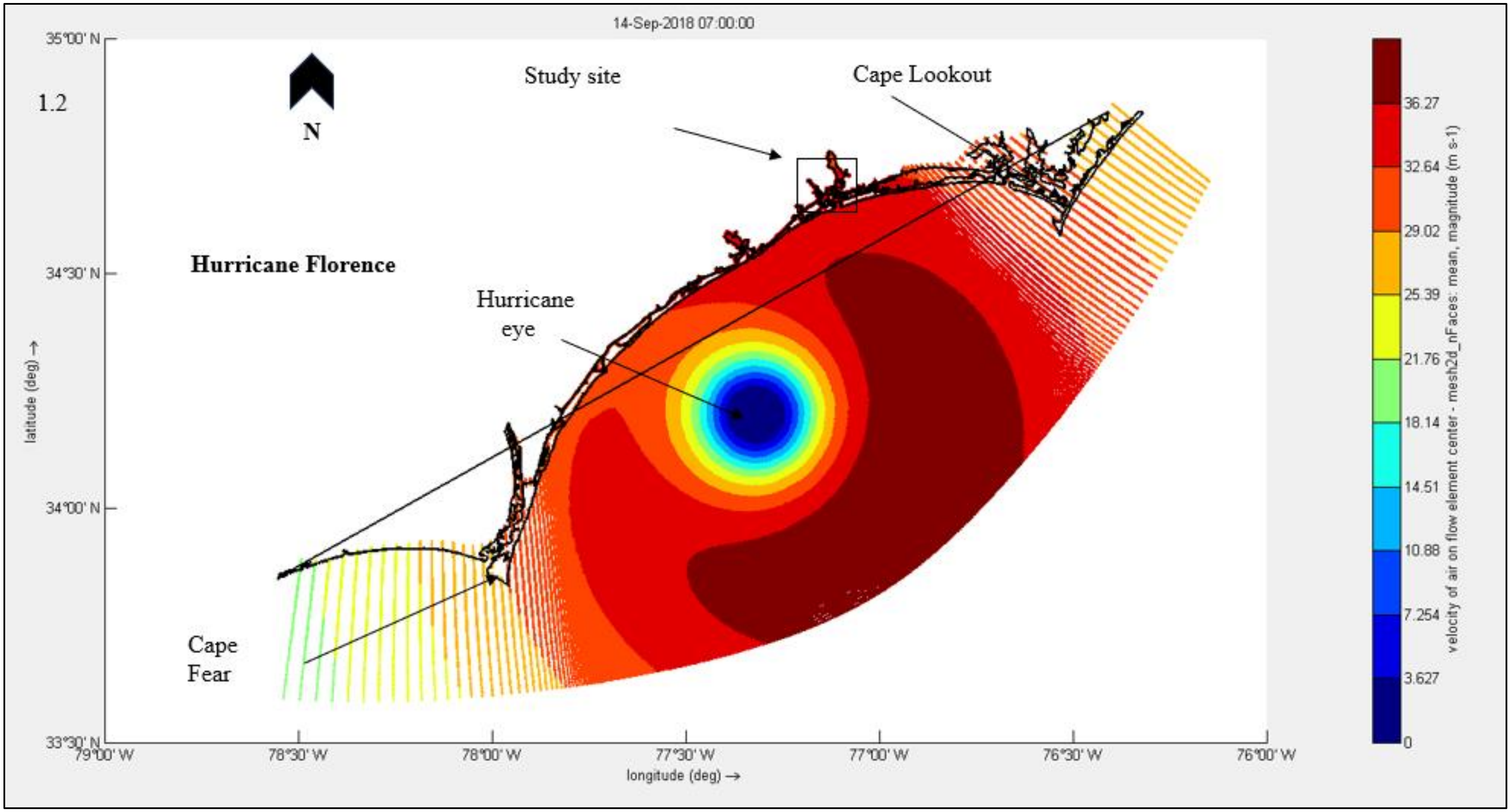
14-Sep-2018 07:00:00
1.2
N
Study site
Cape Lookout
Hurricane Florence
Hurricane
eye
Cape
Fear
35°00' N
34°30' N
34°00' N
33°30' N
79°00' W
78°30' W
78°00' W
77°30' W
77°00' W
76°30' W
76°00' W
latitude (deg) →
longitude (deg) →
36.27
32.64
29.02
25.39
21.76
18.14
14.51
10.88
7.254
3.627
0
velocity of air on flow element center - mesh2d_nFaces: mean, magnitude (m s-1)

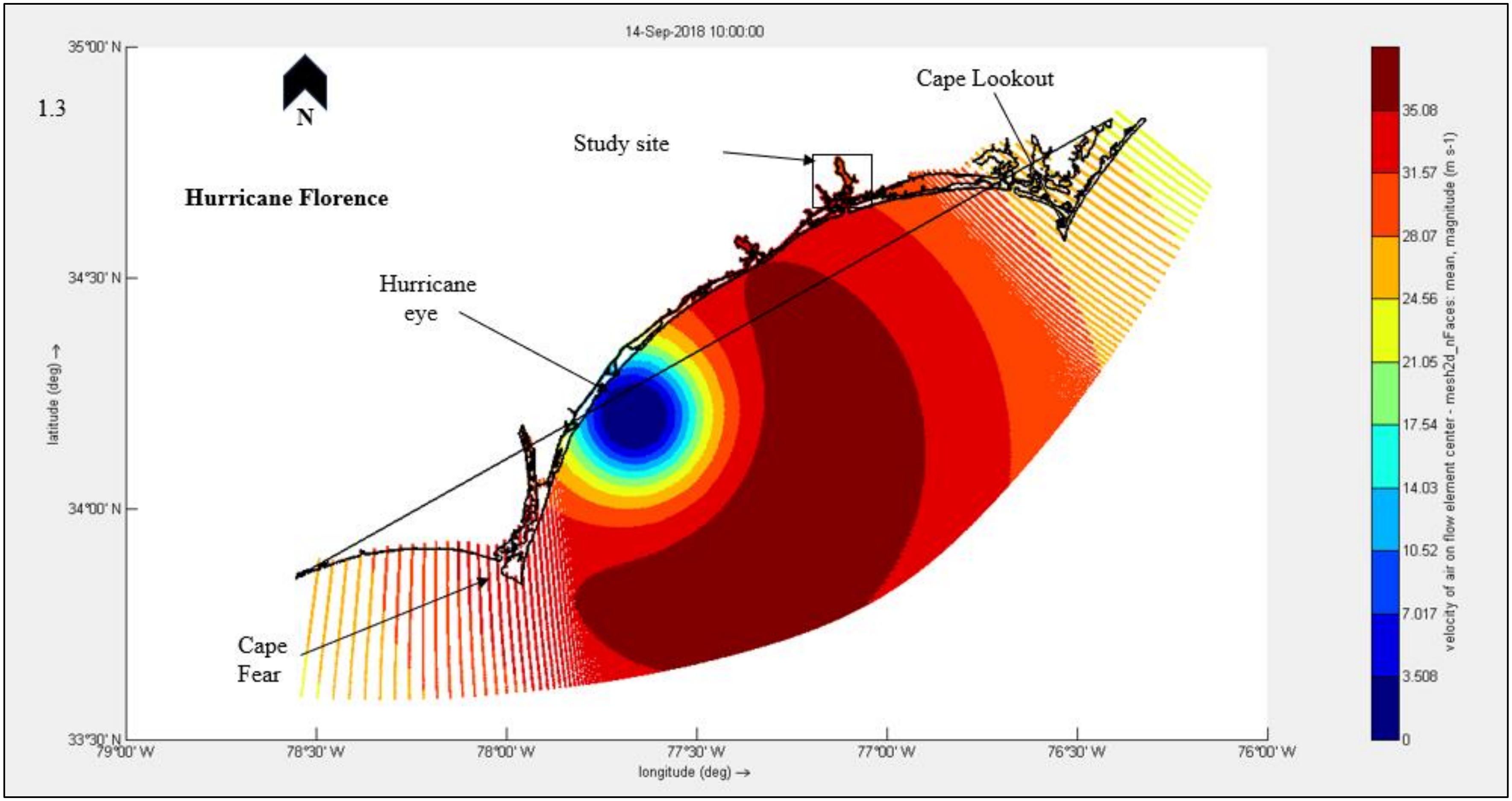
14-Sep-2018 10:00:00
1.3
N
Hurricane Florence
Study site
Cape Lookout
Hurricane eye
Cape Fear
35°00' N
34°30' N
34°00' N
33°30' N
79°00' W
78°30' W
78°00' W
77°30' W
77°00' W
76°30' W
76°00' W
latitude (deg) →
longitude (deg) →
35.08
31.57
28.07
24.56
21.05
17.54
14.03
10.52
7.017
3.508
0
velocity of air on flow element center - mesh2d_nFaces: mean, magnitude (m s-1)

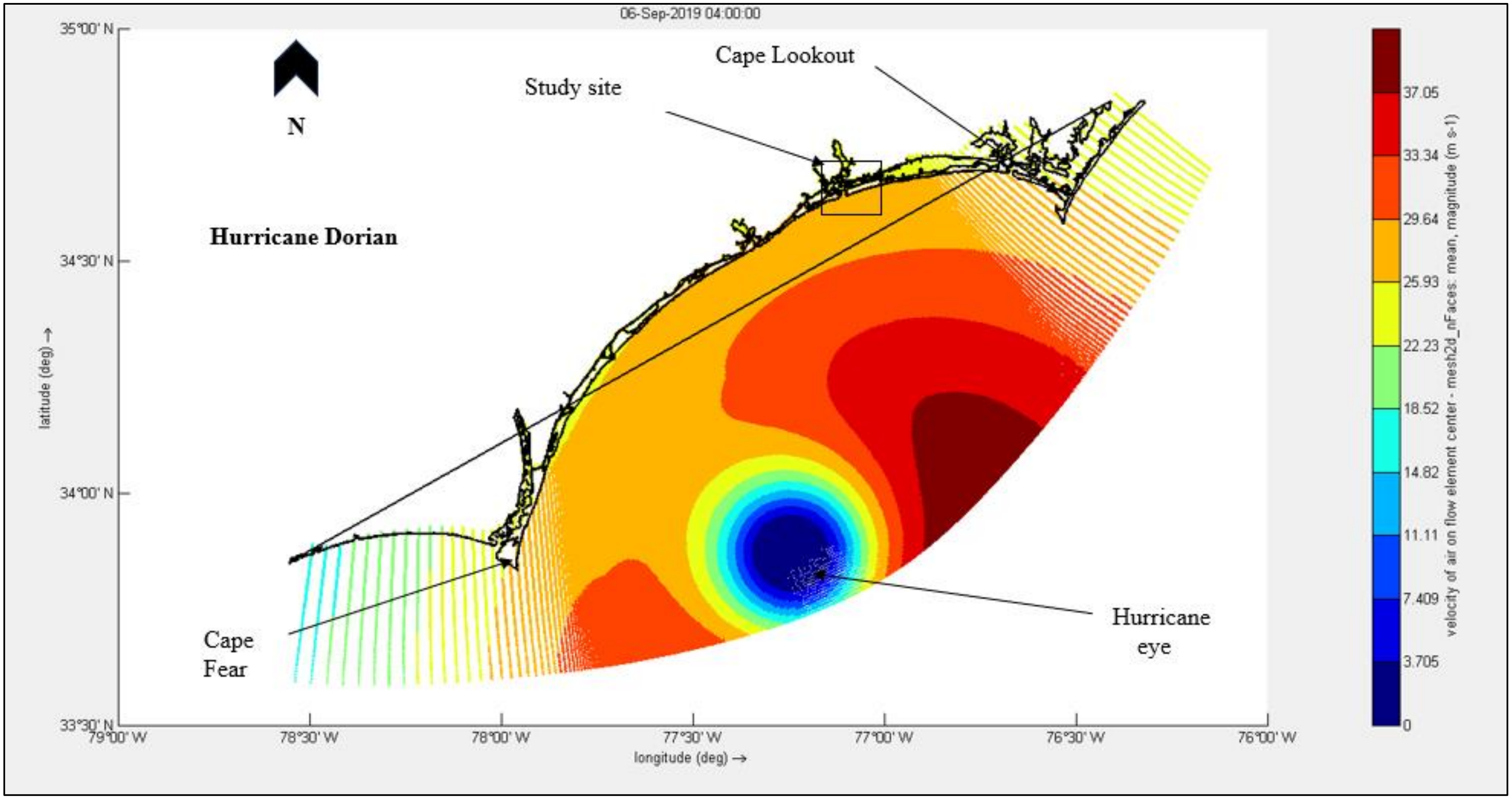
06-Sep-2019 04:00:00
N
Hurricane Dorian
Study site
Cape Lookout
Cape Fear
Hurricane eye
35°00' N
34°30' N
34°00' N
33°30' N
79°00' W
78°30' W
78°00' W
77°30' W
77°00' W
76°30' W
76°00' W
latitude (deg) →
longitude (deg) →
velocity of air on flow element center - mesh2d_nFaces: mean, magnitude (m s-1)
37.05
33.34
29.64
25.93
22.23
18.52
14.82
11.11
7.409
3.705
0

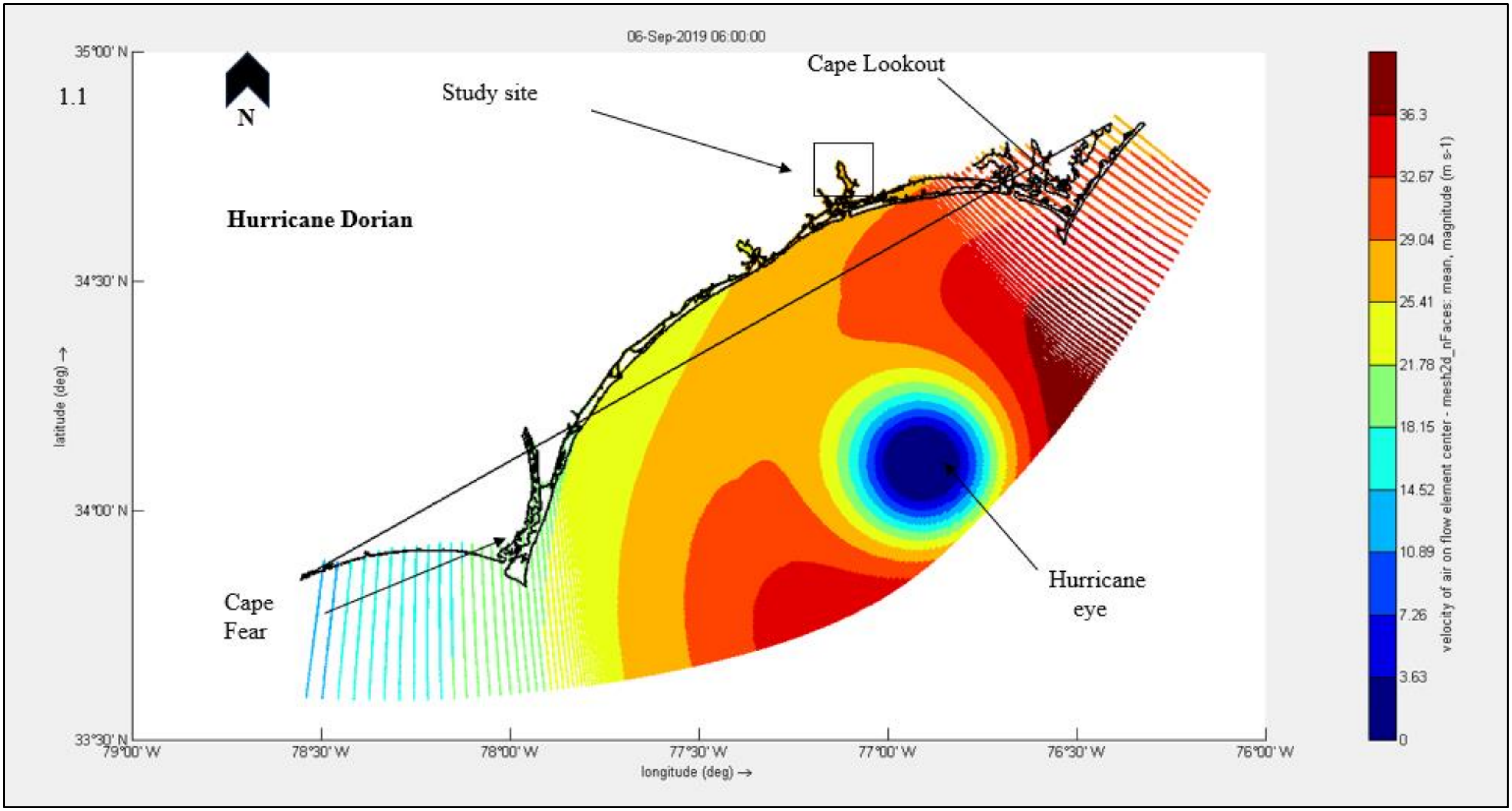
06-Sep-2019 06:00:00
1.1
N
Study site
Cape Lookout
Hurricane Dorian
Cape
Fear
Hurricane
eye
35°00' N
34°30' N
34°00' N
33°30' N
latitude (deg) →
79°00' W
78°30' W
78°00' W
77°30' W
77°00' W
76°30' W
76°00' W
longitude (deg) →
36.3
32.67
29.04
25.41
21.78
18.15
14.52
10.89
7.26
3.63
0
velocity of air on flow element center - mesh2d_nFaces: mean, magnitude (m s-1)

1.2

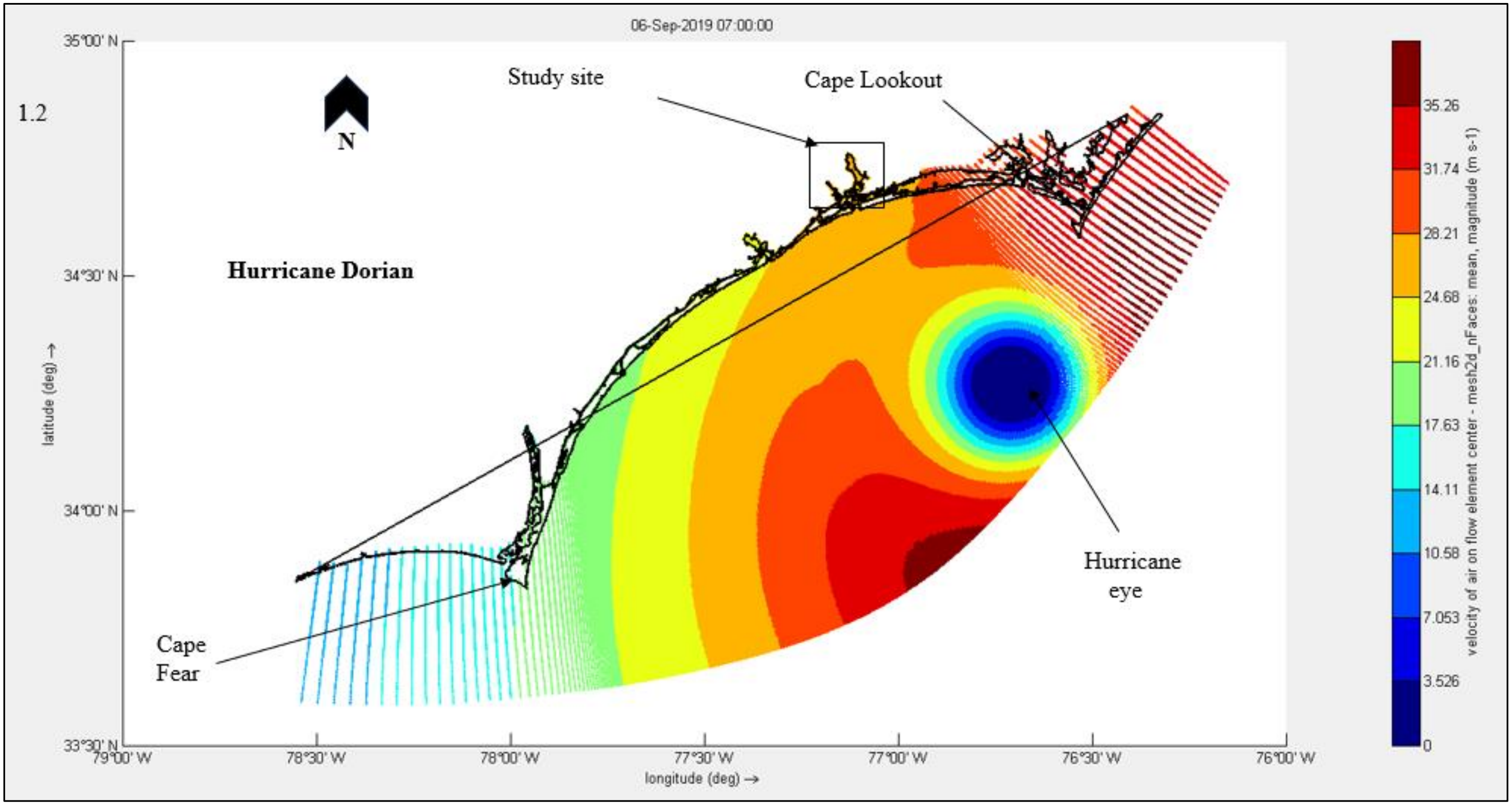
06-Sep-2019 07:00:00
Study site
Cape Lookout
N
Hurricane Dorian
Hurricane
eye
Cape
Fear
35°00' N
34°30' N
34°00' N
33°30' N
79°00' W
78°30' W
78°00' W
77°30' W
77°00' W
76°30' W
76°00' W
latitude (deg) →
longitude (deg) →
35.26
31.74
28.21
24.68
21.16
17.63
14.11
10.58
7.053
3.526
0
velocity of air on flow element center - mesh2d_nFaces: mean, magnitude (m s-1)

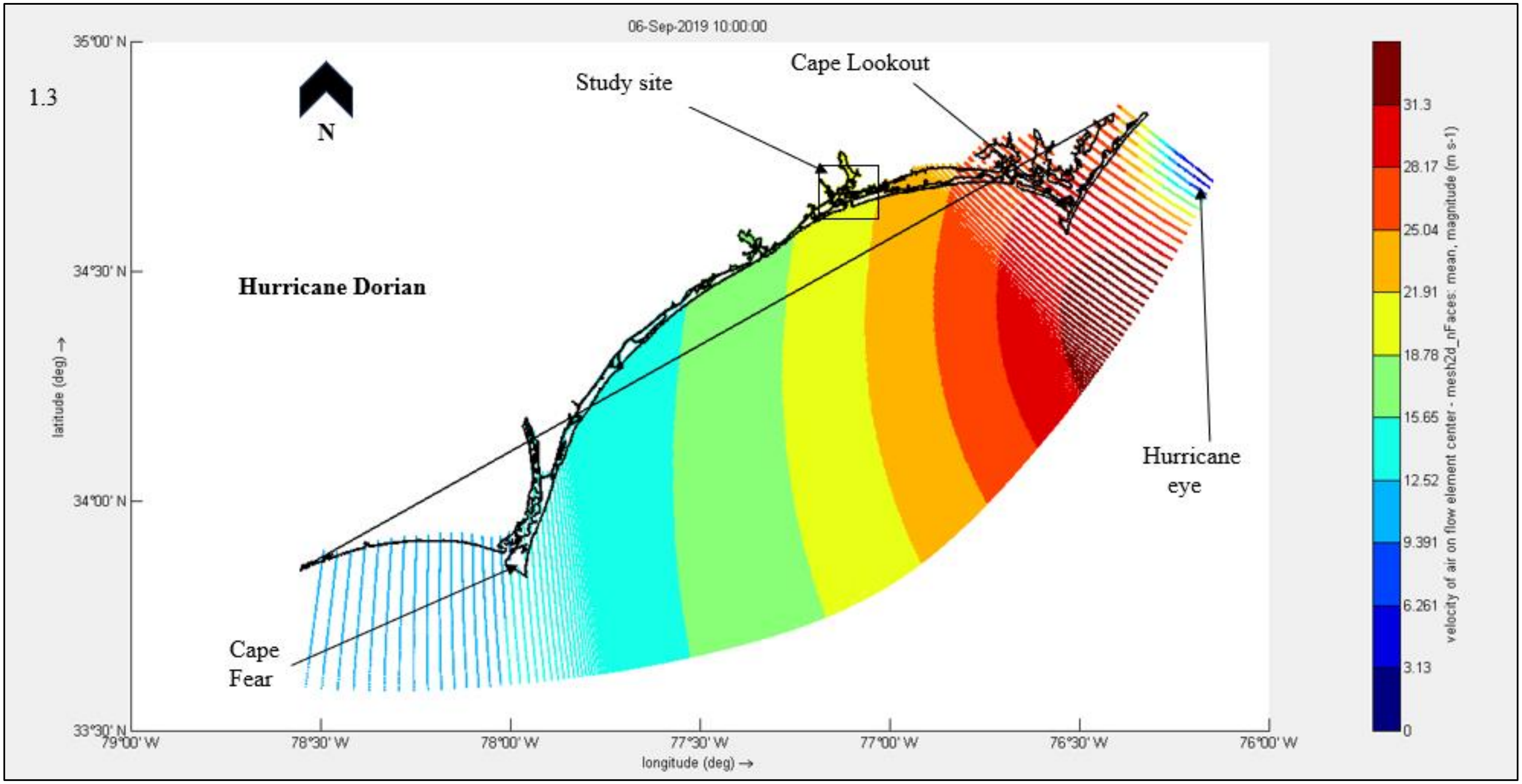
06-Sep-2019 10:00:00
1.3
N
Study site
Cape Lookout
Hurricane Dorian
Hurricane eye
Cape Fear
35°00' N
34°30' N
34°00' N
33°30' N
latitude (deg) →
79°00' W
78°30' W
78°00' W
77°30' W
77°00' W
76°30' W
76°00' W
longitude (deg) →
31.3
28.17
25.04
21.91
18.78
15.65
12.52
9.391
6.261
3.13
0
velocity of air on flow element center - mesh2d_nFaces: mean, magnitude (m s-1)

Appendix E: Grain size distribution and characteristics of Bogue Inlet

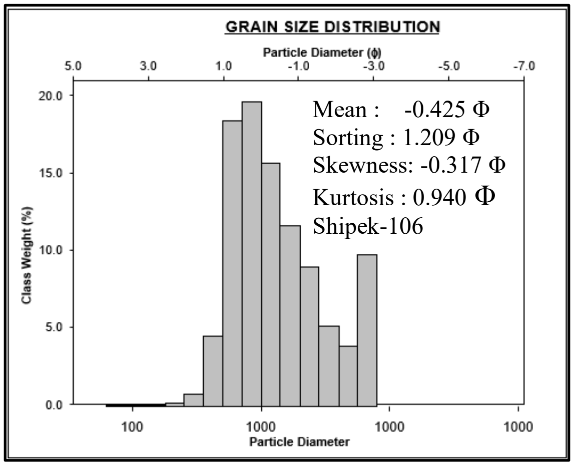

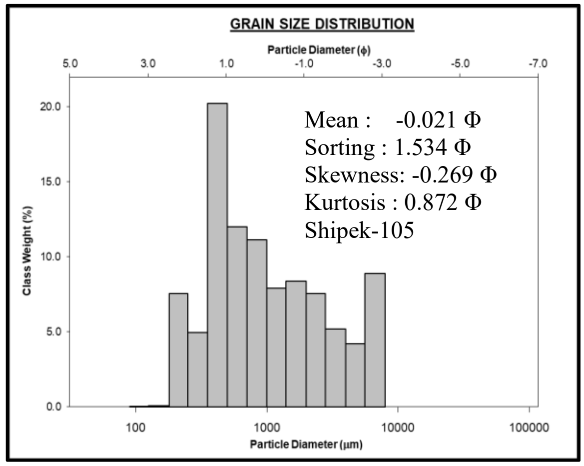

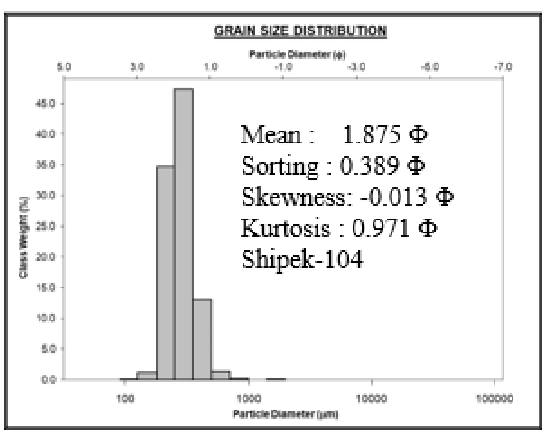

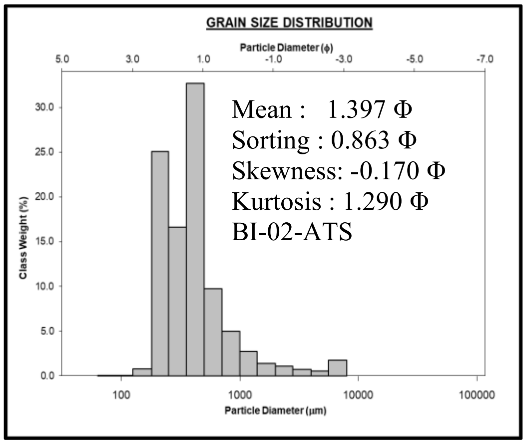
GRAIN SIZE DISTRIBUTION
Particle Diameter (ϕ)
Class Weight (%)
Particle Diameter (μm)
Mean : 1.397 Φ
Sorting : 0.863 Φ
Skewness: -0.170 Φ
Kurtosis : 1.290 Φ
BI-02-ATS

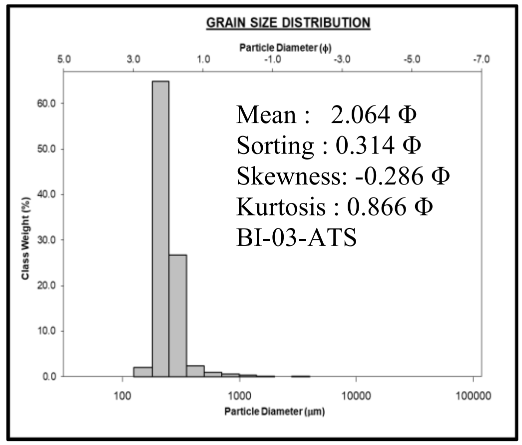
GRAIN SIZE DISTRIBUTION
Particle Diameter (ϕ)
Class Weight (%)
Particle Diameter (μm)
Mean : 2.064 Φ
Sorting : 0.314 Φ
Skewness: -0.286 Φ
Kurtosis : 0.866 Φ
BI-03-ATS


BI-ATS-04
BI-23-06
BI-23-05
BI-23-02
BI-23-07
Bogue Banks
BI-23-03
BI-23-04
BI-23-01
BI-ATS-02
Bear Island
BI-ATS-03
Shipek-106
Shipek-105
Shipek-104
Google Earth
Onslow Bay
1 km
N

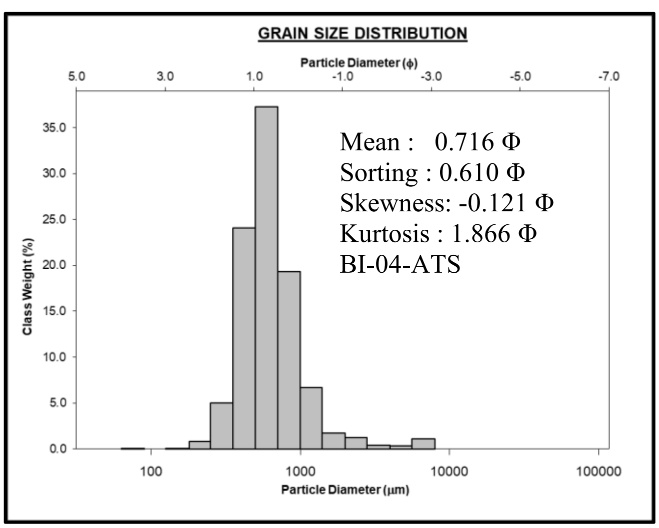
GRAIN SIZE DISTRIBUTION
Particle Diameter (ϕ)
Class Weight (%)
Particle Diameter (μm)
Mean : 0.716 Φ
Sorting : 0.610 Φ
Skewness: -0.121 Φ
Kurtosis : 1.866 Φ
BI-04-ATS

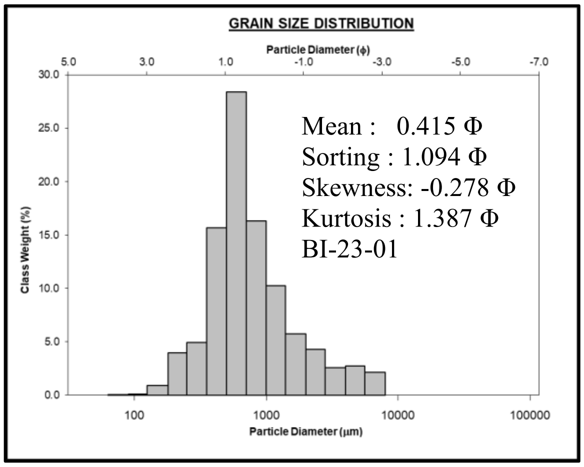
GRAIN SIZE DISTRIBUTION
Particle Diameter (ϕ)
Class Weight (%)
Particle Diameter (μm)
Mean : 0.415 Φ
Sorting : 1.094 Φ
Skewness: -0.278 Φ
Kurtosis : 1.387 Φ
BI-23-01

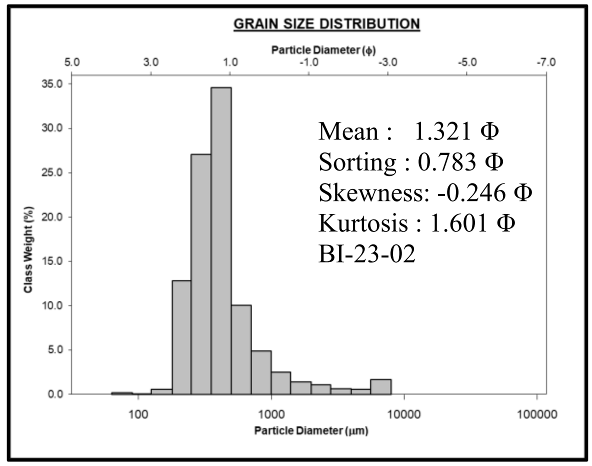
GRAIN SIZE DISTRIBUTION
Particle Diameter (ϕ)
Class Weight (%)
Particle Diameter (μm)
Mean : 1.321 Φ
Sorting : 0.783 Φ
Skewness: -0.246 Φ
Kurtosis : 1.601 Φ
BI-23-02


BI-ATS-04
BI-23-06
BI-23-05
BI-23-02
BI-23-07
Bogue Banks
BI-23-03
BI-23-04
BI-23-01
BI-ATS-02
Shipek-106
BI-ATS-03
Bear Island
Shipek-105
Shipek-104
Google Earth
Onslow Bay
N
1 km

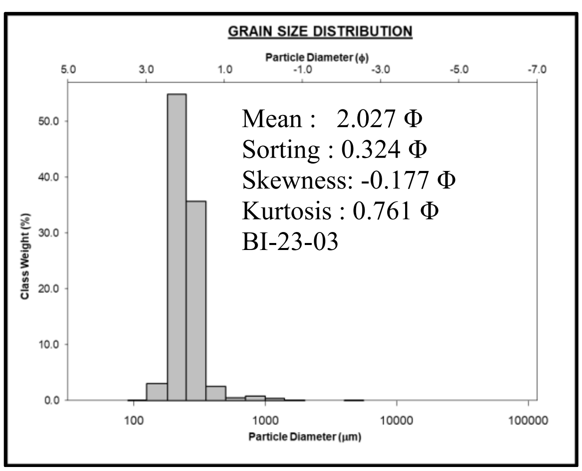
GRAIN SIZE DISTRIBUTION
Particle Diameter (ϕ)
Class Weight (%)
Particle Diameter (μm)
Mean : 2.027 Φ
Sorting : 0.324 Φ
Skewness: -0.177 Φ
Kurtosis : 0.761 Φ
BI-23-03

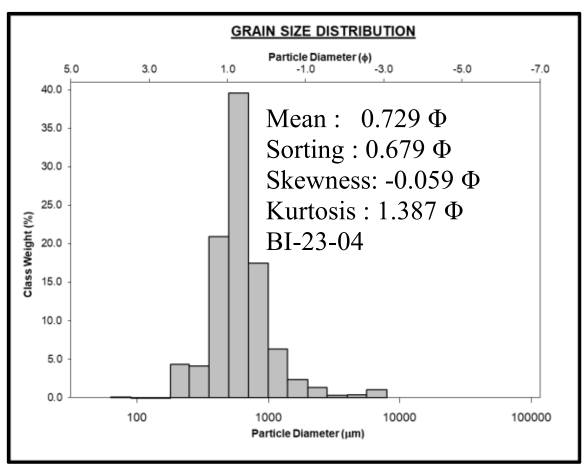
GRAIN SIZE DISTRIBUTION
Particle Diameter (ϕ)
Class Weight (%)
Particle Diameter (μm)
Mean : 0.729 Φ
Sorting : 0.679 Φ
Skewness: -0.059 Φ
Kurtosis : 1.387 Φ
BI-23-04

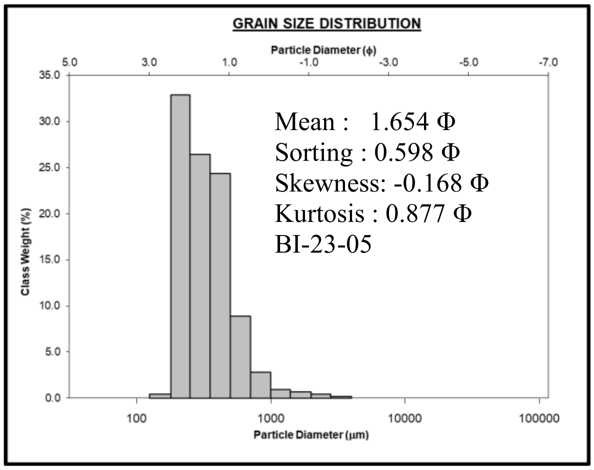
GRAIN SIZE DISTRIBUTION
Particle Diameter (ϕ)
Class Weight (%)
Particle Diameter (µm)
Mean : 1.654 Φ
Sorting : 0.598 Φ
Skewness: -0.168 Φ
Kurtosis : 0.877 Φ
BI-23-05

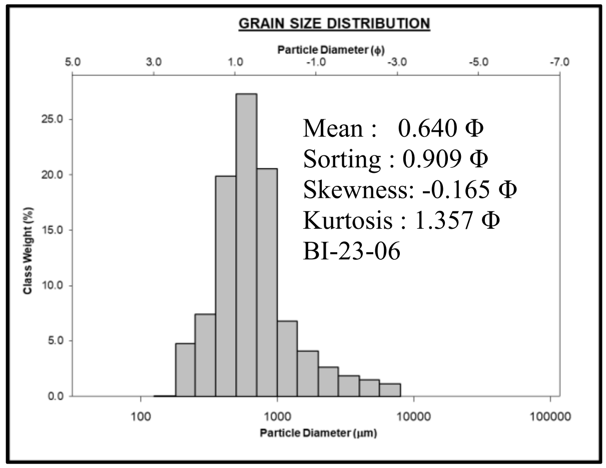
GRAIN SIZE DISTRIBUTION
Particle Diameter (ϕ)
Class Weight (%)
Particle Diameter (µm)
Mean : 0.640 Φ
Sorting : 0.909 Φ
Skewness: -0.165 Φ
Kurtosis : 1.357 Φ
BI-23-06


BI-ATS-04
BI-23-06
BI-23-05
BI-23-02
BI-23-07
Bogue Banks
BI-23-03
BI-23-04
BI-23-01
BI-ATS-02
BI-ATS-03
Shipek-106
Bear Island
Shipek-105
Shipek-104
Google Earth
Image © 2024 Airbus
Image © 2024 TerraMetrics
Onslow Bay
N
1 km

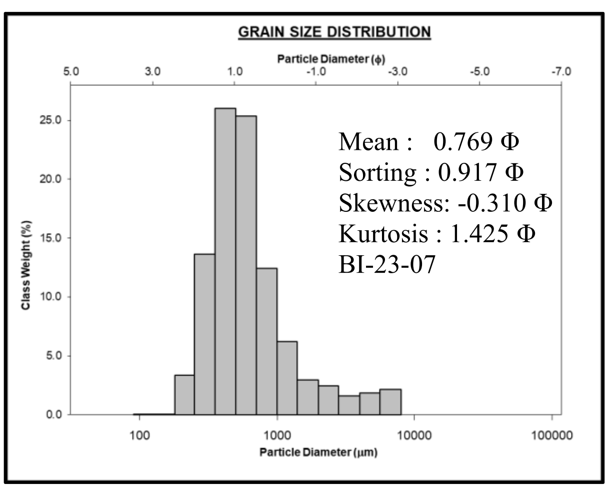
GRAIN SIZE DISTRIBUTION
Particle Diameter (ϕ)
Class Weight (%)
Particle Diameter (µm)
Mean : 0.769 Φ
Sorting : 0.917 Φ
Skewness: -0.310 Φ
Kurtosis : 1.425 Φ
BI-23-07

Appendix F: All modern foraminiferal samples, relative percentage, and locations

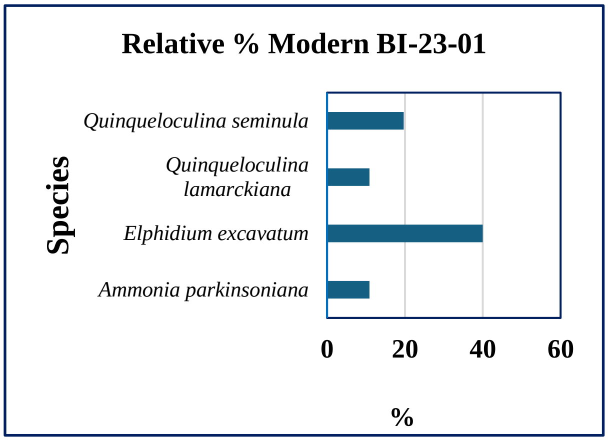

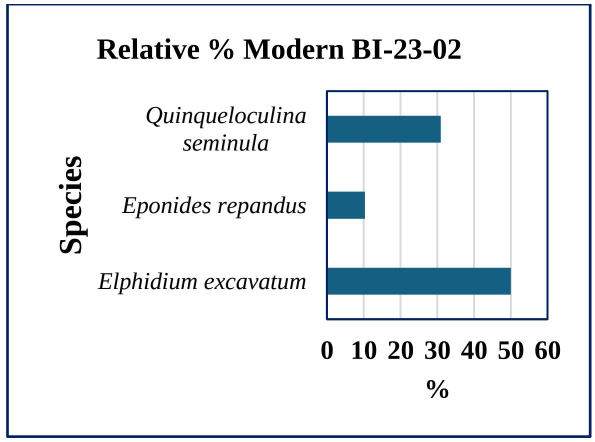

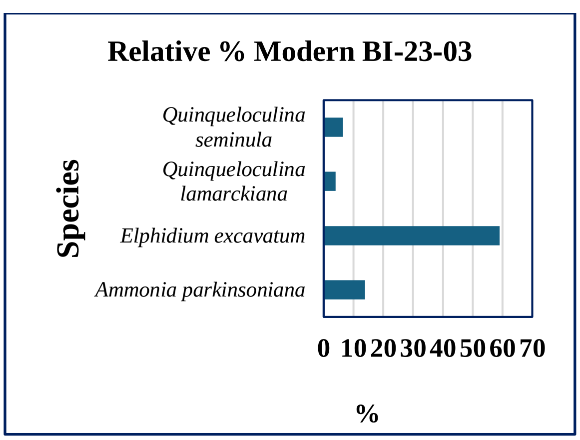

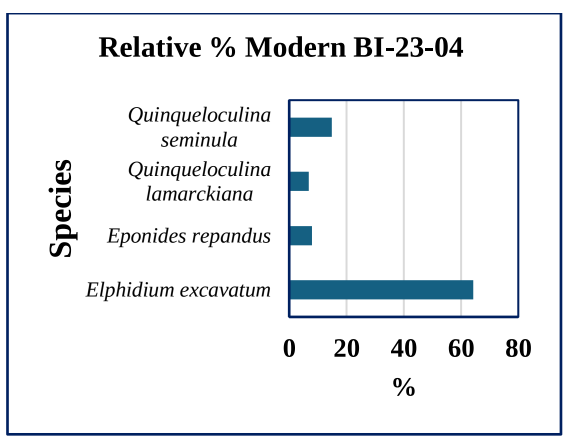

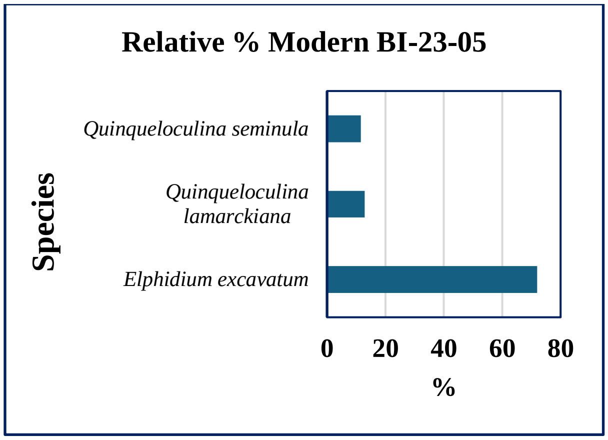
Relative % Modern BI-23-05
Species
Quinqueloculina seminula
Quinqueloculina lamarckiana
Elphidium excavatum
0
20
40
60
80
%

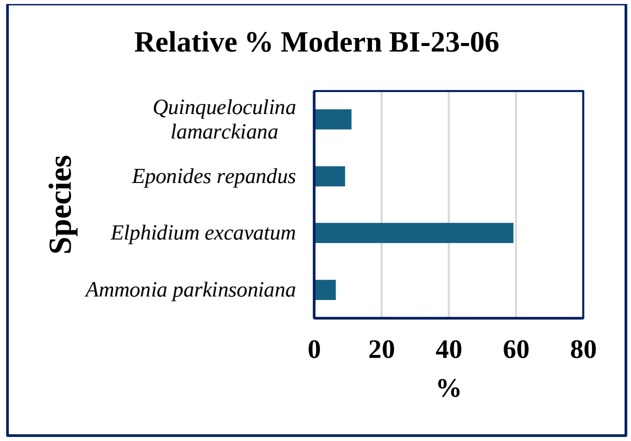
Relative % Modern BI-23-06
Species
Quinqueloculina lamarckiana
Eponides repandus
Elphidium excavatum
Ammonia parkinsoniana
0
20
40
60
80
%


Fossil_Sample_Location
Image 09/2024
BI-ATS-04
BI-ATS-05
BI-23-02
BI-23-04
BI-23-05
BI-23-07
BI-23-03
BI-23-06
BI-23-01
Bear Island
Bogue Banks
Shipek-106
Shipek-105
Shipek-104
Onslow Bay
Google Earth
N
1 km

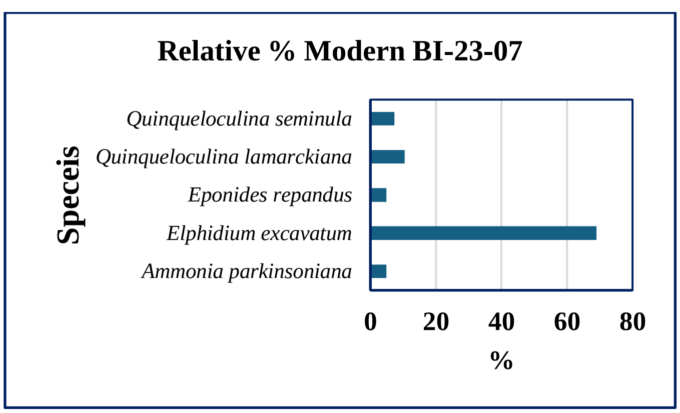
Relative % Modern BI-23-07
Speceis
Quinqueloculina seminula
Quinqueloculina lamarckiana
Eponides repandus
Elphidium excavatum
Ammonia parkinsoniana
0
20
40
60
80
%

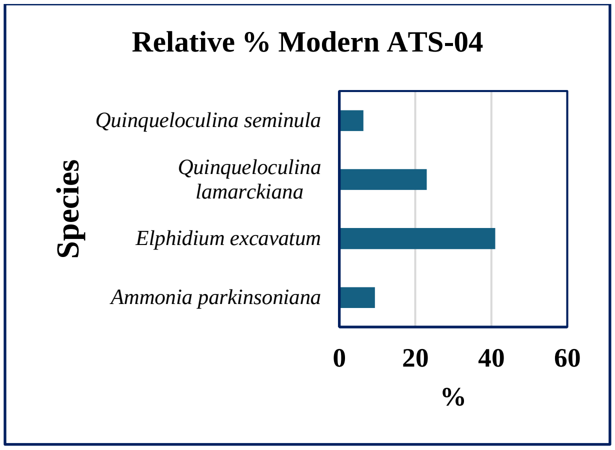
Relative % Modern ATS-04
Species
Quinqueloculina seminula
Quinqueloculina lamarckiana
Elphidium excavatum
Ammonia parkinsoniana
0
20
40
60
%

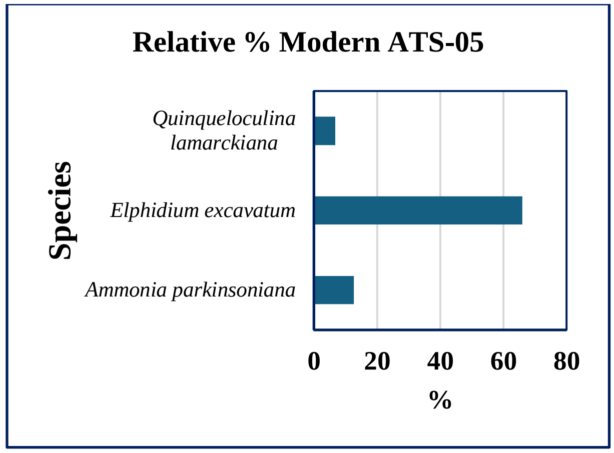
Relative % Modern ATS-05
Species
Quinqueloculina lamarckiana
Elphidium excavatum
Ammonia parkinsoniana
0
20
40
60
80
%


Fossil_Sample_Location
Image 09/2024
BI-ATS-04
BI-ATS-05
BI-23-02
BI-23-04
BI-23-05
BI-23-07
BI-23-03
BI-23-06
BI-23-01
Bear Island
Bogue Banks
Shipek-106
Shipek-105
Shipek-104
Onslow Bay
N
Google Earth
1 km

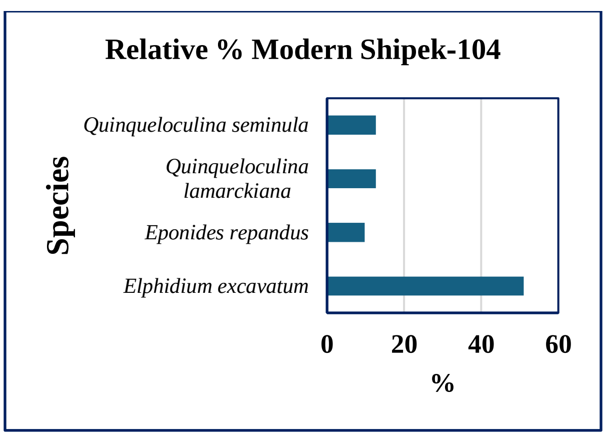
Relative % Modern Shipek-104
Species
Quinqueloculina seminula
Quinqueloculina lamarckiana
Eponides repandus
Elphidium excavatum
0
20
40
60
%

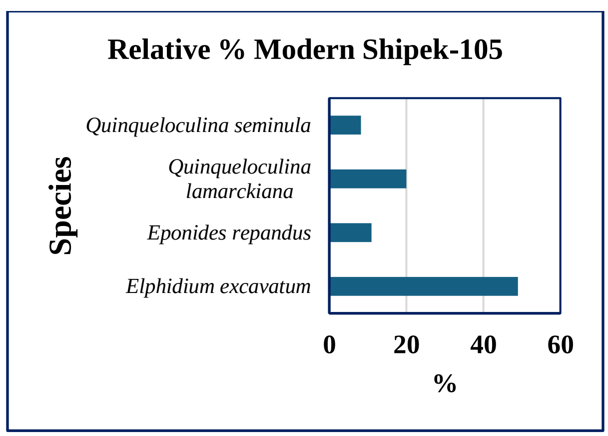
Relative % Modern Shipek-105
Species
Quinqueloculina seminula
Quinqueloculina lamarckiana
Eponides repandus
Elphidium excavatum
0
20
40
60
%